ESTIMATING EXTREME RESPONSES USING A NON-UNIFORM PHASE DISTRIBUTION

by

Laura Kay Alford

A dissertation submitted in partial fulfillment
of the requirements for the degree of
Doctor of Philosophy
(Naval Architecture and Marine Engineering)
in The University of Michigan
2008

Doctoral Committee:

Professor Armin W. Troesch, Chair
Professor Robert F. Beck
Professor Charles R. Doering
Professor William W. Schultz

DEDICATION

In loving memory of my grandparents,
Blanche and Bobby Frazier

ACKNOWLEDGMENTS

This dissertation is the culmination of twenty-two and half years of schooling, starting in kindergarten and continuing through college. It would be utterly impossible for me to thank everyone who has helped me along the way, but there are some people whom I would especially like to thank.

My committe chair, Professor Armin Troesch, has been an unfailingly supportive friend and mentor these past five years. Always ready with enthusiasm, encouragement, and constructive criticism, he has helped me develop his own ideas into some remarkable insights on random processes. I hope I have done them justice.

Professor Charles Doering helped me to organize and focus the results of my research into a coherent story. In doing so, I have gained an even firmer understanding of my findings, and for that I am extremely grateful. Professor Robert Beck enlivened many a meeting and brought his expertise in ship simulations to my aid. Professor William Schultz was an unbiased source of engineering common sense who helped me to see how my work fits within the engineering community.

It has been a joy to be part of the Naval Architecture and Marine Engineering Department for the past nine and a half years. Everyone at the Department has helped me at one time or another, but without Kay Drake I would have lost my sanity a long time ago. I was also fortunate enough to receive funding from the Horace H. Rackham School of Graduate Studies, the National Defense Science and Engineering

Graduate Fellowship, the Naval Architecture and Marine Engineering Department at the University of Michigan, the Office of Naval Research (ONR)-NNRNE Program for Design Loads Generators, the ONR Tools for Multi-Hull Design Optimization Program, and the ONR High-Speed Sea Lift Project.

Mary Beth Snyder has witnessed my whole college career and always reminded me what best friends are for. From BoaS to slurpees to jazz festivals to the Spice Girls . . . it's always a blast. Joseph Tilchen has been a true friend, and despite living three time zones away was always willing to listen to long rambling stories about why simulations wouldn't work. Leigh McCue has been a wonderful source of advice, information, and - most importantly - LaTeXtemplates.

All of my family has been incredibly supportive throughout this time. My grandparents, Fred and Maggie Slavicek, always encouraged me to go as far I could and to do what I want to do. My younger brothers, Matt and Mark Slavicek, never laughed too hard at me because they beat me out of college. My .parents-in-law, Barry Alford and Patricia Taylor, have offered precious advice from their own Ph.D. experiences as well constant support.

My parents, David and Deborah Slavicek, brought me into this world and scrimped and saved that I might receive the best education possible. They then let me go out into the big, big world to make my way. For all of the love, hugs, lightning-speed phone conversations about stuff you have no idea about, and unconditional support I will be forever grateful.

Finally, I must thank my husband, Casey. I could not have done this without you. You were a shoulder to cry on, encouragement, patience, emergency IT support, critic, reality check, chef, pillar of strength, bread-winner, collaborator, and a shelter against the world. I love you.

TABLE OF CONTENTS

CHAPTER

LIST OF FIGURES

Figure

LIST OF TABLES

Table

LIST OF APPENDICES

Appendix

ABSTRACT

Random processes are often modeled as a summation of a finite number of sinusoidal components. Various individual time series are created through the randomly chosen phase angles associated with each component. A specific event of the random process is characterized by the time at which the event happens and the chosen set of phase angles. Together, the time and the phase angle constitute the phase of each component. If many samples of a given event are cataloged, a histogram of the phases can be generated to produce a phase probability density function (PDF) that relates the event to the spectrum of the random process and the number of components used in the simulation.

Simulation of moderately rare events showed the component phase PDFs to be non-uniform and non-identically distributed. These PDFs were modeled using a single parameter, modified Gaussian distribution and used to generate design time series with a specific event at a specific time. To eliminate the need for Monte Carlo simulation, the single parameter of the phase distribution of each component was determined by comparing the PDF of the rare event as calculated using the non-uniform phase distributions to the PDF of the rare event as calculated using Extreme Value Theory. This approach is convenient and efficient as the phase parameters do not have to be estimated via Monte Carlo simulation; it is useful as the parameters can be generated for extremely rare events as easily as moderately rare events. In addition, the comparison to Extreme Value Theory helps to quantify the risk associated with rare events. An example application involving the springing of a Great Lakes bulk carrier shows how the method of non-uniform phases correctly predicts the build up of waves over several periods that produces a large bending moment.

CHAPTER 1

Introduction

1.1 Background

The calculation of design ship responses has taken several traditional forms. Static loads from extreme waves and general guidelines based on previously built ships are two familiar approaches. The advent of more powerful computers and parallel processing has created opportunities for fully nonlinear, physics-based long-term simulation of marine structure responses. However, processing power has not increased so much that brute force simulation is feasible in early design cycles or optimization routines. In recognition of this limitation of simulation, but still needing the information that simulation yields, research has been conducted into generating ship-specific design responses and waves in short time series that can give the same information as long-term simulation.

1.2 Literature Review

Research into design events was originally focused on the generation of freak, or rogue, waves. Part of this research then evolved into design waves in general: generating waves with specific, given characteristics. The approaches used in creating design waves were then applied to generating design *responses*, with linear systems theory allowing for back-calculation of the design wave associated with a given design response.

The following sections focus on existing methods of generating design waves and how they were applied to design responses. Building on this knowledge repository, a new method was devised to emphasize the advantages of previous research and reduce deficiencies.

1.2.1 Design Waves

Tromans et al. [1991] devised a method for predicting the shape of the most likely extreme wave in the immediate vicinity of that same peak. This method is based on linear, broad-banded wave theory and uses probability theory to find the expected value of the wave shape given a particular wave height and zero slope. The random ocean surface is designated as η:

$$\eta(x,y,t) = \sum_{j=1}^{N} \sqrt{2S^{+}(\omega_j)\Delta\omega}\cos(k_j x\cos\theta_j + k_j y\sin\theta_j - \omega_j t + \epsilon_j) \tag{1.1}$$

$S+(\omega_j)$ is the single-sided spectrum that describes the ocean, ω_j is the j^{th} frequency, k_j is the j^{th} wave number, θ_j is the direction of the j^{th} wave, and ϵ_j is a random phase angle uniformly distributed between $-\pi$ and π. Tromans designates $\eta_1(t)$ as the surface elevation at point (x_1, y_1) as a function of time. Suppose a crest passes at some time t_1 ($\eta_1(t_1) = \alpha$ and $\mathrm{d}\eta_1(t_1)/\mathrm{d}t = 0$). The conditional probability of $\eta(t)$ given $\eta_1(t_1) = \alpha$ and $\dot{\eta}_1(t_1) = 0$ is:

$$p(\eta|\eta_1 = \alpha, \dot{\eta}_1 = 0) = \frac{1}{\sqrt{2\pi}\sigma_2}\,\mathrm{e}^{\left(-(\eta^2-\alpha\rho)^2/2\sigma_2^2\right)} \tag{1.2}$$

Equation 1.2[1] is recognized as a Gaussian distribution with a mean of $\alpha\rho$. ρ is

---

[1] See [Tromans *et al.*, 1991] Appendix A for derivation

the autocorrelation function of the original process and defined as:

$$\begin{aligned}\rho(t) &= \Re\left\{\frac{1}{\sigma^2}\int_0^\infty S^+(\omega)\ \mathrm{e}^{i\omega t}\mathrm{d}\omega\right\} && \text{(continuous spectrum)} \\ &\approxeq \frac{1}{\sigma^2}\sum_{j=1}^{N} S^+(\omega)\Delta\omega\cos\omega_j t && \text{(discrete spectrum)} \qquad (1.3)\end{aligned}$$

Therefore, the expected shape of $\eta(t)$, $\mathrm{E}[\eta(t)]$, given a maximum value of α is just the autocorrelation function of the process scaled by α. This result was originally derived analytically by Lindgren [1970] and numerically by Boccotti [1983]. Taylor et al. [1995] inserted this wave profile into any conventionally created random wave train, thus giving the designer the option of producing a more extended irregular wave record.

Another approach to tailoring waves was presented by Steinhagen [2002]. Steinhagen uses the Sequential Quadratic Programming method to optimize the phases associated with an initial random wave train such that the result is the desired extreme waves. Parameters in the optimization include: matching the target wave height, the wavelength of the extreme wave, the maximum crest height, the time of the extreme height, and wavemaker constraints while keeping the phases between $-\pi$ and π . The results, after the optimization routine has run, are the new phases to be used with their respective wave components. This approach was used successfully by Clauss [2002] [2004] in creating the wave train at the wavemaker that results in an extreme wave down-tank. A nonlinear marching technique was then employed to determine the true shape of the wave train down-tank, and this wave train was then used in subsequent numerical experiments.

1.2.2 Design Responses

These approaches are insightful but deal solely with the waves. The response to an extreme wave is still a reasonable prediction of design loads for structures such as offshore platforms since the response is driven primarily by hydrostatic changes. However, for dynamic, moving ships there is no guarantee that the extreme response occurs with the extreme wave. Adegeest et al. [1998] took the natural step of applying Tromans' method to finding the shape of the most likely extreme response. The amplitudes and phases of the incident wave components could then be back-computed via linear theory, giving the tailored wave shape near the desired crest. Pastoor [2002] uses this idea of a most likely extreme response, as well as Volterra models, to predict large responses as part of an overall assessment of nonlinear ship motions and loads. Similarly, Clauss et al. [2003] used the roll response spectrum of the ship to further tailor the waves according to his previous work [Clauss, 2002]. Jensen and Pedersen [2006] employ the First-Order Reliability Method (FORM), often used in structural mechanics, to determine the most likely critical wave episode leading to parametric roll of two containerships.

1.3 Objectives

Computer simulation of ship responses is a valuable tool for designers. As such, it needs to and will be used in early design analysis. In order to efficiently use nonlinear, time domain simulators, short time series of the incident wave profile must be produced such that the design response is achieved. The existing methods of obtaining design responses and their corresponding excitation just described are all sound, but are limited in that they either (A) produce only one design time series, or (B) require a new analysis to produce a new time series. For example, the Tromans model, using the autocorrelation function, has been shown to satisfyingly match the average wave profiles that contain large crests [Pastoor, 2002], but any information on leading or following behavior has been lost due to the averaging process. Any process that builds on this model will also have the same deficiency. The Steinhagen model is theoretically capable of creating random time series, but the optimization scheme must be re-run each time and there is no way to relate the random time series to existing statistics. Neither approach is particularly conducive to quick initial assessment of a potential new ship design.

Ideally, a ship designer would run a single analysis on a particular response, or set of responses, and be able to generate many short time series to then use in additional simulations. The objective of this research is to determine a probabilistic-based algorithm for creating such time series.

This work is based on the main assumption that the wave train that creates a large nonlinear response is similar to the wave train that creates a large linear response [Torhaug *et al.*, 1998]. This assumption is necessary to the methodology as straight-forward, long-term, nonlinear simulation in the time domain is too expensive to use effectively in early design cycles. Therefore, if a large linear response and excitation can by calculated, the search space in the nonlinear time domain can be narrowed to a reasonable period.

This work also, as compared to the most likely extreme response mentioned previously (e.g. [Pastoor, 2002]), generates an ensemble of statistically-equivalent extreme responses. This ensemble, based on the assumptions of stationarity and ergodicity, has a corresponding ensemble of linear design response time series and their associated response-conditioned incident wave trains. Each of these response-conditioned wave trains could then be used by the designer in subsequent nonlinear simulations.

In other words, this approach may be seen as “Round 1” of the analysis of a new design. If the proposed design passes Round 1, it proceeds to “Round 2” - a comprehensive, long-term nonlinear simulation of the design to predict extreme loads. “Round 3” might include model testing.

1.4 Contributions

The research conducted in support of this dissertation was done with an end goal of helping naval architects evaluate potential new designs early in the design cycle. To this end, the method presented here endeavors to create multiple design time series from a single analysis with a minimum of information needed from the designer. Multiple time series means that nonlinear statistics can be generated without costly long-term simulations. A single analysis per case means less wasted resources. A minimum of information means the designer does not have to be an expert in random processes, extreme value theory, and probability to take advantage of the wealth of information available from these research areas.

1.5 Overview

This dissertation begins with an investigation of Monte Carlo simulation of random processes in Chapter 2. In particular, the investigation tries to determine, via numerical simulations, what conditions occur at the time of an extreme value of a random process. Based on these simulations a model is found that re-creates the conditions found in Monte Carlo simulation but without having to actually do the Monte Carlo simulations (Chapter 3). This model allows short time series containing design events to be created with a minimum of information about the random process.

The process of creating design time series is part of a larger methodology of creating design loads for ships or other marine structures. The overall methodology is described in detail with an emphasis on those steps relating to the creation of design time series in Chapter 4. As an example of this methodology, the springing bending moment of a Great Lakes bulk carrier is taken as the desired design response in Chapter 5. The design time series that result from the springing example are compared to those that would have been calculated if the bulk carrier was modeled as a strictly rigid body.

In closing, future research and applications of this method are discussed in Chapter 6. It is a very flexible method and applications are wide-ranging. Also included are appendices that include many examples of this method of creating design time series with extreme values.

CHAPTER 2

Random Processes

2.1 Introduction

The method presented in this paper has its roots in Monte Carlo simulations of extreme events of generic random processes. A general investigation into random simulations of rare events indicates that a specific event, x_m, may be characterized by certain non-uniform phase angle distributions without loss of spectral information. The observations of non-uniform phase angles leads to three hypotheses concerning the relationship between x_m and the finite number of phase angles. These hypotheses are tested, and the results are used to guide the model presented in Chapter 3.

2.2 Monte Carlo Simulation of Random Processes

As previously mentioned, a random process with an associated single-sided frequency spectrum, $S^+(\omega)$, may be approximated by the summation of a finite number of components:

$$x(t) \approxeq \sum_{j=1}^{N} a_j \cos(\omega_j t + \epsilon_j) \tag{2.1}$$

where

$$a_j = \sqrt{2S^+(\omega_j)\Delta\omega} \tag{2.2}$$

and ϵ_j is a random phase angle, uniformly distributed between $-\pi$ and π. The random process can also be described in terms of the moments of its frequency spectrum:

$$m_k = \int_{-\infty}^{\infty} \omega^k S^+(\omega)\mathrm{d}\omega \tag{2.3}$$

The largest value of $x(t)$ that this model can generate is:

$$x_{max} = \sum_{j=1}^{N} a_j \tag{2.4}$$

The random process, $x(t)$, is assumed to be stationary and ergodic. Therefore, the probability density function (PDF) of $x(t)$ is also assumed to be a zero mean, Gaussian distribution,

$$f_x(x) = \frac{1}{\sigma\sqrt{2\pi}}\, \mathrm{e}^{-x^2/2\sigma^2} \tag{2.5}$$

where

$$\sigma^2 = \frac{1}{2}\sum_{j=1}^{N} a_j^2$$

and the cumulative density function (CDF) of $x(t)$ is

$$F_x(x) = \Phi\left(\frac{x}{\sigma}\right) \tag{2.6}$$

For sufficiently large N, the approximation of $x(t)$ in Eq. 2.1 (the right-hand side) can also be considered to be a zero-mean, Gaussian process.

2.2.1 Extreme Value Theory: Large Values vs. Positive Maxima

The stationary and ergodic random process in Eq. 2.1 has an envelope associated with it that tracks the positive maxima and negative minima of the random process (Fig. 2.1). Positive maxima are designated here as $\tilde{x}$ and defined as those values of $x(t)$ where $\dot{x} = 0$ and $\ddot{x} < 0$. If $\tilde{x}$ is expressed in dimensionless form as $\xi = \tilde{x}/\sigma$, Ochi [1990] derives the general PDF and CDF for positive maxima of a Gaussian process

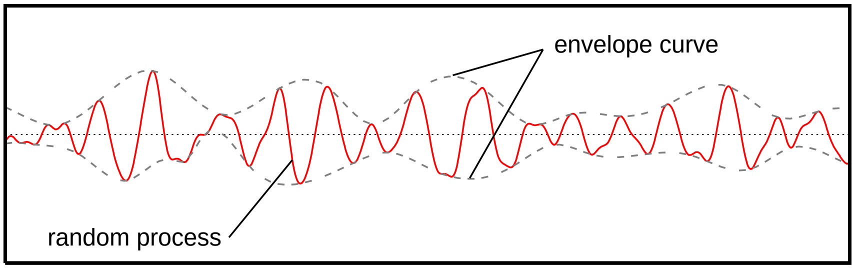

Figure 2.1: A random process, $x(t)$, and its envelope curve, $\tilde{x}(t)$.

as:

$$f_\xi(\xi) = \frac{2}{1+\sqrt{1-\nu^2}}\left[\frac{\nu}{\sqrt{2\pi}}\ \mathrm{e}^{-\xi^2/2\nu^2} + \sqrt{1-\nu^2}\xi\ \mathrm{e}^{-\xi^2/2}\Phi\left(\frac{\sqrt{1-\nu^2}}{\nu}\xi\right)\right] \qquad 0 \le \xi < \infty \tag{2.7}$$

$$F_\xi(\xi) = \frac{2}{1+\sqrt{1-\nu^2}}\left[\frac{1}{2}\left(1-\sqrt{1-\nu^2}\right) + \Phi\left(\frac{\xi}{\nu}\right) - \sqrt{1-\nu^2}\ \mathrm{e}^{-\xi^2/2}\Phi\left(\frac{\sqrt{1-\nu^2}}{\nu}\xi\right)\right], \qquad 0 \le \xi < \infty \tag{2.8}$$

where ν is the bandwidth parameter and is defined in terms of the spectral moments as:

$$\nu = \sqrt{1 - \frac{m_2^2}{m_0 m_4}} \tag{2.9}$$

For example, if the process is narrow-banded, $\nu = 0$ and Eq. 2.7 becomes the Rayleigh distribution:

$$f_\xi(\xi) = \xi\ \mathrm{e}^{-\xi^2/2}, \qquad 0 \le \xi < \infty \tag{2.10}$$

For a wide-band process, $\nu = 1$, and Eq. 2.7 becomes a truncated Gaussian distribution:

$$f_\xi(\xi) = \sqrt{\frac{2}{\pi}}\ \mathrm{e}^{-\xi^2/2}, \qquad 0 \le \xi < \infty \tag{2.11}$$

Continuing from Ochi, the PDF of the largest value in m observations of a random process, z, is defined as:

$$f_{z_m}(z) = m f_z(z) \left(F_z(z)\right)^{m-1} \tag{2.12}$$

Substituting Eqs. 2.5 and 2.6 and expressing x nondimensionally as $\zeta = x/\sigma$ gives the extreme value PDF of the original random process:

$$f_{\zeta_m}(\zeta) = m \frac{1}{\sqrt{2\pi}} \, \mathrm{e}^{-\zeta^2/2} \Big(\Phi(\zeta)\Big)^{m-1} \tag{2.13}$$

Substituting Eqs. 2.7 and 2.8 gives the extreme value PDF of the positive maxima:

$$\begin{aligned} f_{\xi_m}(\xi) = m \frac{2}{1+\sqrt{1-\nu^2}} & \left[\frac{\nu}{\sqrt{2\pi}} \, \mathrm{e}^{-\xi^2/2\nu^2} + \sqrt{1-\nu^2}\xi \, \mathrm{e}^{-\xi^2/2} \Phi\left(\frac{\sqrt{1-\nu^2}}{\nu}\xi\right) \right] \\ & \times \left[\frac{2}{1+\sqrt{1-\nu^2}} \left(\frac{1}{2}\left(1-\sqrt{1-\nu^2}\right) + \Phi\left(\frac{\xi}{\nu}\right) \right. \right. \\ & \qquad \left. \left. - \sqrt{1-\nu^2} \, \mathrm{e}^{-\xi^2/2} \Phi\left(\frac{\sqrt{1-\nu^2}}{\nu}\xi\right) \right) \right]^{m-1} \end{aligned} \tag{2.14}$$

The most likely extreme value in m samples, $\hat{z}_m$, is defined implicitly by:

$$\frac{1}{m} = 1 - F_z(\hat{z}_m) \tag{2.15}$$

Simulating extreme events usually entails looking for the largest value of the random process in a given time period. This extreme value would be, by definition, a maximum. Therefore, one might begin an extreme value investigation by looking to the distribution of the extreme maxima (Eq. 2.14), rather than the distribution of extreme values (Eq. 2.13), as a guide for simulation. Regardless of how the simulation of extreme events is executed, a histogram of the largest observation in m samples should follow the theory compiled by Ochi, either $f_{\zeta_m}(\zeta)$ or $f_{\xi_m}(\xi)$.

A PDF of the extreme value of a process is useful for evaluating statistics and risk-levels, but it cannot describe the specific conditions that caused that extreme value to appear, namely the time of the extreme value, t, and the corresponding phase, ϵ_j. To do that, one has to return to the discrete representation of the random process in Eq. 2.1. If the original process is simulated, then,

$$f_{\zeta_m}(\zeta) \approx P\left(\sum_{j=1}^{N} \frac{a_j}{\sigma}\cos(\omega_j t + \epsilon_j) = \zeta_m\right) \tag{2.16}$$

On the other hand, if only the positive maxima are investigated, then,

$$\begin{aligned} f_{\xi_m}(\xi) \approx P\Bigg(\sum_{j=1}^{N} \frac{a_j}{\sigma}\cos(\omega_j t + \epsilon_j) = \xi_m \Bigg| \sum_{j=1}^{N} -\frac{a_j}{\sigma}\omega_j \sin(\omega_j t + \epsilon_j) = 0, \\ \sum_{j=1}^{N} -\frac{a_j}{\sigma}\omega_j^2 \cos(\omega_j t + \epsilon_j) < 0\Bigg) \end{aligned} \tag{2.17}$$

Determining the PDF of a summation of random variables is difficult, even if the random variables are independent and well-behaved. In this thesis, Eq. 2.16 will be used to determine the phases based on f_{ζ_m} since numerical evaluation of Eq. 2.17 is beyond the scope of this work.

One way of investigating the effect of requiring extreme values to also be maxima is to look at the difference between the left-hand sides of Eqs. 2.16 and 2.17. It so happens that the left-hand sides of Eqs. 2.16 and 2.17 are similarly shaped if their peak values are the same. Consider the following exercise. A Gaussian distribution, a truncated Gaussian distribution, and a Rayleigh distribution are each used to calculate an extreme value PDF (all distributions have been non-dimensionalized). The Gaussian distribution describes a random process, ζ, and the truncated Gaussian and Rayleigh distributions describe the associated envelope curves, ξ, if $\nu = 1$ and $\nu = 0$, respectively. To determine m for each of these three cases, Eq. 2.15 is used with $\hat{z}_m = \alpha$, where $\alpha = 3, 4, 5, 6$. This is equivalent to saying the most likely extreme value in m samples is a 3σ, 4σ, 5σ, 6σ event. Because each of these three distributions have different CDFs, m will be a different number as determined by Eq. 2.15.

Table 2.1 summarizes the number of samples, m, as a function of α and the type of distribution.

$\hat{\zeta}_m$ or $\hat{\xi}_m$ α	ζ: Gaussian	ξ: Truncated Gaussian $\nu = 1$	ξ: Rayleigh $\nu = 0$
3.0	740	370	90
4.0	3.16e4	1.58e4	2980
5.0	3.49e6	1.75e6	2.68e5
6.0	1.01e9	5.05e8	6.56e7

Table 2.1: Number of observations, m.

For each case in Table 2.1, the extreme value PDF is calculated based on m and according to Eq. 2.13 or Eq. 2.14. A comparison of the Gaussian distribution to the truncated Gaussian distribution is shown in Fig. 2.2; the Gaussian distribution as compared to the Rayleigh distribution is shown in Fig. 2.3. In the limiting case of $\nu = 1$, the extreme value PDFs of the Gaussian distribution match those of the truncated Gaussian due to the nature of the two distributions ($m_{trunc.Gaussian} = m_{Gaussian}/2$). In the limiting case of $\nu = 0$, the extreme value PDFs from the Gaussian distribution are slightly more “peaky” than those of the Rayleigh distribution for lower values of α, but become a better match as α increases.

This exercise demonstrates that, given a target event, the extreme value PDF looks essentially the same regardless of whether it is based on extreme values of the process or extreme positive maxima. Since the end goal was to relate an extreme value PDF to the unknown conditions that cause an extreme value in a discrete representation of a random process, it was decided to first concentrate on generating extreme events. The effects of t and ϵ_j can therefore be calculated using the less complex PDF of Eq. 2.16.

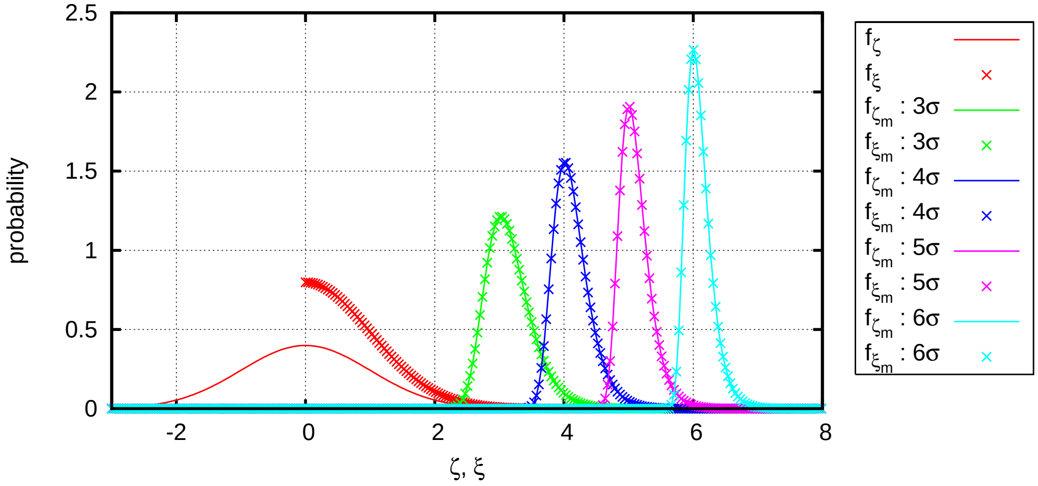

Figure 2.2: Comparison of extreme value PDFs of a random process with a Gaussian distribution and its envelope curve; $\nu = 1$. Lines represent the PDFs of the process and symbols represent the PDFs of the envelope curve.

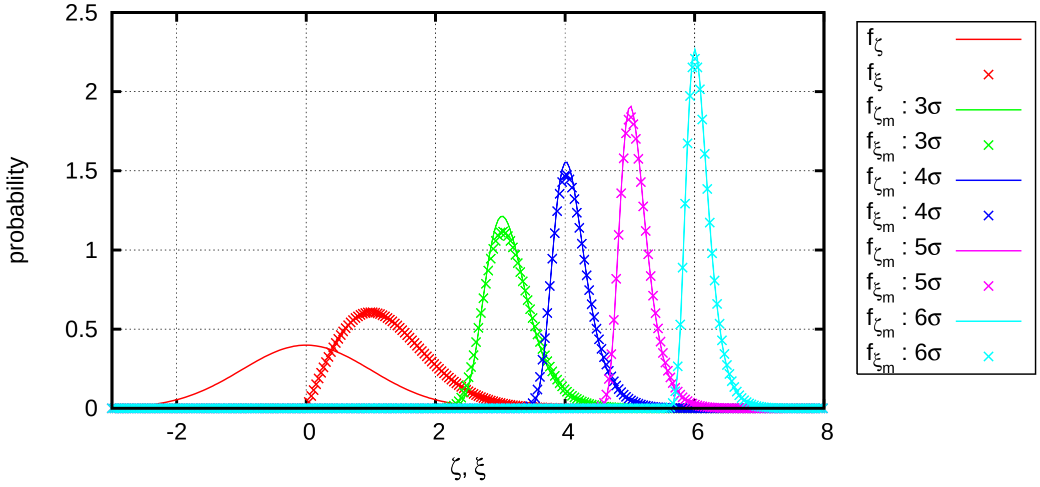

Figure 2.3: Comparison of extreme value PDFs of a random process with a Gaussian distribution and its envelope curve; $\nu = 0$. Lines represent the PDFs of the process and symbols represent the PDFs of the envelope curve.

2.2.2 Conditions That Cause Extreme Events

A typical time series generated by Eq. 2.1 is shown in Fig. 2.4. To determine how to create a time series that has a specific value at a particular time, consider an event x_1 that occurs at time t_1 (Fig. 2.5). x_1 is defined as:

$$x_1 \equiv x(t_1) = \sum_{j=1}^{N} a_j \cos(\omega_j t_1 + \epsilon_j) \tag{2.18}$$

x_1 is a random instant of the Gaussian process $x(t)$. Therefore, x_1 is a random variable with the same Gaussian distribution as $x(t)$. Since $x(t)$ is considered to be a stationary and ergodic process, statistics related to the distribution of x_1 can be considered to be equivalent to statistics of $x(t)$. The time series that contains x_1 at time $t = 0$ may be constructed utilizing the following change of variables:

$$t' = t - t_1 \tag{2.19}$$

Substituting for t in Eq. 2.1 yields:

$$x(t') = \sum_{j=1}^{N} a_j \cos(\omega_j (t' + t_1) + \epsilon_j) \tag{2.20}$$

$$x(t') = \sum_{j=1}^{N} a_j \cos(\omega_j t' + \omega_j t_1 + \epsilon_j) \tag{2.21}$$

Defining a new phase, ϵ'_j, as:

$$\epsilon'_j \equiv \omega_j t_1 + \epsilon_j \tag{2.22}$$

results in $x(t')$ being written as:

$$x(t') = \sum_{j=1}^{N} a_j \cos(\omega_j t' + \epsilon'_j) \tag{2.23}$$

The question, then, is, “What is the effect of t_1 on the distribution of ϵ'_j?” To answer this question, first allow the choice of t_1 to be unconstrained. In this case, t_1 is a random number as is $\omega_j t_1$. Since ϵ_j is uniformly distributed, and adding a

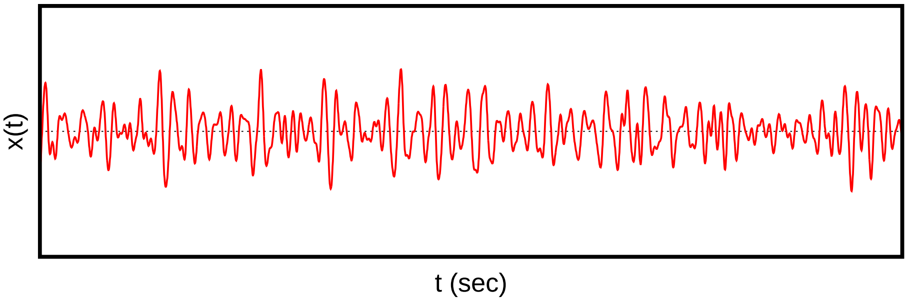

Figure 2.4: A typical random time series.

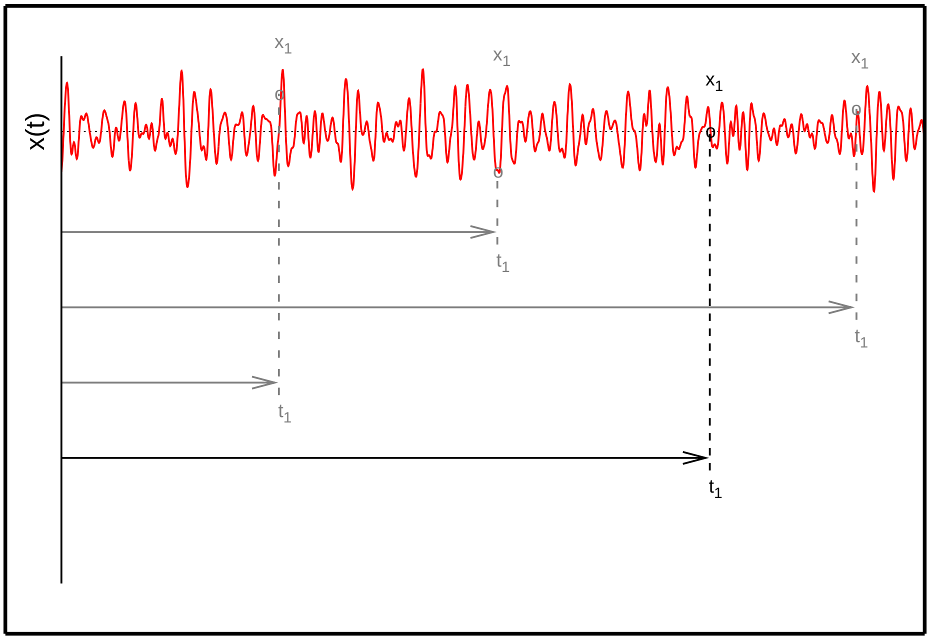

Figure 2.5: Random events of a typical time series as determined by t_1.

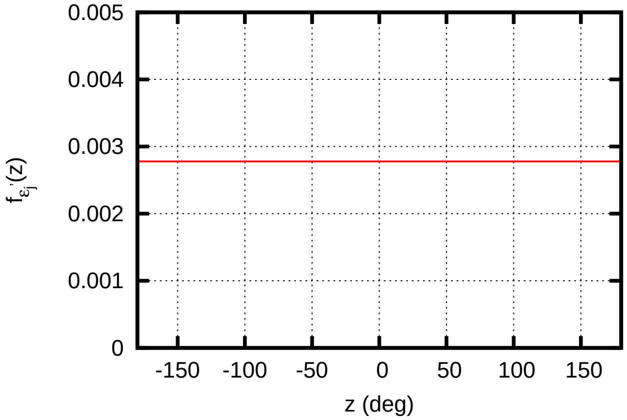

Figure 2.6: Effect of t_1 on ϵ_j': t_1 is unconstrained, resulting in a uniform distribution for ϵ_j'.

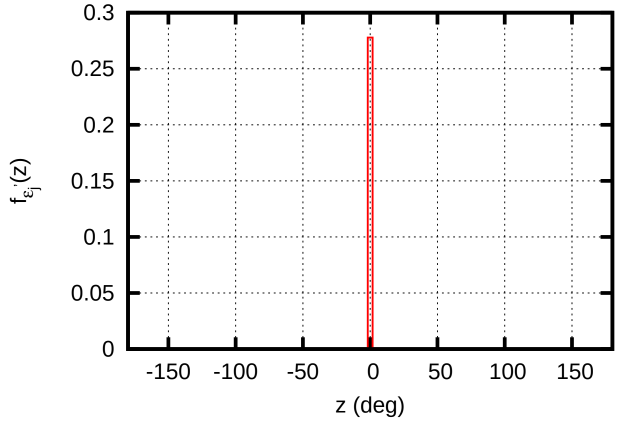

Figure 2.7: Effect of t_1 on ϵ_j': t_1 is the location of x_{max}, resulting in the distribution for ϵ_j' being a delta function.

number to a uniform distribution results in a uniform distribution, ϵ_j' is also uniformly distributed (see Fig. 2.6).

Now consider if t_1 is the location of $x(t) = x_{max}$. In this case, $\omega_j t_1 + \epsilon_j$ has to equal zero for $j = 1, 2, \cdots N$. Therefore, ϵ_j' must also be zero for all j, and the resulting PDF of ϵ_j' is a delta function (see Fig. 2.7).

However, a designer will be interested in a **specific value** of $x(t_1)$ that is **less than** x_{max}. So, what does the distribution of ϵ_j' look like in this case? It is assumed that the distribution morphs from a uniform distribution to a delta function as $x_1 \rightarrow x_{max}$, but what, exactly, is this transformation?

In the following analysis, the target value of x_1 is actually x_m, the largest value of x_1 in m samples. x_m is itself a random variable whose PDF may be calculated via Extreme Value Theory [Ochi, 1990]:

$$f_{x_m}(x) = m f_x(x) \left(F_x(x)\right)^{m-1} \tag{2.24}$$

Substituting Eqs. 2.5 and 2.6 gives:

$$f_{x_m}(x) = m \frac{1}{\sigma\sqrt{2\pi}} \, \mathrm{e}^{-x^2/2\sigma^2} \left(\Phi\left(\frac{x}{\sigma}\right)\right)^{m-1} \tag{2.25}$$

The most likely extreme value in m samples, $\hat{x}_m$, is defined implicitly by:

$$\frac{1}{m} = 1 - F_x(\hat{x}_m) \tag{2.26}$$

In this example,

$$\frac{1}{m} = 1 - \Phi\left(\frac{\hat{x}_m}{\sigma}\right) \tag{2.27}$$

Equation 2.27 states that the designer need specify either m or $\hat{x}_m$ to determine Eq. 2.25.

2.3 Determining Phase PDFs

For a particular value of x_1, t_1 is unknown. However, in t'-space, x_1 will always occur at zero regardless of the value of t_1. Therefore, histograms of ϵ'_j may be generated by directly simulating Eq. 2.23. In fact, because x_1 will always occur at $t' = 0$, Eq. 2.23 may be reduced to:

$$x_1 = x(t' = 0) = \sum_{j=1}^{N} a_j \cos(\epsilon'_j) \tag{2.28}$$

2.3.1 Investigating the Nature of Phase PDFs

To examine what sort of phase distribution leads to x_m values, m samples of x_1 are taken, and the set of ϵ'_j that corresponds to the largest of these samples is saved. This process is repeated many times to generate a subset of ϵ'_j that correspond to instances of x_m.

Hypothesis 1. *For a given value of* $\boldsymbol{m}$*, the phases,* ϵ'_j*, are independent and identically distributed (iid). In other words,*

$$f_{\epsilon'_1\epsilon'_2\cdots\,\epsilon'_N}(z_1, z_2, \cdots, z_N|x_m) = f_{\epsilon'}(z_1|x_m)f_{\epsilon'}(z_2|x_m)\cdots f_{\epsilon'}(z_N|x_m) \tag{2.29}$$

The validity of Hypothesis 1 may be checked by generating a phase histogram corresponding to a given extreme value and then using that phase histogram, in lieu of the original uniform distribution, to directly calculate a set of x_m. If Hypothesis 1 is correct, the PDF of x_m generated from Hypothesis 1 will match $f_{x_m}(x)$ in Eq. 2.25.

To generate the phase histogram corresponding to an x_m event, Eq. 2.28 is calculated using a uniform distribution for ϵ'_j. In the example that follows, a_j is determined from an ITTC Sea State 3 spectrum ($h_{peak} = 0.88$, $T_{peak} = 7.5$) with $N = 101$. Other examples, using more severe sea states and different spectra altogether, may be found in Appendix A. The frequencies, ω_j, are equally spaced and are bounded by $\omega_{min} \leq \omega_j \leq \omega_{max}$. ω_{min} and ω_{max} are defined as the smallest and largest frequency such that $S^+(\omega_{min}) = S^+(\omega_{max}) = 0.001S^+(\omega_{peak})$. Also, $m = 740$, which corresponds to the peak value of $f_{x_m}(x)$ being 3.0σ (more examples with different parameters may be found in Appendix A). 78,000,000 total samples of x_1 were generated, so there are $M = 50,000$ samples of x_m.

Figure 2.9 shows the phase histogram of all ϵ'_j that result from this set of parameters. This phase distribution is decidedly non-uniform and looks rather like a

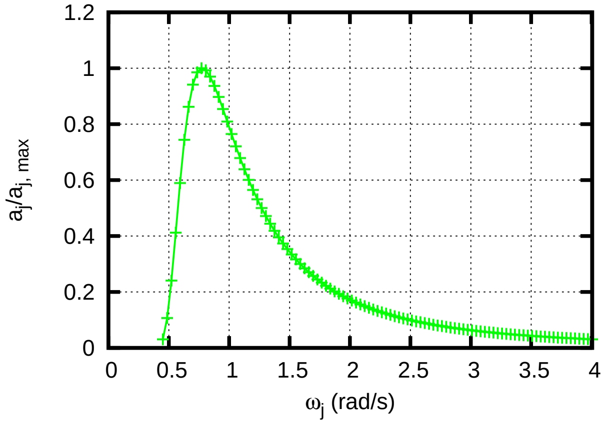

Figure 2.8: Amplitudes corresponding to ITTC Sea State 3: $h_{peak} = 0.88$, $T_{peak} = 7.5$, $N = 101$.

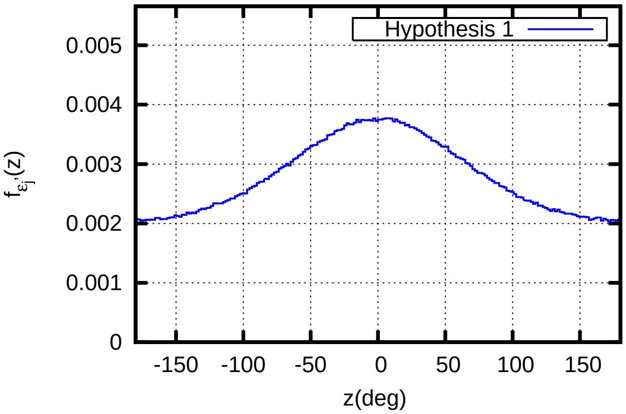

Figure 2.9: Phase histogram for Hypothesis 1. ITTC Sea State 3: $h_{peak} = 0.88$, $T_{peak} = 7.5$, $N = 101$, $m = 740$ (a 3.0σ event). $M = 50,000$ samples.

Gaussian distribution perched on top of a uniform distribution. The phase distribution in Fig. 2.9 was then used to directly generate ϵ_j' in Eq. 2.28. The resulting PDF of x_1 is plotted against that of x_m, as calculated from Eq. 2.12, in Fig. 2.10. Visually, it is clear that $f_{x_1}(x) \neq f_{x_m}(x)$. The results shown in Appendix A are similar because x has been non-dimensionalized on σ.

One quantitative measurement between two PDFs is the Kullback-Leibler divergence (also known as information divergence, information gain, or relative entropy)

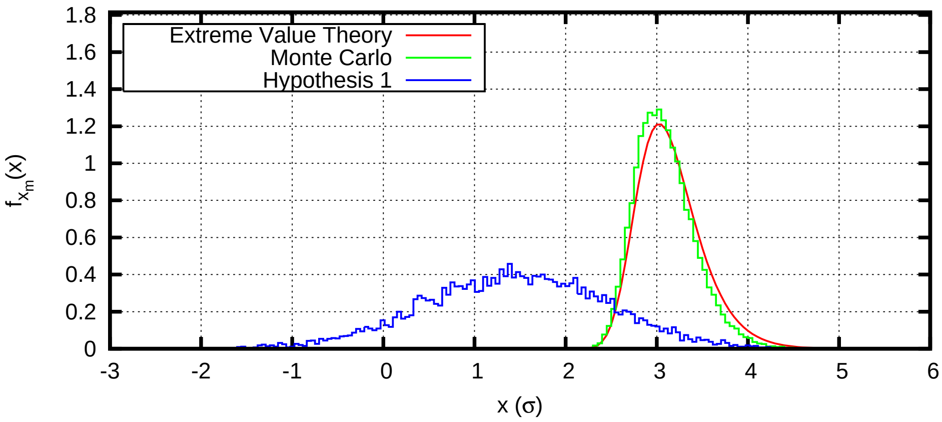

Figure 2.10: Comparison of $f_{x_m}(x)$, denoted "Extreme Value Theory", and $f_{x_1}(x)$ as calculated by Hypothesis 1. ITTC Sea State 3: $h_{peak} = 0.88$, $T_{peak} = 7.5$, $N = 101$, $m = 740$ (a 3.0σ event). $M = 50,000$ samples.

[Kullback & Leibler, 1951]. The Kullback-Leibler divergence between two PDFs, P and Q, is denoted as $D_{KL}(P\|Q)$. $D_{KL}(P\|Q)$ is defined for continuous functions as:

$$D_{KL}(P\|Q) = \int_{-\infty}^{\infty} p(x) \ln \frac{p(x)}{q(x)} \mathrm{d}x \tag{2.30}$$

In Eq. 2.30, P is typically the target PDF, and Q would be the estimated PDF. Substituting $f_{x_m}(x)$ for P and $f_{x_1}(x)$ for Q yields:

$$D_{KL}(f_{x_m}(x)\|f_{x_1}(x)) = \int_{-\infty}^{\infty} f_{x_m}(x) \ln \frac{f_{x_m}(x)}{f_{x_1}(x)} \mathrm{d}x \tag{2.31}$$

$D_{KL}(f_{x_m}(x)\|f_{x_1}(x)) = 0$ indicates a perfect match; for this example where $m = 740$, $D_{KL}(f_{x_m}(x)\|f_{x_1}(x)) = 1.76$. The discrepancy between $f_{x_m}(x)$ and $f_{x_1}(x)$ indicates that Hypothesis 1 is incorrect.

Hypothesis 2. *For a given value of* $\boldsymbol{m}$, *the phases,* ϵ'_j, *are independent and non-identically distributed (inid). In other words,*

$$f_{\epsilon'_1\epsilon'_2\cdots\ \epsilon'_N}(z_1, z_2, \cdots, z_N|x_m) = f_{\epsilon'_1}(z_1|x_m) f_{\epsilon'_2}(z_2|x_m) \cdots f_{\epsilon'_N}(z_N|x_m) \tag{2.32}$$

Hypothesis 2, may be tested in the same manner as Hypothesis 1. Consequently, the same simulation is carried out as was done to test Hypothesis 1; however, now ϵ'_j is separated by component. Each component, therefore, has its own phase histogram. Figure 2.11 shows the component phase histograms that resulted from the same conditions as before: ITTC Sea State 3 spectrum ($h_{peak} = 0.88$, $T_{peak} = 7.5$) with $N = 101$ and $m = 740$, corresponding to the peak value of $f_{x_m}(x)$ being 3.0σ, and $M = 50,000$ (more examples with different parameters may be found in Appendix A). Clearly, the phase distributions vary by component. Components with large amplitudes (see Fig. 2.8) have phase distributions that are focused about $\epsilon'_j = 0$, while components that are small retain their near-uniform distribution. Those components with non-uniform distributions look like Gaussian-type distributions, similar to the distribution seen in Fig. 2.9.

As before, the phase distributions in Fig. 2.11 are used to directly generate ϵ'_j in Eq. 2.28 and estimate the PDF of x_1. Figure 2.12 shows the comparison between $f_{x_m}(x)$ and the new PDF of x_1. Visually, this $f_{x_1}(x)$ is much improved over the $f_{x_1}(x)$ in Fig. 2.10. Quantitatively, $D_{KL}(f_{x_m}(x) \| f_{x_1}(x)) = 0.39$, showing the distinct improvement over the results with Hypothesis 1. However, $f_{x_1}(x)$ still does not equal $f_{x_m}(x)$, it is far too broad, meaning that Hypothesis 2 is also incorrect.

Hypothesis 3. *For a given value of* $\boldsymbol{m}$, *the phases,* ϵ'_j, *are fully and jointly distributed. In other words,*

$$f_{\epsilon'_1 \epsilon'_2 \cdots \epsilon'_N}(z_1, z_2, \cdots, z_N | x_m) = f(z_1, z_2, \cdots, z_n, a_1, a_2, \cdots, a_N | x_m) \tag{2.33}$$

Hypothesis 3 may, in theory, be tested in the same manner as Hypotheses 1 and 2. However, this would require estimating the joint phase PDF as an N-dimensional phase histogram and this is difficult to do. For example, if the range

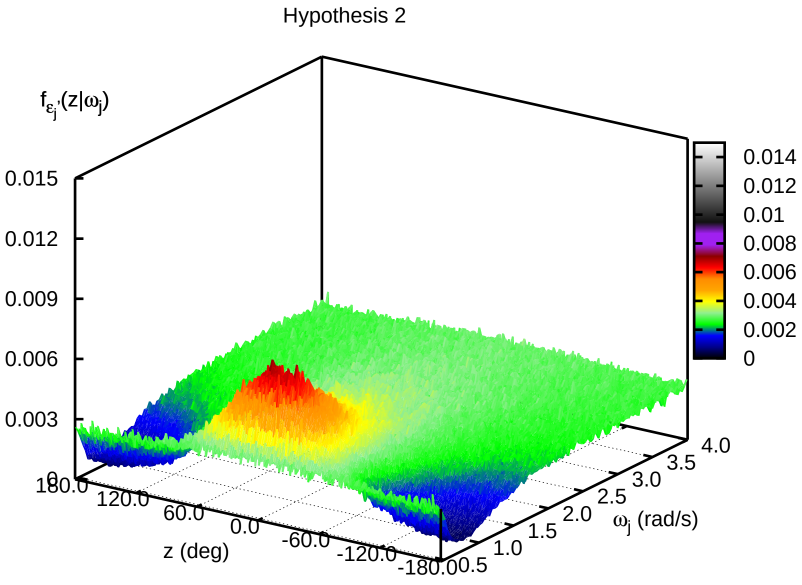

Figure 2.11: Phase histogram for Hypothesis 2. ITTC Sea State 3: $h_{peak} = 0.88$, $T_{peak} = 7.5$, $N = 101$, $m = 740$ (a 3.0σ event). $M = 50,000$ samples.

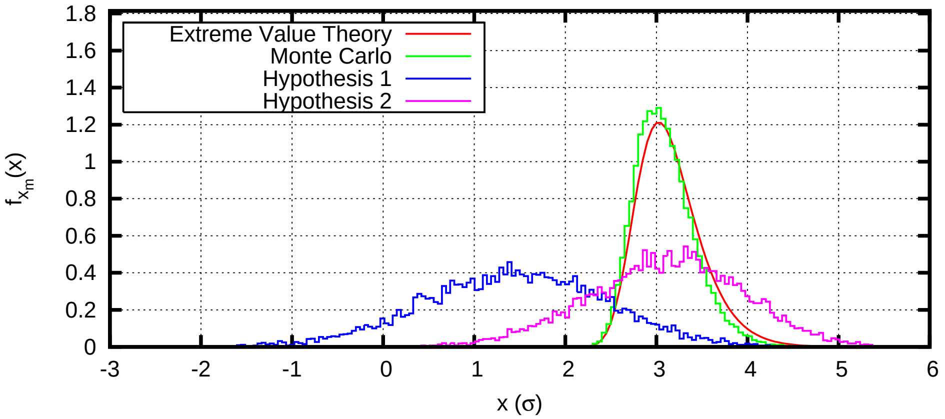

Figure 2.12: Comparison of $f_{x_m}(x)$, denoted "Extreme Value Theory", and $f_{x_1}(x)$ as calculated by Hypotheses 1 and 2. ITTC Sea State 3: $h_{peak} = 0.88$, $T_{peak} = 7.5$, $N = 101$, $m = 740$ (a 3.0σ event). $M = 50,000$ samples.

of ϵ'_j is coarsely split into 10 intervals, then the number of "bins" required to estimate $f_{\epsilon'_1\epsilon'_2\cdots\ \epsilon'_N}(z_1, z_2, \cdots, z_N|x_m)$ is 10^N. If N is as few as 10, then 10,000,000,000 bins are required to estimate $f_{\epsilon'_1\epsilon'_2\cdots\ \epsilon'_N}(z_1, z_2, \cdots, z_N|x_m)$ (compared to $10 \times N = 100$ bins to generate a histogram similar to that in Fig. 2.11). On top of this, a sufficient number of samples would need to be generated to populate the 10,000,000,000 bins. The generation of this data is not feasible in this work.

It should be possible, however, to at least obtain an idea of the correlations that exist between component phases, even if the actual dependencies are unknown. The correlation function between the phases ϵ'_1 and ϵ'_2 is defined as:

$$\rho_{\epsilon'_1,\epsilon'_2} = \frac{E(\epsilon'_1\epsilon'_2) - E(\epsilon'_1)E(\epsilon'_2)}{\sqrt{E({\epsilon'_1}^2) - E(\epsilon'_1)^2}\sqrt{E({\epsilon'_2}^2) - E(\epsilon'_2)^2}} \tag{2.34}$$

$$\rho_{\epsilon'_1,\epsilon'_2} = \frac{M\sum_{k=1}^{M}\epsilon'_{1k}\epsilon'_{2k} - \left(\sum_{k=1}^{M}\epsilon'_{1k}\right)\left(\sum_{k=1}^{M}\epsilon'_{2k}\right)}{\sqrt{M\sum_{k=1}^{M}{\epsilon'_{1k}}^2 - \left(\sum_{k=1}^{M}\epsilon'_{1k}\right)^2}\sqrt{M\sum_{k=1}^{M}{\epsilon'_{2k}}^2 - \left(\sum_{k=1}^{M}\epsilon'_{2k}\right)^2}} \tag{2.35}$$

In general, for the phases ϵ'_i and ϵ'_j, the correlation function is:

$$\rho_{\epsilon'_i,\epsilon'_j} = \frac{M\sum_{k=1}^{M}\epsilon'_{ik}\epsilon'_{jk} - \left(\sum_{k=1}^{M}\epsilon'_{ik}\right)\left(\sum_{k=1}^{M}\epsilon'_{jk}\right)}{\sqrt{M\sum_{k=1}^{M}{\epsilon'_{ik}}^2 - \left(\sum_{k=1}^{M}\epsilon'_{ik}\right)^2}\sqrt{M\sum_{k=1}^{M}{\epsilon'_{jk}}^2 - \left(\sum_{k=1}^{M}\epsilon'_{jk}\right)^2}} \tag{2.36}$$

To investigate the correlation between all pairs of phase components, Eq. 2.36 is calculated for $i = 1, 2, \cdots, N$ and $j = 1, 2, \cdots, N$. The result of this calculation is shown in Fig. 2.13. It is clear that no pairs of phases are correlated except for the trivial case of $i = j$ in which they are perfectly correlated, as they should be. Although Figure 2.13 indicates that the phase angles are uncorrelated, this does not mean that the phases are independent.

Returning to Fig. 2.12, the PDF of x_1 from Hypothesis 2 is not unusable from an engineering standpoint. The expected value $f_{x_1}(x)$ is near the expected value of $f_{x_m}(x)$, although $f_{x_1}(x)$ is much broader than the target PDF, $f_{x_m}(x)$. In practice, this

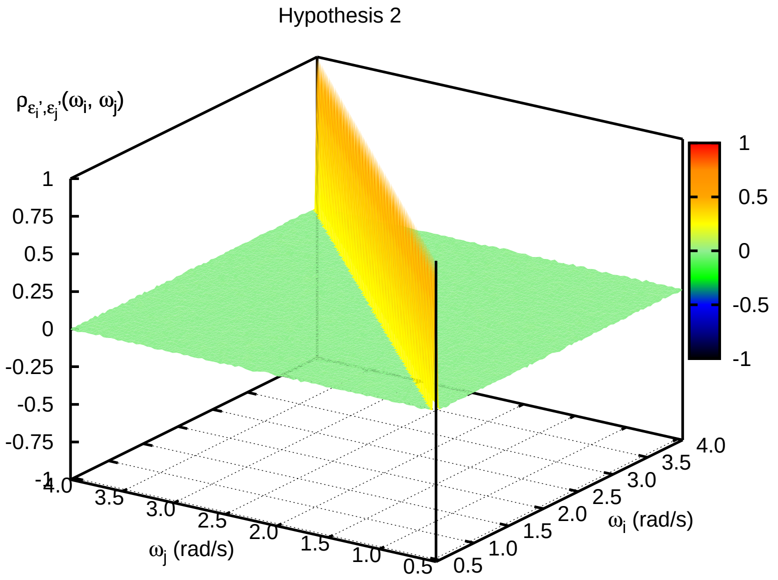

Figure 2.13: Correlation of phase pairs (ϵ_i',ϵ_j') for Hypothesis 2. ITTC Sea State 3: $h_{peak} = 0.88$, $T_{peak} = 7.5$, $N = 101$, $m = 740$ (a 3.0σ event). $M = 50,000$ samples.

would result in more "scatter" when generating x_1 values from the non-uniform distributions of ϵ_j', but this an improvement since generating x_1 from uniformly distributed phases results in a Gaussian distribution of x_1 centered about $x = 0$. However, it is not feasible to generate even Fig. 2.11 for rare events since the PDFs are based on extensive numerical simulation. Therefore, a method needs to be found that will allow a designer to estimate Fig. 2.11 without resorting to Monte Carlo simulation. One possible method is presented in the next chapter.

CHAPTER 3

Modified Gaussian Phase Distribution

3.1 Introduction

Several steps are required to use non-uniform phase distributions to simulate short time series that have a given extreme value. First, a random process, $x(t)$ is acknowledged to be approximated as a summation of components with non-uniform phase angles. Next, a model for the non-uniform phase distribution is determined based on numerical simulation. Then, the model's parameters are specified according to the extreme value, and sample time series are generated using the resulting non-uniform phase distributions.

To begin, start with Eq. 2.23 and drop the prime from t:

$$x(t) = \sum_{j=1}^{N} a_j \cos(\omega_j t + \epsilon'_j) \tag{3.1}$$

Recall that ϵ'_j represents the random phase angle associated with frequency ω_j, and that it is *non*-uniformly distributed between $-\pi$ and π. To emphasize this, and to distinguish Eq. 3.1 from a usual random process with uniform phases (Eq. 2.1), mark x with a prime:

$$x'(t) = \sum_{j=1}^{N} a_j \cos(\omega_j t + \epsilon'_j) \tag{3.2}$$

The prime mark indicates a time series and set of phase angles associated with an extreme value at $t = 0$. Equation 3.2 defines a random process with a PDF of $f_{x'}(x)$ and a CDF of $F_{x'}(x)$.

3.2 Modeling Non-Uniform Phase Distributions

Numerical experiments (Section 2.3 and Appendix A) suggest that, due to the finite number of components, the presence of a specific large value at time $t = 0$ requires a non-uniform phase distribution that is able to vary from component to component. It was also observed that the phase PDFs appear to be Gaussian-type distributions combined with some degree of uniform distribution. A model that exhibits similar behavior was derived and is here termed a "Modified Gaussian" distribution. The Modified Gaussian distribution is defined as the following on the interval $-\pi \leq z \leq \pi$:

$$\begin{aligned} f_{\epsilon'_j}(z) &\equiv \frac{1}{\lambda_j\sqrt{2\pi}}\,\mathrm{e}^{-z^2/2\lambda_j^2} + C && (3.3) \\ F_{\epsilon'_j}(z) &\equiv \frac{1}{2}\,\mathrm{erf}\left(\frac{z}{\lambda_j\sqrt{2}}\right) + \frac{1}{2}\,\mathrm{erf}\left(\frac{\pi}{\lambda_j\sqrt{2}}\right) + C(z+\pi) && (3.4) \end{aligned}$$

C may be solved by utilizing the definition of a PDF, namely that

$$\begin{aligned} 1 &= \int_{-\pi}^{\pi} \frac{1}{\lambda_j\sqrt{2\pi}}\,\mathrm{e}^{-z^2/2\lambda_j^2} + C \\ &= \frac{1}{2}\,\mathrm{erf}\left(\frac{\pi}{\lambda_j\sqrt{2}}\right) + \frac{1}{2}\,\mathrm{erf}\left(\frac{\pi}{\lambda_j\sqrt{2}}\right) + C(\pi+\pi) \\ &= \mathrm{erf}\left(\frac{\pi}{\lambda_j\sqrt{2}}\right) + 2\pi C && (3.5) \\ &\therefore \\ C &= \frac{1}{2\pi}\left(1 - \mathrm{erf}\left(\frac{\pi}{\lambda_j\sqrt{2}}\right)\right) && (3.6) \end{aligned}$$

Therefore, the model for the phase distribution is:

$$f_{\epsilon'_j}(z) = \frac{1}{\lambda_j\sqrt{2\pi}}\,\mathrm{e}^{-z^2/2\lambda_j^2} + \frac{1}{2\pi}\left(1 - \mathrm{erf}\left(\frac{\pi}{\lambda_j\sqrt{2}}\right)\right) \qquad (3.7)$$

The first term of the right-hand side of Eq. 3.7 is recognized as a typical Gaussian distribution. The second term of the right-hand side is, in essence, a uniform distribution that corrects the overall distribution by “bumping it up” such that it integrates to 1. Equation 3.7 is extremely attractive as it has just one parameter per component: λ_j. Generally, λ_j can take any non-negative, real value, but it is practically limited to $0 \leq \lambda_j \leq 10$, as can be seen in Figs. 3.1-3.3. For a uniform distribution, $\lambda_j = 10$, and for a delta function, $\lambda_j = 0$. This phase model can now be fitted to the phase distribution of each component via the single parameter, λ_j.

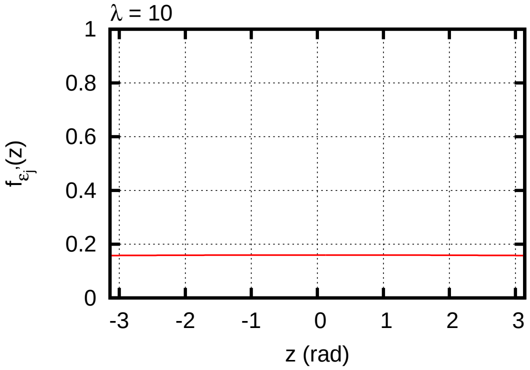

Figure 3.1: Modified Gaussian phase PDF resulting from Eq. 3.7 with $\lambda = 10$.

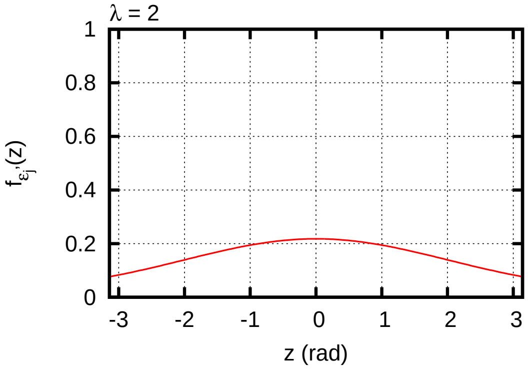

Figure 3.2: Modified Gaussian phase PDF resulting from Eq. 3.7 with $\lambda = 2$.

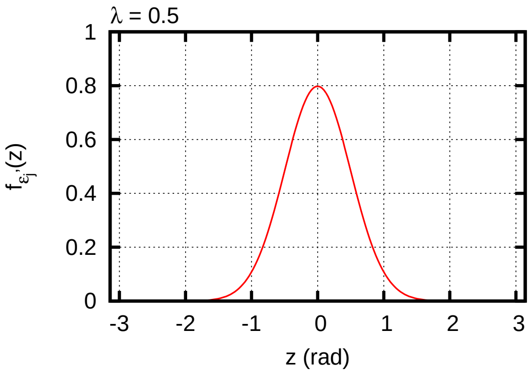

Figure 3.3: Modified Gaussian phase PDF resulting from Eq. 3.7 with $\lambda = 0.5$.

3.2.1 Comparison of Modified Gaussian Distribution to Monte Carlo Simulation

There are three ways of testing the validity of using Eq. 3.7 as a model for non-uniform phases:

1. Compare extreme value PDFs: $f_{x_m}(x) = f_{x'}(x)$
2. Compare phase PDFs: $f_{\epsilon_j',MC}(z) = f_{\epsilon_j',MG}(z)$
3. Compare time series: average time series should approach $\alpha\rho(t)$

For items 1 and 2, the Kullback-Leibler divergence is again employed along with visual verification. For item 3, sample time series are generated using the Modified Gaussian phase distribution and compared to both Monte Carlo generated random time series and to the average time series, $\alpha\rho(t)$, where $\alpha = \hat{x}_m$.

Continuing from Section 2.3, the same ITTC Sea State 3 spectrum ($h_{peak} = 0.88$, $T_{peak} = 7.5$) is used with $N = 101$ and $m = 740$ (recall that this corresponds to the peak value of $f_{x_m}(x)$ being 3.0σ). Starting with the Hypothesis 2 phase distribution (Fig. 2.11), λ_j was chosen such that $D_{KL}(f_{\epsilon_j',MC}(z)\|f_{\epsilon_j',MG}(z))$ is minimized. The Modified Gaussian fit to the Hypothesis 2 phase PDF is termed "Hypothesis 2 Curve

Fit," and the results of this curve fitting are shown in Figs 3.4-3.9. It is clear, both visually and from the D_{KL} values in Fig. 3.6, that Eq. 3.7 is a reasonable fit for the Hypothesis 2 phase distribution from Sec. 2.3. Comparing the extreme value PDFs, $D_{KL}(f_{x_m}(x) \| f_{x'}(x)) = 0.40$, very similar to $D_{KL}(f_{x_m}(x) \| f_{x_1}(x))$ based on Hypothesis 2. λ_j appears to somewhat track the amplitudes, a_j, used to simulate the system, indicating that the larger the amplitude, the more focused the phases will be to obtain a given extreme value.

Fig. 3.9 shows sample design time series created using the phase PDFs determined from Hypothesis 2 and Hypothesis 2 Curve Fit (Figs. 3.4 and 3.5). 2000 total time series were generated from each phase PDF and an average time series calculated. The two averaged time series (pink and teal lines) are so close to the scaled autocorrelation function, $\hat{x}_m \rho(t)$ (red line), that the autocorrelation function completely obscures the two averaged time series. That these three time series match is an indication that the Modified Gaussian phase distribution can be used to model the phase distributions. To better examine how the two averaged time series compare to each other, the difference between the two time series is shown in Fig. 3.10. In this figure, x' is non-dimensionalized on σ, and the difference between the two time series is small compared to the maximum value, $\hat{x}_m$.

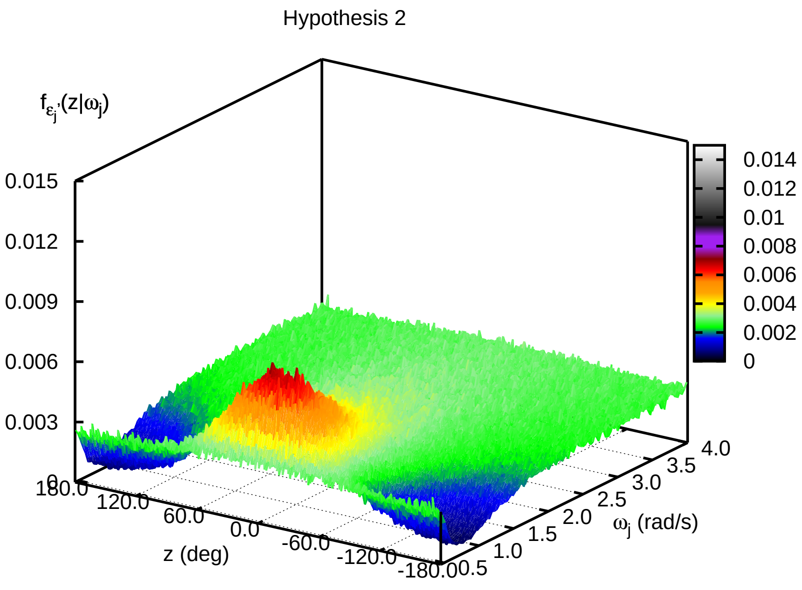

Figure 3.4: Phase PDF for Hypothesis 2. ITTC Sea State 3: $h_{peak} = 0.88$, $T_{peak} = 7.5$, $N = 101$, $m = 740$ (a 3.0σ event).

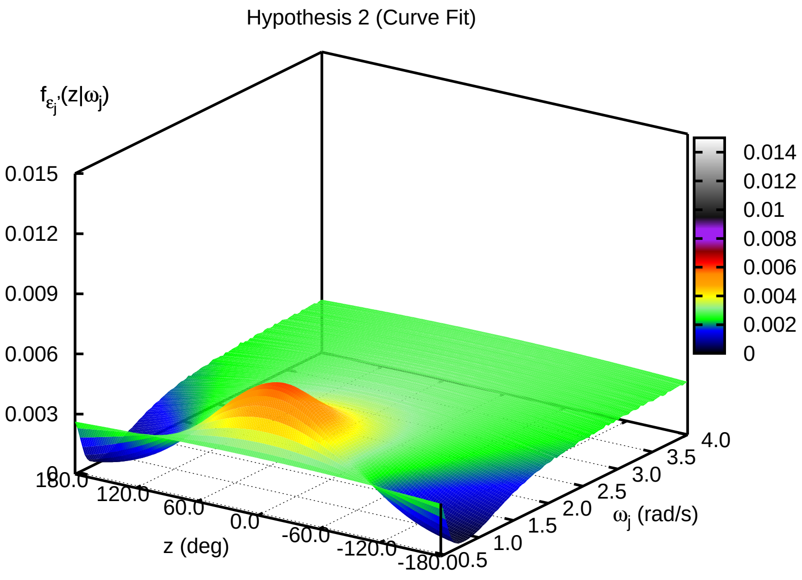

Figure 3.5: Phase PDF for Hypothesis 2 Curve Fit. ITTC Sea State 3: $h_{peak} = 0.88$, $T_{peak} = 7.5$, $N = 101$, $m = 740$ (a 3.0σ event).

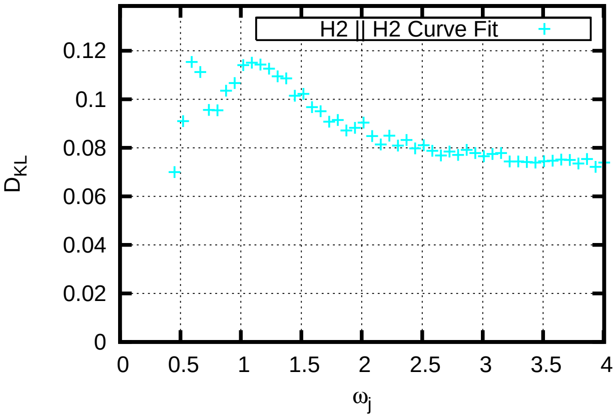

Figure 3.6: Comparison of Hypothesis 2 and Hypothesis 2 Curve Fit phase PDFs using the Kullback-Leibler divergence, $D_{KL}(f_{\epsilon'_j,MC}(z)\|f_{\epsilon'_j,MG}(z))$. ITTC Sea State 3: $h_{peak} = 0.88$, $T_{peak} = 7.5$, $N = 101$, $m = 740$ (a 3.0σ event).

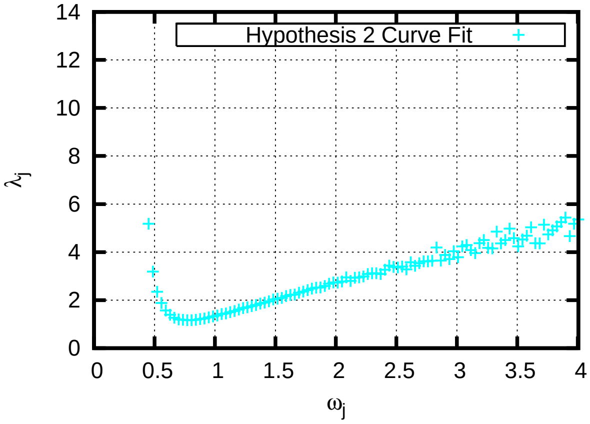

Figure 3.7: λ_j as determined by minimizing the Kullback-Leibler divergence, $D_{KL}(f_{\epsilon'_j,MC}(z)\|f_{\epsilon'_j,MG}(z))$. λ_j is practically capped at 10, as $\lambda_j \geq 10$ results in a uniform phase distribution. ITTC Sea State 3: $h_{peak} = 0.88$, $T_{peak} = 7.5$, $N = 101$, $m = 740$ (a 3.0σ event).

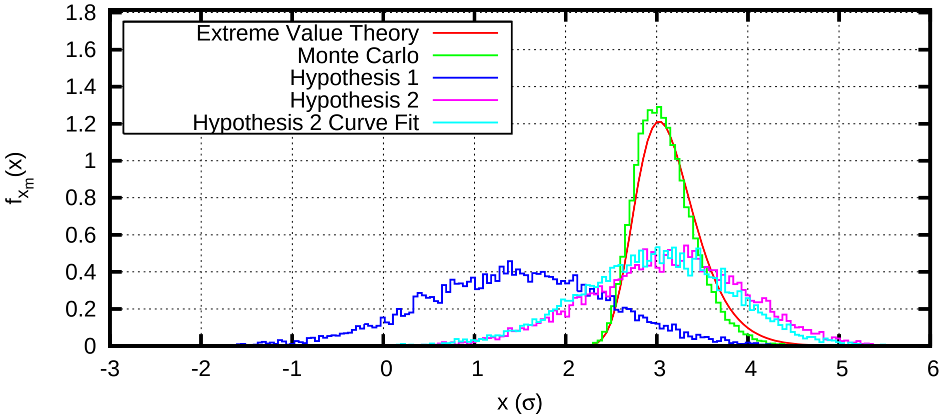

Figure 3.8: Comparison of $f_{x_m}(x)$, denoted “Extreme Value Theory”, and $f_{x_1}(x)$ as calculated by Hypotheses 1 and 2, and Hypothesis 2 Curve Fit. ITTC Sea State 3: $h_{peak} = 0.88$, $T_{peak} = 7.5$, $N = 101$, $m = 740$ (a 3.0σ event).

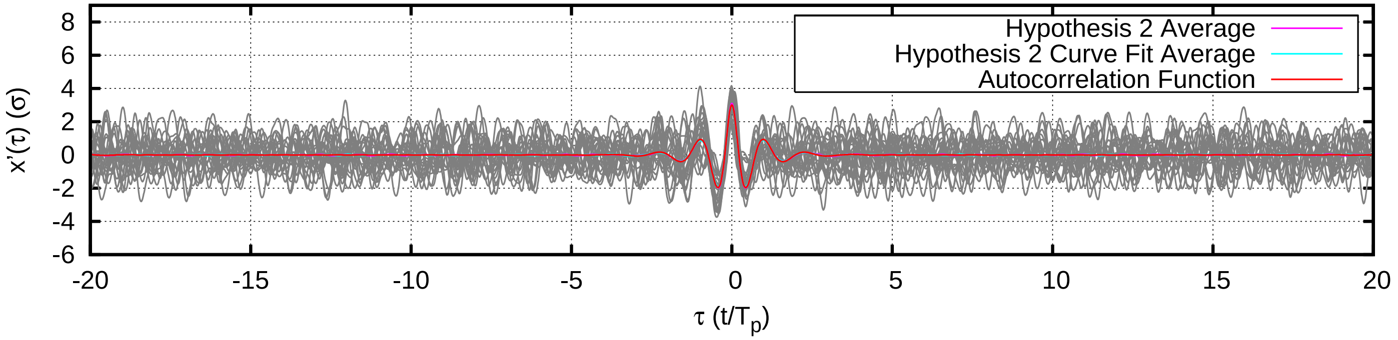

Figure 3.9: Sample time series generated by Hypothesis 2 and Hypothesis 2 Curve Fit phases. ITTC Sea State 3: $h_{peak} = 0.88$, $T_{peak} = 7.5$, $N = 101$, $m = 740$ (a 3.0σ event). Average time series generated from 2000 sample time series; 20 sample time series are plotted.

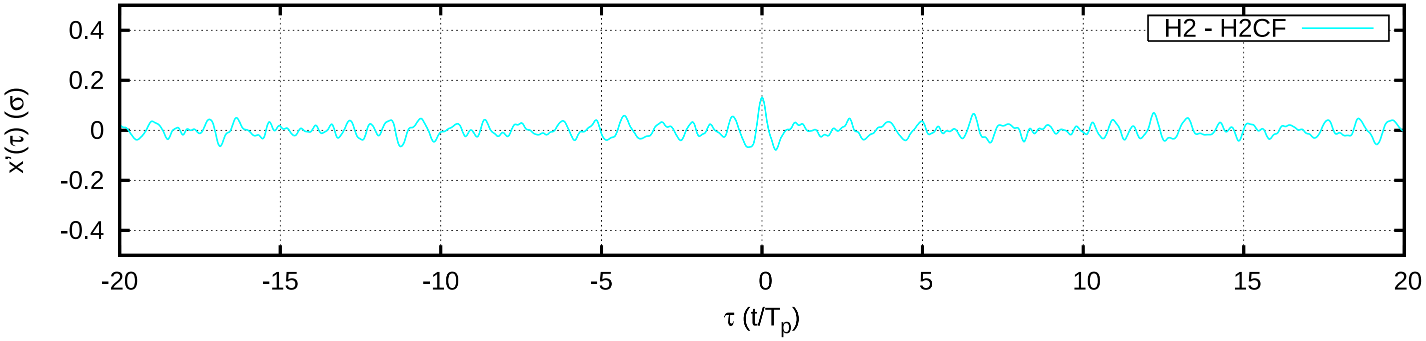

Figure 3.10: Comparison of Hypothesis 2 and Hypothesis 2 Curve Fit average time series. The difference between these two average time series is plotted. ITTC Sea State 3: $h_{peak} = 0.88$, $T_{peak} = 7.5$, $N = 101$, $m = 740$ (a 3.0σ event).

Other numerical simulations may be found in Appendix A. These simulations indicate that Eq. 3.7 is also a reasonable model even for different spectra, m, and N values. λ_j ultimately determines the PDF of $x'(t)$ (Eq. 3.2). The conditions of Eq. 3.2 ensure that a specific design event will occur at time $t = 0$. In other words:

$$x'(0) = x' = \sum_{j=1}^{N} a_j \cos(\epsilon'_j) \tag{3.8}$$

The PDF of x' can be used to determine λ_j. This PDF, $f_{x'}(x)$, should match the PDF of the extreme value that is specified by the designer. As in Sec. 2.3, the target extreme value is denoted x_m, the largest value in m samples of x, the original random process. Therefore, Equation 2.25 needs to match the PDF of Eq. 3.2, but calculating the PDF of a summation of random variable is challenging. Instead, one may use the Characteristic Functions of the PDFs. The Characteristic Function contains the same information as the PDF (similar to how Fourier Transforms in the frequency domain contain the same information as the original time series in the time domain), but is considerably easier to work with than PDFs for summations of variables.

3.3 Determining λ_j via Characteristic Functions

The Characteristic Function is, essentially, the Fourier Transform of the PDF ([Rozanov, 1969], page 75). Similar to a Fourier Transform pair, the transformation between a PDF and its Characteristic Function is fully invertible, and all information regarding the random process is retained. The Characteristic Function, $\psi(s)$, of a continuous random variable, Z, with PDF $f_Z(z)$ is defined as:

$$\psi_Z(s) = E[\mathrm{e}^{isz}] = \int_{-\infty}^{\infty} \mathrm{e}^{isz} f_Z(z)\mathrm{d}z \ , \ -\infty \leq s \leq \infty \tag{3.9}$$

For example, the Characteristic Function of $f_{x_m}(x)$ is:

$$\begin{aligned}\psi_{x_m}(s) &= \int_{-\infty}^{\infty} \mathrm{e}^{isx} f_{x_m}(x)\mathrm{d}x \\ &= \int_{-\infty}^{\infty} \frac{m}{\sigma\sqrt{2\pi}}\ \mathrm{e}^{isx}\ \mathrm{e}^{-x^2/2\sigma^2} \left(\Phi\left(\frac{x}{\sigma}\right)\right)^{m-1} \mathrm{d}x \end{aligned} \tag{3.10}$$

To determine the Characteristic Function of $f_{x'}$, let us first define a new variable Y_j:

$$Y_j = \cos\epsilon'_j \tag{3.11}$$

Now

$$x' = \sum_{j=1}^{N} a_j Y_j \tag{3.12}$$

The CDF of Y_j can be determined using $F_{\epsilon'_j}(z)$ through a variable transformation:

$$\begin{aligned} F_{Y_j}(y) &= \begin{cases} 0, & y \le -1 \\ P(\cos\epsilon'_j \le y), & -1 \le y \le 1 \\ 1, & 1 \le y \end{cases} \\ &= \begin{cases} 0, & y \le -1 \\ P(\epsilon'_j \ge \arccos y), & -1 \le y \le 1 \\ 1, & 1 \le y \end{cases} \\ &= \begin{cases} 0, & y \le -1 \\ 2(1 - F_{\epsilon'_j}(\arccos y)), & -1 \le y \le 1 \\ 1, & 1 \le y \end{cases} \end{aligned} \tag{3.13}$$

$$= \begin{cases} 0, & y \leq -1 \\ 1 - \operatorname{erf}\left(\dfrac{\arccos y}{\lambda_j \sqrt{2}}\right) + \dfrac{\arccos y}{\pi}\left(\operatorname{erf}\left(\dfrac{\pi}{\lambda_j \sqrt{2}}\right) - 1\right), & -1 \leq y \leq 1 \\ 1, & 1 \leq y \end{cases} \tag{3.14}$$

Differentiating Eq. 3.14 yields the PDF of Y_j:

$$\begin{aligned} f_{Y_j}(y) &= \begin{cases} 0, & y \leq -1 \\ \dfrac{\mathrm{d}}{\mathrm{d}y} F_{Y_j}(y), & -1 \leq y \leq 1 \\ 0, & 1 \leq y \end{cases} \\ &= \begin{cases} 0, & y \leq -1 \\ \dfrac{\sqrt{2\pi}\ \mathrm{e}^{-(\arccos y)^2/2\lambda_j^2} - \lambda_j \ \operatorname{erf}\left(\frac{\pi}{\lambda_j\sqrt{2}}\right) + \lambda_j}{\pi \lambda_j \sqrt{1-y^2}}, & -1 \leq y \leq 1 \\ 0, & 1 \leq y \end{cases} \end{aligned} \tag{3.15}$$

The characteristic function of $f_{Y_j}(y)$ is:

$$\begin{aligned} \psi_{Y_j}(s) &= \int_{-\infty}^{\infty} \mathrm{e}^{isy} f_{Y_j}(y) \mathrm{d}y \\ &= \int_{-\infty}^{-1} \mathrm{e}^{isy} f_{Y_j}(y) \mathrm{d}y + \int_{-1}^{1} \mathrm{e}^{isy} f_{Y_j}(y) \mathrm{d}y + \int_{1}^{\infty} \mathrm{e}^{isy} f_{Y_j}(y) \mathrm{d}y \\ &= \int_{-\infty}^{-1} \mathrm{e}^{isy} 0 \mathrm{d}y \\ &\quad + \int_{-1}^{1} \mathrm{e}^{isy} \frac{\sqrt{2\pi}\ \mathrm{e}^{-(\arccos y)^2/2\lambda_j^2} - \lambda_j \ \operatorname{erf}\left(\frac{\pi}{\lambda_j\sqrt{2}}\right) + \lambda_j}{\pi \lambda_j \sqrt{1-y^2}} \ \mathrm{d}y \\ &\quad + \int_{1}^{\infty} \mathrm{e}^{isy} 0 \mathrm{d}y \\ &= 0 + \int_{-1}^{1} \mathrm{e}^{isy} \frac{\sqrt{2\pi}\ \mathrm{e}^{-(\arccos y)^2/2\lambda_j^2} - \lambda_j \ \operatorname{erf}\left(\frac{\pi}{\lambda_j\sqrt{2}}\right) + \lambda_j}{\pi \lambda_j \sqrt{1-y^2}} \ \mathrm{d}y + 0 \end{aligned}$$

$$= \int_{-1}^{1} \mathrm{e}^{isy} \frac{\sqrt{2\pi}\ \mathrm{e}^{-(\arccos y)^2/2\lambda_j^2} - \lambda_j\ \mathrm{erf}\left(\frac{\pi}{\lambda_j\sqrt{2}}\right) + \lambda_j}{\pi\lambda_j\sqrt{1-y^2}}\ \mathrm{d}y \tag{3.16}$$

The Characteristic Function of $f_{x'}(x)$ can now be determine thusly:

$$\begin{aligned}
\psi_{x'}(s) &= E[\mathrm{e}^{isx}] \\
&= E[\mathrm{e}^{is(a_1y_1+a_2y_2+\cdots+a_Ny_N)}] \\
&= E[\mathrm{e}^{isa_1y_1}\ \mathrm{e}^{isa_2y_2}\cdots\ \mathrm{e}^{isa_Ny_N}] \\
&= E[\mathrm{e}^{isa_1y_1}]E[\mathrm{e}^{isa_2y_2}]\cdots E[\mathrm{e}^{isa_Ny_N}] \\
&= \prod_{j=1}^{N} E[\mathrm{e}^{isa_jy_j}] \\
&= \prod_{j=1}^{N} \int_{-\infty}^{\infty} \mathrm{e}^{isa_jy_j} f_{Y_j}(y)\mathrm{d}y \\
&= \prod_{j=1}^{N} \psi_{Y_j}(a_js) \qquad (3.17)
\end{aligned}$$

If the designer chooses a return period or risk-level then m is known. Also, a_j is assumed to be known. To determine λ_j, set the PDF of the extreme value (Eq. 2.25) equal to the PDF of the summation with non-uniform phases (Eq. 3.12):

$$f_{x_m}(x) = f_{x'}(x) \tag{3.18}$$

or, alternatively, equate their respective Characteristic Functions:

$$\psi_{x_m}(x) = \psi_{x'}(x) \tag{3.19}$$

Substituting in Eqs. 3.10, 3.16, and 3.17 results in the following equation to be solved:

$$\begin{aligned}
&\int_{-\infty}^{\infty} \frac{m}{\sigma\sqrt{2\pi}}\ \mathrm{e}^{isx}\ \mathrm{e}^{-x^2/2\sigma^2} \left(\Phi\left(\frac{x}{\sigma}\right)\right)^{m-1} \mathrm{d}x \\
&= \prod_{j=1}^{N} \int_{-1}^{1} \mathrm{e}^{ia_jsy} \frac{\sqrt{2\pi}\ \mathrm{e}^{-(\arccos y)^2/2\lambda_j^2} - \lambda_j\ \mathrm{erf}\left(\frac{\pi}{\lambda_j\sqrt{2}}\right) + \lambda_j}{\pi\lambda_j\sqrt{1-y^2}}\ \mathrm{d}y
\end{aligned} \tag{3.20}$$

There is one set of N unknowns in this equation: λ_j. Unfortunately, Eq. 3.20 is not easily integrable by analytical means, so it must be evaluated numerically. A more difficult problem is the number of unknowns.

3.3.1 Subplex Optimization

As previously stated, λ_j can take any non-negative, real value. Therefore, there are an infinite number of combinations of λ_j. It is possible that, given a starting set of λ_j and their corresponding characteristic functions, an optimization routine might be able to determine the needed set of λ_j by comparing the characteristic function based on λ_j (Eq. 3.17) to the characteristic function based on extreme value statitics (Eq. 3.10).

There is a major hurdle, though, to implementing such an optimization algorithm. Most optimization routines appear to be some form of the Nelder-Mead Simplex Method [Nelder & Mead, 1965]. These approaches bracket an N-dimensional solution with $N + 1$ equally spaced indices. A cost function is checked at each index and the solution is arrived at by moving around the indices via reflection, expansion, contraction, and shrinkage. In this application, however, unless N is trivially small (say, $N = 2$), moving just one index around results in the same value for the cost function. In other words, the Simplex Method is unable to determine the effect of one single component on the overall process due to the large number of components.

A solution to this problem was developed by Rowan [1990]. His routine breaks down N-dimensional problems into several lower-order problems that the Nelder-Mead Simplex routines can handle. This approach was coined the Subplex Method, and was used successfully by Steinhagen [2002].

Rowan has graciously put his Subplex routines into the public domain. These routines have been obtained and implemented to solve for λ_j given a specific m or $\hat{x}_m$

by minimizing the following cost function:

$$f = \sum_{k=1}^{N_s} \left| \psi_{x_m}(s_k) - \prod_{j=1}^{N} \psi_{Y_j}(s_k) \right| \tag{3.21}$$

Returning to the ITTC Sea State 3 example, the above cost function was minimized to determine λ_j. The results are shown in Figs. 3.12-3.14. The main difference between generating λ_j from Monte Carlo simulation and generating λ_j from Subplex optimization is hidden in Eq. 3.20. In Eq. 3.20, the right-hand side is $\psi_{x'}(s)$ and depends upon both λ_j and a_j. The presence of a_j means that the Subplex algorithm can recognize that different components have different effects on the process as a whole. This is why the components with larger amplitudes have even more focused phase distributions in Fig. 3.12 than in Figs. 2.11 or 3.5. To compensate for the larger focusing of phases for the large amplitudes resulting from the Subplex approach, more of the smaller components end up having a uniform phase distribution.

Comparing extreme value PDFs (Fig. 3.13), $D_{KL}(f_{x_m}(x) \| f_{x'}(x)) = 0.25$, which is actually better than the comparison from Hypothesis 2 Curve Fit. This is likely due to the effects of a_j as described above. The time series in Fig. 3.14 do not quite average out to the scaled autocorrelation function, $\hat{x}_m \rho(t)$ due to the extreme focusing of the phases of just a few components. As N increases, this focusing becomes less extreme and the average time series smooths towards $\hat{x}_m \rho(t)$ (see Appendix A). The other numerical simulations in Appendix A show that the Subplex approach works equally well for other spectra, N, and m values.

The advantage of using the Subplex optimization approach is that it does not depend upon Monte Carlo simulation. The only parameters that are needed are N, a_j, and either m or $\hat{x}_m$. This capability is important for cases where $\hat{x}_m$ is a rare event and Monte Carlo simulation is not feasible, such as in Appendix A. For lower values, such as 3σ events, it is easy to use both Monte Carlo simulation and the Subplex method to get sample time series. For larger events, such as 5σ events, the Subplex method gives useful information in a reasonable amount of time (approximately one hour of computation time on a Dell Inspiron ME051 with Intel Pentium M 1.80 GHz processor and 1 GB of RAM), whereas Monte Carlo simulation is too time-consuming and impractical.

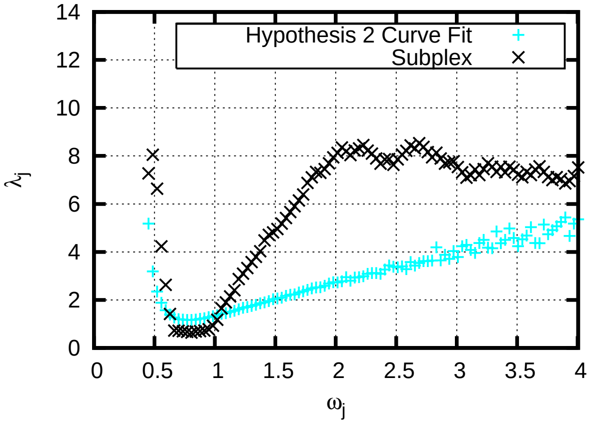

Figure 3.11: λ_j as determined by Subplex optimization compared to λ_j as determined by minimizing $D_{KL}(f_{\epsilon'_j,MC}(z)\|f_{\epsilon'_j,MG}(z))$. λ_j is practically capped at 10, as $\lambda_j \geq 10$ results in a uniform phase distribution. ITTC Sea State 3: $h_{peak} = 0.88$, $T_{peak} = 7.5$, $N = 101$, $m = 740$ (a 3.0σ event).

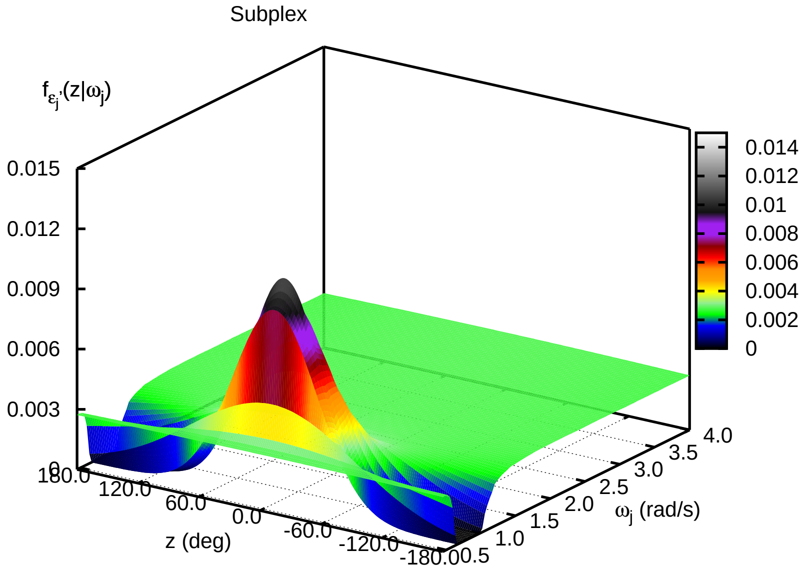

Figure 3.12: Phase PDF from Subplex optimization of λ_j. ITTC Sea State 3: $h_{peak} = 0.88$, $T_{peak} = 7.5$, $N = 101$, $m = 740$ (a 3.0σ event).

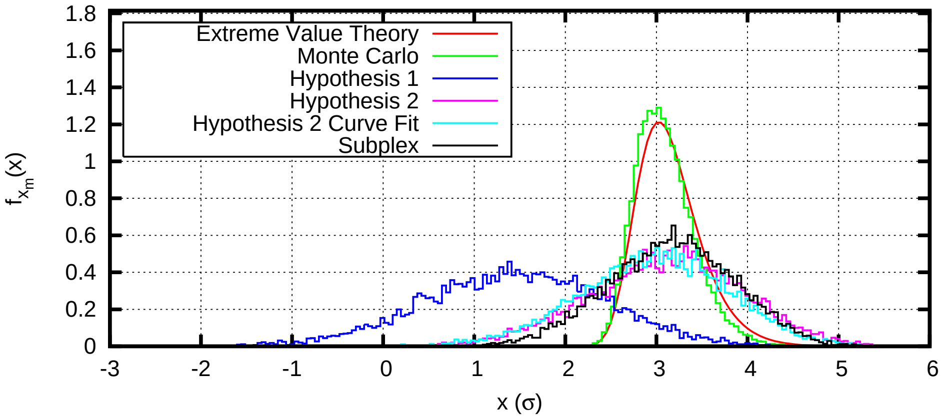

Figure 3.13: Comparison of $f_{x_m}(x)$, denoted “Extreme Value Theory”, and $f_{x_1}(x)$ as calculated by Hypotheses 1 and 2, Hypothesis 2 Curve Fit, and Subplex optimization. ITTC Sea State 3: $h_{peak} = 0.88$, $T_{peak} = 7.5$, $N = 101$, $m = 740$ (a 3.0σ event).

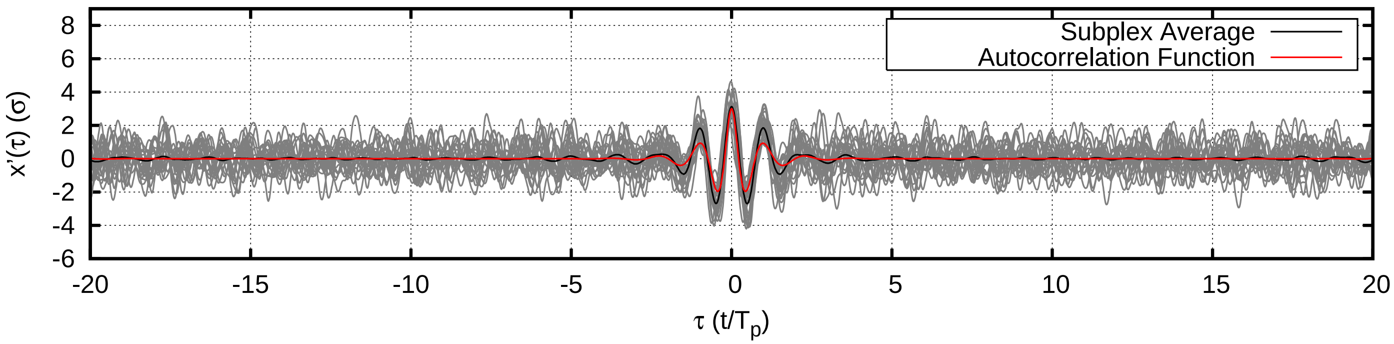

Figure 3.14: Sample time series generated by Hypothesis 2 and Hypothesis 2 Curve Fit phases. ITTC Sea State 3: $h_{peak} = 0.88$, $T_{peak} = 7.5$, $N = 101$, $m = 740$ (a 3.0σ event). Average time series generated from 2000 sample time series; 20 sample time series are plotted.

CHAPTER 4

Method: Creating a Design Response

4.1 Introduction

In practice, the simulation of random processes assumes that a random process is satisfactorily described by the summation of a large number of discrete components. To create a design response, one also may assume that the incident wave that creates a large linear response will be similar to the incident wave that creates a large nonlinear response. Given these assumptions, there are three main elements to the methodology presented here:

- non-uniform response phases are used to create an ensemble of different response time series
- linear systems theory is used to generate the incident wave profiles from the ensemble of response phases
- nonlinear seakeeping code simulates the responses of the ship to the ensemble of incident waves

To summarize the first point, we have a random process,

$$x' = \sum_{j=1}^{N} a_j Y_j \tag{4.1}$$

where,

$$Y_j = \cos \epsilon'_j \tag{4.2}$$

The phases, ϵ'_j, are being modeled as:

$$f_{\epsilon'_j}(z) = \frac{1}{\lambda_j \sqrt{2\pi}} \; \mathrm{e}^{-z^2/2\lambda_j^2} + \frac{1}{2\pi} \left(1 - \; \mathrm{erf} \left(\frac{\pi}{\lambda_j \sqrt{2}} \right) \right) \tag{4.3}$$

This PDF of x', $f_{x'}(x)$, is compared to the PDF of the maximum value in m occurrences, $f_{x_m}(x)$, and results in the following equation to solve:

$$\begin{aligned} &\int_{-\infty}^{\infty} \frac{m}{\sigma\sqrt{2\pi}} \; \mathrm{e}^{isx} \; \mathrm{e}^{-x^2/2\sigma^2} \left(\Phi \left(\frac{x}{\sigma} \right) \right)^{m-1} \mathrm{d}x \\ &\quad = \prod_{j=1}^{N} \int_{-1}^{1} \; \mathrm{e}^{ia_j sy} \frac{\sqrt{2\pi} \; \mathrm{e}^{-(\arccos y)^2/2\lambda_j^2} - \lambda_j \; \mathrm{erf} \left(\frac{\pi}{\lambda_j \sqrt{2}} \right) + \lambda_j}{\pi \lambda_j \sqrt{1-y^2}} \; \mathrm{d}y \end{aligned} \tag{4.4}$$

There is one set of N unknowns in this equation: λ_j, which are solved for via the Subplex Optimization routine.

The application of linear systems theory to design responses is straightforward and described in Sec. 4.2. The nonlinear seakeeping code may be any of a variety of physics-based simulators, from in-house productions to commercial codes such as FLUENT$^{\mathrm{TM}}$. The steps necessary to creating design responses using this method are detailed in Sec. 4.3.

This method of creating design responses depends upon numerical approximations to spectra, integrals, and optimum vectors. The computer program that implements these approximations and runs the optimization algorithm is not of particular interest, but the particulars of the numerical approximations should be documented. The OPTLAMBDA program is a FORTRAN 90 program that implements the Subplex Optimization process. A short description of this program may be found in Sec. 4.4 along with explanations of the nuances specific to this application.

4.2 Linear Systems Theory

A linear system may be represented by the schematic in Fig. 4.1. For a given frequency, ω_j, if one knows the response, $Y(t)$, and the linear transfer function, $H(\omega)$, then the input amplitude and phase may be calculated algebraically as:

$$x_j = \frac{y_j}{|H(\omega_j)|} \tag{4.5}$$

$$\beta_j = \alpha_j - \gamma_j \tag{4.6}$$

In this application, the input function is the incident wave, the linear function is the Response Amplitude Operator (RAO) of the response, and the output function is the design response. The relationships in Eqns. 4.5 and 4.6 hold for$j = 1, 2, , N$ because of the properties of superposition and orthogonality in linear systems. Therefore, the incident wave may be calculated by:

$$\eta(x, y, t) = \sum_{j=1}^{N} \zeta_j \cos(\omega_j t - \cos\theta k_j x + \sin\theta k_j y + \beta_j) \tag{4.7}$$

Here, θ is the heading angle, α_j is the response phase which will be determined via the previous analysis for ϵ'_j, and β_j is the incident wave random phase calculated from Eq. 4.6.

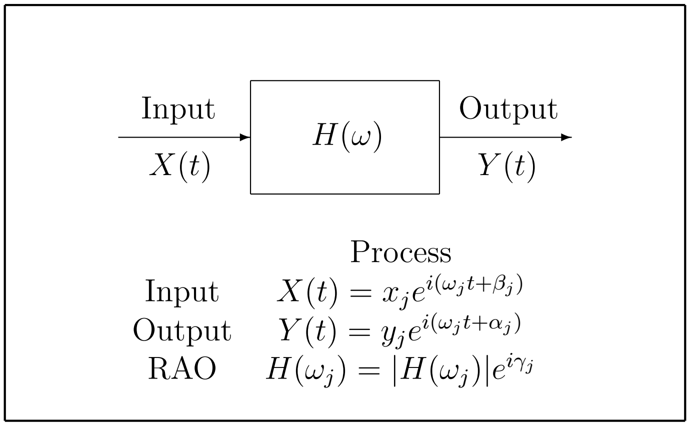

Figure 4.1: Definition of the Variables in a Linear System.

4.3 Algorithm

A flowchart showing the steps to create design responses using the method laid out above is shown in Fig. 4.2. Highlights of the process are detailed in the following sections.

4.3.1 Choosing a Response

The stochastic response can be anything that can be described by a linear transform, either directly or indirectly. Examples include: roll, bending moment, torsion, and relative motion/velocity of the bow to the ocean surface.

4.3.2 Calculating Input Spectrum and Transfer Function

A critical decision by the designer is the choice of operating conditions to explore. First, a sea state must be chosen. Winterstein and Engebretsen (1998) describe how design contours of significant wave height and peak period may be used to determine input sea states of interest. Once the sea state is selected, an RAO may be calculated by a linear seakeeping analysis. The RAO of the response of interest is also a function of speed and heading angle. The authors suggest using polar plots to graph the root-mean-square (RMS, designated by σ) of the process versus heading angle for each speed. In the case of station dependent processes, such as bending moment, polar plots can be created for each of the ships stations. Then, the designer can look for the largest overall RMS value, thus determining the speed, heading angle, and possibly station, to be used in generating the RAO.

4.3.3 Estimating Exposure Time and the Target Extreme Value (TEV)

There are several ways to describe the design response of a process. One method simply states that the design response is the largest response in a time period, or

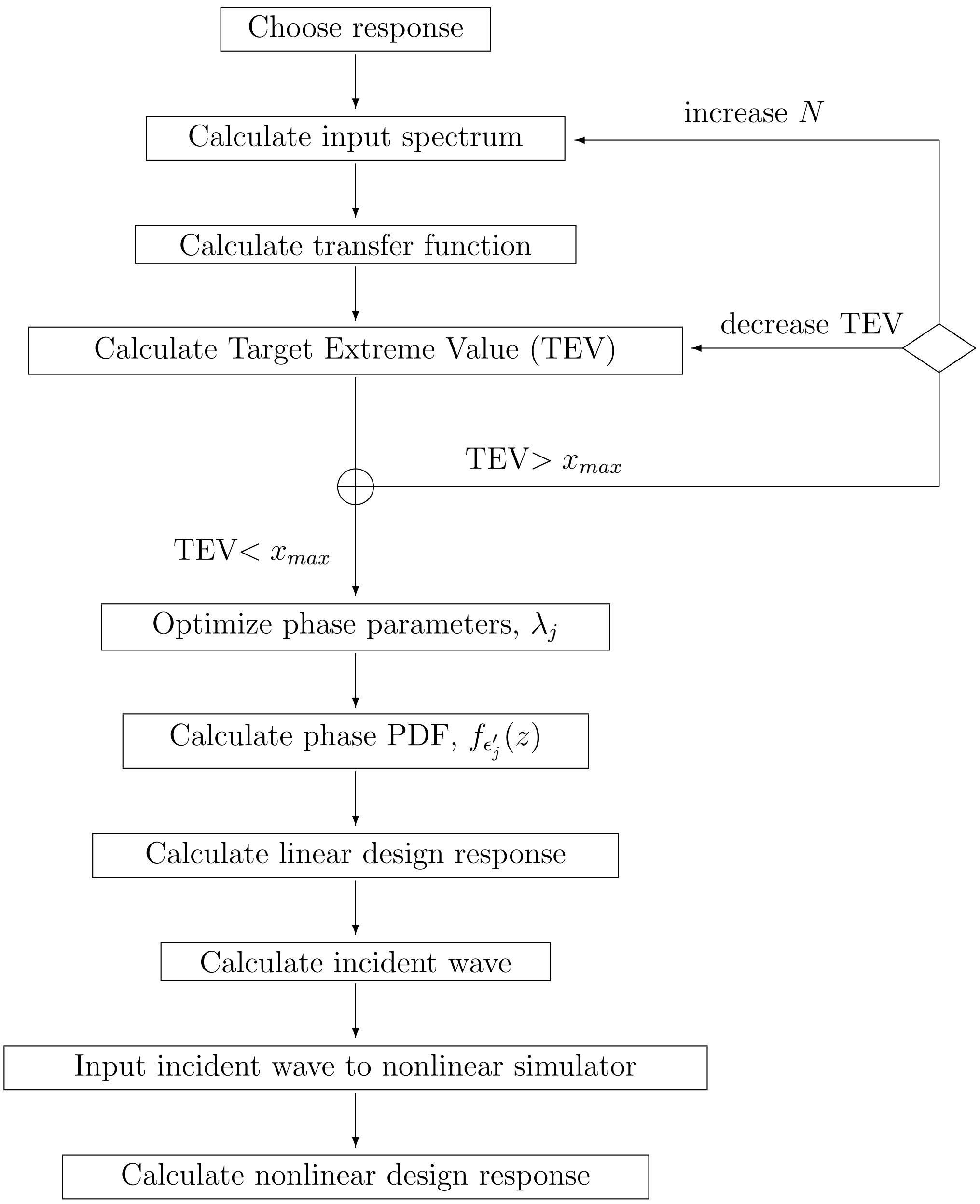

Figure 4.2: Flowchart for design loads generation algorithm

return period (3 hours, 30 days, 30 years, etc.). If the process has an inherent time scale, this exposure could be related to an average number of encounters. An alternative is to specify a particular response value that must be met, for example, from ship classification rules. In either case, the design response has an associated risk level. This risk level is related, in turn, to the normalized Target Extreme Value (TEV). The TEV is the ensemble averaged response value that will be the maximum response produced in the linear time series. For a design response specified by an exposure time, the TEV is calculated by (Ochi, 1990, Eqn. 11.141):

$$TEV = \left(2\ln\left(\frac{T_{exposure}}{2\pi}(60)^2\sqrt{m_2/m_0}\right)\right)^{1/2} \tag{4.8}$$

Here, $T_{exposure}$ is the exposure time in hours and m_0 and m_2 are the zeroth and second moment of the response spectrum, respectively. For a design response specified by an actual response value, the TEV is calculated by:

$$TEV = \frac{\text{design response}}{\sigma_{response}} \tag{4.9}$$

In other words, the Target Extreme Value is normalized by the RMS of the process. For example, if the TEV is 3.0, then the design response can be said to be a *three-sigma event.*

4.3.4 Checking for Sufficient Number of Components

As a result of the discretization of the response's frequency spectrum, there is an upper bound on the response due to Eq. 2.4:

$$Y_{max} = \sum_{j=1}^{N} y_j \tag{4.10}$$

As an engineer, the designer must deal properly with this limitation of computer simulation. If, after choosing the frequency range and number of components, the

TEV is greater than Y_{max}, the maximum attainable value of the model, the designer has one of two alternatives. The recommended choice is to increase the number of components, N, in order to increase the maximum attainable response and recalculate the response RAO. If this is not feasible, then a lower TEV must be used.

4.3.5 Optimizing λ_j

The optimization of λ_j is the most time consuming step of this method. For example, optimizing λ_j for $N = 101$ takes approximately 1.5 hours on a Dell Inspiron ME051 with Intel Pentium M 1.80 GHz processor and 1 GB of RAM. However, once the λ_j parameters have been determined for a given TEV, an infinite number of individual time series can be generated.

4.3.6 Calculating the Incident Wave

To calculate the incident wave, reassign the variables from Sec. 4.2 according to Table 4.1. At this step, every variable will be known except for α_j, which can be solved for using Eq. 4.6. The incident wave may now be input to a nonlinear seakeeping or fluid dynamics program to determine the final predicted design load.

Table 4.1: Assignment of variables for calculating the incident wave

Variable	**Description**
x_j	wave amplitude at frequency ω_j
β_j	wave phase at frequency ω_j
$\lvert H(\omega)\rvert$	RAO amplitude at frequency ω_j
γ_j	RAO phase at frequency ω_j
y_j	response amplitude at frequency ω_j
α_j	response phase at frequency ω_j

4.4 Computer Program: OPTLAMBDA

A computer program was needed to implement the subplex optimization routine in order to solve for λ_j without resorting to Monte Carlo simulation. The OPTLAMBDA program calculates the phase parameters, λ_j, for a given response and TEV.

This is a program written in Fortran 90. In general, OPTLAMBDA reads in a discretized input spectrum and linear transfer function. The user then inputs the TEV in terms of the RMS, σ, of the response. For example, for a TEV of 5.45σ, the user would enter `5.45` as the target response. OPTLAMBDA then populates arrays of $f_{Y_j}(y)$ for a set number of λ_j, creating a look-up table to facilitate later calculations of characteristic functions. The target PDF, $f_{x_m}(x)$, is then calculated numerically along with its characteristic function. The subplex optimization routine is then implemented using the cost function defined in Eq. 3.21.

Tables of the input and output files, modules, subroutines, and functions may be found in Appendix B.

4.4.1 Precalculating $f_{Y_j}(y)$

A hurdle in using this approach to design loads is the singularity at $y = \pm 1$ in $f_{Y_j}(y)$ (Eq. 3.15). This singularity means that $\psi_{Y_j}(s)$ (Eq. 3.16) is not easily evaluated numerically. It is also essential that $\psi_{Y_j}(0) = 1$ to the limits of machine accuracy. If this condition is not ensured, then $\prod_{j=1}^{N} \psi_{Y_j}(0) \neq 1$, as it should, due to machine inaccuracy and the entire characteristic function would be calculated incorrectly as well. Therefore, an algorithm was devised to evaluate $\psi_{Y_j}(s)$ numerically and ensure that $\psi_{Y_j}(0) = 1$ for all j.

To begin, Eq. 3.15 may be rewritten thusly:

$$\begin{aligned} f_{Y_j}(y) &= \frac{\sqrt{2\pi}\ \mathrm{e}^{-(\arccos y)^2/2\lambda_j^2} - \lambda_j\ \mathrm{erf}\left(\frac{\pi}{\lambda_j\sqrt{2}}\right) + \lambda_j}{\pi\lambda_j\sqrt{1-y^2}} \\ &= \frac{p_j}{q_j} \end{aligned} \tag{4.11}$$

where

$$p_j(y) = \frac{\sqrt{2\pi}\ \mathrm{e}^{-(\arccos y)^2/2\lambda_j^2} - \lambda_j\ \mathrm{erf}\left(\frac{\pi}{\lambda_j\sqrt{2}}\right) + \lambda_j}{\pi\lambda_j} \tag{4.12}$$

$$q_j(y) = \sqrt{1-y^2} \tag{4.13}$$

A probability density function must integrate to zero. Therefore,

$$1 = \int_{-1}^{1} f_{Y_j}(y)\mathrm{d}y \tag{4.14}$$

Evaluating this numerically using a simple integration scheme (in this case, the trapezoid rule) gives:

$$\begin{aligned} 1 &= \sum_{k=1}^{NY-1} \frac{1}{2}\big(f_{Y_j}(y_k) + f_{Y_j}(y_{k+1})\big)\Delta y \\ 1 &= \sum_{k=1}^{NY-1} \frac{1}{2}\left(\frac{p_j(y_k)}{q_j(y_k)} + \frac{p_j(y_{k+1})}{q_j(y_{k+1})}\right)\Delta y \end{aligned} \tag{4.15}$$

An equal sign is used in Eq. 4.15 to ensure that the summation equals 1, even though it is an approximation to an integral. Since $\lambda_j > 0$, $p_j(y_k)$ is defined for all y; however, $q_j(y_k)$ is undefined analytically at $y = \pm 1$, the limits of integration, so Eq. 4.15 cannot be calculated directly.

The discretized nature of Eq. 4.15 requires a value to be substituted for $q_j(y_1)$ and $q_j(y_{NY})$ such that the summation in Eq. 4.15 equals 1. Since the nature of the singularity is the same, $1/0$, and a uniform Δy is being used, the same value can be substituted for $q_j(y_1)$ and $q_j(y_{NY})$. The value to be substituted is designated q_j^* and is determined using the following analysis.

First, segregate the singular terms, $q_j(y_1)$ and $q_j(y_{NY})$, in Eq. 4.15:

$$\begin{aligned}
1 &= \frac{1}{2}\left(\frac{p_j(y_1)}{q_j(y_1)} + \frac{p_j(y_2)}{q_j(y_2)}\right)\Delta y + \sum_{k=2}^{NY-2}\frac{1}{2}\left(\frac{p_j(y_k)}{q_j(y_k)} + \frac{p_j(y_{k+1})}{q_j(y_{k+1})}\right)\Delta y \\
&\quad + \frac{1}{2}\left(\frac{p_j(y_{NY-1})}{q_j(y_{NY-1})} + \frac{p_j(y_{NY})}{q_j(y_{NY})}\right)\Delta y \\
1 &= \sum_{k=2}^{NY-2}\frac{1}{2}\left(\frac{p_j(y_k)}{q_j(y_k)} + \frac{p_j(y_{k+1})}{q_j(y_{k+1})}\right)\Delta y + \frac{1}{2}\left(\frac{p_j(y_2)}{q_j(y_2)}\right)\Delta y + \frac{1}{2}\left(\frac{p_j(y_{NY-1})}{q_j(y_{NY-1})}\right)\Delta y \\
&\quad + \frac{1}{2}\left(\frac{p_j(y_1)}{q_j(y_1)}\right)\Delta y + \frac{1}{2}\left(\frac{p_j(y_{NY})}{q_j(y_{NY})}\right)\Delta y \\
1 &= \sum_{k=2}^{NY-2}\frac{1}{2}\left(\frac{p_j(y_k)}{q_j(y_k)} + \frac{p_j(y_{k+1})}{q_j(y_{k+1})}\right)\Delta y + \frac{1}{2}\left(\frac{p_j(y_2)}{q_j(y_2)}\right)\Delta y + \frac{1}{2}\left(\frac{p_j(y_{NY-1})}{q_j(y_{NY-1})}\right)\Delta y \\
&\quad + \left(\frac{p_j(y_1)\Delta y}{2}\right)\left(\frac{1}{q_j(y_1)}\right) + \left(\frac{p_j(y_{NY})\Delta y}{2}\right)\left(\frac{1}{q_j(y_{NY})}\right) \qquad (4.16)
\end{aligned}$$

Then, substitute q_j^* for $q_j(y_1)$ and $q_j(y_{NY})$ in Eq. 4.16.

$$\begin{aligned}
1 &= \sum_{k=2}^{NY-2}\frac{1}{2}\left(\frac{p_j(y_k)}{q_j(y_k)} + \frac{p_j(y_{k+1})}{q_j(y_{k+1})}\right)\Delta y + \frac{1}{2}\left(\frac{p_j(y_2)}{q_j(y_2)}\right)\Delta y + \frac{1}{2}\left(\frac{p_j(y_{NY-1})}{q_j(y_{NY-1})}\right)\Delta y \\
&\quad + \left(\frac{p_j(y_1)\Delta y}{2}\right)\left(\frac{1}{q_j^*}\right) + \left(\frac{p_j(y_{NY})\Delta y}{2}\right)\left(\frac{1}{q_j^*}\right) \qquad (4.17)
\end{aligned}$$

Finally, solve for q_j^*:

$$\begin{aligned}
1 &= \sum_{k=2}^{NY-2}\frac{1}{2}\left(\frac{p_j(y_k)}{q_j(y_k)} + \frac{p_j(y_{k+1})}{q_j(y_{k+1})}\right)\Delta y + \frac{1}{2}\left(\frac{p_j(y_2)}{q_j(y_2)}\right)\Delta y + \frac{1}{2}\left(\frac{p_j(y_{NY-1})}{q_j(y_{NY-1})}\right)\Delta y \\
&\quad + \frac{1}{q_j^*}\left(\frac{p_j(y_1)\Delta y}{2} + \frac{p_j(y_{NY})\Delta y}{2}\right) \\
q_j^* &= \frac{\left(\frac{p_j(y_1)\Delta y}{2} + \frac{p_j(y_{NY})\Delta y}{2}\right)}{1 - \sum_{k=2}^{NY-2}\frac{1}{2}\left(\frac{p_j(y_k)}{q_j(y_k)} + \frac{p_j(y_{k+1})}{q_j(y_{k+1})}\right)\Delta y + \frac{1}{2}\left(\frac{p_j(y_2)}{q_j(y_2)} + \frac{p_j(y_{NY-1})}{q_j(y_{NY-1})}\right)\Delta y} \qquad (4.18)
\end{aligned}$$

Once q_j^* is calculated, then $\psi_{Y_j}(s_k)$ can be evaluated numerically as

$$\psi_{Y_j}(s_k) = \sum_{k=1}^{NY-1}\left(e^{-ix_j s y_k}\frac{1}{2}\big(f_{Y_j}(y_k)\big)\Delta y + e^{-ix_j s y_{k+1}}\frac{1}{2}\big(f_{Y_j}(y_{k+1})\big)\Delta y\right) \qquad (4.19)$$

where q_j^* is used in the calculation of $f_{Y_j}(y_1)$ and $f_{Y_j}(y_{NY})$ using Eq. 4.11.

The calculation for q_j^* must be done for λ_j every time $\psi_{Y_j}(s)$ is needed. During the course of optimization, this calculation will be done thousands, if not millions, of times. In an effort to expedite the optimization process, $f_Y(y)$ is calculated for a large, but finite, number of possible values of λ and saved as a look-up table. This approach is possible as λ is effectively bounded between 0 and 10. $\lambda = 0$ is a Delta Function and $\lambda = 10$ is near enough to a uniform distribution as to make no difference. When OPTLAMBDA is run, λ_j is rounded to the nearest of the possible values of λ ($\Delta\lambda = 0.02$), and $f_{Y_j}(y)$ is located according to the new value of λ_j.

4.4.2 Calculating Characteristic Functions

Evaluating the characteristic functions $\psi_{x_m}(s)$ and $\psi_{x'}(s)$ numerically (Eq. 4.19) requires a range of s along with an interval, Δs. Due to the similarity of the characteristic function - probability density function pair to a Fourier Transform pair, the range of s is calculated similar to the calculation of the frequency range when performing a discrete Fourier Transform.

The maximum attainable value of the response is x_{max} (Eq. 2.4); this is analogous to record length when using the Fourier Transform. The maximum frequency in the frequency domain after a Fourier Transform is:

$$\omega_{max} = \frac{4\pi}{T_{record}} \tag{4.20}$$

Following this equation, the maximum value of s is calculated as:

$$s_{max} = \frac{4\pi}{x_{max}} \tag{4.21}$$

Just as the discrete Fourier Transform gives amplitudes and phases for $-\omega_{max} \leq \omega_j \leq \omega_{max}$, the characteristic function has a range of $-s_{max} \leq s_k \leq s_{max}$. Unlike the Fourier Transform, however, there is no fixed number of points, k, at which the characteristic function must be evaluated. Therefore, for a given number of points,

NS, the s-step is calculated as:

$$\Delta s = \frac{2s_{max}}{NS-1} \tag{4.22}$$

In this way, the number of points at which the characteristic functions are evaluated remains the same. Since the characteristic function is bounded by -1 and 1, this allows for direct comparison of the final error between $\psi_{x_m}(s)$ and $\psi_{x'}(s)$ for different response cases.

4.4.3 The `subplx` Routine

The OPTLAMBDA implements the Subplex optimization method worked out by Thomas Rowan [Rowan, 1990]. The Subplex method is an involved program best described by Rowan himself ([Rowan, 1990], Section 5.3):

> The Subplex method is designed to remove the weaknesses of the simplex method and to retain the positive features. Because of the difficulties NMS[1] has on high-dimensional problems, the Subplex method's approach is to decompose the problem into low-dimensional subspaces that the simplex method can search efficiently. Although SUBPLEX must be able to maximize B_L^*, it is designed as a general-purpose optimization method and is not tailored to any particular application.

The Subplex method routines were successfully used by OPTLAMBDA to determine λ_j, but the author assumes no responsibility for any documentation, bugs, features, etc. related to the Subplex method. A listing of the dependencies of the Subplex method may be found in Table B.5.

---

[1] Refers to the Nelder-Mead Simplex Optimization routine, an algorithm frequently used in optimizing noisy functions [Nelder & Mead, 1965].

CHAPTER 5

Examples

5.1 Introduction

The best way to understand the intricacies and implications of the method presented in Chapter 4 is to look at an example. A stochastic process that includes both quasi-static and dynamic response is ship springing. Springing occurs when the encounter frequency of the waves, or a harmonic of the encounter frequency, excites the ship at its two-noded natural frequency. When springing occurs, it can greatly add to the bending moment of the ship. Typically, the long Great Lakes ships (1000+ ft, 305+ m) have been the ships concerned with the effects of springing; however, as Very Large Crude Carriers and other ocean-going ships continue to increase their size, springing becomes an important response to analyze.

The example presented below is a comparison of bending moment predictions for the Great Lakes bulk carrier *M/V Stewart J. Cort.* Two different Target Extreme Values (TEVs) are used for both a rigid body analysis and an elastic body analysis. It will be shown that the effects of springing (the elastic body response) change the expected shape of the extreme response. This, in turn, changes the shape of the wave train that produces the large responses. The method for determining design responses presented here is shown to reasonably reproduce both the linear bending moment response and the incident wave that leads to the large response. The difference in the wave profiles shows the need to address design responses, not just design waves.

5.2 Example: Springing of a Great Lakes Bulk Carrier

The *M/V Stewart J. Cort* has been measured extensively as to the effects of springing on the ship's hull [Various, 1979]. Particulars of the *Cort* may be found in Table 5.1. Figure 5.1 shows a set of typical response spectra for midship bending stress of the *Cort* [Various, 1979]. It is clear that there are two peak frequencies with which a designer should be concerned. The lower frequency relates to wave-induced bending stress and is associated with rigid body dynamics. The higher frequency is related to the effects of springing and is associated with an elastic body analysis. The three spectra that are shown in Fig. 5.1 emphasize that the effects of springing should be included in the design analysis. Storm 1 produced more stress at the lower frequencies, but Storms 2 and 3 produced much more stress at the higher frequencies.

Table 5.1: Main particulars of the *Stewart J. Cort*

Particular	**Value**
LOA	1000 ft (305 m)
LBP	989 ft (301 m)
B	105 ft (32 m)
T	25.8 ft (7.86 m)
Δ	68,300 LT (69,400 t)
C_B	0.924
V_k	12.5 knots

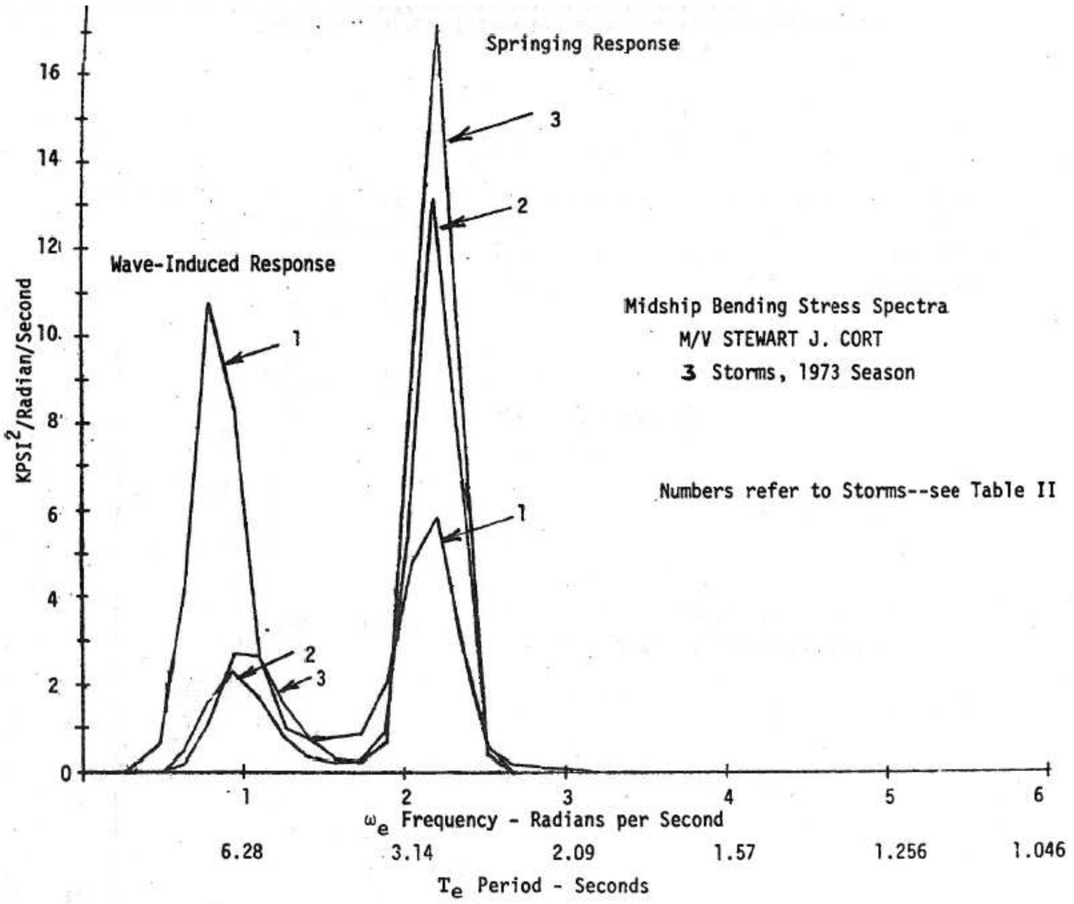

Figure 7. Typical Stress Response Spectra, Showing Wave-Induced and Springing Stresses (8)

Figure 5.1: Typical bending moment response spectra of the *Stewart J. Cort.* Figure reproduced from "Great Lakes Carriers Hull Stress Monitoring System," U.S. Department of Commerce, Maritime Administration, January 1979.

The implications of considering the springing phenomenon may be seen in Fig. 5.2. The top signal is the combined bending stress at midship as measured aboard the *Cort.* This signal was then filtered using a high-pass filter to produce the middle signal, which is the bending stress due to springing. When the combined signal is filtered using a low-pass filter, the bottom signal is produced, which is the bending stress due to the waves.

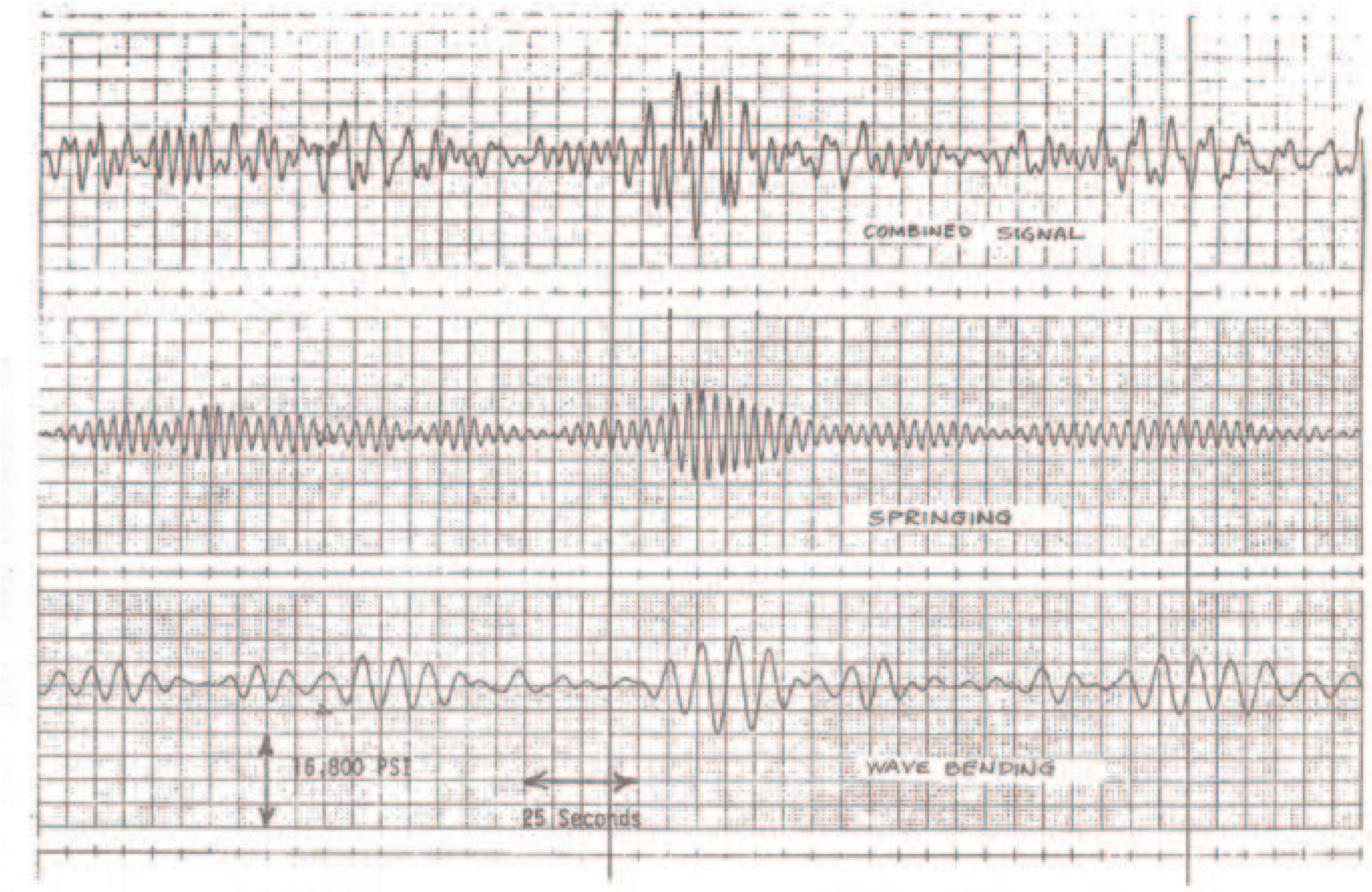

Figure 5.2: Sample time series of bending moment as measured aboard the *Stewart J. Cort*. Figure reproduced from ”Great Lakes Carriers Hull Stress Monitoring System,” U.S. Department of Commerce, Maritime Administration, January 1979.

It is clear that not only is the maximum of the combined signal nearly twice that of either springing by itself or wave-induced bending stress by itself, but the maximum does not coincide with the maxima of either of the two other signals. Therefore, it is important to capture the response of the ship due to both wave-induced effects and springing.

The following examples will calculate sample design loads for vertical midship bending moment. The wave spectrum was determined by a storm measured at Eagle Harbor on November 28, 1966. It is a two parameter spectrum with $H_{sig} = 5.58$m and $T_{peak} = 8.8$s. The rigid body transfer function was estimated using the SHIPMO program [Beck & Troesch, 1990] with a heading angle of 180°, forward speed of 6.43 m/s (12.5 knots), and 101 components. The elastic body transfer function was approximated as follows.

The elastic body analysis follows the analysis used by Troesch [1984]. First-order (linear) springing excitation and response are investigated in this work. In the model used by Troesch, the first-order springing excitation is the wave-induced midship bending moment of a rigid, inelastic hull (such as calculated by SHIPMO, above). In this example, a linear transfer function is applied to the rigid body bending moment to estimate the linear midship bending moment response of an elastic ship. The elastic analysis is capable of capturing the springing phenomenon.

Designating the rigid body transfer function as H_{rigid} (determined from SHIPMO), the elastic body transfer function is calculated as:

$$H_{elastic}(\omega_e) = 2H_{rigid}(\omega_e)\left(\frac{1}{1 + 2i\zeta_o\omega_e/\omega_n - \omega_e^2/\omega_n^2}\right) \tag{5.1}$$

where ω_e is the encounter frequency, ω_n is the ship's natural frequency, and ζ_o is the damping ratio. For this example, $\omega_n = 1.9$ rad/s and $\zeta_o = 0.0154$. The range of ω_o and ω_e is such that the response spectra are well approximated without bias by zero amplitude components, similar to how the range of ω was determined in Section 2.3.1. Using 101 components, the maximum attainable rigid body midship bending moment response was $8.3\sigma_{\text{rigid BM}}$, and the maximum attainable elastic body midship bending moment response was $8.5\sigma_{\text{elastic BM}}$. Two TEVs were used, 3.0σ and 5.0σ, both of which are less than the maximum attainable value for both the rigid body case and the elastic body case.

For $TEV = 3.0$, the phase parameters, λ_j, of the rigid body response and the elastic body response were determined by matching the Hypothesis 2 phase distribution as well as via the OPTLAMBDA program. Sample design time series for each case were calculated using Eq. 3.2 with $\epsilon_j' = \alpha_j$, and the corresponding linear wave time series were calculated using the relationships in Eqs. 4.5 and 4.6. Comparisons to nonlinear responses have not been done at this time; however, the wave phase angles, β_j, that correspond to each individual time series can be recorded and used in future comparisons of linear vs. nonlinear simulations.

5.2.1 Target Extreme Value (TEV): $3.0\sigma_{BM}$

The Modified Gaussian phase distribution was shown in Chapter 3 to be a reasonable approximation to the non-uniform phase distribution that results from using a finite number of Fourier components to create a large value of a random process. Even though it is necessary to adopt Hypothesis 2 (i.e. the phases are independent but non-identically distributed), the resulting sample time series have an average profile similar to theoretical mean, the scaled autocorrelation function. Having arrived at Hypothesis 2 via Monte Carlo simulation, the subplex optimization routine was shown to generate the necessary phase parameters without resorting to brute force simulation. This alternative approach is important as it allows for the simulation of rare events that are difficult to find in Monte Carlo simulation. The subplex optimization approach assumes the phases follow Hypothesis 2, and again the sample time series have an average profile that matches the scaled autocorrelation.

To validate this method of producing design loads, both the design responses and their attendant incident wave trains as calculated from the subplex method should be compared to those as generated by brute force simulation. This comparison is done for a 3.0σ value of vertical bending moment at midship for the *Cort*.

Rigid Body Analysis

Figures 5.3- 5.15 highlight the results for a $3.0\sigma_{BM}$ value of the vertical bending moment at midship for the *Cort* as estimated using rigid body dynamics only (the full analysis may be found in Appendix A). Figure 5.3 shows the component amplitudes used in the rigid body analysis. The largest amplitude is at $\omega_j \approx 0.55$ rad/s, but there are many other significant amplitudes at frequencies greater than 0.55 rad/s.

Various extreme value PDFs for the response are shown in Fig. 5.4. These PDFs are similar to those found in the earlier analysis using the nicely-behaved ITTC sea spectrum. The phase PDFs based on Monte Carlo simulation using Hypothesis 2 (Figs. 5.5 and 5.6) show how the amplitude of a given component affects the phase distribution of that component. The "ripples" in the phase PDFs mirror track the peaks in the amplitudes (Fig. 5.3). Since the extreme value PDFs are similar to those found earlier, it appears that the phase PDF developed from Hypothesis 2 is an adequate description of the phases even for the more complex response spectrum of this bending moment response.

The phase parameters, λ_j, found from the Subplex method are compared to those found from Monte Carlo simulation in Fig. 5.7. For the largest amplitudes, λ_j as calculated by Subplex optimization is less than λ_j from Monte Carlo simulation. For the smalller amplitudes, there is more scatter to the Subplex λ_j because they are determined from an optimization algorithm which necessarily must be stopped at some point in the calculations. However, the difference between the Hypothesis 2 phases (Fig. 5.5) and the Subplex phases (Fig. 5.9) shows that the overall process is not sensitive to individual changes of phase distributions because the extreme value PDFs in Fig. are similar. It is the focusing of several to many component phases that is important in producing the desired response at time $\tau = 0$.

In this particular example, the characteristic functions do not match well (Fig. 5.8). This is mostly due to the inherent limitations associated with restricting the phases to be independent. It is possible that characteristic function agreement could be improved by adjusting the parameters of the optimization routine.

Example response design time series are shown in Figs. 5.10, 5.12, and 5.14. The average response time series all match the response's autocorrelation function, which supports the conclusion that useful design time series are created despite the non-agreement of the extreme value PDFs. Individual response time series tend to exhibit responses of $\pm 2\sigma_{BM}$ followed by the build up of several response cycles to reach the design response at time $\tau = 0$. The effect of phase independence is shown in the variance of the maximum response at $\tau = 0$; one of the individual maximums is a $4.5\sigma_{BM}$ response. There is also evidence of signal repetition in the time series, an indication that the frequency discretization was not fine enough in this example.

The interesting portion of this exercise, of course, is the resulting incident wave time series (Figs. 5.11, 5.13, and 5.15). The incident wave, as measured at midship of the moving ship, was calculated using the relations in Eqs. 4.5 and 4.6. In this case of rigid body bending moment, the average wave profile that produces a $3.0\sigma_{BM}$ response is not a large peak or trough, such as would be described by the autocorrelation function (the autocorrelation function is plotted for reference in each set of wave time series). Instead, it is a series of waves, with large peaks and troughs occurring about two wave periods before and after the target event that occurs at time $\tau = 0$. The individual time series have peaks and troughs that are equal to $3.0\sigma_{wave}$, they just do not occur at $\tau = 0$. This quick investigation indicates that using a large design wave to estimate large bending moment at midship would be inappropriate because the wave autocorrelation function does not match the average wave profile that has been conditioned by the response.

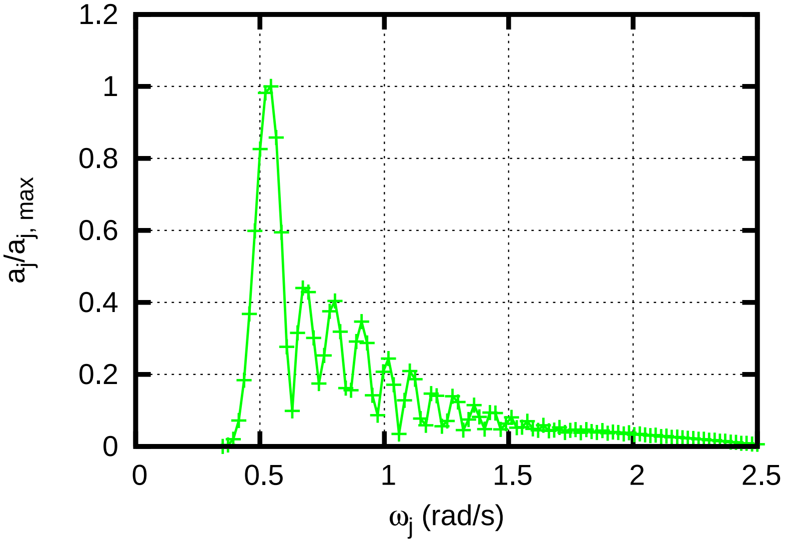

Figure 5.3: Rigid body analysis: *Stewart J. Cort.* Amplitudes for midship bending moment. $N = 101$, heading angle = 180°, forward speed = 12.5 knots.

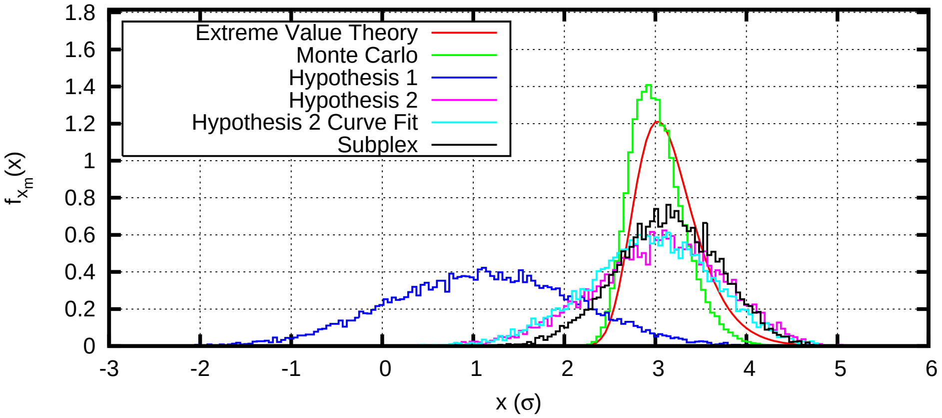

Figure 5.4: Rigid body analysis: *Stewart J. Cort*. Extreme value PDFs for midship bending moment. TEV $= 3.0\sigma_{BM}$, $N = 101$, heading angle $= 180°$, forward speed $= 12.5$ knots.

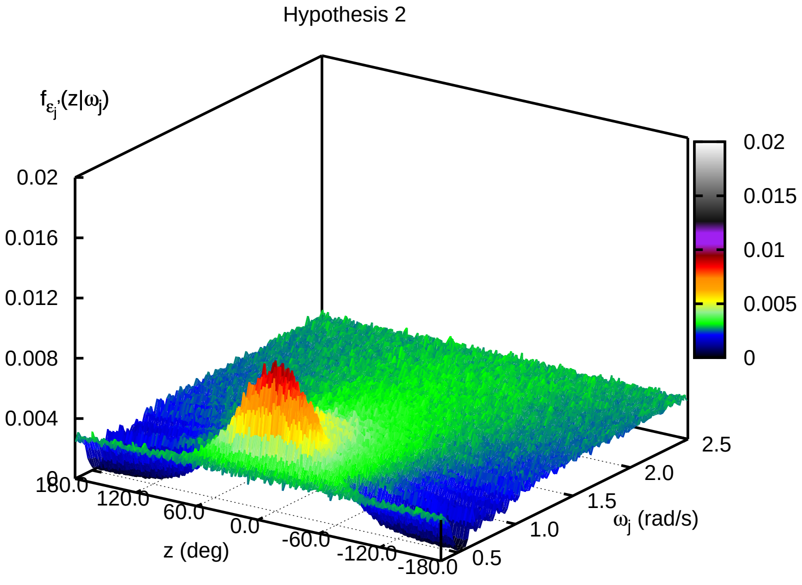

Figure 5.5: Rigid body analysis: *Stewart J. Cort*. Phase PDF: Hypothesis 2 for midship bending moment. TEV $= 3.0\sigma_{BM}$, $N = 101$, heading angle $= 180°$, forward speed $= 12.5$ knots.

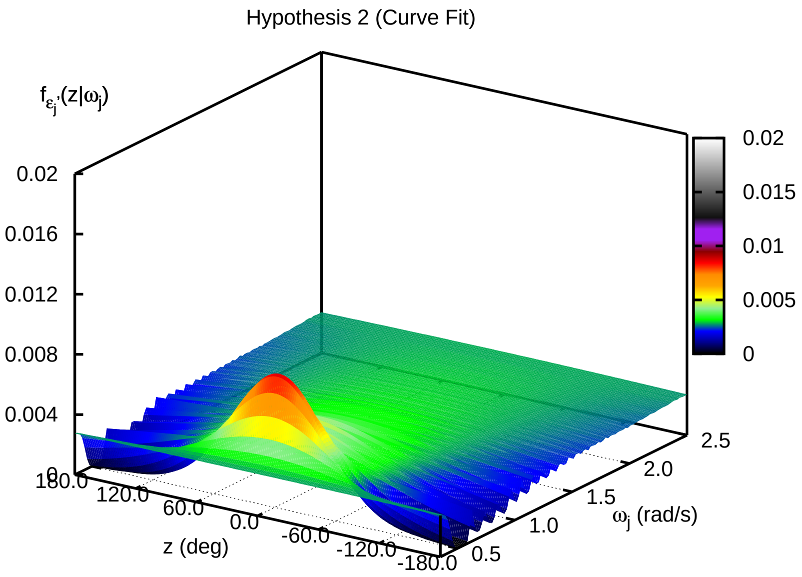

Figure 5.6: Rigid body analysis: *Stewart J. Cort.* Phase PDF: Hypothesis 2 (curve fit) for midship bending moment. TEV = $3.0\sigma_{BM}$, $N = 101$, heading angle = 180°, forward speed = 12.5 knots.

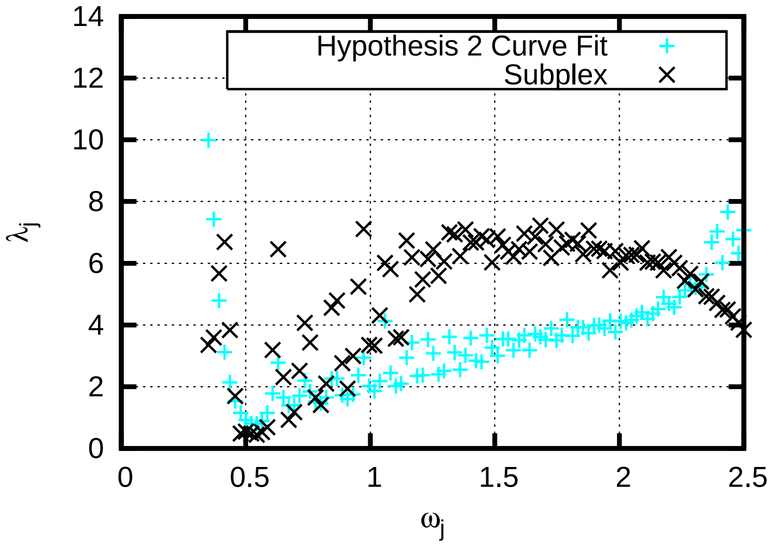

Figure 5.7: Rigid body analysis: *Stewart J. Cort.* λ_j for midship bending moment. TEV = $3.0\sigma_{BM}$, $N = 101$, heading angle = 180°, forward speed = 12.5 knots.

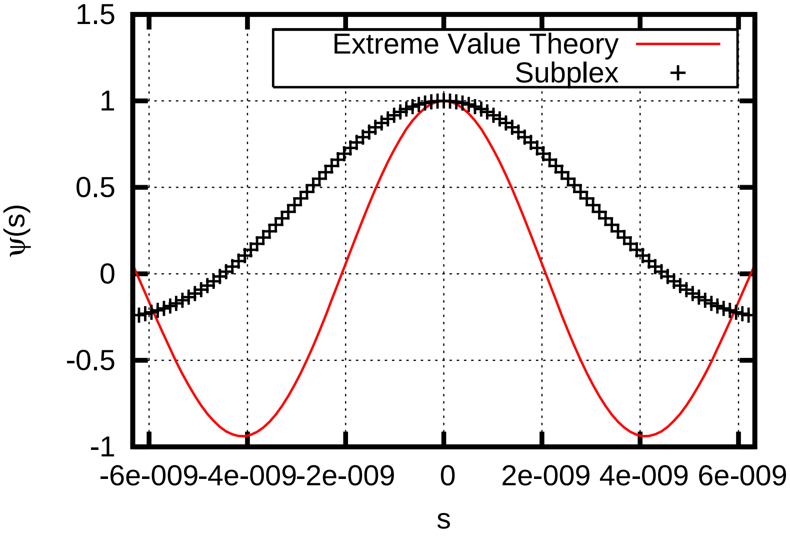

Figure 5.8: Rigid body analysis: *Stewart J. Cort*. Characteristic functions for midship bending moment. TEV $= 3.0\sigma_{BM}$, $N =$ 101, heading angle = 180°, forward speed = 12.5 knots.

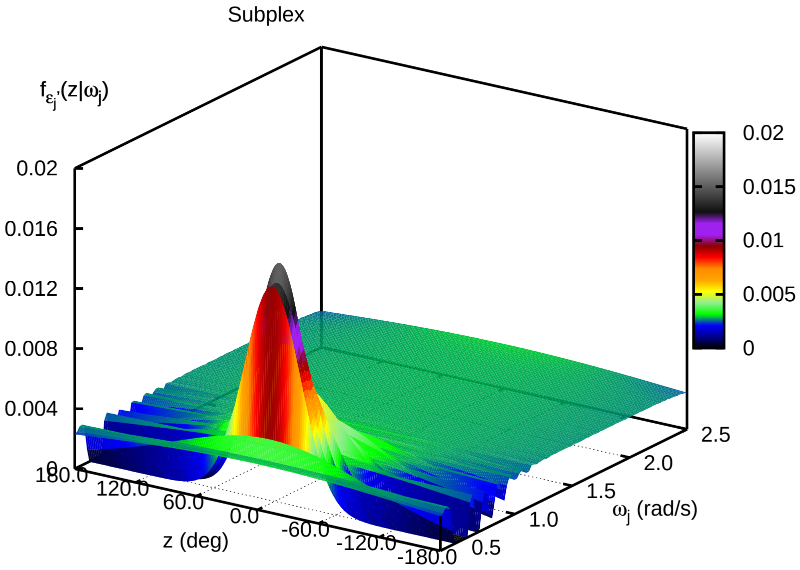

Figure 5.9: Rigid body analysis: *Stewart J. Cort*. Phase PDF: Subplex for midship bending moment. TEV $= 3.0\sigma_{BM}$, $N =$ 101, heading angle = 180°, forward speed = 12.5 knots.

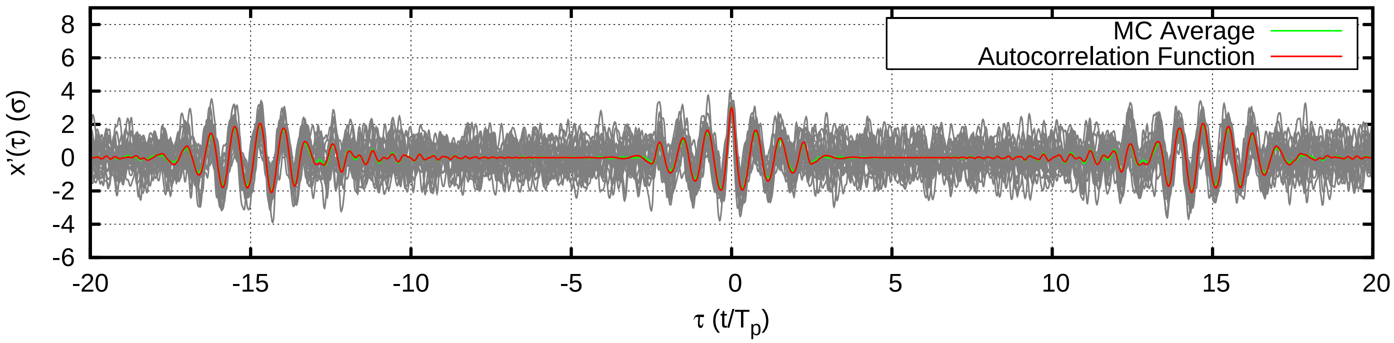

Figure 5.10: Rigid body analysis: *Stewart J. Cort.* Sample bending moment time series at midship: Monte Carlo Simulation for midship bending moment. TEV = $3.0\sigma_{BM}$, $N = 101$, heading angle = 180°, forward speed = 12.5 knots. Average time series generated from 2000 sample time series; 20 sample time series are plotted.

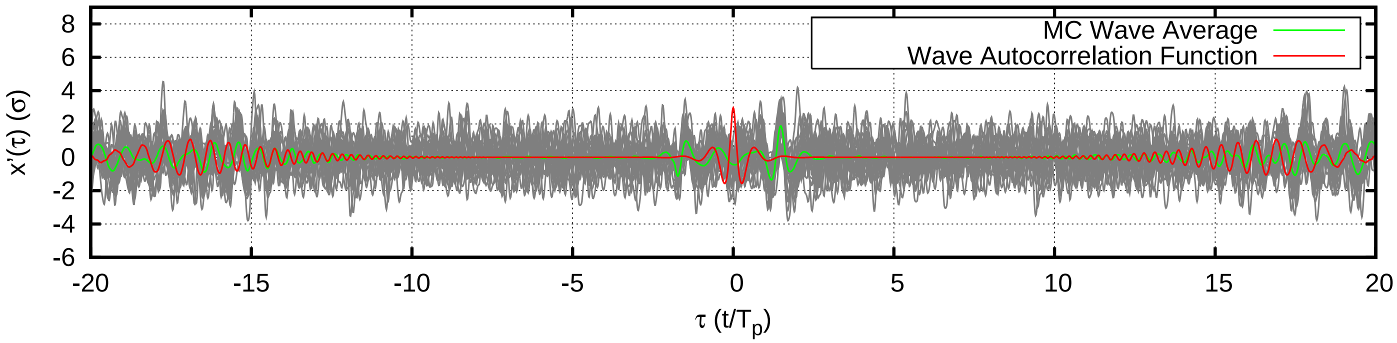

Figure 5.11: Rigid body analysis: *Stewart J. Cort.* Sample wave time series at midship: Monte Carlo Simulation for midship bending moment. TEV = $3.0\sigma_{BM}$, $N = 101$, heading angle = 180°, forward speed = 12.5 knots. Average time series generated from 2000 sample time series; 20 sample time series are plotted.

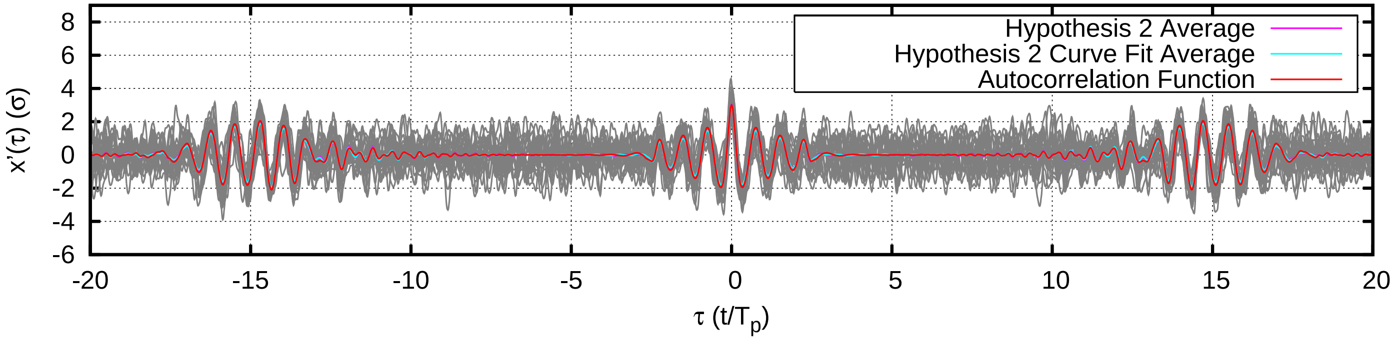

Figure 5.12: Rigid body analysis: *Stewart J. Cort*. Sample bending moment time series at midship: Hypothesis 2 and Hypothesis 2 Curve Fit for midship bending moment. TEV = $3.0\sigma_{BM}$, $N = 101$, heading angle = 180°, forward speed = 12.5 knots. Average time series generated from 2000 sample time series; 20 sample time series are plotted.

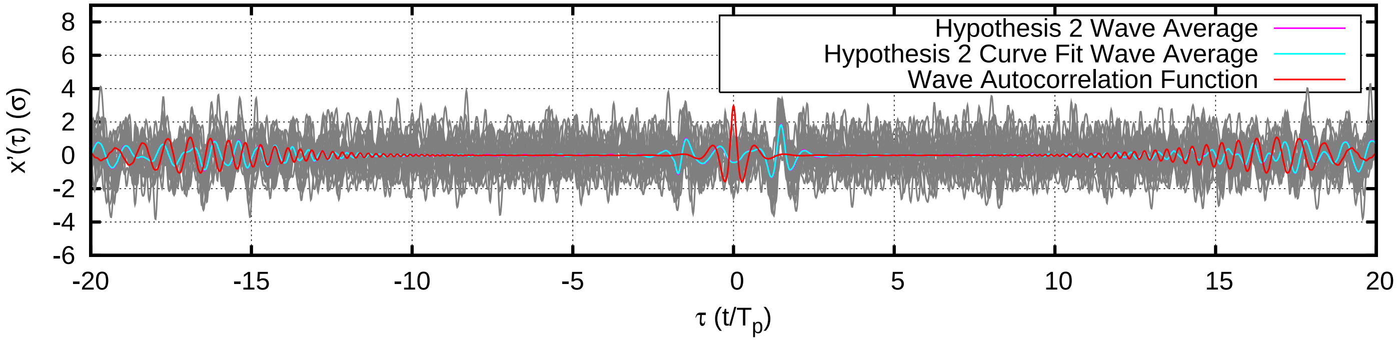

Figure 5.13: Rigid body analysis: *Stewart J. Cort*. Sample wave time series at midship: Hypothesis 2 and Hypothesis 2 Curve Fit for midship bending moment. TEV = $3.0\sigma_{BM}$, $N = 101$, heading angle = 180°, forward speed = 12.5 knots. Average time series generated from 2000 sample time series; 20 sample time series are plotted.

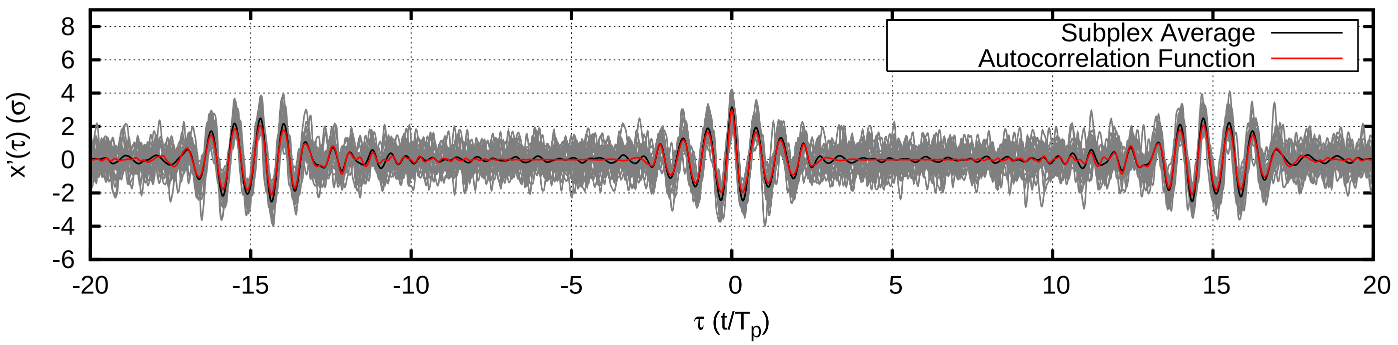

Figure 5.14: Rigid body analysis: *Stewart J. Cort*. Sample bending moment time series at midship: Subplex for midship bending moment. TEV = $3.0\sigma_{BM}$, $N = 101$, heading angle = 180°, forward speed = 12.5 knots. Average time series generated from 2000 sample time series; 20 sample time series are plotted.

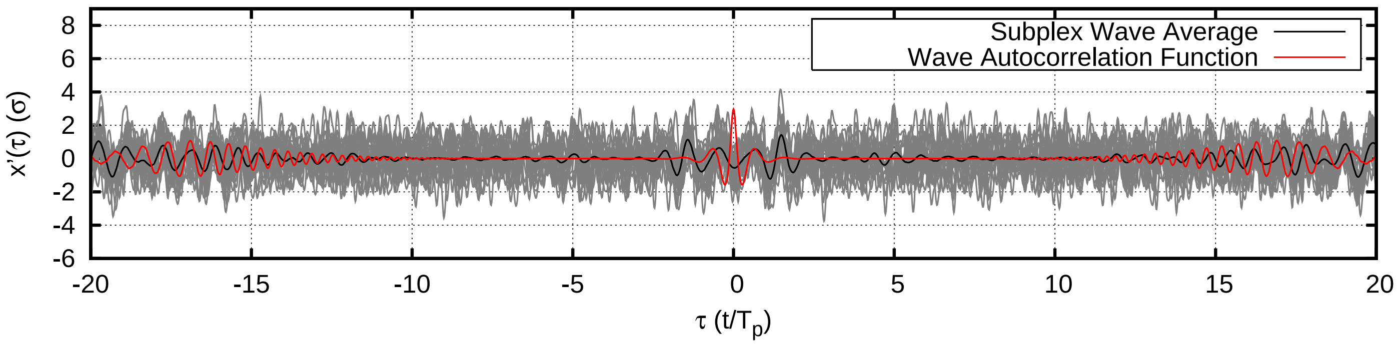

Figure 5.15: Rigid body analysis: *Stewart J. Cort*. Sample wave time series at midship: Subplex for midship bending moment. TEV = $3.0\sigma_{BM}$, $N = 101$, heading angle = 180°, forward speed = 12.5 knots. Average time series generated from 2000 sample time series; 20 sample time series are plotted.

Elastic Body Analysis

Figures 5.16 - 5.28 highlight the results for a $3.0\sigma_{BM}$ value of the vertical bending moment at midship for the *Cort* as estimated using elastic body dynamics (the full analysis may be found in Appendix A). Figure 5.16 shows the component amplitudes used in the elastic body analysis. Comparing these amplitudes to the amplitudes used in the rigid body analysis, one can see how the largest amplitude has shifted to a frequency of 1.9 rad/s.

The various extreme value PDFs for the elastic body response are shown in Fig. 5.17. Again, these PDFs are similar to those found in the earlier analysis using the ITTC sea spectrum. The phase PDFs based on Monte Carlo simulation using Hypothesis 2 (Figs. 5.18 and 5.19) show several regions of phase focusing, the greatest focusing corresponding to the largest amplitude in Fig. 5.16. Since the extreme value PDFs are similar to those found earlier, it again appears that the phase PDF developed from Hypothesis 2 is an adequate description of the phases even for the complex response spectrum of this bending moment response that has many significant amplitudes spread throughout the frequency range.

The phase parameters, λ_j, found from the Subplex method are compared to those found from Monte Carlo simulation in Fig. 5.20. For the largest amplitudes, λ_j as calculated by Subplex optimization is slightly less than λ_j from Monte Carlo simulation. For the smalller amplitudes, λ_j from the Subplex method is about twice as large as λ_j from Monte Carlo simulation. The effects of the difference between the Hypothesis 2 phases (Fig. 5.18) and the Subplex phases (Fig. 5.22) are apparent in that their corresponding extreme value PDFs are not exactly the same. However, the extreme value PDFs are still generally similar and support the claim that the overall process is not sensitive to individual changes of phase distributions.

The characteristic functions from the elastic body analysis (Fig. 5.21) are a poorer match than was found for the rigid body analysis. It is presumed that the larger number of significant amplitudes makes it more challenging for the Subplex optimization to determine the effects of each component. Appendix A contains examples in which the agreement between characteristic functions is better.

Example response design time series are shown in Figs. 5.23, 5.25, and 5.27. The autocorrelation function of the elastic body bending moment exhibits the ringing behavior characteristic of springing. In other words, the bending moment builds up over many wave periods. The average response time series from Monte Carlo simulation and using the Modified Gaussian phase distribution exhibit this same behavior. Individual response time series are closer to the average time series than they were for the rigid body case. This could be due to the dominance of the largest amplitude at the system's natural frequency. The effect of phase independence is shown in the variance of the maximum response at $\tau = 0$.

The resulting incident wave time series are shown in Figs. 5.24, 5.26, and 5.28. The incident wave, as measured at midship of the moving ship, was calculated using the relations in Eqs. 4.5 and 4.6. In this case of elastic body bending moment, the average wave profile that produces a $3.0\sigma_{BM}$ response is not a large peak or trough, such as would be described by the autocorrelation function (the autocorrelation function is plotted for reference in each set of wave time series). Instead, the waves exhibit a "ringing" phenomenon that mimics the response, although the period of primary wave build-up is much shorter than the period of response build-up. The frequency of the waves in the time shortly prior to the design response (at time $\tau = 0$) seems to be of particular importance. In this time period, most of the individual wave time series have collapsed to similar profiles, with several wave encounters in a row being

$3.0\sigma_{wave}$ events. The rest of the time series do not appear to share common characteristics. As seen with the rigid body analysis, it is clear that using a large design wave to estimate large bending moment at midship would be inappropriate because the wave autocorrelation function does not match the average wave profile that has been conditioned by the response.

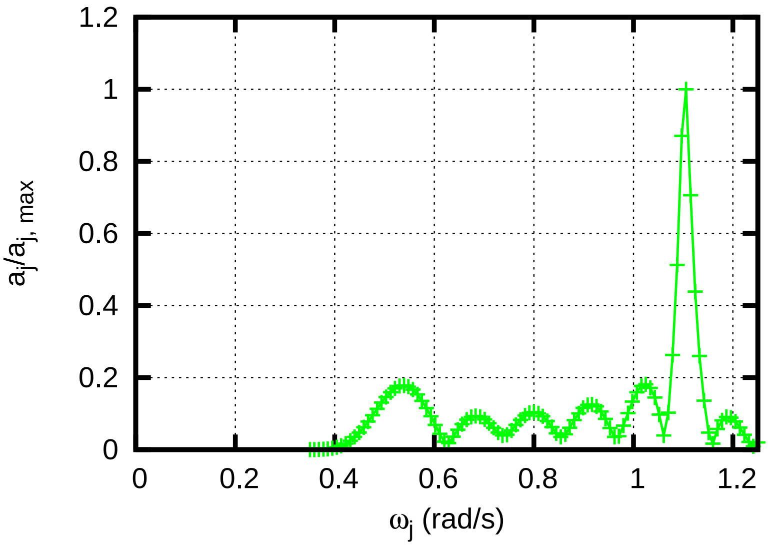

Figure 5.16: Elastic body analysis: *Stewart J. Cort.* Amplitudes for midship bending moment. $N = 101$, heading angle $= 180°$, forward speed $= 12.5$ knots.

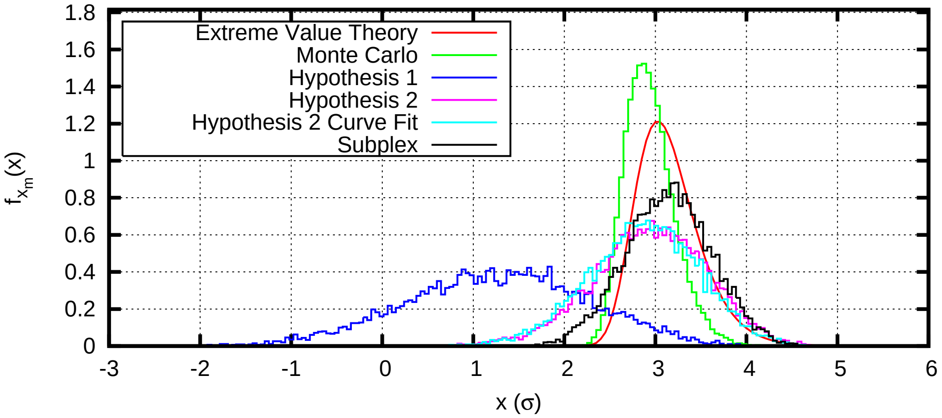

Figure 5.17: Elastic body analysis: *Stewart J. Cort*. Extreme value PDFs for midship bending moment. TEV = $3.0\sigma_{BM}$, $N =$ 101, heading angle = 180°, forward speed = 12.5 knots.

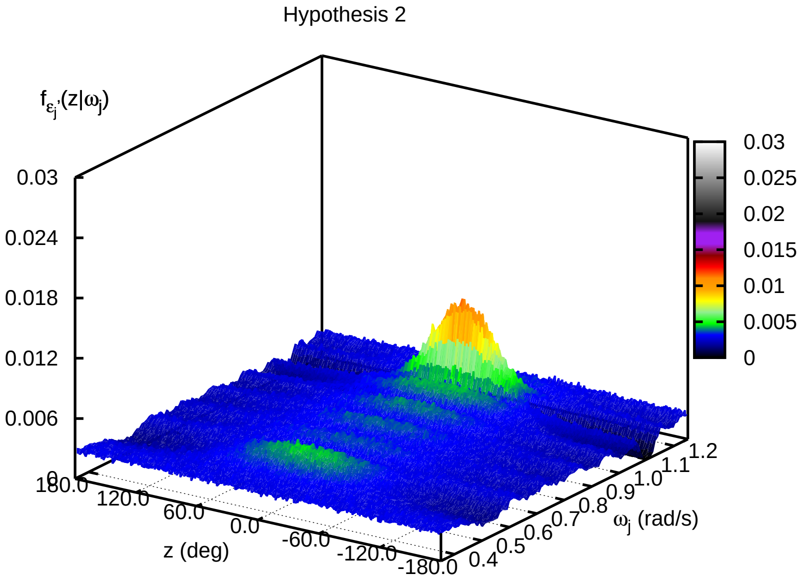

Figure 5.18: Elastic body analysis: *Stewart J. Cort*. Phase PDF: Hypothesis 2 for midship bending moment. TEV = $3.0\sigma_{BM}$, $N =$ 101, heading angle = 180°, forward speed = 12.5 knots.

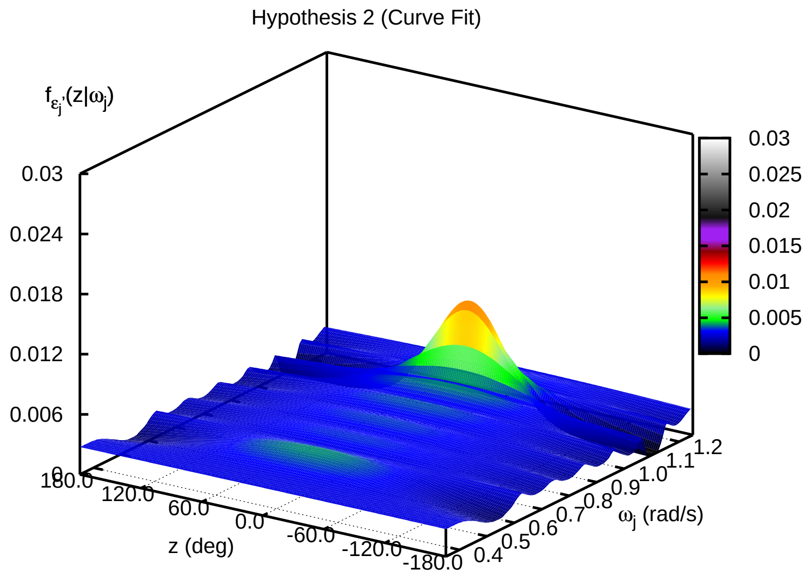

Figure 5.19: Elastic body analysis: *Stewart J. Cort.* Phase PDF: Hypothesis 2 (curve fit) for midship bending moment. TEV = $3.0\sigma_{BM}$, $N = 101$, heading angle = 180°, forward speed = 12.5 knots.

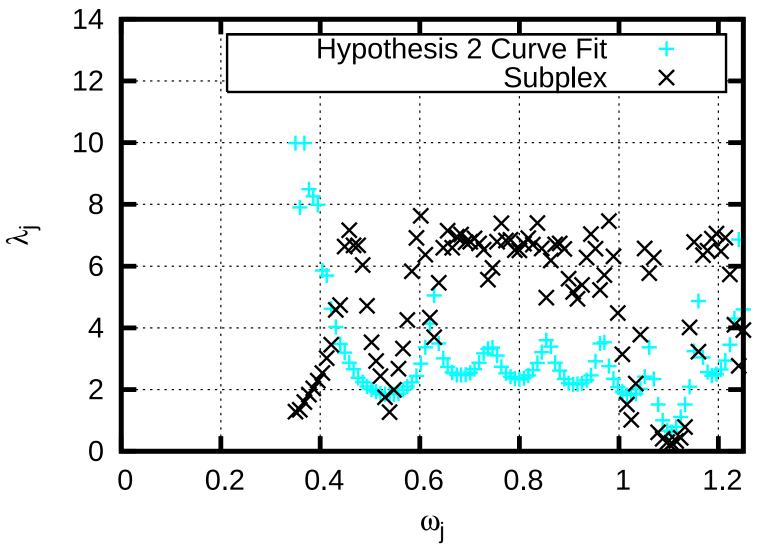

Figure 5.20: Elastic body analysis: *Stewart J. Cort.* λ_j for midship bending moment. TEV = $3.0\sigma_{BM}$, $N = 101$, heading angle = 180°, forward speed = 12.5 knots.

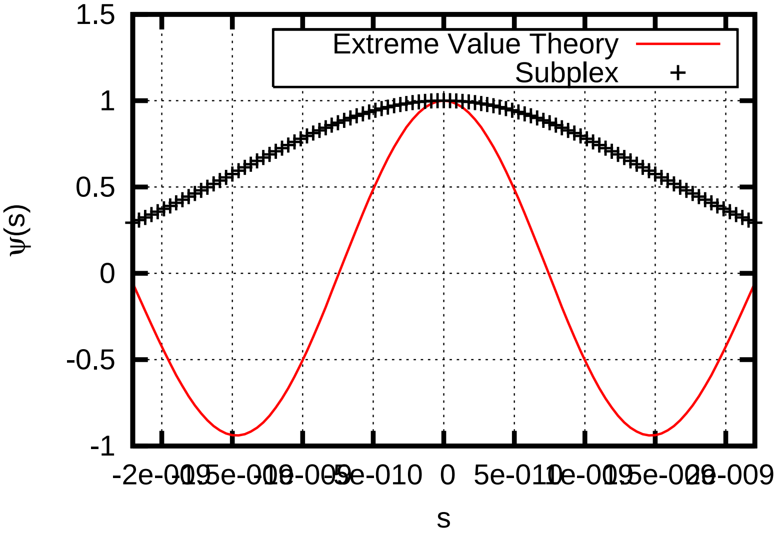

Figure 5.21: Elastic body analysis: *Stewart J. Cort*. Characteristic Functions for midship bending moment. TEV $= 3.0\sigma_{BM}$, $N = 101$, heading angle = 180°, forward speed = 12.5 knots.

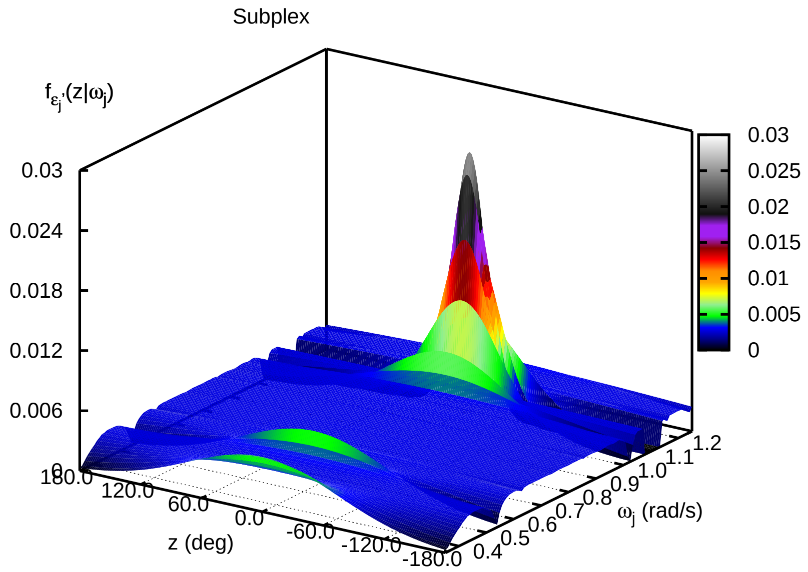

Figure 5.22: Elastic body analysis: *Stewart J. Cort*. Phase PDF: Subplex for midship bending moment. TEV $= 3.0\sigma_{BM}$, $N = 101$, heading angle = 180°, forward speed = 12.5 knots.

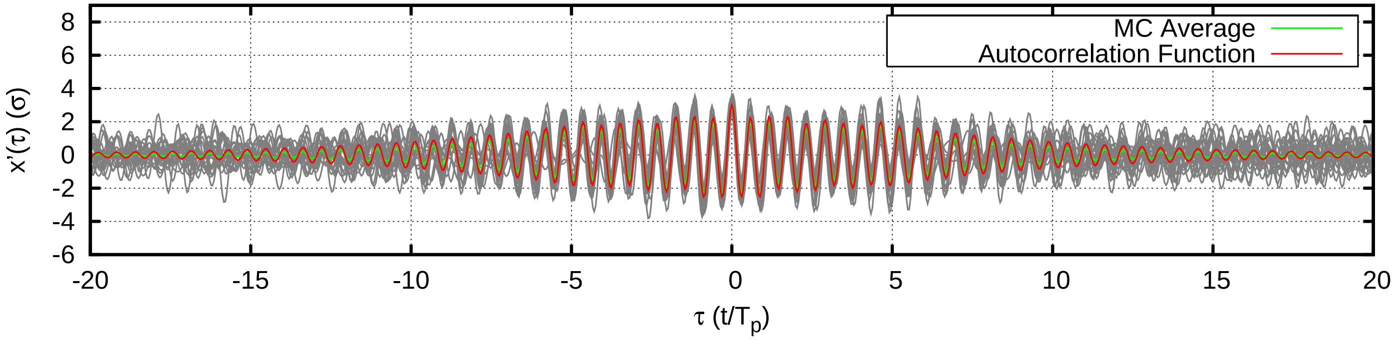

Figure 5.23: Elastic body analysis: *Stewart J. Cort.* Sample bending moment time series at midship: Monte Carlo Simulation for midship bending moment. TEV = $3.0\sigma_{BM}$, $N = 101$, heading angle = 180°, forward speed = 12.5 knots. Average time series generated from 2000 sample time series; 20 sample time series are plotted.

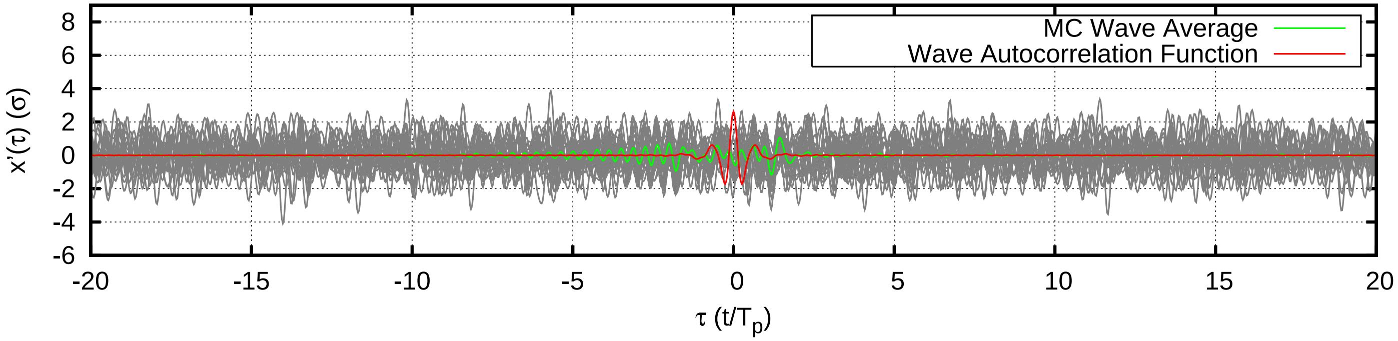

Figure 5.24: Elastic body analysis: *Stewart J. Cort.* Sample wave time series at midship: Monte Carlo Simulation for midship bending moment. TEV = $3.0\sigma_{BM}$, $N = 101$, heading angle = 180°, forward speed = 12.5 knots. Average time series generated from 2000 sample time series; 20 sample time series are plotted.

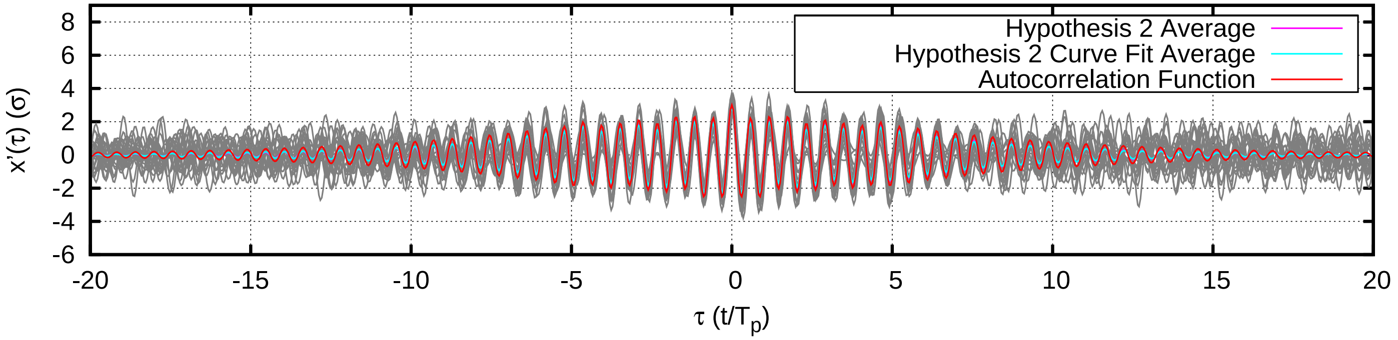

Figure 5.25: Elastic body analysis: *Stewart J. Cort.* Sample bending moment time series at midship: Hypothesis 2 and Hypothesis 2 Curve Fit for midship bending moment. TEV = $3.0\sigma_{BM}$, $N = 101$, heading angle = 180°, forward speed = 12.5 knots. Average time series generated from 2000 sample time series; 20 sample time series are plotted.

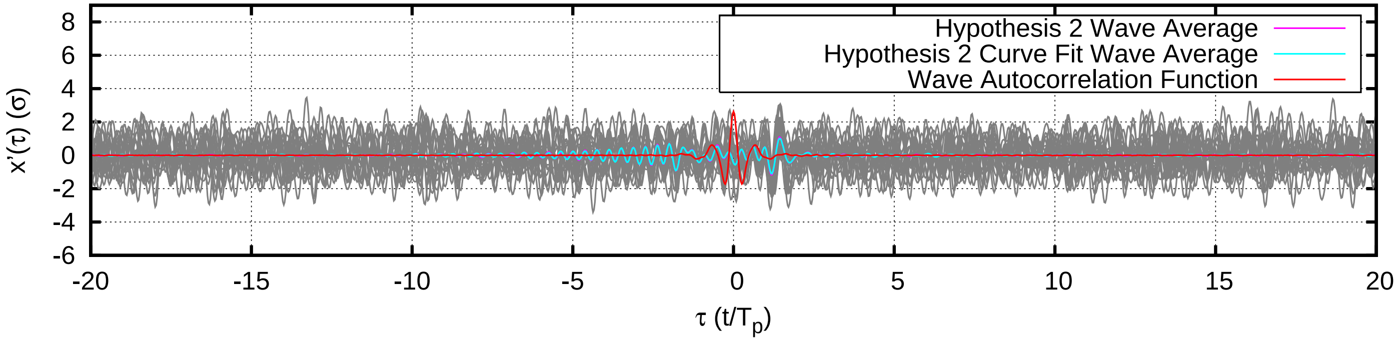

Figure 5.26: Elastic body analysis: *Stewart J. Cort.* Sample wave time series at midship: Hypothesis 2 and Hypothesis 2 Curve Fit for midship bending moment. TEV = $3.0\sigma_{BM}$, $N = 101$, heading angle = 180°, forward speed = 12.5 knots. Average time series generated from 2000 sample time series; 20 sample time series are plotted.

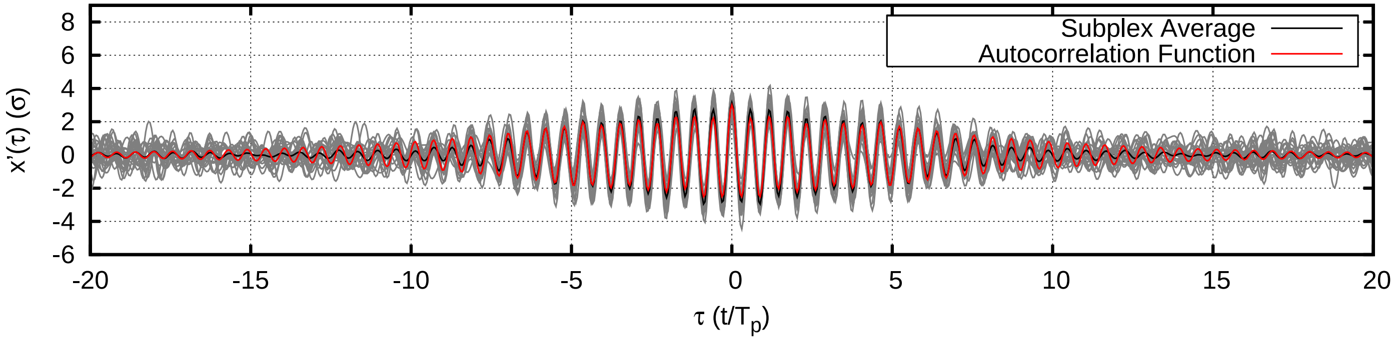

Figure 5.27: Elastic body analysis: *Stewart J. Cort*. Sample bending moment time series at midship: Subplex for midship bending moment. TEV $= 3.0\sigma_{BM}$, $N = 101$, heading angle $= 180°$, forward speed $= 12.5$ knots. Average time series generated from 2000 sample time series; 20 sample time series are plotted.

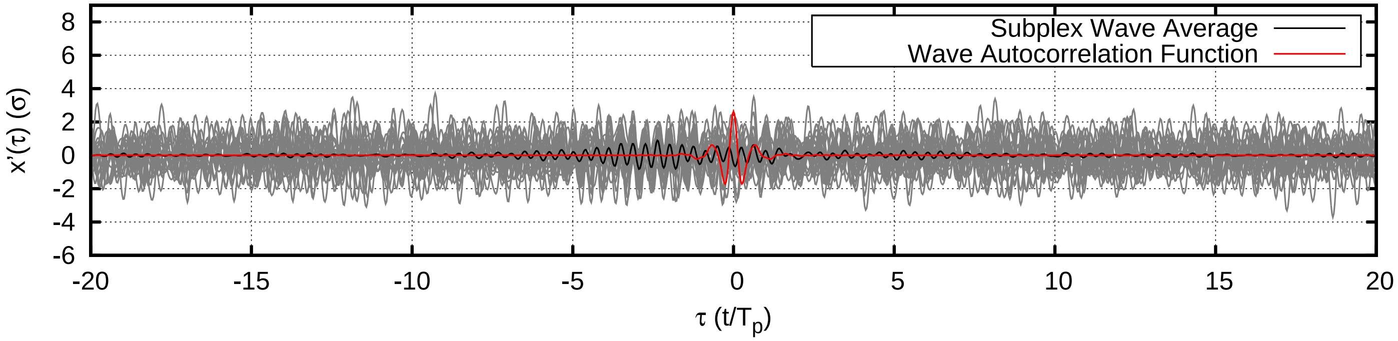

Figure 5.28: Elastic body analysis: *Stewart J. Cort*. Sample wave time series at midship: Subplex for midship bending moment. TEV $= 3.0\sigma_{BM}$, $N = 101$, heading angle $= 180°$, forward speed $= 12.5$ knots. Average time series generated from 2000 sample time series; 20 sample time series are plotted.

5.2.2 Target Extreme Value (TEV): $5.0\sigma_{BM}$

The extensive simulations conducted for $3.0\sigma_{BM}$ responses in the previous section indicate that generating design loads using the Modified Gaussian distribution yields useful results. The extreme value PDFs do not quite match, yet, but the resulting time series for the response have the proper average (the autocorrelation function). The average of the wave time series generated with via subplex optimization also matches the average of those generated by Monte Carlo simulation, which justifies using subplex optimization to directly generate the phase parameters, λ_j.

To show how valuable this method is, consider a design event of 5.0σ. A 5.0σ event is much more rare than a 3.0σ event and is accordingly much harder to simulate. Certainly, generating 50,000 samples of a 5.0σ event is difficult. A fraction of that potential simulation time could instead be used to generate λ_j directly, and design response time series created using the Modified Gaussian non-uniform phase distribution. This was done for both rigid body and elastic body bending moment at midship of the *Cort*.

Rigid Body Analysis

The amplitudes used for this $5.0\sigma_{BM}$ example are the same as were used for the $3.0\sigma_{BM}$ example because the same response conditions are being tested, just a larger TEV is desired. Figures 5.29- 5.34 highlight the results for a $5.0\sigma_{BM}$ value of the vertical bending moment at midship for the *Cort* as estimated using rigid body dynamics only (the full analysis may be found in Appendix A).

The extreme value PDFs from extreme value theory and the Subplex method for the response are shown in Fig. 5.29. The two PDFs are a better match for this $5.0\sigma_{BM}$ event than the $3.0\sigma_{BM}$ event, likely due to the TEV being closer to the maximum attainable value. In other words, as the target extreme value approaches the maximum value attainable by the discretization of the response spectrum, the phase PDFs will each approach a delta function. Therefore, there is less variance in the phases and less variance to the response PDF that results from the concentrated phase PDFs.

The phase parameters, λ_j, found from the Subplex method are shown in Fig. 5.30. All of the phase parameters are smaller than they were for the $3.0\sigma_{BM}$ event, reflecting how the phases must be more concentrated to produce a larger TEV given the same set of amplitudes. The characteristic functions (Fig. 5.31) are a much better match than for the $3.0\sigma_{BM}$ event. This is also likely due to the TEV being closer to the maximum attainable value. The Subplex phase PDF in Fig. 5.32 shows how all of the phases must be concentrated, to varying degrees, to produce this $5.0\sigma_{BM}$ event.

Sample response design time series generated using the Subplex phase PDF are shown in Fig. 5.33. The average response time series matches well with the response's autocorrelation function, which supports the conclusion that useful design time series are created using the Subplex method without prior Monte Carlo simulation. The individual response time series collapse to nearly the same behavior as the autocorrelation function about $\tau = 0$. As with the $3.0\sigma_{BM}$ event, there is also evidence of signal repetition in the time series, an indication that the frequency discretization was not fine enough in this example.

The corresponding incident wave time series for these response time series are shown in Fig. 5.34. The incident wave, as measured at midship of the moving ship, was calculated using the relations in Eqs. 4.5 and 4.6. As seen with the $3.0\sigma_{BM}$ event, the average wave profile that produces a $5.0\sigma_{BM}$ response is not a large peak or trough, such as would be described by the autocorrelation function (the autocorrelation function is plotted for reference in each set of wave time series). Instead, there is a large trough before $\tau = 0$ and a large peak after. The trough and the peak could both be described as $5.0\sigma_{wave}$ events, but only when they occur at the proper time do they produce a $5.0\sigma_{BM}$ response.

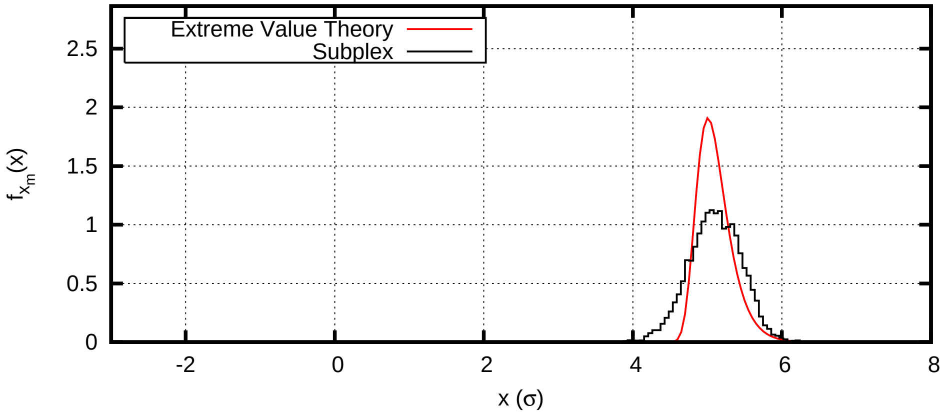

Figure 5.29: Rigid body analysis: *Stewart J. Cort*. Extreme value PDFs for midship bending moment. TEV = $5.0\sigma_{BM}$, $N = 101$, heading angle = 180°, forward speed = 12.5 knots.

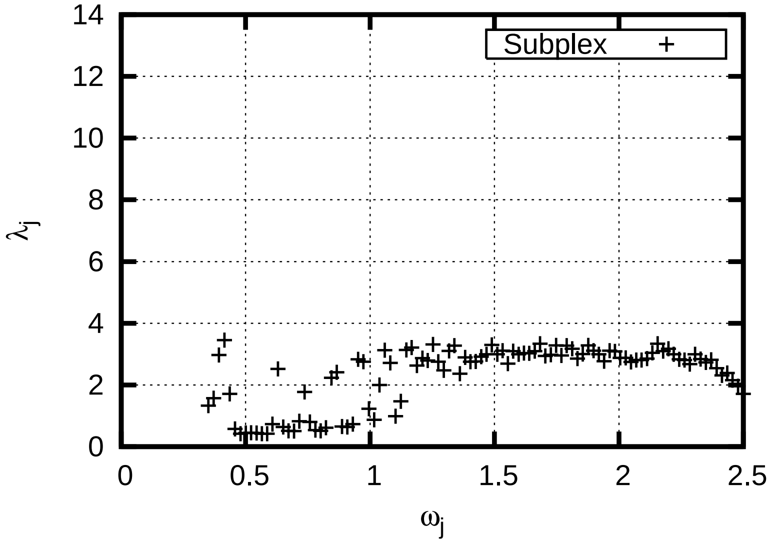

Figure 5.30: Rigid body analysis: *Stewart J. Cort.* λ_j for midship bending moment. TEV $= 5.0\sigma_{BM}$, $N = 101$, heading angle $= 180°$, forward speed $= 12.5$ knots.

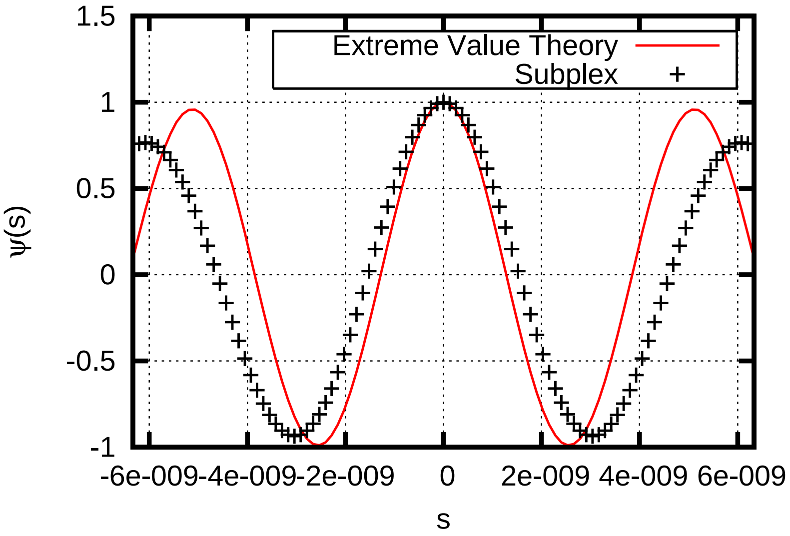

Figure 5.31: Rigid body analysis: *Stewart J. Cort.* Characteristic functions for midship bending moment. TEV $= 5.0\sigma_{BM}$, $N = 101$, heading angle $= 180°$, forward speed $= 12.5$ knots.

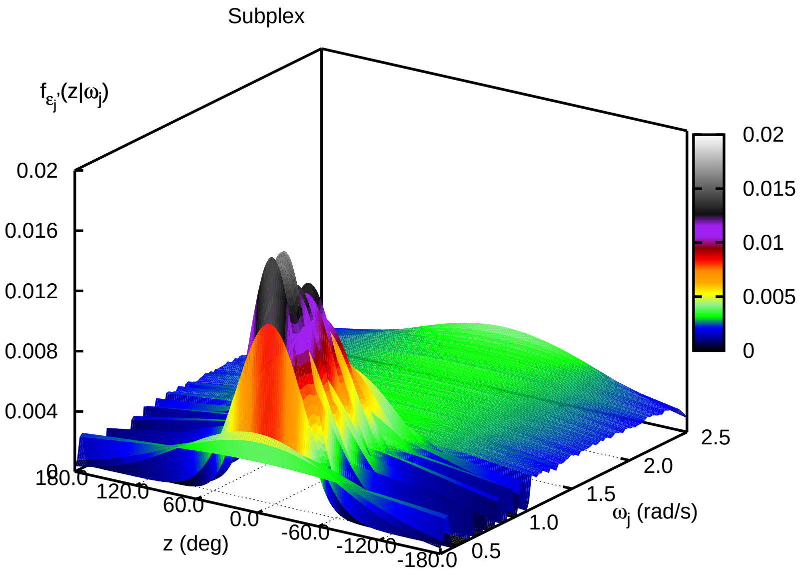

Figure 5.32: Rigid body analysis: *Stewart J. Cort*. Phase PDF: Subplex for midship bending moment. TEV = $5.0\sigma_{BM}$, N = 101, heading angle = 180°, forward speed = 12.5 knots.

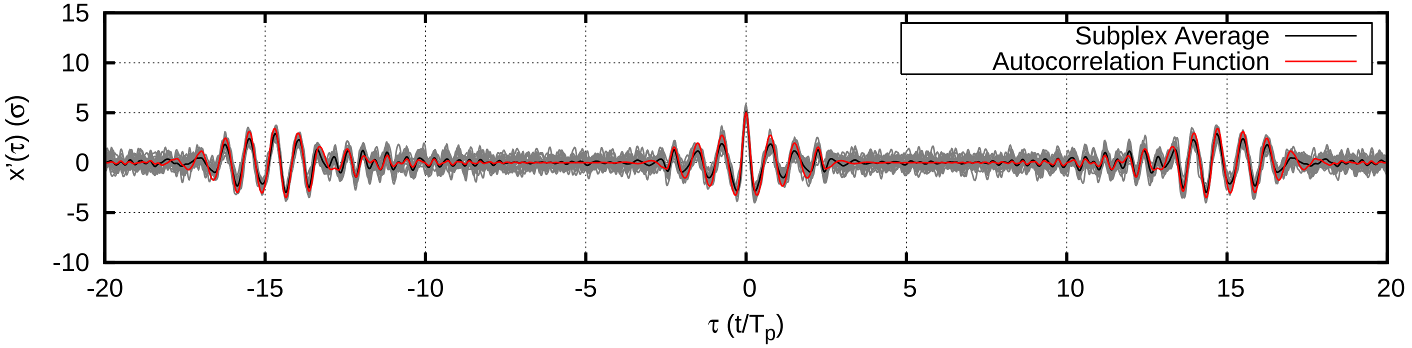

Figure 5.33: Rigid body analysis: *Stewart J. Cort*. Sample bending moment time series at midship: Subplex for midship bending moment. TEV = $5.0\sigma_{BM}$, $N = 101$, heading angle = 180°, forward speed = 12.5 knots. Average time series generated from 2000 sample time series; 20 sample time series are plotted.

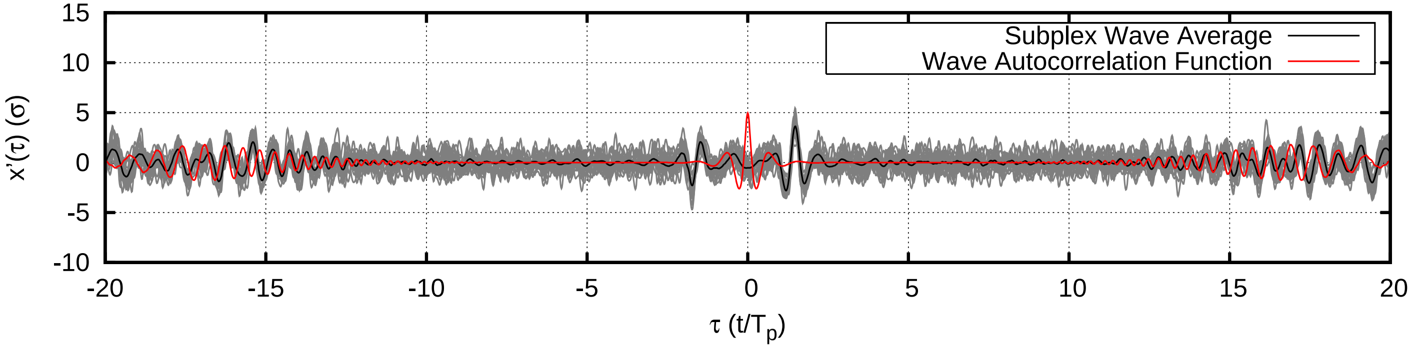

Figure 5.34: Rigid body analysis: *Stewart J. Cort*. Sample wave time series at midship: Subplex for midship bending moment. TEV = $5.0\sigma_{BM}$, $N = 101$, heading angle = 180°, forward speed = 12.5 knots. Average time series generated from 2000 sample time series; 20 sample time series are plotted.

Elastic Body Analysis

The amplitudes used for this $5.0\sigma_{BM}$ example are the same as were used for the $3.0\sigma_{BM}$ example because the same response conditions are being tested, just a larger TEV is desired. Figures 5.35- 5.40 highlight the results for a $5.0\sigma_{BM}$ value of the vertical bending moment at midship for the *Cort* as estimated using an elastic body analysis (the full analysis may be found in Appendix A).

The extreme value PDFs from extreme value theory and the Subplex method for the response are shown in Fig. 5.35. The two PDFs are a better match for this $5.0\sigma_{BM}$ event than the $3.0\sigma_{BM}$ event, again likely due to the TEV being closer to the maximum attainable value. However, the extreme value PDFs from the rigid body analysis for a $5.0\sigma_{BM}$ event are a better match than those in Fig. 5.35.

The phase parameters, λ_j, found from the Subplex method are shown in Fig. 5.36. All of the phase parameters are smaller than they were for the $3.0\sigma_{BM}$ event, reflecting how the phases must be more concentrated to produce a larger TEV given the same set of amplitudes. The variation in λ_j still tracks the variation in the amplitudes, though.

The characteristic functions (Fig. 5.37) are a much better match than for the $3.0\sigma_{BM}$ event, though not as good as the rigid body $5.0\sigma_{BM}$ event. The improvement is likely due to the TEV being closer to the maximum attainable value, while the number of significant amplitudes negatively impacts the results from the Subplex optimization. The Subplex phase PDF in Fig. 5.38 shows how all of the phases must be concentrated, to varying degrees, to produce this $5.0\sigma_{BM}$ event.

Sample response design time series generated using the Subplex phase PDF are shown in Fig. 5.39. The average response time series shows the same ringing behavior of the response's autocorrelation function, but the average appears to under-predict the response (as compared to the autocorrelation function) except for at $\tau = 0$. The individual response time series also seem to under-predict the response except for at $\tau = 0$.

The corresponding incident wave time series for these response time series are shown in Fig. 5.40. The incident wave, as measured at midship of the moving ship, was calculated using the relations in Eqs. 4.5 and 4.6. Here, it is clear that a design wave that is merely a large peak or trough would not result in the desired design response. The conditioned incident waves show both a period of build-up in height before the design response at $\tau = 0$ and a large trough-peak-trough combination following the large response. In addition, there is, on average, a moderately large trough before the design response occurs, but the large troughs and peak that occur afterward could all be described as near-$5.0\sigma_{wave}$ events.

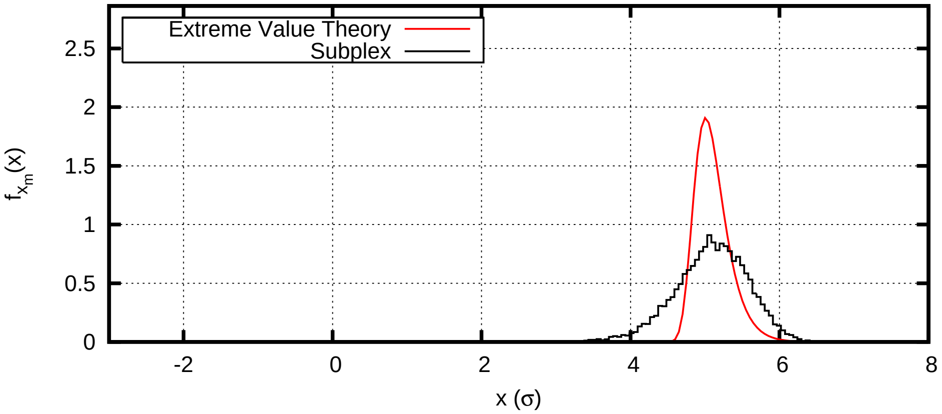

Figure 5.35: Elastic body analysis: *Stewart J. Cort.* Extreme value PDFs for midship bending moment. TEV $= 5.0\sigma_{BM}$, $N = 101$, heading angle = 180°, forward speed = 12.5 knots.

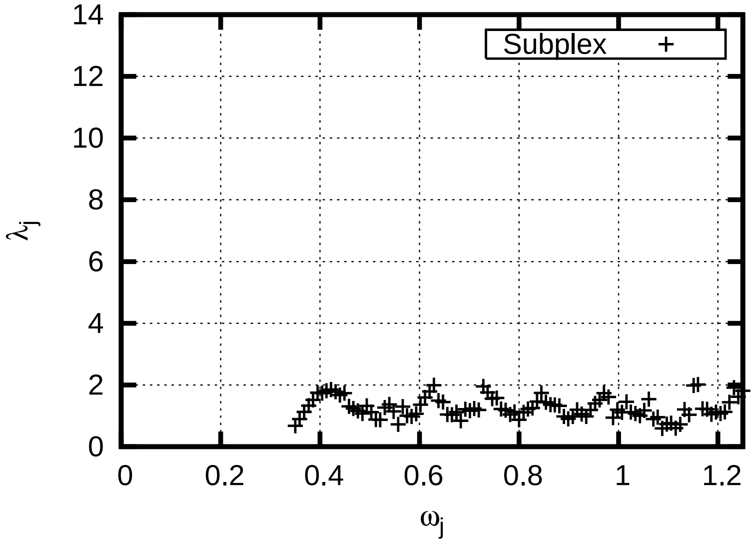

Figure 5.36: Elastic body analysis: *Stewart J. Cort.* λ_j for midship bending moment. TEV $= 5.0\sigma_{BM}$, $N = 101$, heading angle = 180°, forward speed = 12.5 knots.

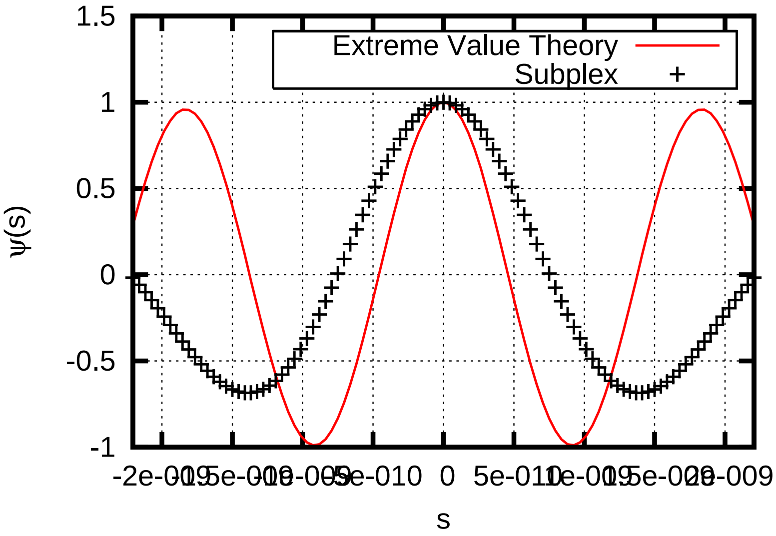

Figure 5.37: Elastic body analysis: *Stewart J. Cort.* Characteristic Functions for midship bending moment. TEV $= 5.0\sigma_{BM}$, $N = 101$, heading angle = 180°, forward speed = 12.5 knots.

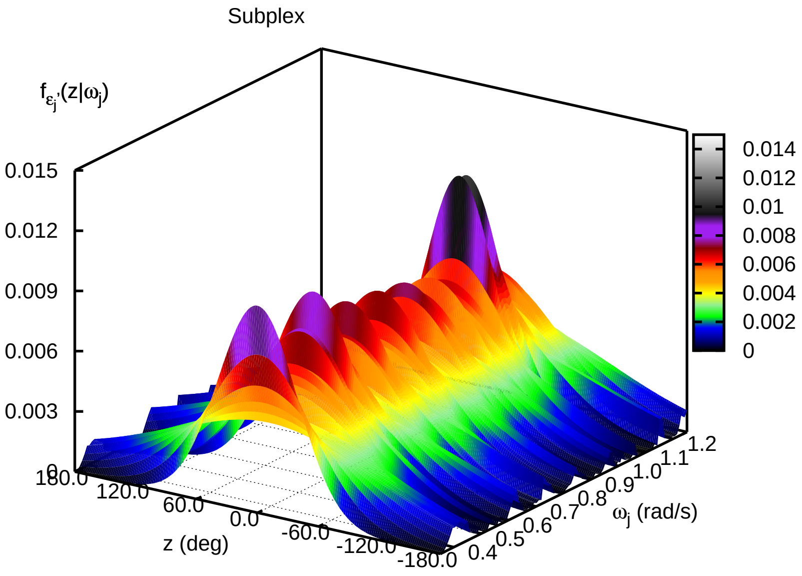

Figure 5.38: Elastic body analysis: *Stewart J. Cort*. Phase PDF: Subplex for midship bending moment. TEV = $5.0\sigma_{BM}$, $N = 101$, heading angle = 180°, forward speed = 12.5 knots.

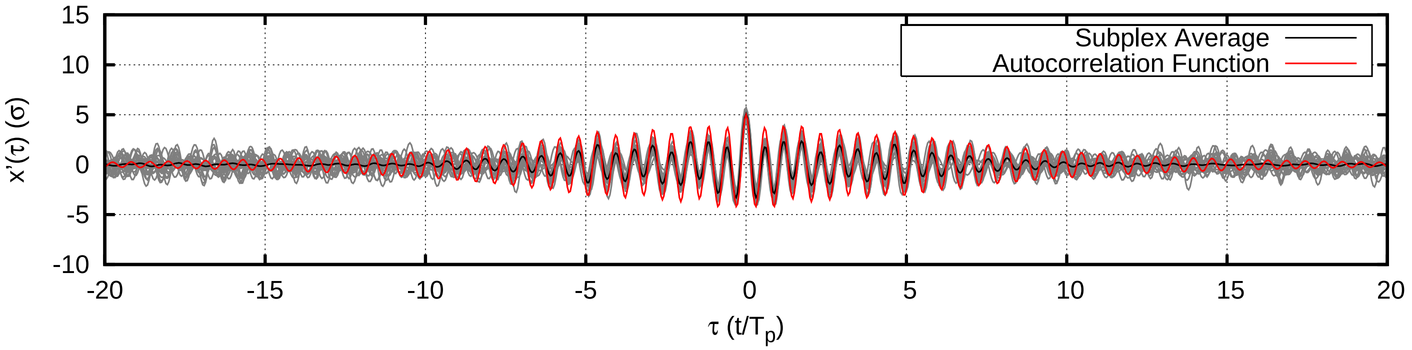

Figure 5.39: Elastic body analysis: *Stewart J. Cort*. Sample bending moment time series at midship: Subplex for midship bending moment. TEV $= 5.0\sigma_{BM}$, $N = 101$, heading angle = 180°, forward speed = 12.5 knots. Average time series generated from 2000 sample time series; 20 sample time series are plotted.

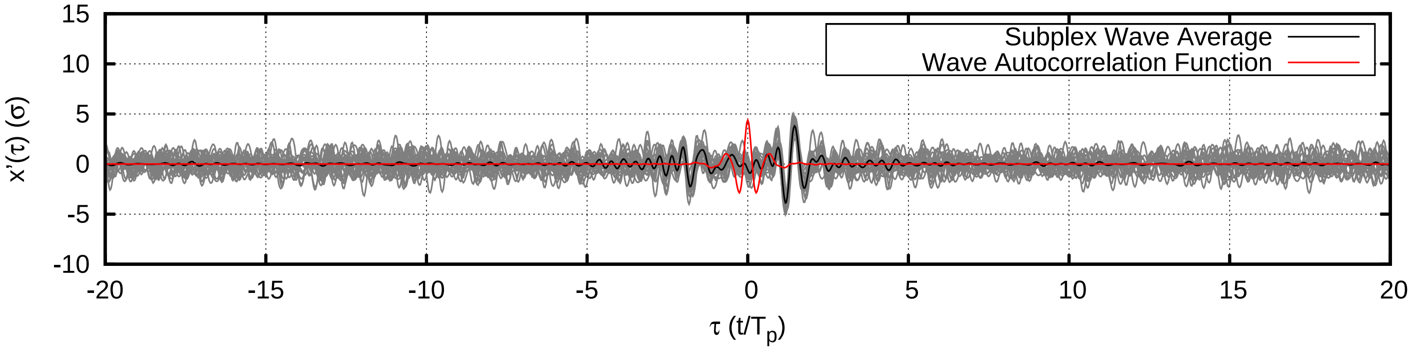

Figure 5.40: Elastic body analysis: *Stewart J. Cort*. Sample wave time series at midship: Subplex for midship bending moment. TEV $= 5.0\sigma_{BM}$, $N = 101$, heading angle = 180°, forward speed = 12.5 knots. Average time series generated from 2000 sample time series; 20 sample time series are plotted.

CHAPTER 6

Conclusions and Recommendations

6.1 Concluding Remarks

The research presented in this dissertation was primarily directed at the effect of extreme values of a random process on the phase angles of its random components. In particular, the PDFs of the component phases were found to be non-uniform when a finite number of components is used. The non-uniform phase distributions were then modeled with the Modified Gaussian distribution and related back to the extreme value. In this way, statistically-equivalent design time series may be produced that have a given extreme value at time $t = 0$.

The method presented here has several strengths. First, it is related to extreme value theory, which is an established arm of mathematics and useful for quantifying risk. Second, a single analysis results in many sample design scenarios that can be used to estimate nonlinear statistics. Third, it is versatile; not only can any response with a transfer function be analyzed, but the method does not restrict the form of the response in any manner. These aspects are all important to a naval architect charged with analyzing new, potential designs.

Based on the work presented in this dissertation, there must be a balance between properly describing the response spectrum and producing an extreme value PDF that approaches the PDF predicted by extreme value theory. The limited number of examples in Appendix A suggest that the number of components be just sufficient that the extreme value PDF for a 3.0σ event from Monte Carlo simulation match the extreme value PDF as predicted by extreme value theory and that the target design response is less than 75% of the maximum attainable response.

Measures of merit for the final comparison of target design response PDFs (extreme value theory PDF vs. PDF resulting from phases with Modified Gaussian distributions) include the average extreme values, the variance of the extreme values, the most likely extreme values, and the divergence (such as Kullback-Leibler) of the two PDFs. At a minimum, the average extreme value should be equal. The variance of the extreme values will be different due to the necessary assumption that the phases are independent, but this difference should be minimized. The most likely extreme values should be similar in value, and the divergence, of course, should be minimized.

The major measure of merit concerning response design time series is that the average response design time series should be equal to the response's autocorrelation function scaled by the target response value. Recall that this measure of merit does *not* apply to the resulting incident wave time series that have been conditioned by the response.

The end application of this method is to calculate short design time series that are used with nonlinear, physics-based models to estimate long-term statistics without costly long-term simulations in early design. The efficiency and versatility of this method will allow a designer to make intelligent checks on the feasibility of new designs before the design particulars are locked in and changes become expensive. Optimization routines that analyze hundreds of different configurations can use this approach of determining design loads to estimate ship motions and stresses for each and every configuration. This ability to intelligently check for designs that are very good or very bad will reduce the search space for parameters and reduce the risk associated with new designs.

6.1.1 Applications

The method presented in Chapter 4 of producing design response time series can be directly applied to any ship or offshore structure response that can be described by a linear transfer function. In addition to calculating design time series, the method also provides a way to estimate the PDF of other responses given an extreme value of another response. For example, a structural engineer may wish to know how an extreme bending moment at midship affects the secondary and tertiary stresses in certain members. The PDF of the member's stress given an extreme bending moment at midship may not be immediately obvious. However, if this method is used to get the phase distributions of the bending moment response, the bending moment transfer function will determine the phase distribution of the incident wave components. If a finite element analysis is used to determine a transfer function for the member in question, it can be used in conjunction with the incident wave phase distributions to determine the phase distributions of the stress in the member. By the right-hand side of Eq. 3.20, one can calculate the characteristic function of the stress in that member given that the midship bending moment is large, and the corresponding PDF can be found by inversing the characteristic function transformation in Eq. 3.9.

6.2 Recommendations for Future Research

There are two major areas that should be addressed in future research. The first is to investigate the dependencies of $f_{\epsilon'_1\epsilon'_2\cdots\,\epsilon'_N}(z_1, z_2, \cdots, z_N|x_m)$. The second is to expand the method to maximize/minimize multiple processes at the same time.

Addressing these two areas will render this method a very powerful tool and will create an analysis particularly suited to early design optimization cycles.

In addition to these two major areas of research, more extensive simulations should be performed to better define the relationships between the number of components, the maximum response attainable due to discretization, and the target design response. These simulations should include cases with increased number of components (say, $N = 201, 501, 1001$), as well multiple design response values and response spectra.

6.2.1 Phase Dependencies

An obvious candidate for future research are the unknown dependencies of the joint phase PDF, $f_{\epsilon'_1\epsilon'_2\cdots\,\epsilon'_N}(z_1, z_2, \cdots, z_N|x_m)$. The phase model in Chap. 3 and its solution via Subplex optimization is an engineering approximation that is useful in that it consistently generates an extreme value PDF that has the same peak value as predicted by statistical theory. However, the PDF of x_m as estimated using the Modified Gaussian phase distribution is still too broad due to the assumption that the phases are independent. A natural starting point would be to investigate numerically the effects of spectrum, N, and m on the joint phase PDF. These numerical simulations would then hopefully lead to either an analytical solution or a convenient model similar in vein to the Modified Gaussian phase distribution.

6.2.2 Expanding to Multiple Processes

There are many examples of situations where a designer wishes to maximize not just one process but several. Slamming, while a highly nonlinear process, could be predicted using a wave train designed to maximize both relative motion and relative velocity at the bow. Relative motion, defined as the motion of the ship relative to the ocean surface, and relative velocity are linear processes and candidates for analysis using this method. The relative motion at a point near the bow, η, and the relative velocity, $\dot{\eta}$, have a joint extreme value PDF, $f_{\eta_m,\dot{\eta}_n}(z_1, z_2)$. Following the approach in Chapter 3, one would solve:

$$f_{\eta_m,\dot{\eta}_n}(z_1, z_2) = f_{\eta',\dot{\eta}'}(z_1, z_2) \tag{6.1}$$

$$\psi_{\eta_m,\dot{\eta}_n}(s_1, s_2) = \psi_{\eta',\dot{\eta}'}(s_1, s_2) \tag{6.2}$$

Because η and $\dot{\eta}$ can be related back to the incident wave via linear systems theory, the solution to Eq. 6.1 could be formulated such that the result is one set of λ_j that would define the phase PDF of the incident wave components, rather than the response (as done in Chapter 4). Once λ_j has been calculated, sample design time series would be generated which would maximize both relative motion and relative velocity. These time series would then be used in nonlinear seakeeping programs that are capable of detecting slamming.

Another example of a highly desirable combination of linear events is roll angle and roll velocity. In capsize analysis, the roll angle of the ship is often not enough to predict the onset of capsize (see reference to roll stuff). If this analysis can be expanded to two incorporate two processes, however, both roll and roll velocity can be maximized with a single design wave train. The same could be done for any of the many combinations of stress and shear at different points of a ship's hull.

APPENDICES

APPENDIX A

Test Cases

Table A.1: Test Cases Matrix

Case No.	**Spectrum**	**TEV**	**N**
1	ITTC SS3	3.0σ	51
2	ITTC SS9	3.0σ	51
3	ITTC SS3	5.0σ	51
4	ITTC SS9	5.0σ	51
5	ITTC SS3	3.0σ	101
6	ITTC SS9	3.0σ	101
7	ITTC SS3	5.0σ	101
8	ITTC SS9	5.0σ	101
9	*S.J. Cort* rigid body BM	3.0σ	101
10	*S.J. Cort* rigid body BM	5.0σ	101
11	*S.J. Cort* elastic body BM	3.0σ	101
12	*S.J. Cort* elastic body BM	5.0σ	101

A.1 Case 1

Case	**1**	
H_{sig}	0.88	m
T_{peak}	7.50	sec
N	51	
ω_{min}	0.451	rad/s
ω_{max}	4.005	rad/s
$\sigma_{spectrum}$	0.220	m
$\sigma_{simulation}$	0.220E+00	MKS units
$\sigma_{simulation}/\sigma_{spectrum}$	99.98%	
maximum attainable value	6.80	σ_{sim}
TEV	3.00	σ_{sim}
TEV/maximum attainable value	0.44	
m	740	
Monte Carlo Simulation	yes	
time to run subplex optimization	12106.	sec

Case	**1**
Extreme Value PDF Comparison	
μ_{Ochi}	**3.15**
μ_{MC}	3.03
μ_{H1}	1.45
μ_{H2}	3.02
μ_{H2CF}	2.95
$\mu_{subplex}$	3.12
σ_{Ochi}	**0.36**
σ_{MC}	0.30
σ_{H1}	0.98
σ_{H2}	0.70
σ_{H2CF}	0.67
$\sigma_{subplex}$	0.69
MC: $D_{KL}(f_{x_m}(x) \| f_{x_1}(x))$	0.08
H1: $D_{KL}(f_{x_m}(x) \| f_{x_1}(x))$	1.77
H2: $D_{KL}(f_{x_m}(x) \| f_{x_1}(x))$	0.29
H2CF: $D_{KL}(f_{x_m}(x) \| f_{x_1}(x))$	0.28
Subplex: $D_{KL}(f_{x_m}(x) \| f_{x_1}(x))$	0.18

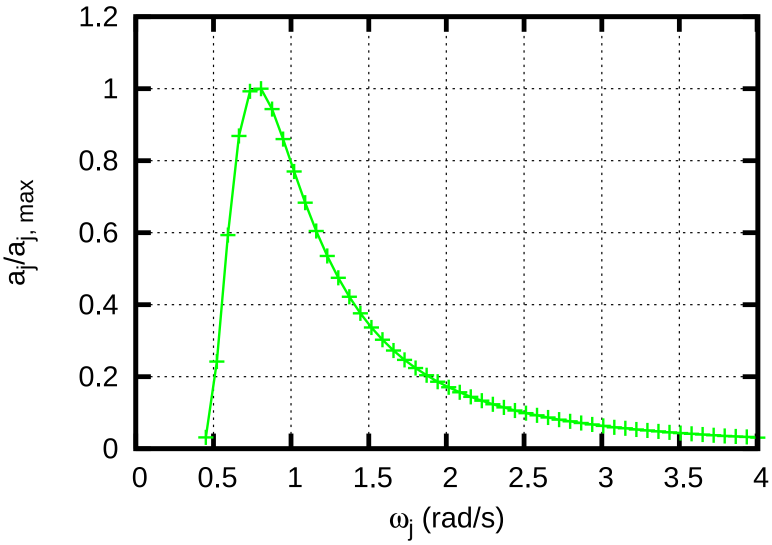

Figure A.1: Amplitudes corresponding to ITTC Sea State 3: $h_{peak} = 0.88$ m, $T_{peak} = 7.5$ s, $N = 51$.

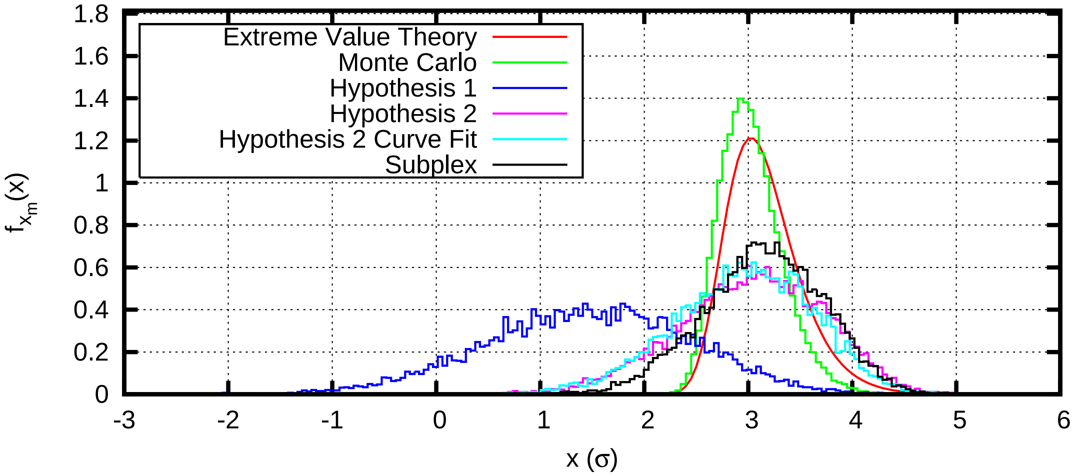

Figure A.2: Comparison of $f_{x_m}(x)$, denoted "Extreme Value Theory", and $f_{x_1}(x)$ as calculated by Hypotheses 1 and 2, Hypothesis 2 Curve Fit, and Subplex optimization. ITTC Sea State 3: $h_{peak} = 0.88$ m, $T_{peak} = 7.5$ s, $N = 51$, $m = 740$ (a 3.0σ event).

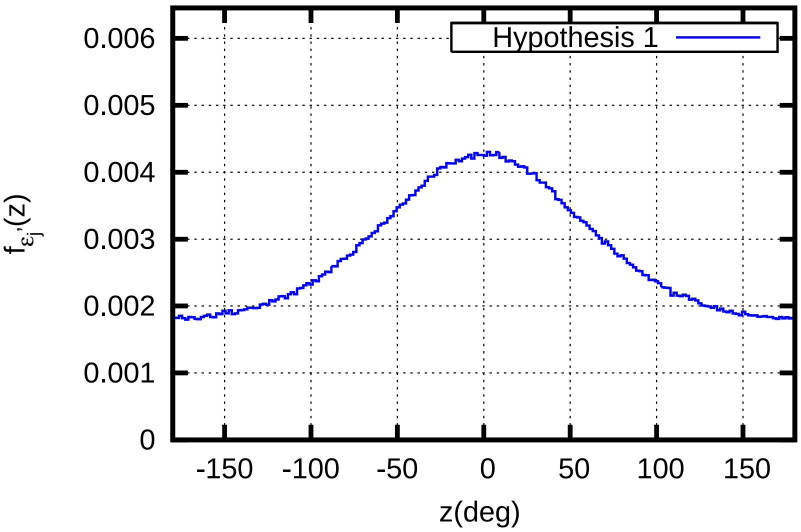

Figure A.3: Phase histogram for Hypothesis 1. ITTC Sea State 3: $h_{peak} = 0.88$ m, $T_{peak} = 7.5$ s, $N = 51$, $m = 740$ (a 3.0σ event). $M = 50,000$ samples.

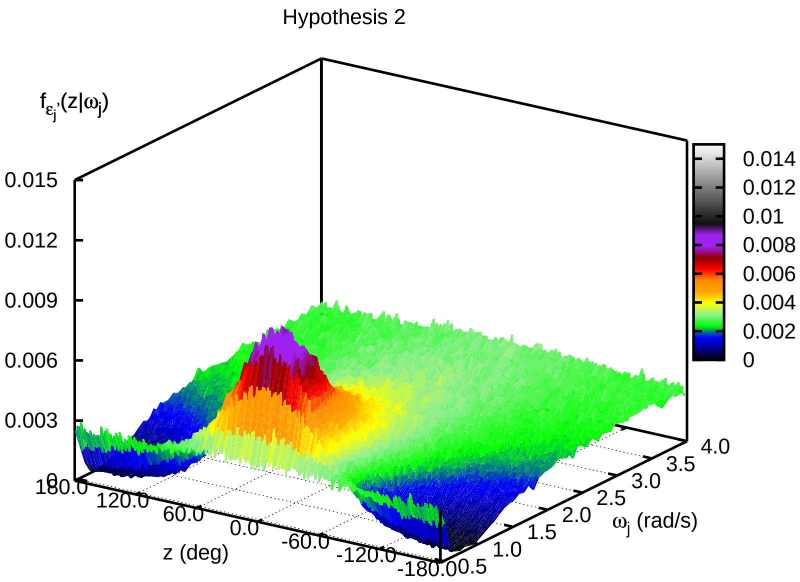

Figure A.4: Phase histogram for Hypothesis 2. ITTC Sea State 3: $h_{peak} = 0.88$ m, $T_{peak} = 7.5$ s, $N = 51$, $m = 740$ (a 3.0σ event). $M = 50,000$ samples.

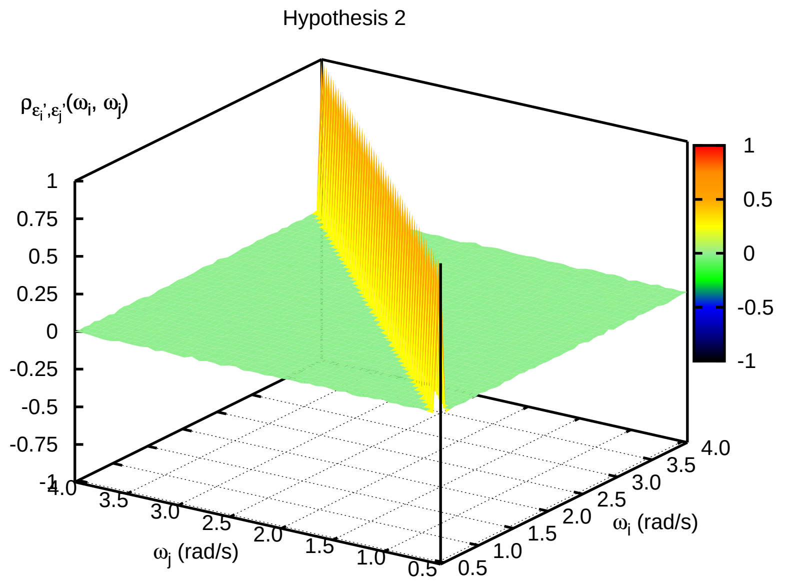

Figure A.5: Correlation of phase pairs (ϵ_i',ϵ_j') for Hypothesis 2. ITTC Sea State 3: $h_{peak} = 0.88$ m, $T_{peak} = 7.5$ s, $N = 51$, $m = 740$ (a 3.0σ event). $M = 50,000$ samples.

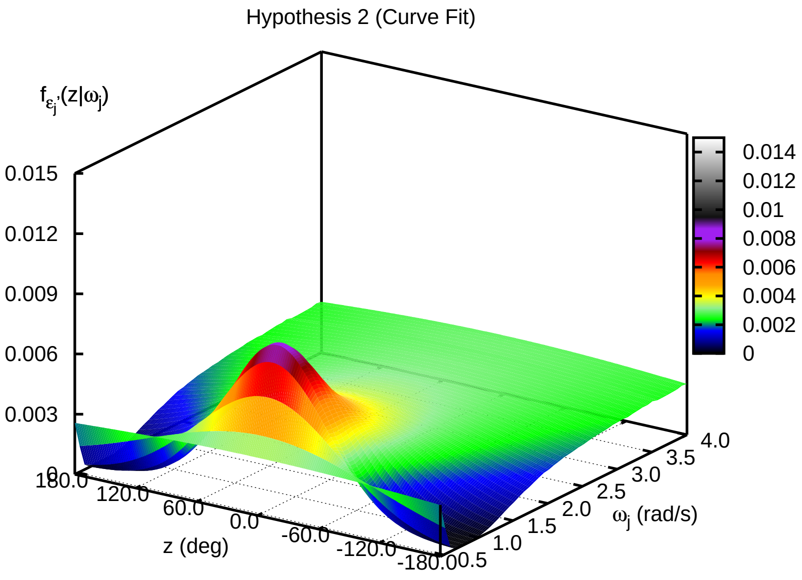

Figure A.6: Phase PDF for Hypothesis 2 Curve Fit. ITTC Sea State 3: $h_{peak} = 0.88$ m, $T_{peak} = 7.5$ s, $N = 51$, $m = 740$ (a 3.0σ event).

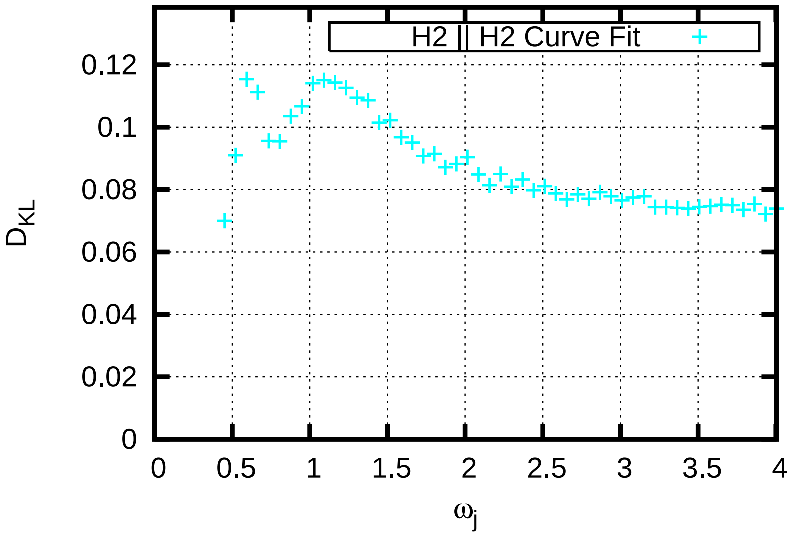

Figure A.7: Comparison of Hypothesis 2 and Hypothesis 2 Curve Fit phase PDFs using the Kullback-Leibler divergence, $D_{KL}(f_{\epsilon'_j,MC}(z) \| f_{\epsilon'_j,MG}(z))$. ITTC Sea State 3: $h_{peak} = 0.88$ m, $T_{peak} = 7.5$ s, $N = 51$, $m = 740$ (a 3.0σ event).

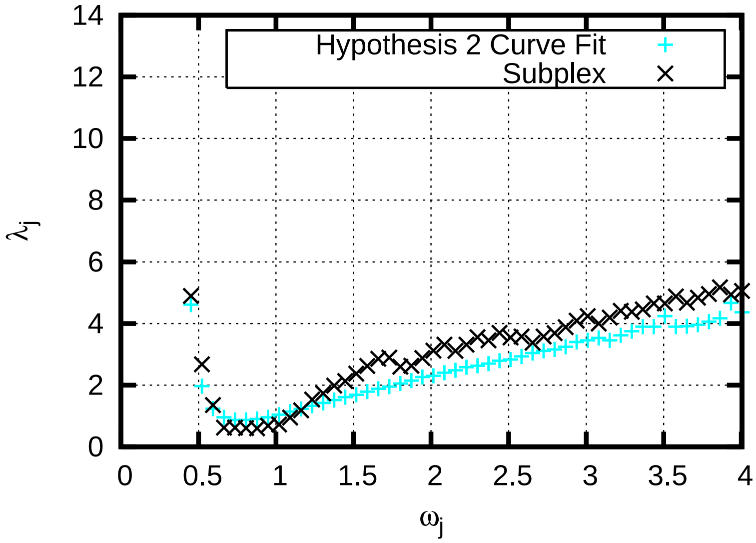

Figure A.8: λ_j as determined by Subplex optimization compared to λ_j as determined by minimizing $D_{KL}(f_{\epsilon'_j,MC}(z) \| f_{\epsilon'_j,MG}(z))$. λ_j is practically capped at 10, as $\lambda_j \geq 10$ results in a uniform phase distribution. ITTC Sea State 3: $h_{peak} = 0.88$ m, $T_{peak} = 7.5$ s, $N = 51$, $m = 740$ (a 3.0σ event).

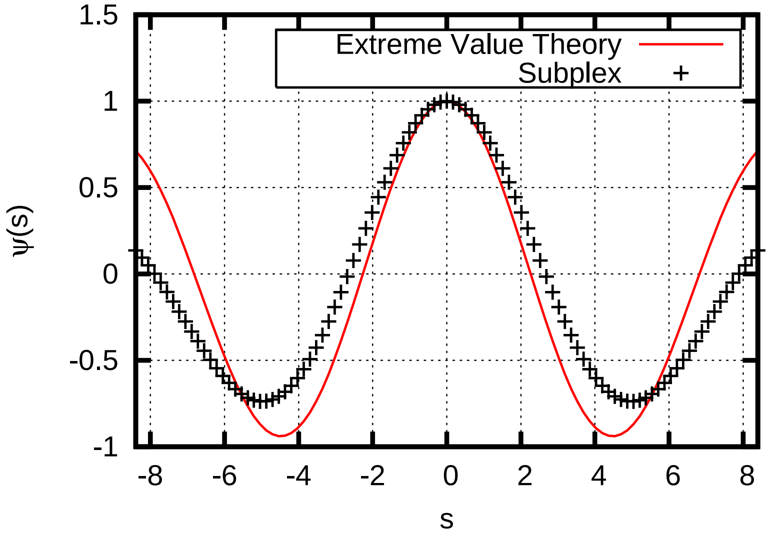

Figure A.9: Comparison of characteristic functions $\psi_{x_m}(x)$, denoted "Extreme Value Theory", and $\psi_{x_1}(s)$ as calculated by Subplex optimization. ITTC Sea State 3: $h_{peak} = 0.88$ m, $T_{peak} = 7.5$ s, $N = 51$, $m = 740$ (a 3.0σ event).

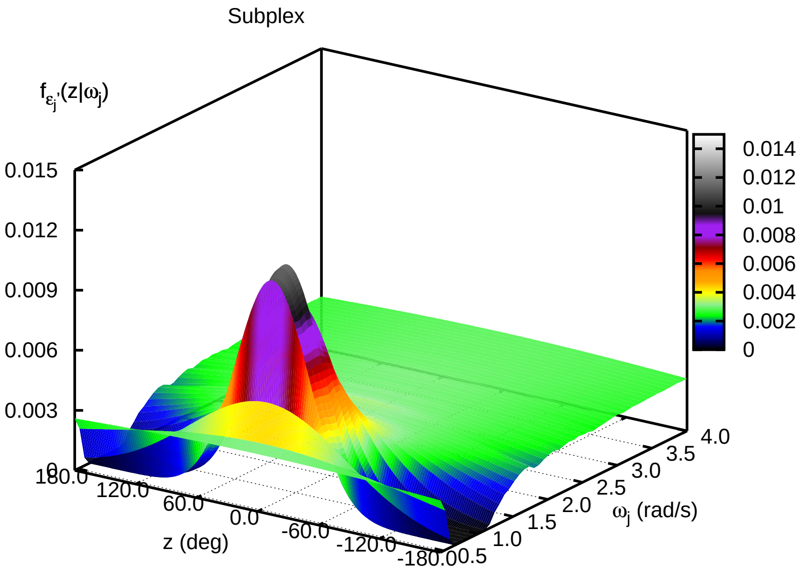

Figure A.10: Phase PDF from Subplex optimization of λ_j. ITTC Sea State 3: $h_{peak} = 0.88$ m, $T_{peak} = 7.5$ s, $N = 51$, $m = 740$ (a 3.0σ event).

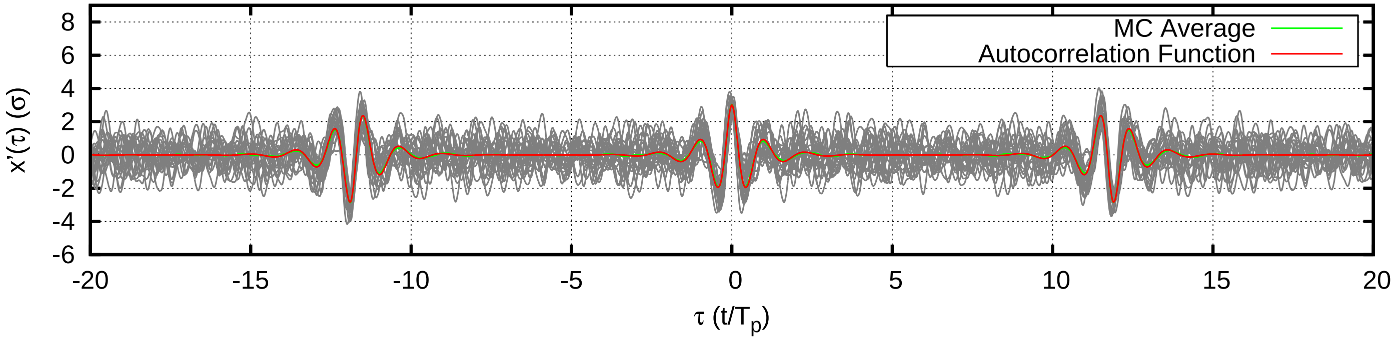

Figure A.11: Sample time series generated by Monte Carlo simulation. ITTC Sea State 3: $h_{peak} = 0.88$ m, $T_{peak} = 7.5$ s, $N = 51$, $m = 740$ (a 3.0σ event). Average time series generated from 2000 sample time series; 20 sample time series are plotted.

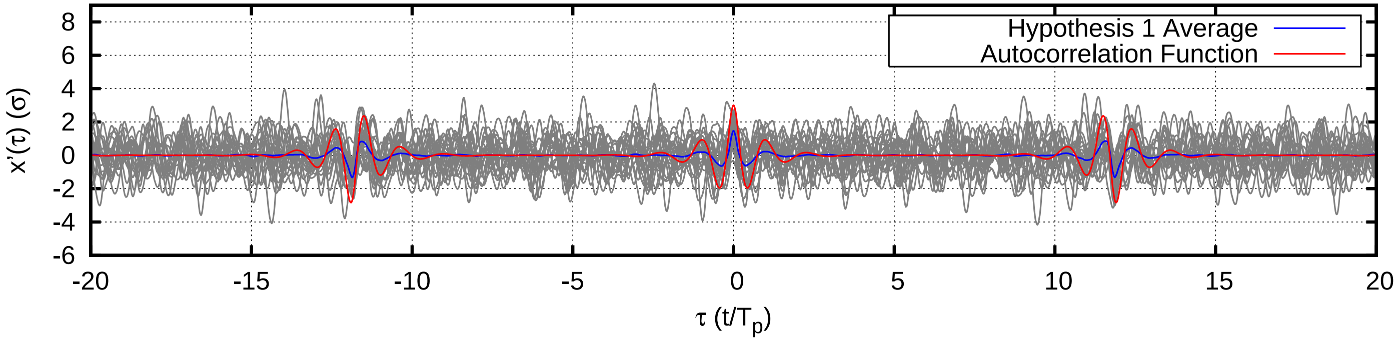

Figure A.12: Sample time series generated by Hypothesis 1 phases. ITTC Sea State 3: $h_{peak} = 0.88$ m, $T_{peak} = 7.5$ s, $N = 51$, $m = 740$ (a 3.0σ event). Average time series generated from 2000 sample time series; 20 sample time series are plotted.

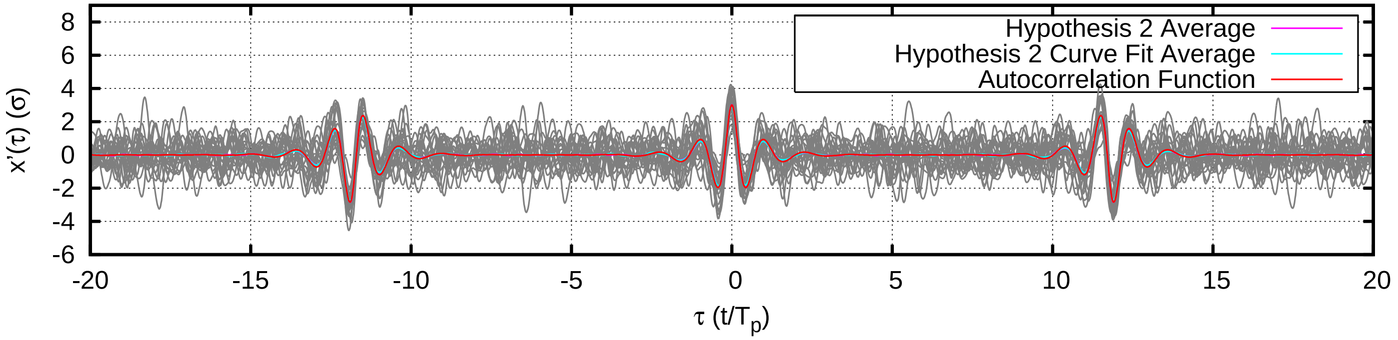

Figure A.13: Sample time series generated by Hypothesis 2 and Hypothesis 2 Curve Fit phases. ITTC Sea State 3: $h_{peak} = 0.88$ m, $T_{peak} = 7.5$ s, $N = 51$, $m = 740$ (a 3.0σ event). Average time series generated from 2000 sample time series; 20 sample time series are plotted.

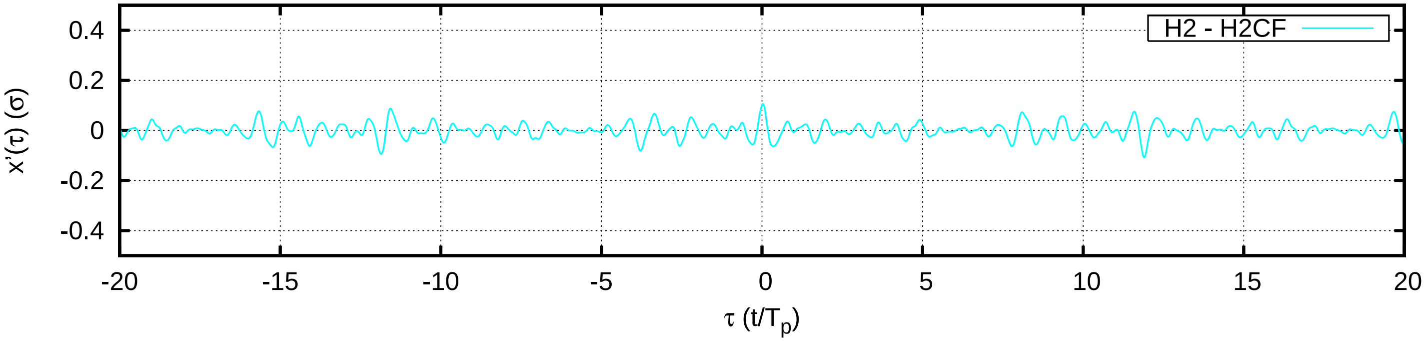

Figure A.14: Comparison of Hypothesis 2 and Hypothesis 2 Curve Fit average time series. The difference between these two average time series is plotted. ITTC Sea State 3: $h_{peak} = 0.88$ m, $T_{peak} = 7.5$ s, $N = 51$, $m = 740$ (a 3.0σ event).

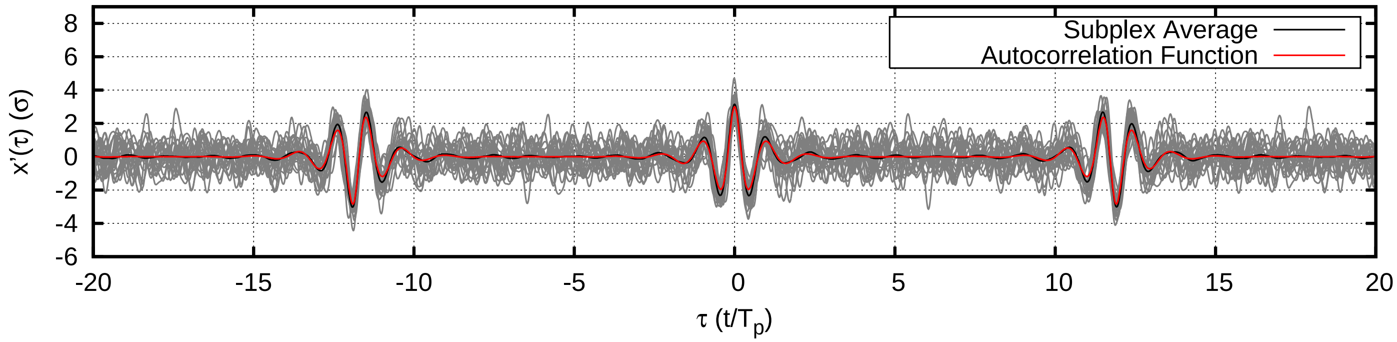

Figure A.15: Sample time series generated by Subplex optimization phases. ITTC Sea State 3: $h_{peak} = 0.88$ m, $T_{peak} = 7.5$ s, $N = 51$, $m = 740$ (a 3.0σ event). Average time series generated from 2000 sample time series; 20 sample time series are plotted.

A.2 Case 2

Case	**2**	
H_{sig}	14.00	m
T_{peak}	20.00	sec
N	51	
ω_{min}	0.169	rad/s
ω_{max}	1.502	rad/s
$\sigma_{spectrum}$	3.500	m
$\sigma_{simulation}$	0.350E+01	MKS units
$\sigma_{simulation}/\sigma_{spectrum}$	99.98%	
maximum attainable value	6.80	σ_{sim}
TEV	3.00	σ_{sim}
TEV/maximum attainable value	0.44	
m	740	
Monte Carlo Simulation	yes	
time to run subplex optimization	18340.	sec

Case	**2**
Extreme Value PDF Comparison	
μ_{Ochi}	**3.15**
μ_{MC}	3.03
μ_{H1}	1.45
μ_{H2}	3.02
μ_{H2CF}	2.95
$\mu_{subplex}$	3.13
σ_{Ochi}	**0.36**
σ_{MC}	0.30
σ_{H1}	0.99
σ_{H2}	0.70
σ_{H2CF}	0.67
$\sigma_{subplex}$	0.69
MC: $D_{KL}(f_{x_m}(x) \| f_{x_1}(x))$	0.08
H1: $D_{KL}(f_{x_m}(x) \| f_{x_1}(x))$	1.76
H2: $D_{KL}(f_{x_m}(x) \| f_{x_1}(x))$	0.29
H2CF: $D_{KL}(f_{x_m}(x) \| f_{x_1}(x))$	0.28
Subplex: $D_{KL}(f_{x_m}(x) \| f_{x_1}(x))$	0.17

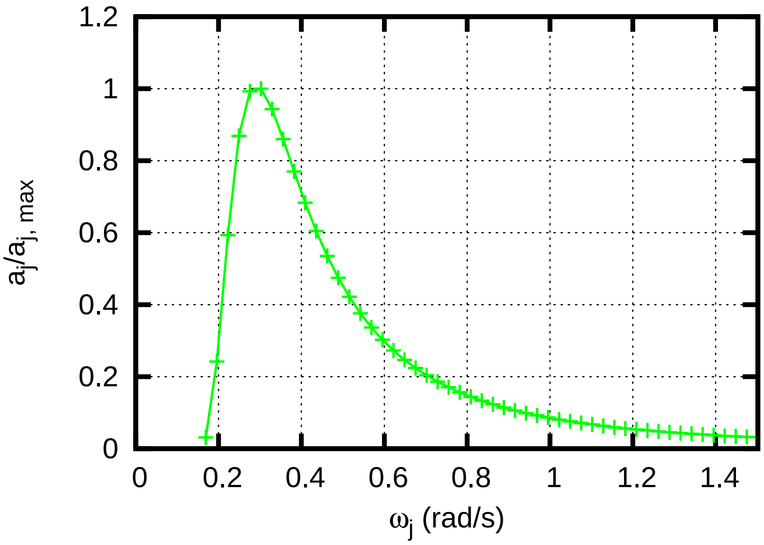

Figure A.16: Amplitudes corresponding to ITTC Sea State 9: $h_{peak} = 14.0$ m, $T_{peak} = 20.0$ s, $N = 51$.

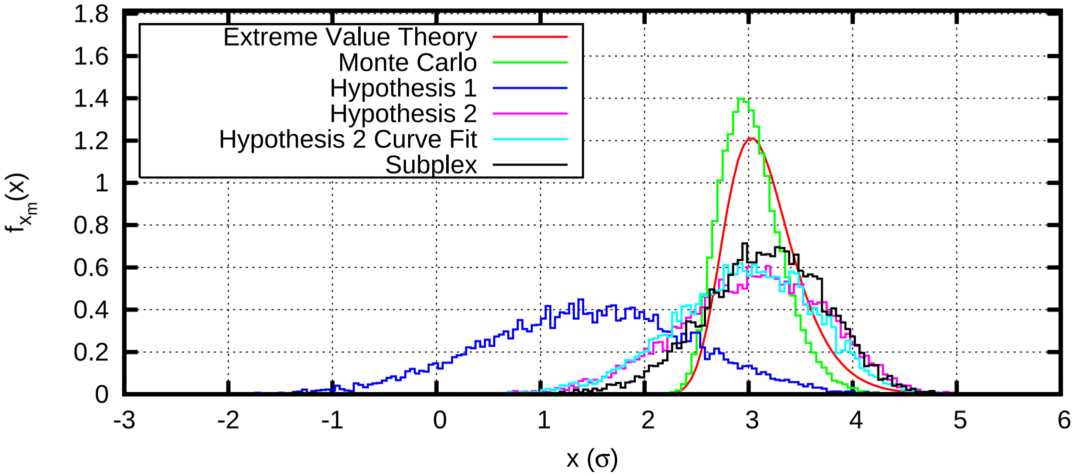

Figure A.17: Comparison of $f_{x_m}(x)$, denoted "Extreme Value Theory", and $f_{x_1}(x)$ as calculated by Hypotheses 1 and 2, Hypothesis 2 Curve Fit, and Subplex optimization. ITTC Sea State 9: $h_{peak} = 14.0$ m, $T_{peak} = 20.0$ s, $N = 51$, $m = 740$ (a 3.0σ event).

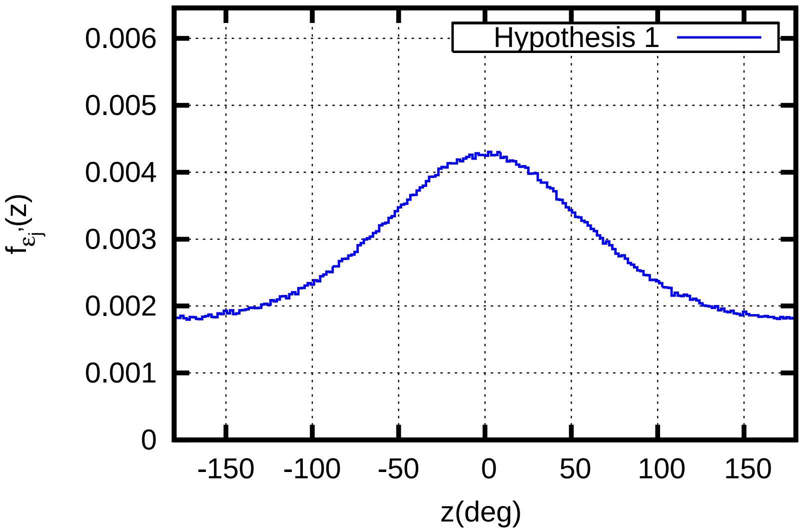

Figure A.18: Phase histogram for Hypothesis 1. ITTC Sea State 9: h_{peak} = 14.0 m, T_{peak} = 20.0 s, N = 51, m = 740 (a 3.0σ event). $M = 50,000$ samples.

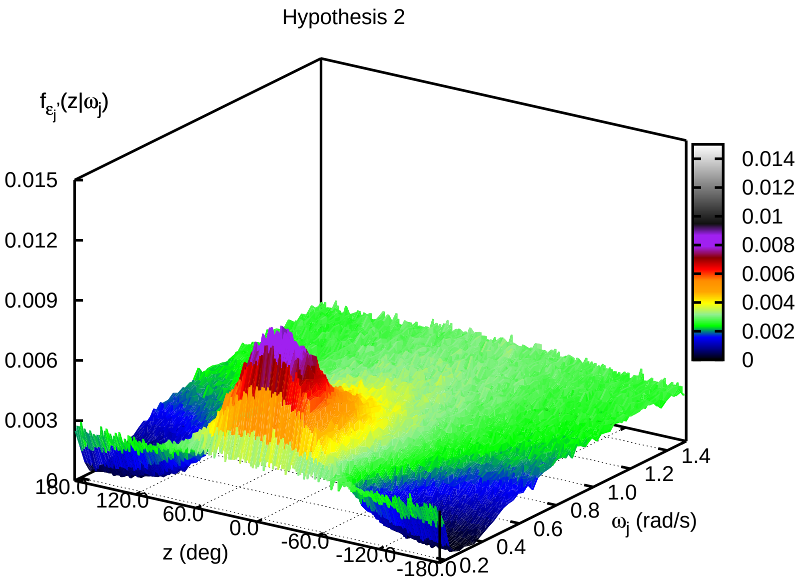

Figure A.19: Phase histogram for Hypothesis 2. ITTC Sea State 9: h_{peak} = 14.0 m, T_{peak} = 20.0 s, N = 51, m = 740 (a 3.0σ event). $M = 50,000$ samples.

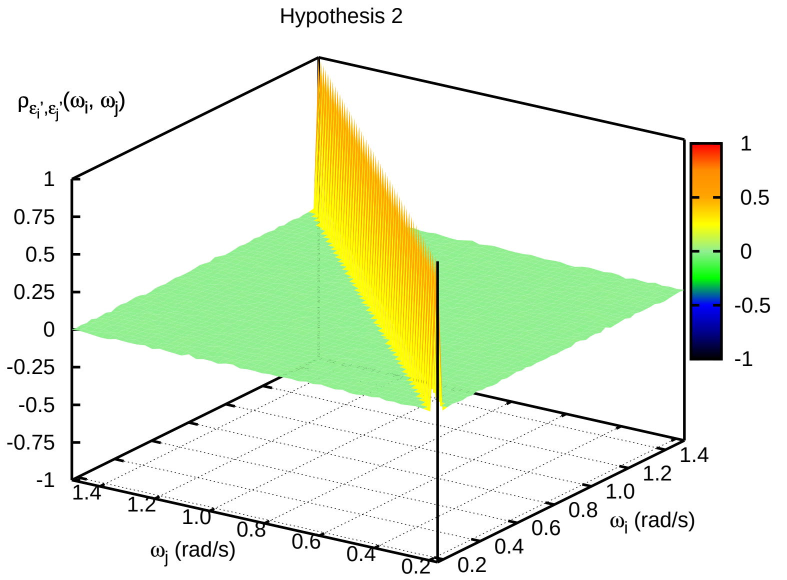

Figure A.20: Correlation of phase pairs (ϵ_i',ϵ_j') for Hypothesis 2. ITTC Sea State 9: $h_{peak} = 14.0$ m, $T_{peak} = 20.0$ s, $N = 51$, $m = 740$ (a 3.0σ event). $M = 50,000$ samples.

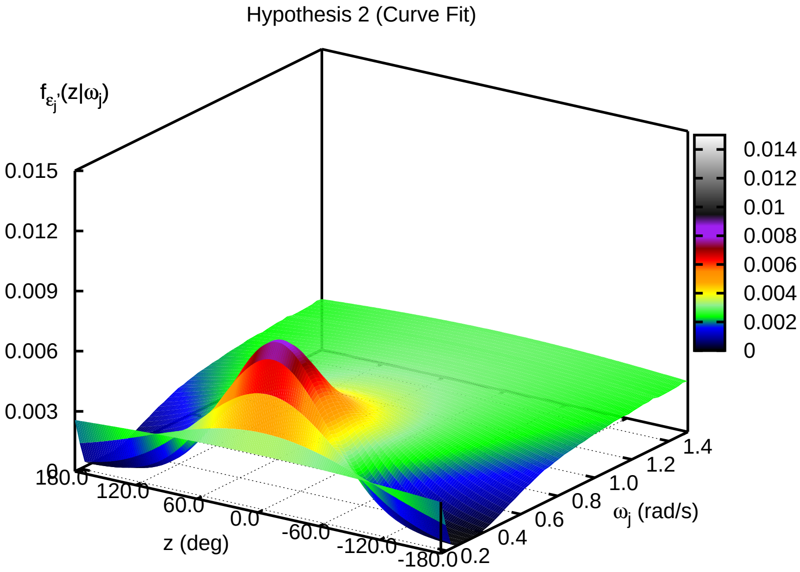

Figure A.21: Phase PDF for Hypothesis 2 Curve Fit. ITTC Sea State 9: $h_{peak} = 14.0$ m, $T_{peak} = 20.0$ s, $N = 51$, $m = 740$ (a 3.0σ event).

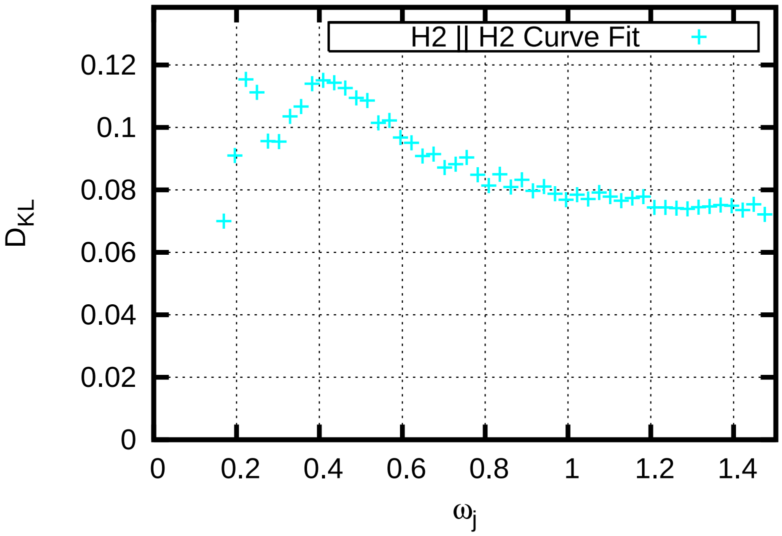

Figure A.22: Comparison of Hypothesis 2 and Hypothesis 2 Curve Fit phase PDFs using the Kullback-Leibler divergence, $D_{KL}(f_{\epsilon'_j,MC}(z) \| f_{\epsilon'_j,MG}(z))$. ITTC Sea State 9: $h_{peak} = 14.0$ m, $T_{peak} = 20.0$ s, $N = 51$, $m = 740$ (a 3.0σ event).

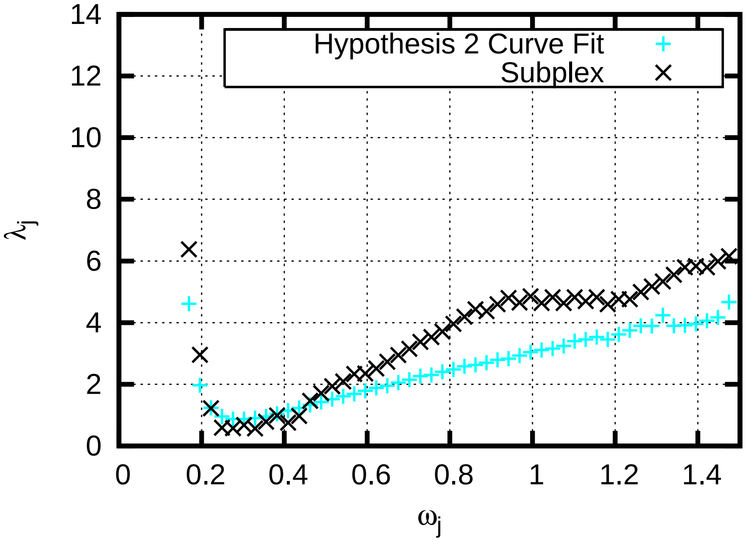

Figure A.23: λ_j as determined by Subplex optimization compared to λ_j as determined by minimizing $D_{KL}(f_{\epsilon'_j,MC}(z) \| f_{\epsilon'_j,MG}(z))$. λ_j is practically capped at 10, as $\lambda_j \geq 10$ results in a uniform phase distribution. ITTC Sea State 9: $h_{peak} = 14.0$ m, $T_{peak} = 20.0$ s, $N = 51$, $m = 740$ (a 3.0σ event).

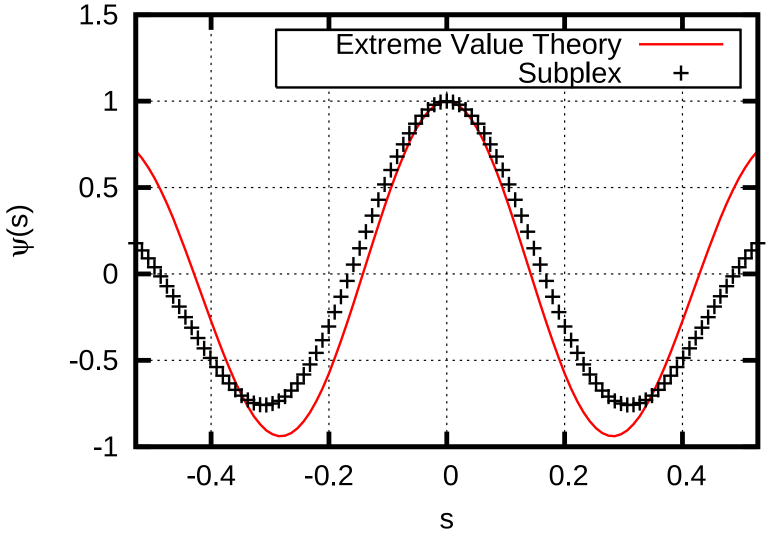

Figure A.24: Comparison of characteristic functions $\psi_{x_m}(x)$, denoted “Extreme Value Theory”, and $\psi_{x_1}(s)$ as calculated by Subplex optimization. ITTC Sea State 9: $h_{peak} = 14.0$ m, $T_{peak} = 20.0$ s, $N = 51$, $m = 740$ (a 3.0σ event).

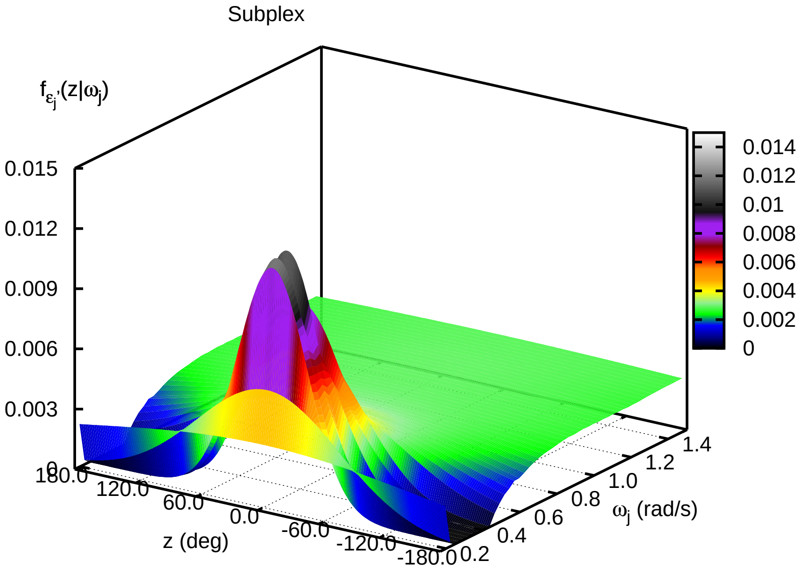

Figure A.25: Phase PDF from Subplex optimization of λ_j. ITTC Sea State 9: $h_{peak} = 14.0$ m, $T_{peak} = 20.0$ s, $N = 51$, $m = 740$ (a 3.0σ event).

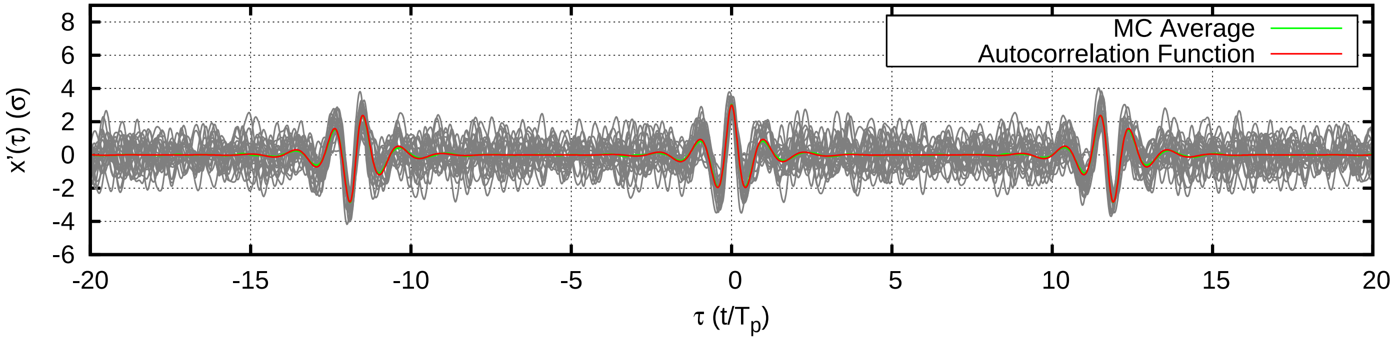

Figure A.26: Sample time series generated by Monte Carlo simulation. ITTC Sea State 9: $h_{peak} = 14.0$ m, $T_{peak} = 20.0$ s, $N = 51$, $m = 740$ (a 3.0σ event). Average time series generated from 2000 sample time series; 20 sample time series are plotted.

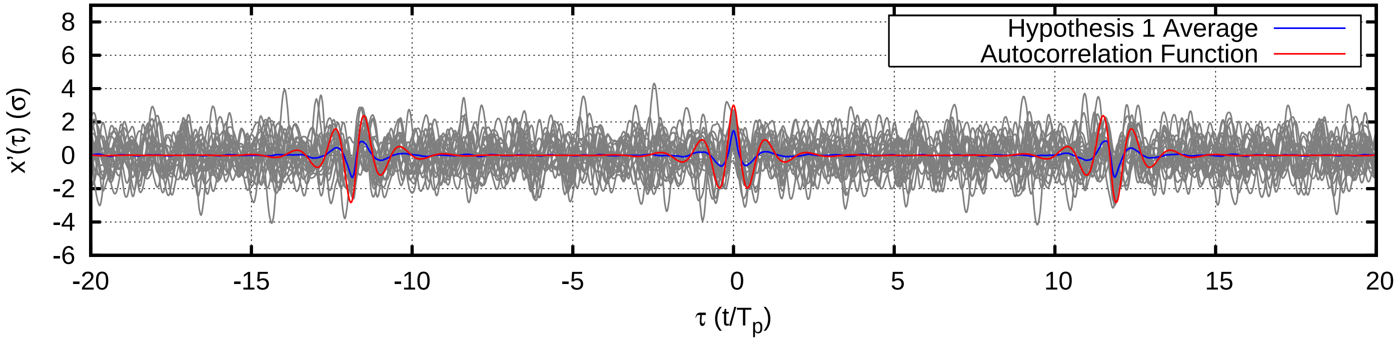

Figure A.27: Sample time series generated by Hypothesis 1 phases. ITTC Sea State 9: $h_{peak} = 14.0$ m, $T_{peak} = 20.0$ s, $N = 51$, $m = 740$ (a 3.0σ event). Average time series generated from 2000 sample time series; 20 sample time series are plotted.

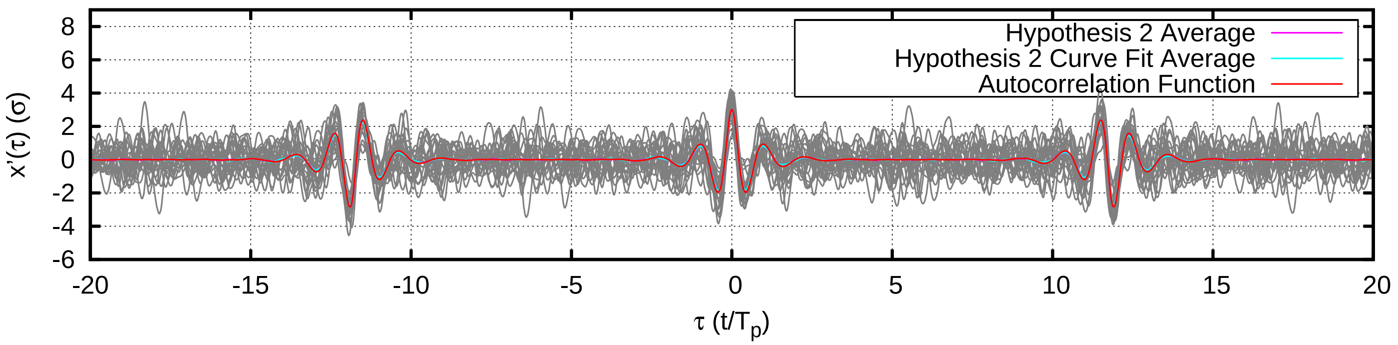

Figure A.28: Sample time series generated by Hypothesis 2 and Hypothesis 2 Curve Fit phases. ITTC Sea State 9: $h_{peak} = 14.0$ m, $T_{peak} = 20.0$ s, $N = 51$, $m = 740$ (a 3.0σ event). Average time series generated from 2000 sample time series; 20 sample time series are plotted.

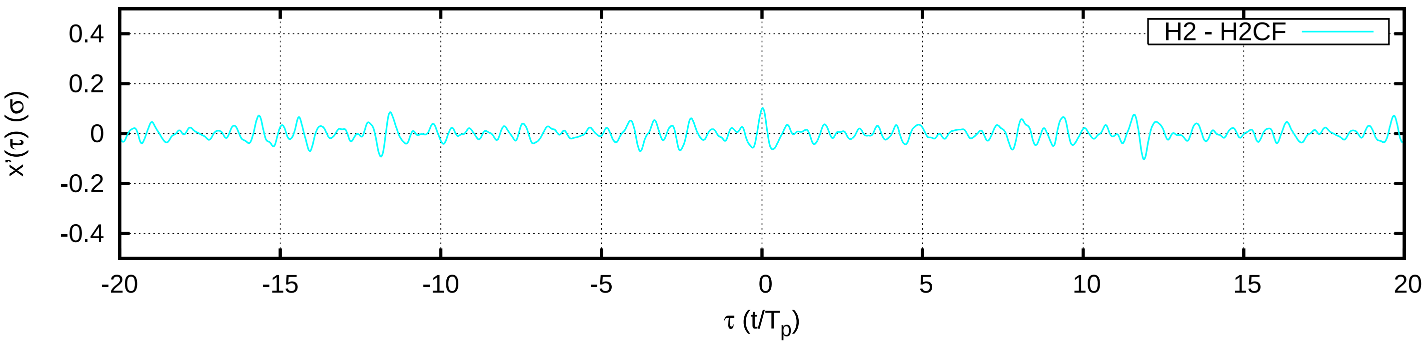

Figure A.29: Comparison of Hypothesis 2 and Hypothesis 2 Curve Fit average time series. The difference between these two average time series is plotted. ITTC Sea State 9: $h_{peak} = 14.0$ m, $T_{peak} = 20.0$ s, $N = 51$, $m = 740$ (a 3.0σ event).

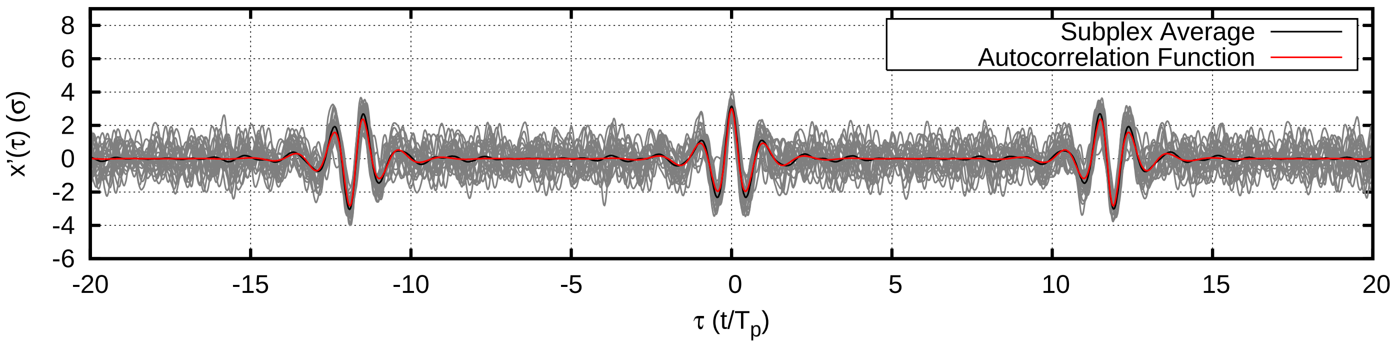

Figure A.30: Sample time series generated by Subplex optimization phases. ITTC Sea State 9: $h_{peak} = 14.0$ m, $T_{peak} = 20.0$ s, $N = 51$, $m = 740$ (a 3.0σ event). Average time series generated from 2000 sample time series; 20 sample time series are plotted.

A.3 Case 3

Case	**3**	
H_{sig}	0.88	m
T_{peak}	7.50	sec
N	51	
ω_{min}	0.451	rad/s
ω_{max}	4.005	rad/s
$\sigma_{spectrum}$	0.220	m
$\sigma_{simulation}$	0.220E+00	MKS units
$\sigma_{simulation}/\sigma_{spectrum}$	99.98%	
maximum attainable value	6.80	σ_{sim}
TEV	5.00	σ_{sim}
TEV/maximum attainable value	0.74	
m	3488555	
Monte Carlo Simulation	no	
time to run subplex optimization	4341.	sec
Extreme Value PDF Comparison		
μ_{Ochi}	**5.10**	
$\mu_{subplex}$	5.07	
σ_{Ochi}	**0.24**	
$\sigma_{subplex}$	0.64	
Subplex: $D_{KL}(f_{x_m}(x) \| f_{x_1}(x))$	0.22	

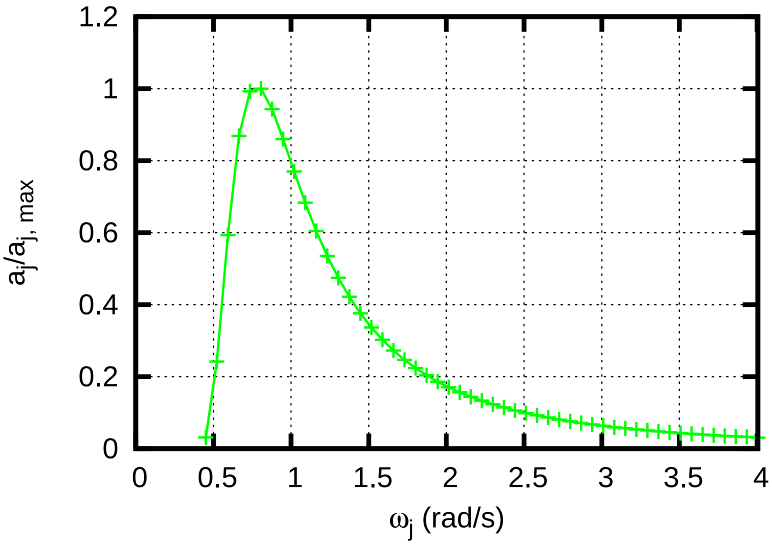

Figure A.31: Amplitudes corresponding to ITTC Sea State 3: $h_{peak} = 0.88$ m, $T_{peak} = 7.5$ s, $N = 51$.

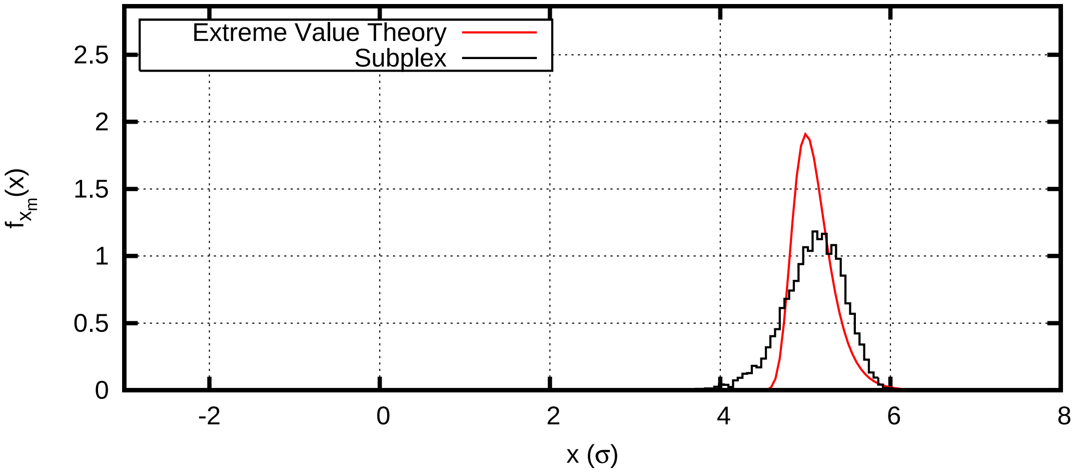

Figure A.32: Comparison of $f_{x_m}(x)$, denoted "Extreme Value Theory", and $f_{x_1}(x)$ as calculated by Hypotheses 1 and 2, Hypothesis 2 Curve Fit, and Subplex optimization. ITTC Sea State 3: $h_{peak} = 0.88$ m, $T_{peak} = 7.5$ s, $N = 51$, $m = 3,488,555$ (a 5.0σ event).

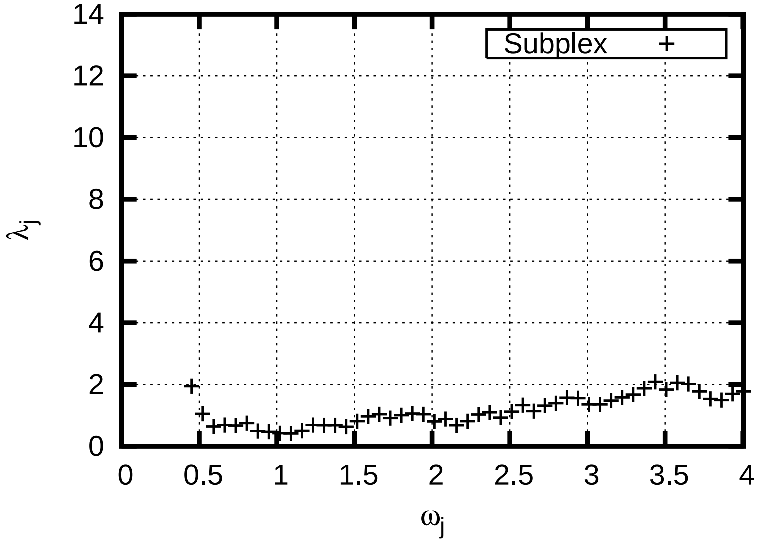

Figure A.33: λ_j as determined by Subplex optimization. λ_j is practically capped at 10, as $\lambda_j \geq 10$ results in a uniform phase distribution. ITTC Sea State 3: $h_{peak} = 0.88$ m, $T_{peak} = 7.5$ s, $N = 51$, $m = 3,488,555$ (a 5.0σ event).

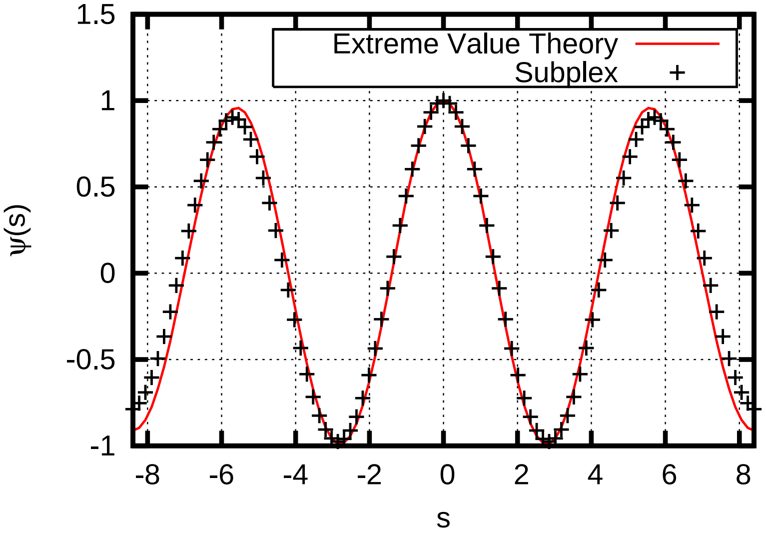

Figure A.34: Comparison of characteristic functions $\psi_{x_m}(x)$, denoted “Extreme Value Theory”, and $\psi_{x_1}(s)$ as calculated by Subplex optimization. ITTC Sea State 3: $h_{peak} = 0.88$ m, $T_{peak} = 7.5$ s, $N = 51$, $m = 3,488,555$ (a 5.0σ event).

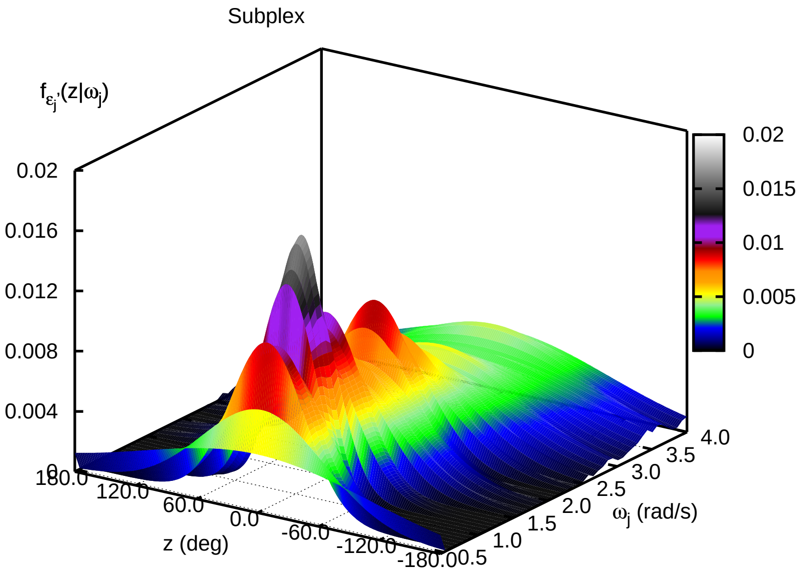

Figure A.35: Phase PDF from Subplex optimization of λ_j. ITTC Sea State 3: $h_{peak} = 0.88$ m, $T_{peak} = 7.5$ s, $N = 51$, $m = 3,488,555$ (a 5.0σ event).

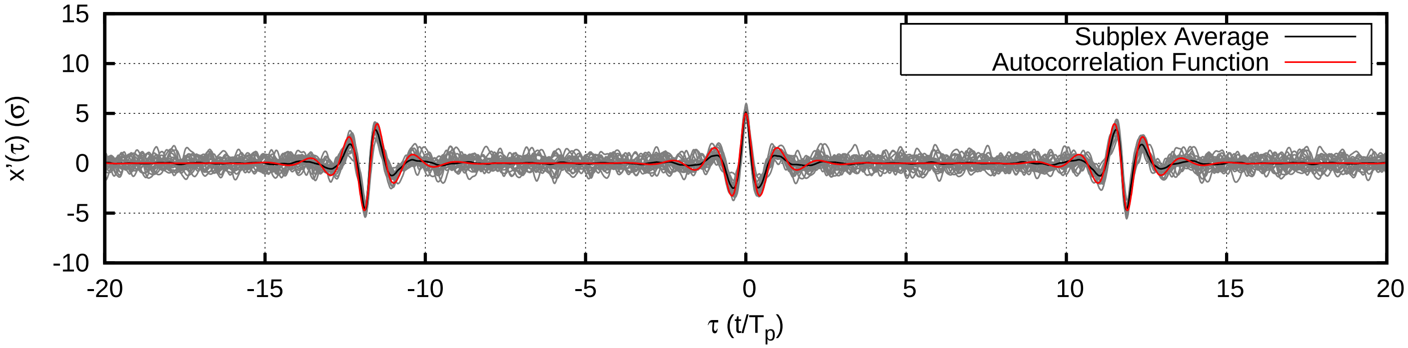

Figure A.36: Sample time series generated by Subplex optimization phases. ITTC Sea State 3: $h_{peak} = 0.88$ m, $T_{peak} = 7.5$ s, $N = 51$, $m = 3,488,555$ (a 5.0σ event). Average time series generated from 2000 sample time series; 20 sample time series are plotted.

A.4 Case 4

Case	**4**	
H_{sig}	14.00	m
T_{peak}	20.00	sec
N	51	
ω_{min}	0.169	rad/s
ω_{max}	1.502	rad/s
$\sigma_{spectrum}$	3.500	m
$\sigma_{simulation}$	0.350E+01	MKS units
$\sigma_{simulation}/\sigma_{spectrum}$	99.98%	
maximum attainable value	6.80	σ_{sim}
TEV	5.00	σ_{sim}
TEV/maximum attainable value	0.74	
m	3488555	
Monte Carlo Simulation	no	
time to run subplex optimization	5182.	sec
Extreme Value PDF Comparison		
μ_{Ochi}	**5.10**	
$\mu_{subplex}$	5.08	
σ_{Ochi}	**0.24**	
$\sigma_{subplex}$	0.63	
Subplex: $D_{KL}(f_{x_m}(x) \| f_{x_1}(x))$	0.20	

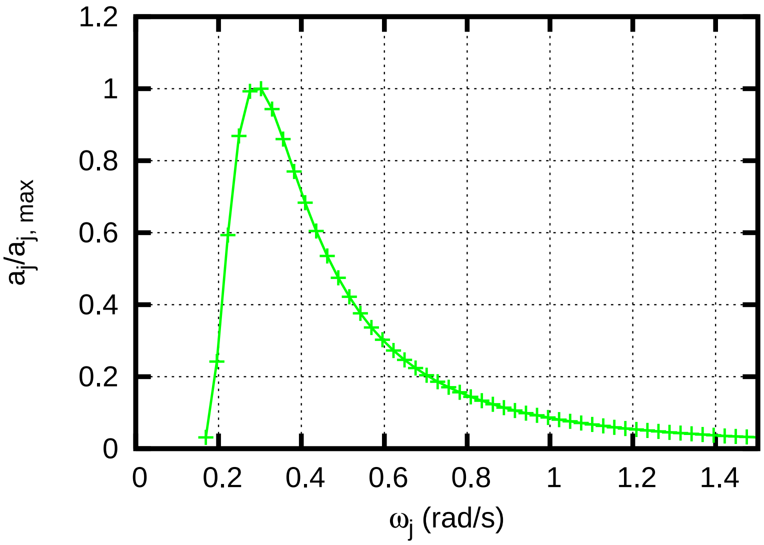

Figure A.37: Amplitudes corresponding to ITTC Sea State 9: $h_{peak} = 14.0$ m, $T_{peak} = 20.0$ s, $N = 51$.

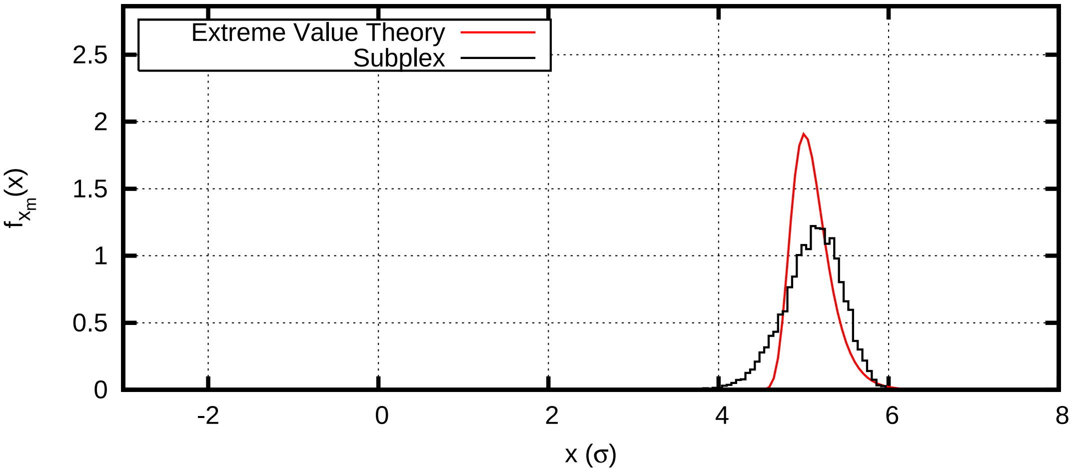

Figure A.38: Comparison of $f_{x_m}(x)$, denoted "Extreme Value Theory", and $f_{x_1}(x)$ as calculated by Hypotheses 1 and 2, Hypothesis 2 Curve Fit, and Subplex optimization. ITTC Sea State 9: $h_{peak} = 14.0$ m, $T_{peak} = 20.0$ s, $N = 51$, $m = 3,488,555$ (a 5.0σ event).

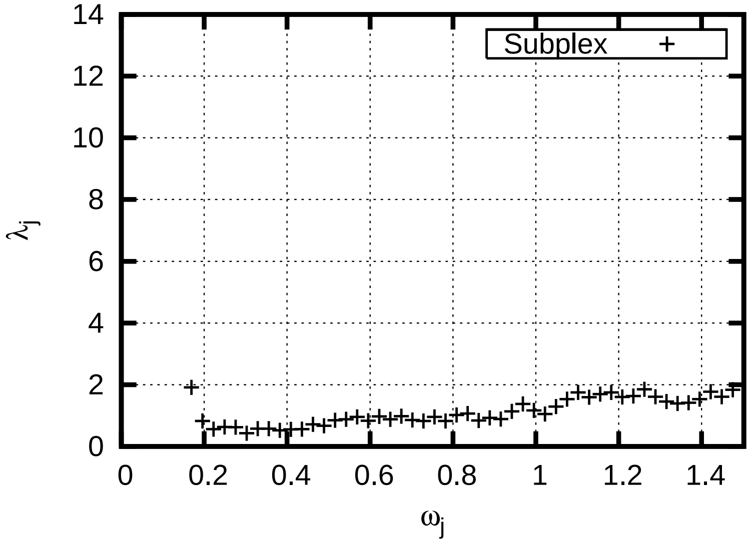

Figure A.39: λ_j as determined by Subplex optimization. λ_j is practically capped at 10, as $\lambda_j \geq 10$ results in a uniform phase distribution. ITTC Sea State 9: $h_{peak} = 14.0$ m, $T_{peak} = 20.0$ s, $N = 51$, $m = 3,488,555$ (a 5.0σ event).

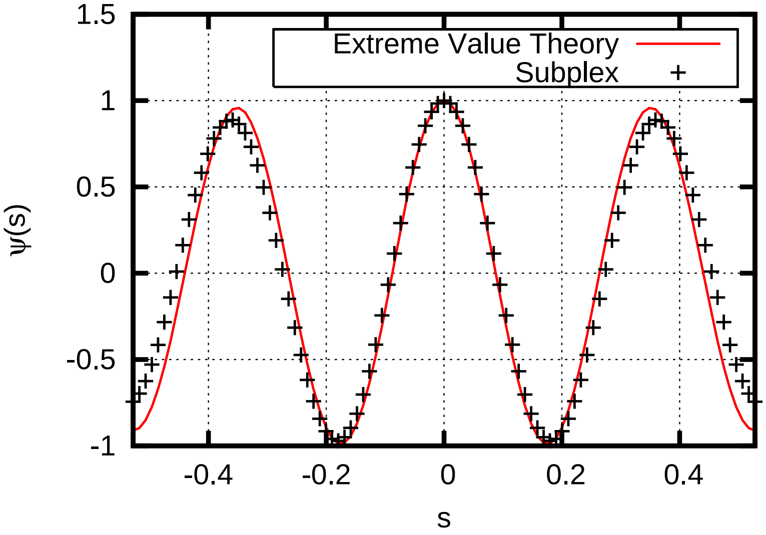

Figure A.40: Comparison of characteristic functions $\psi_{x_m}(x)$, denoted "Extreme Value Theory", and $\psi_{x_1}(s)$ as calculated by Subplex optimization. ITTC Sea State 9: $h_{peak} = 14.0$ m, $T_{peak} = 20.0$ s, $N = 51$, $m = 3,488,555$ (a 5.0σ event).

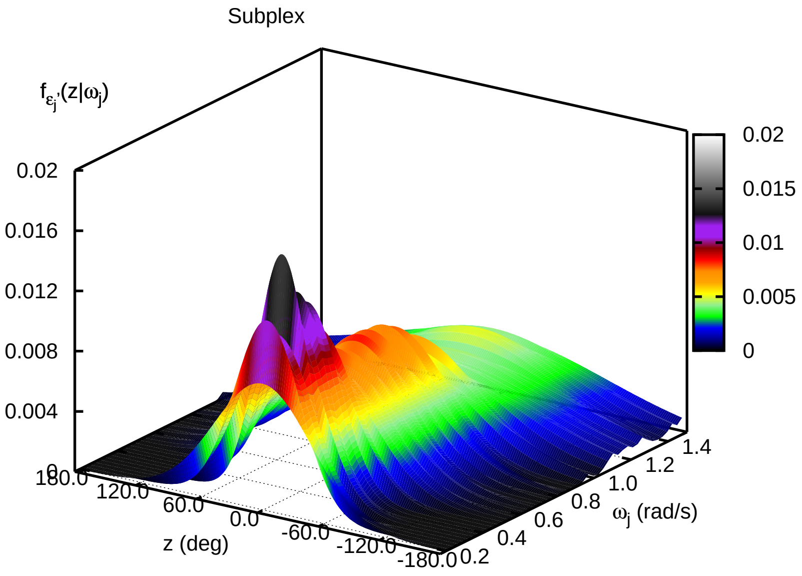

Figure A.41: Phase PDF from Subplex optimization of λ_j. ITTC Sea State 9: $h_{peak} = 14.0$ m, $T_{peak} = 20.0$ s, $N = 51$, $m = 3,488,555$ (a 5.0σ event).

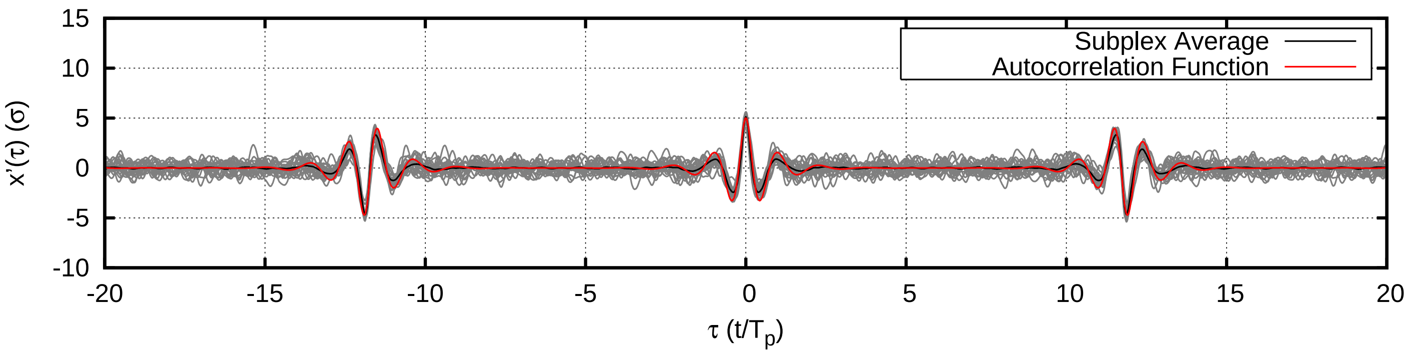

Figure A.42: Sample time series generated by Subplex optimization phases. ITTC Sea State 9: $h_{peak} = 14.0$ m, $T_{peak} = 20.0$ s, $N = 51$, $m = 3,488,555$ (a 5.0σ event). Average time series generated from 2000 sample time series; 20 sample time series are plotted.

A.5 Case 5

Case	**5**	
H_{sig}	0.88	m
T_{peak}	7.50	sec
N	101	
ω_{min}	0.451	rad/s
ω_{max}	4.005	rad/s
$\sigma_{spectrum}$	0.220	m
$\sigma_{simulation}$	0.220E+00	MKS units
$\sigma_{simulation}/\sigma_{spectrum}$	99.98%	
maximum attainable value	9.61	σ_{sim}
TEV	3.00	σ_{sim}
TEV/maximum attainable value	0.31	
m	740	
Monte Carlo Simulation	yes	
time to run subplex optimization	55136.	sec

Case	**5**
Extreme Value PDF Comparison	
μ_{Ochi}	**3.15**
μ_{MC}	3.09
μ_{H1}	1.44
μ_{H2}	3.10
μ_{H2CF}	2.96
$\mu_{subplex}$	3.14
σ_{Ochi}	**0.36**
σ_{MC}	0.33
σ_{H1}	1.00
σ_{H2}	0.84
σ_{H2CF}	0.82
$\sigma_{subplex}$	0.79
MC: $D_{KL}(f_{x_m}(x) \| f_{x_1}(x))$	0.02
H1: $D_{KL}(f_{x_m}(x) \| f_{x_1}(x))$	1.77
H2: $D_{KL}(f_{x_m}(x) \| f_{x_1}(x))$	0.38
H2CF: $D_{KL}(f_{x_m}(x) \| f_{x_1}(x))$	0.38
Subplex: $D_{KL}(f_{x_m}(x) \| f_{x_1}(x))$	0.28

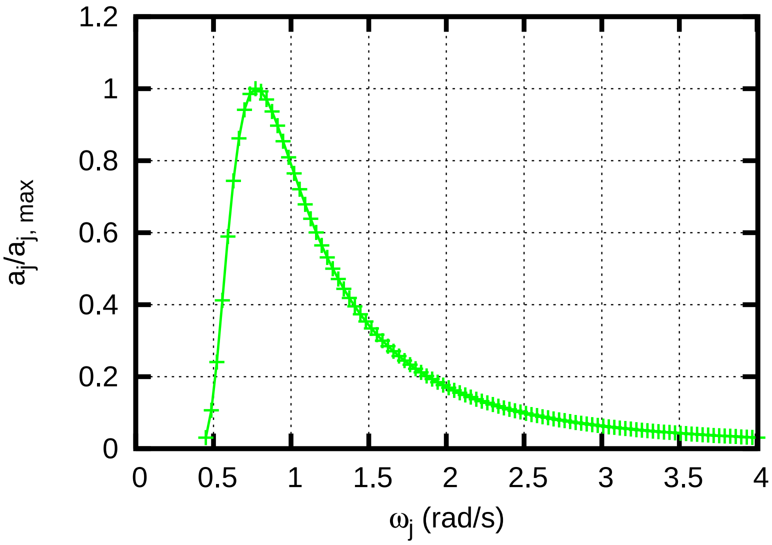

Figure A.43: Amplitudes corresponding to ITTC Sea State 3: $h_{peak} = 0.88$ m, $T_{peak} = 7.5$ s, $N = 101$.

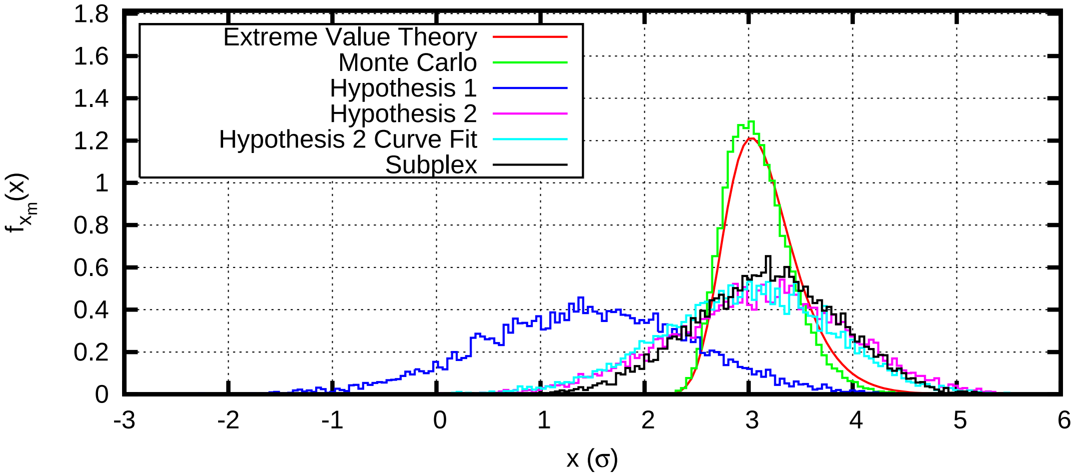

Figure A.44: Comparison of $f_{x_m}(x)$, denoted "Extreme Value Theory", and $f_{x_1}(x)$ as calculated by Hypotheses 1 and 2, Hypothesis 2 Curve Fit, and Subplex optimization. ITTC Sea State 3: $h_{peak} = 0.88$ m, $T_{peak} = 7.5$ s, $N = 101$, $m = 740$ (a 3.0σ event).

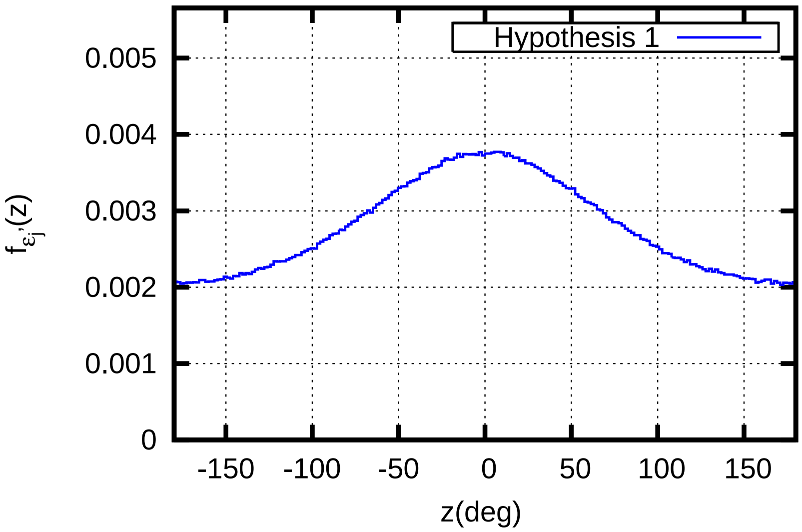

Figure A.45: Phase histogram for Hypothesis 1. ITTC Sea State 3: $h_{peak} = 0.88$ m, $T_{peak} = 7.5$ s, $N = 101$, $m = 740$ (a 3.0σ event). $M = 50,000$ samples.

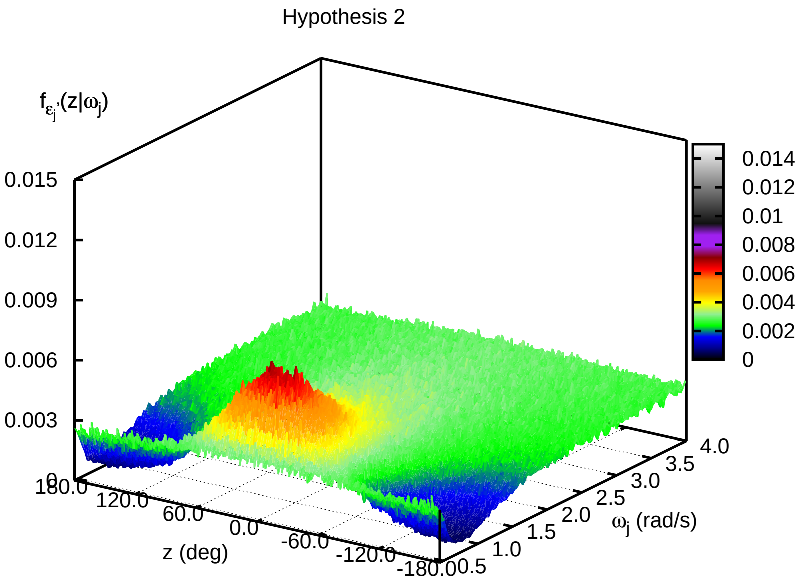

Figure A.46: Phase histogram for Hypothesis 2. ITTC Sea State 3: $h_{peak} = 0.88$ m, $T_{peak} = 7.5$ s, $N = 101$, $m = 740$ (a 3.0σ event). $M = 50,000$ samples.

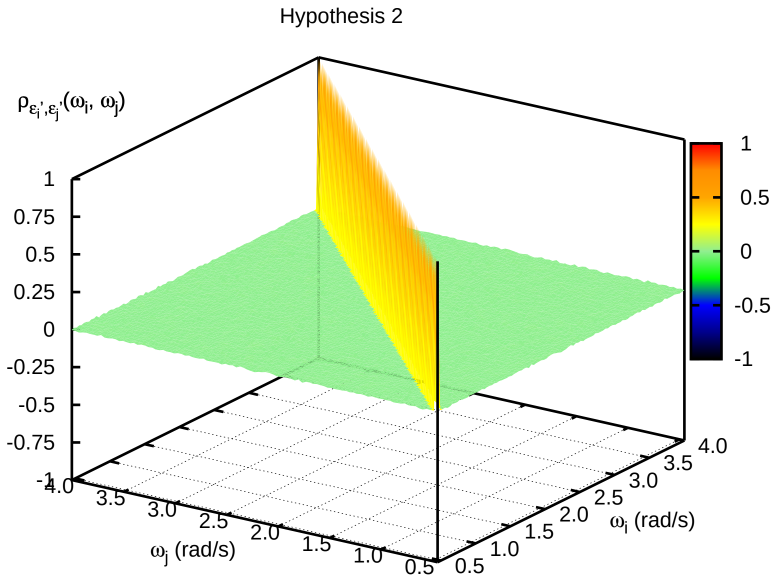

Figure A.47: Correlation of phase pairs $(\epsilon_i',\epsilon_j')$ for Hypothesis 2. ITTC Sea State 3: $h_{peak} = 0.88$ m, $T_{peak} = 7.5$ s, $N = 101$, $m = 740$ (a 3.0σ event). $M = 50,000$ samples.

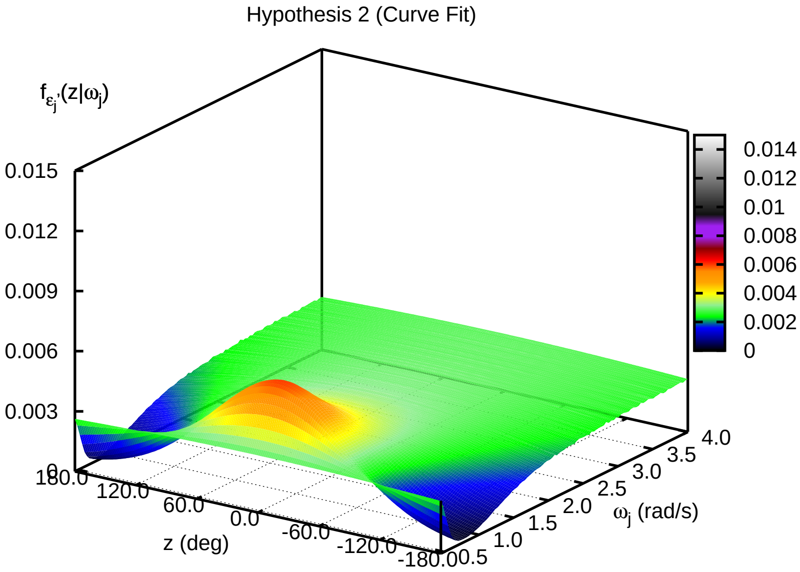

Figure A.48: Phase PDF for Hypothesis 2 Curve Fit. ITTC Sea State 3: $h_{peak} = 0.88$ m, $T_{peak} = 7.5$ s, $N = 101$, $m = 740$ (a 3.0σ event).

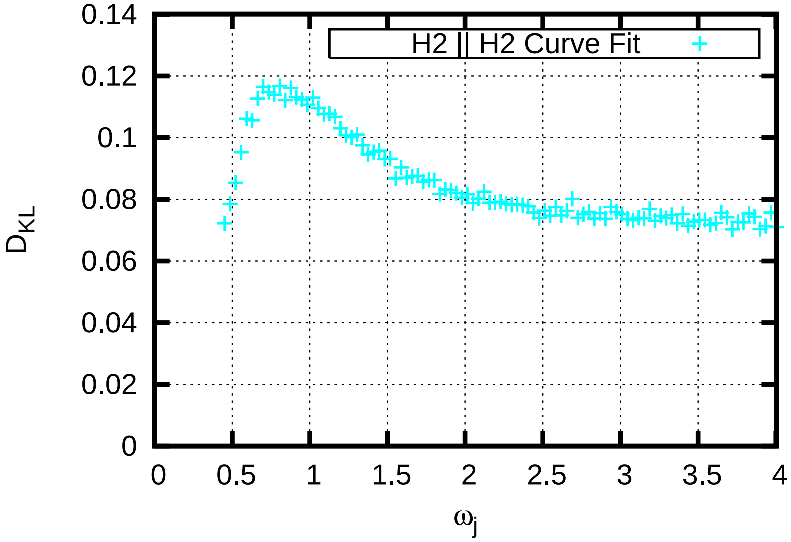

Figure A.49: Comparison of Hypothesis 2 and Hypothesis 2 Curve Fit phase PDFs using the Kullback-Leibler divergence, $D_{KL}(f_{\epsilon'_j,MC}(z)\|f_{\epsilon'_j,MG}(z))$. ITTC Sea State 3: $h_{peak} = 0.88$ m, $T_{peak} = 7.5$ s, $N = 101$, $m = 740$ (a 3.0σ event).

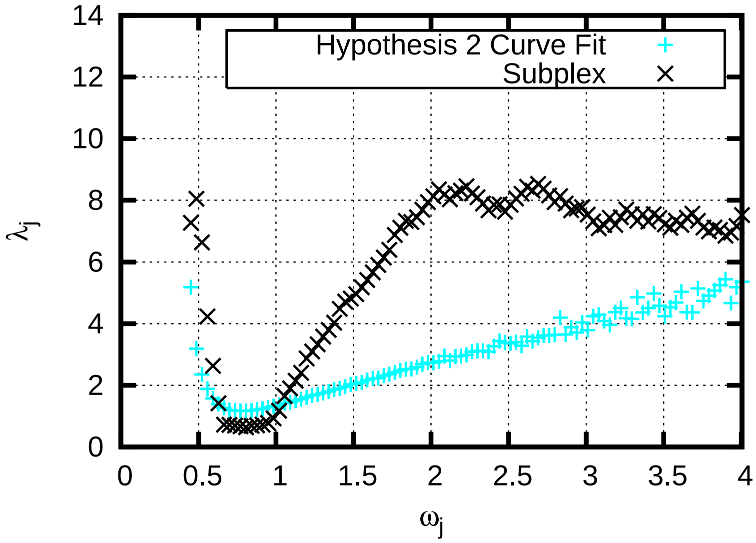

Figure A.50: λ_j as determined by Subplex optimization compared to λ_j as determined by minimizing $D_{KL}(f_{\epsilon'_j,MC}(z)\|f_{\epsilon'_j,MG}(z))$. λ_j is practically capped at 10, as $\lambda_j \geq 10$ results in a uniform phase distribution. ITTC Sea State 3: $h_{peak} = 0.88$ m, $T_{peak} = 7.5$ s, $N = 101$, $m = 740$ (a 3.0σ event).

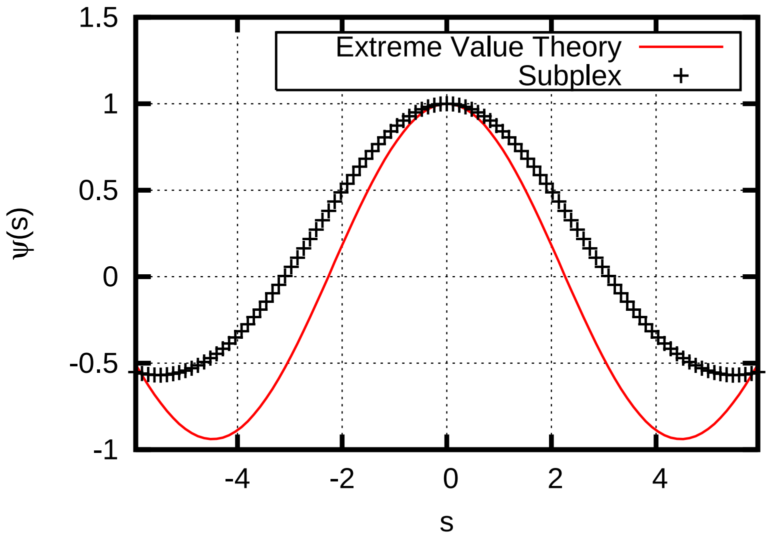

Figure A.51: Comparison of characteristic functions $\psi_{x_m}(x)$, denoted "Extreme Value Theory", and $\psi_{x_1}(s)$ as calculated by Subplex optimization. ITTC Sea State 3: $h_{peak} = 0.88$ m, $T_{peak} = 7.5$ s, $N = 101$, $m = 740$ (a 3.0σ event).

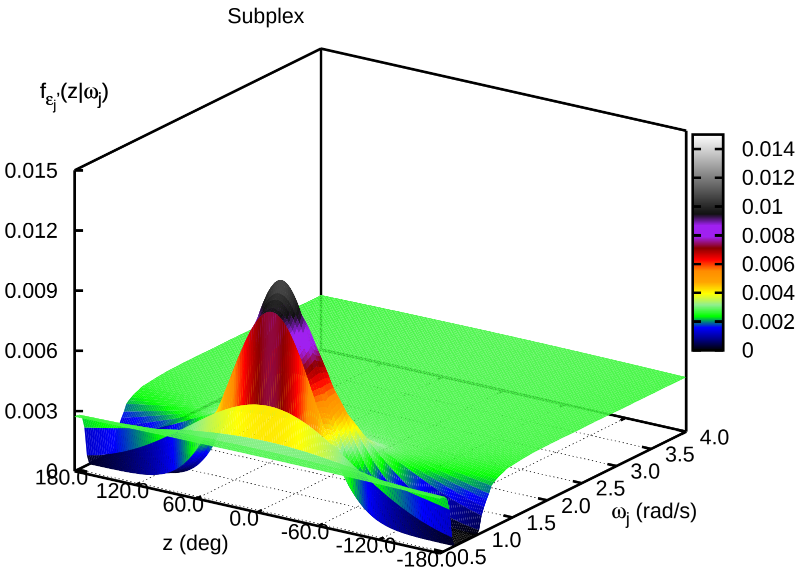

Figure A.52: Phase PDF from Subplex optimization of λ_j. ITTC Sea State 3: $h_{peak} = 0.88$ m, $T_{peak} = 7.5$ s, $N = 101$, $m = 740$ (a 3.0σ event).

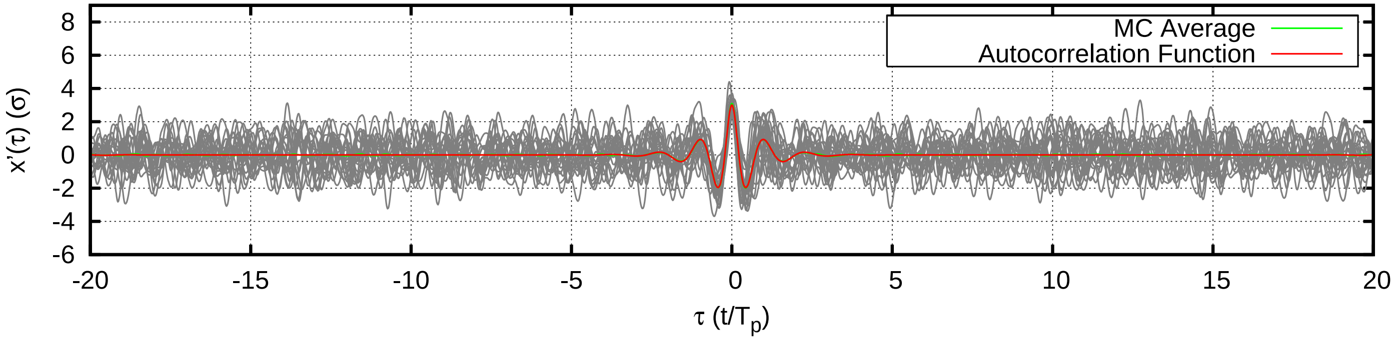

Figure A.53: Sample time series generated by Monte Carlo simulation. ITTC Sea State 3: $h_{peak} = 0.88$ m, $T_{peak} = 7.5$ s, $N = 101$, $m = 740$ (a 3.0σ event). Average time series generated from 2000 sample time series; 20 sample time series are plotted.

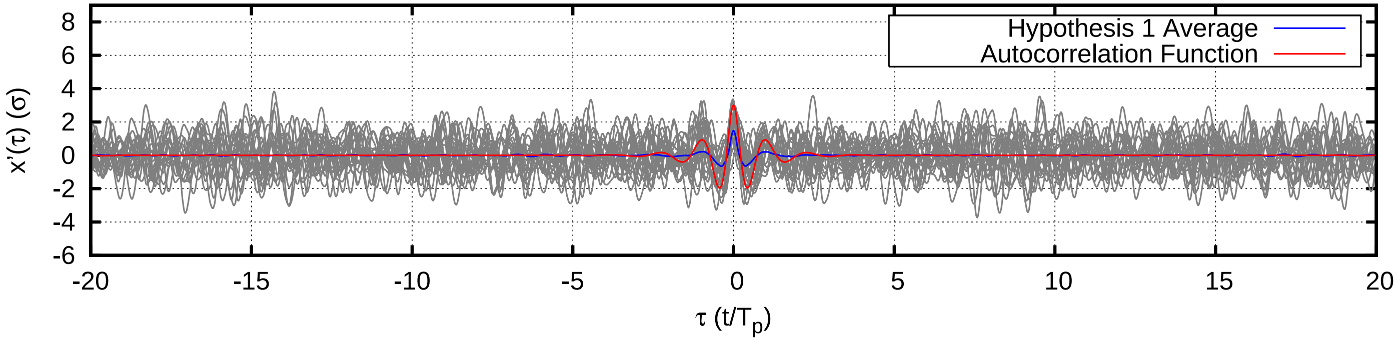

Figure A.54: Sample time series generated by Hypothesis 1 phases. ITTC Sea State 3: $h_{peak} = 0.88$ m, $T_{peak} = 7.5$ s, $N = 101$, $m = 740$ (a 3.0σ event). Average time series generated from 2000 sample time series; 20 sample time series are plotted.

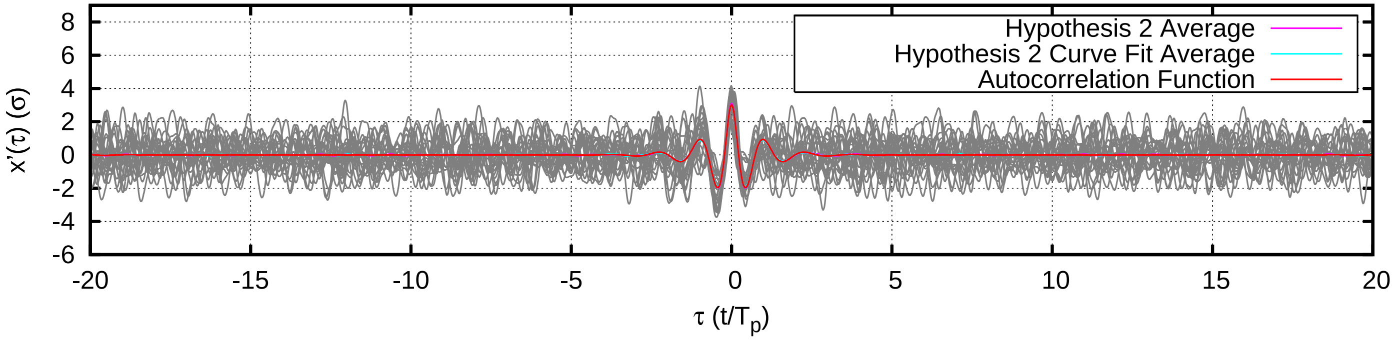

Figure A.55: Sample time series generated by Hypothesis 2 and Hypothesis 2 Curve Fit phases. ITTC Sea State 3: $h_{peak} = 0.88$ m, $T_{peak} = 7.5$ s, $N = 101$, $m = 740$ (a 3.0σ event). Average time series generated from 2000 sample time series; 20 sample time series are plotted.

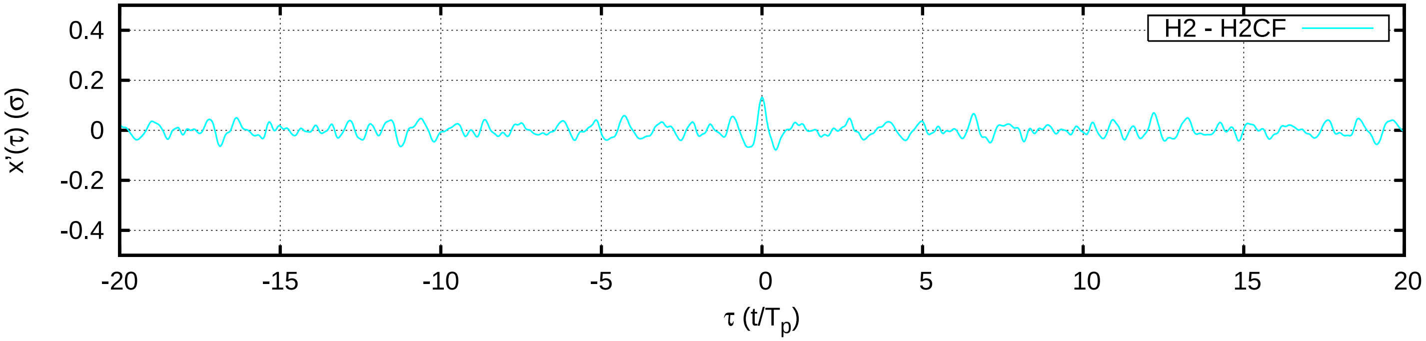

Figure A.56: Comparison of Hypothesis 2 and Hypothesis 2 Curve Fit average time series. The difference between these two average time series is plotted. ITTC Sea State 3: $h_{peak} = 0.88$ m, $T_{peak} = 7.5$ s, $N = 101$, $m = 740$ (a 3.0σ event).

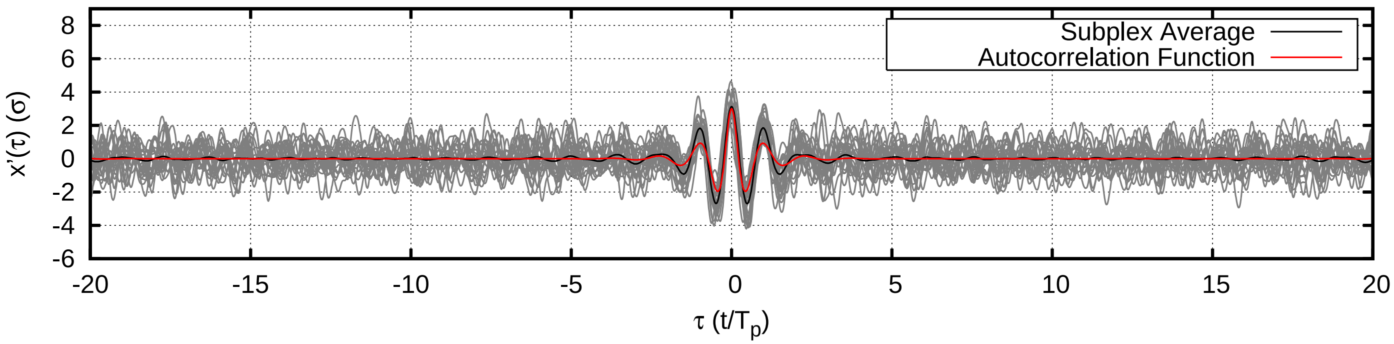

Figure A.57: Sample time series generated by Subplex optimization phases. ITTC Sea State 3: $h_{peak} = 0.88$ m, $T_{peak} = 7.5$ s, $N = 101$, $m = 740$ (a 3.0σ event). Average time series generated from 2000 sample time series; 20 sample time series are plotted.

A.6 Case 6

Case	**6**	
H_{sig}	14.00	m
T_{peak}	20.00	sec
N	101	
ω_{min}	0.169	rad/s
ω_{max}	1.502	rad/s
$\sigma_{spectrum}$	3.500	m
$\sigma_{simulation}$	0.350E+01	MKS units
$\sigma_{simulation}/\sigma_{spectrum}$	99.98%	
maximum attainable value	9.61	σ_{sim}
TEV	3.00	σ_{sim}
TEV/maximum attainable value	0.31	
m	740	
Monte Carlo Simulation	yes	
time to run subplex optimization	55775.	sec

Case	**6**
Extreme Value PDF Comparison	
μ_{Ochi}	**3.15**
μ_{MC}	3.09
μ_{H1}	1.43
μ_{H2}	3.10
μ_{H2CF}	2.96
$\mu_{subplex}$	3.14
σ_{Ochi}	**0.36**
σ_{MC}	0.33
σ_{H1}	1.00
σ_{H2}	0.85
σ_{H2CF}	0.83
$\sigma_{subplex}$	0.79
MC: $D_{KL}(f_{x_m}(x) \| f_{x_1}(x))$	0.02
H1: $D_{KL}(f_{x_m}(x) \| f_{x_1}(x))$	1.76
H2: $D_{KL}(f_{x_m}(x) \| f_{x_1}(x))$	0.39
H2CF: $D_{KL}(f_{x_m}(x) \| f_{x_1}(x))$	0.39
Subplex: $D_{KL}(f_{x_m}(x) \| f_{x_1}(x))$	0.26

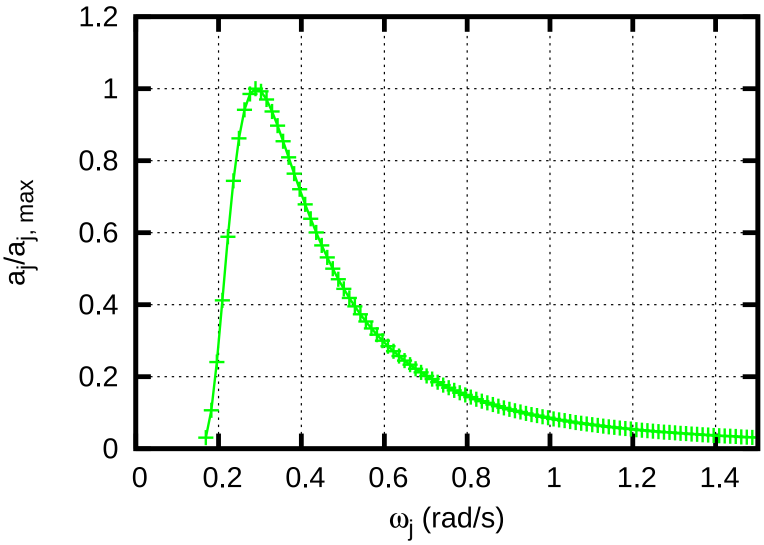

Figure A.58: Amplitudes corresponding to ITTC Sea State 9: $h_{peak} = 14.0$ m, $T_{peak} = 20.0$ s, $N = 101$.

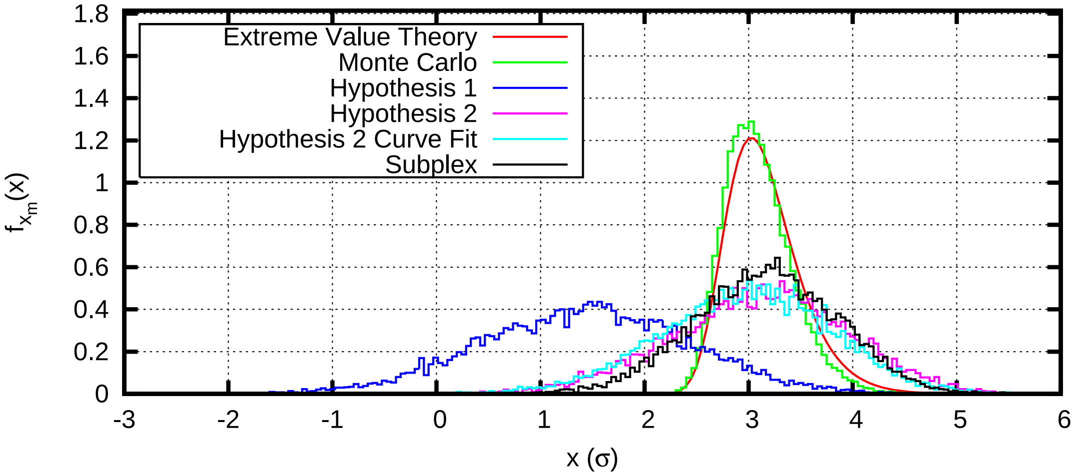

Figure A.59: Comparison of $f_{x_m}(x)$, denoted "Extreme Value Theory", and $f_{x_1}(x)$ as calculated by Hypotheses 1 and 2, Hypothesis 2 Curve Fit, and Subplex optimization. ITTC Sea State 9: $h_{peak} = 14.0$ m, $T_{peak} = 20.0$ s, $N = 101$, $m = 740$ (a 3.0σ event).

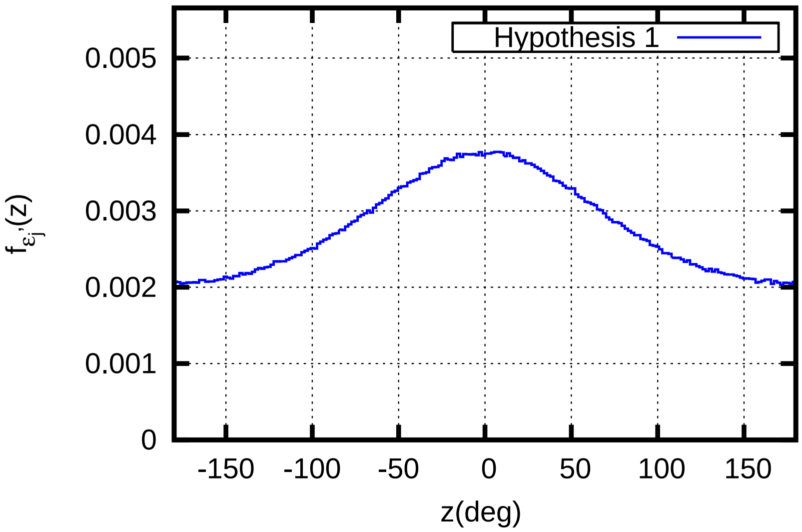

Figure A.60: Phase histogram for Hypothesis 1. ITTC Sea State 9: $h_{peak} = 14.0$ m, $T_{peak} = 20.0$ s, $N = 101$, $m = 740$ (a 3.0σ event). $M = 50,000$ samples.

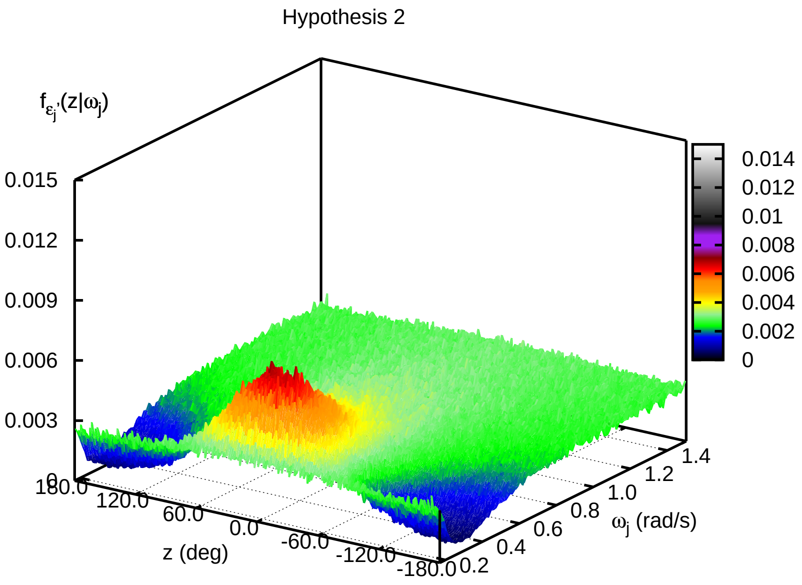

Figure A.61: Phase histogram for Hypothesis 2. ITTC Sea State 9: $h_{peak} = 14.0$ m, $T_{peak} = 20.0$ s, $N = 101$, $m = 740$ (a 3.0σ event). $M = 50,000$ samples.

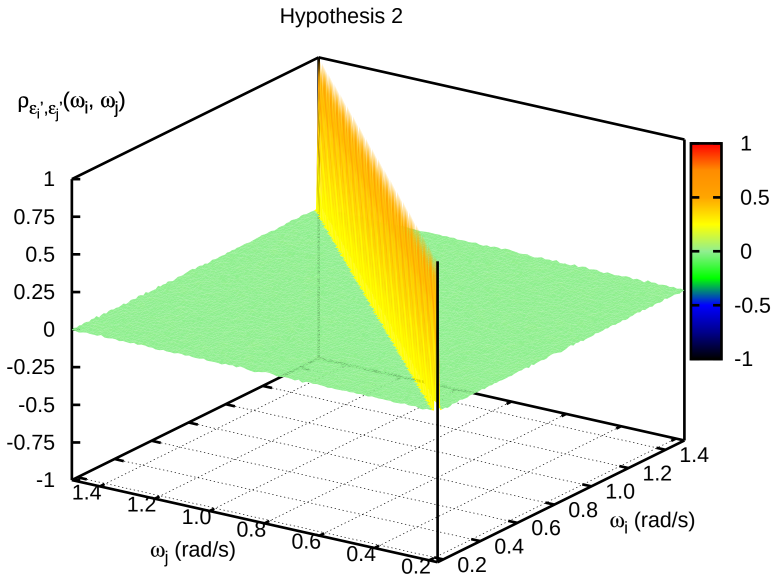

Figure A.62: Correlation of phase pairs (ϵ_i',ϵ_j') for Hypothesis 2. ITTC Sea State 9: $h_{peak} = 14.0$ m, $T_{peak} = 20.0$ s, $N = 101$, $m = 740$ (a 3.0σ event). $M = 50,000$ samples.

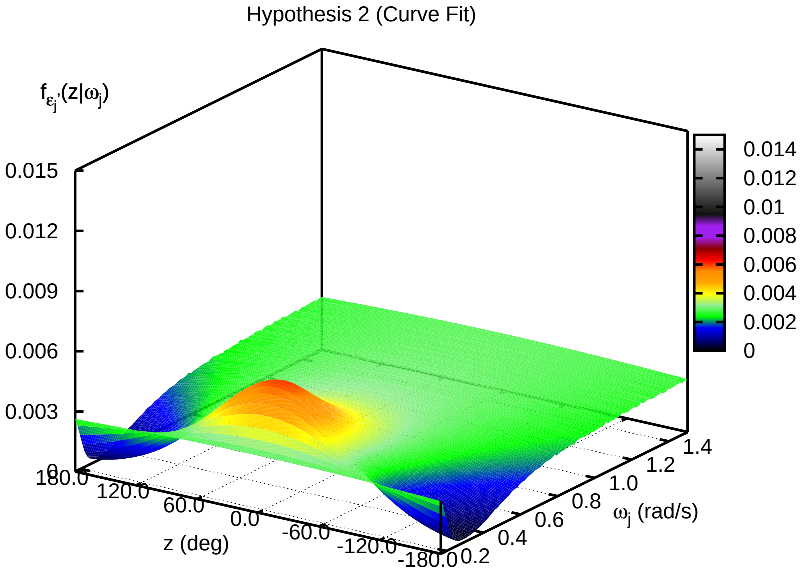

Figure A.63: Phase PDF for Hypothesis 2 Curve Fit. ITTC Sea State 9: $h_{peak} = 14.0$ m, $T_{peak} = 20.0$ s, $N = 101$, $m = 740$ (a 3.0σ event).

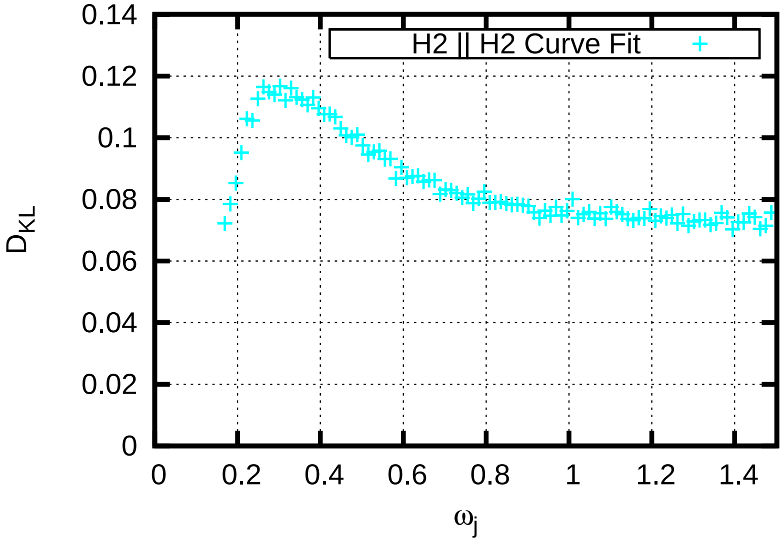

Figure A.64: Comparison of Hypothesis 2 and Hypothesis 2 Curve Fit phase PDFs using the Kullback-Leibler divergence, $D_{KL}(f_{\epsilon'_j,MC}(z)\|f_{\epsilon'_j,MG}(z))$. ITTC Sea State 9: $h_{peak} = 14.0$ m, $T_{peak} = 20.0$ s, $N = 101$, $m = 740$ (a 3.0σ event).

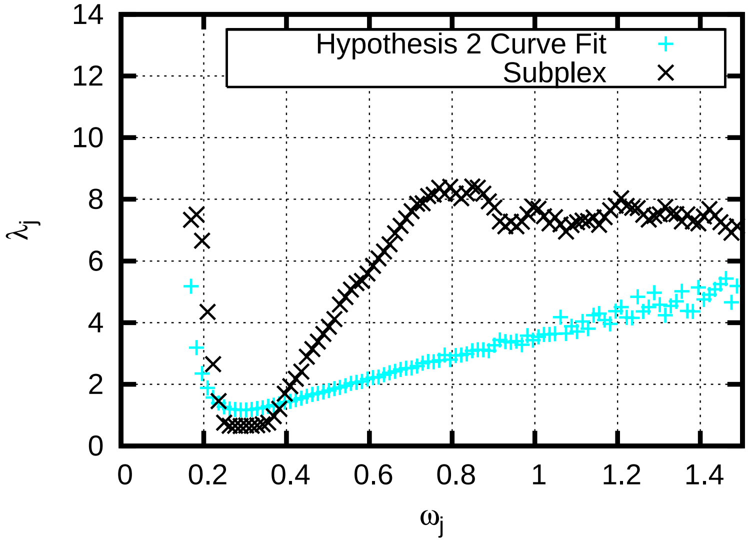

Figure A.65: λ_j as determined by Subplex optimization compared to λ_j as determined by minimizing $D_{KL}(f_{\epsilon'_j,MC}(z)\|f_{\epsilon'_j,MG}(z))$. λ_j is practically capped at 10, as $\lambda_j \geq 10$ results in a uniform phase distribution. ITTC Sea State 9: $h_{peak} = 14.0$ m, $T_{peak} = 20.0$ s, $N = 101$, $m = 740$ (a 3.0σ event).

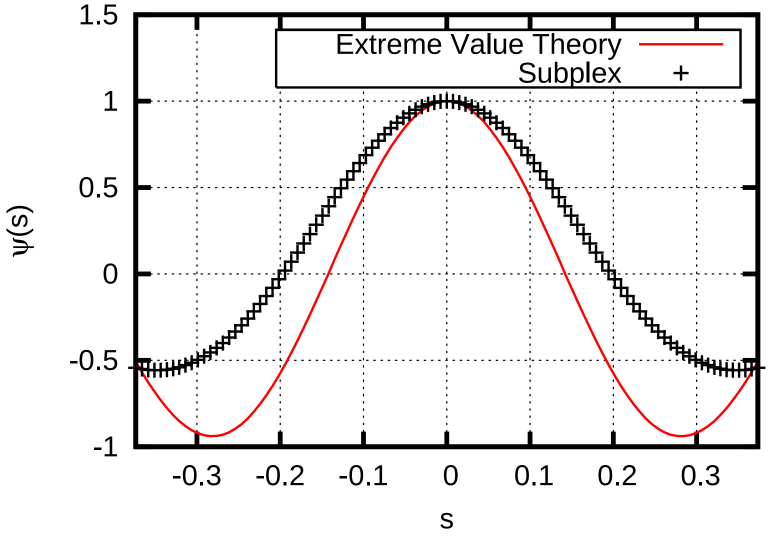

Figure A.66: Comparison of characteristic functions $\psi_{x_m}(x)$, denoted "Extreme Value Theory", and $\psi_{x_1}(s)$ as calculated by Subplex optimization. ITTC Sea State 9: $h_{peak} = 14.0$ m, $T_{peak} = 20.0$ s, $N = 101$, $m = 740$ (a 3.0σ event).

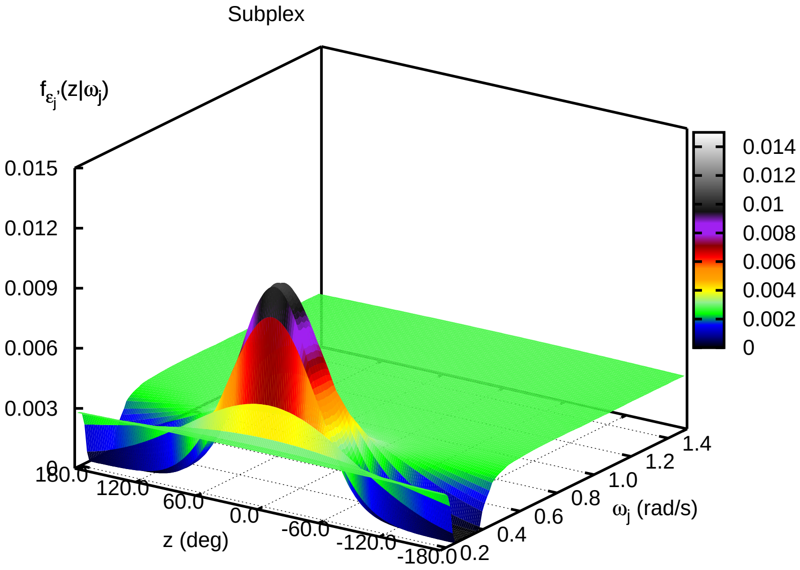

Figure A.67: Phase PDF from Subplex optimization of λ_j. ITTC Sea State 9: $h_{peak} = 14.0$ m, $T_{peak} = 20.0$ s, $N = 101$, $m = 740$ (a 3.0σ event).

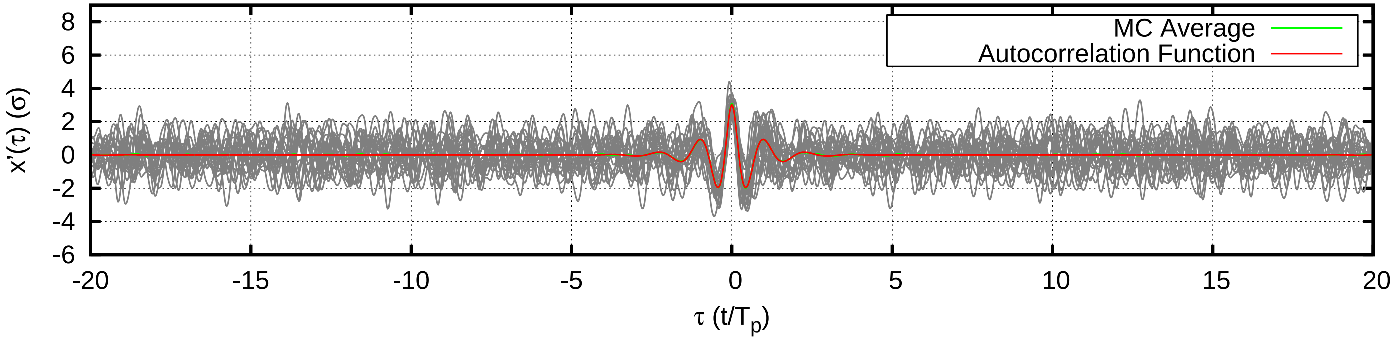

Figure A.68: Sample time series generated by Monte Carlo simulation. ITTC Sea State 9: $h_{peak} = 14.0$ m, $T_{peak} = 20.0$ s, $N = 101$, $m = 740$ (a 3.0σ event). Average time series generated from 2000 sample time series; 20 sample time series are plotted.

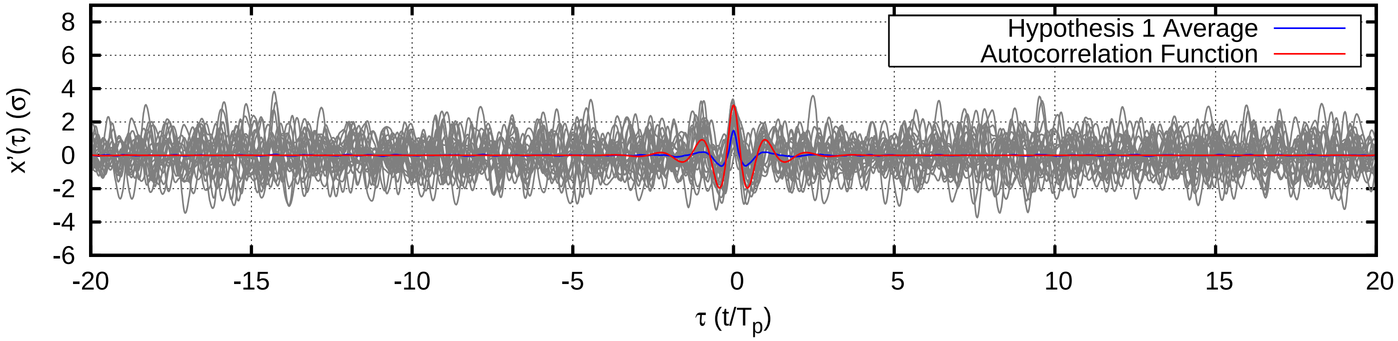

Figure A.69: Sample time series generated by Hypothesis 1 phases. ITTC Sea State 9: $h_{peak} = 14.0$ m, $T_{peak} = 20.0$ s, $N = 101$, $m = 740$ (a 3.0σ event). Average time series generated from 2000 sample time series; 20 sample time series are plotted.

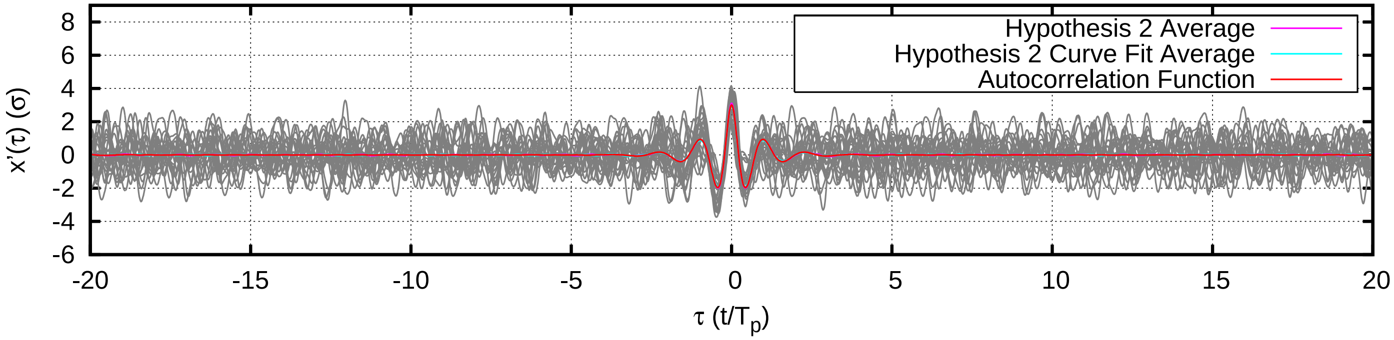

Figure A.70: Sample time series generated by Hypothesis 2 and Hypothesis 2 Curve Fit phases. ITTC Sea State 9: $h_{peak} = 14.0$ m, $T_{peak} = 20.0$ s, $N = 101$, $m = 740$ (a 3.0σ event). Average time series generated from 2000 sample time series; 20 sample time series are plotted.

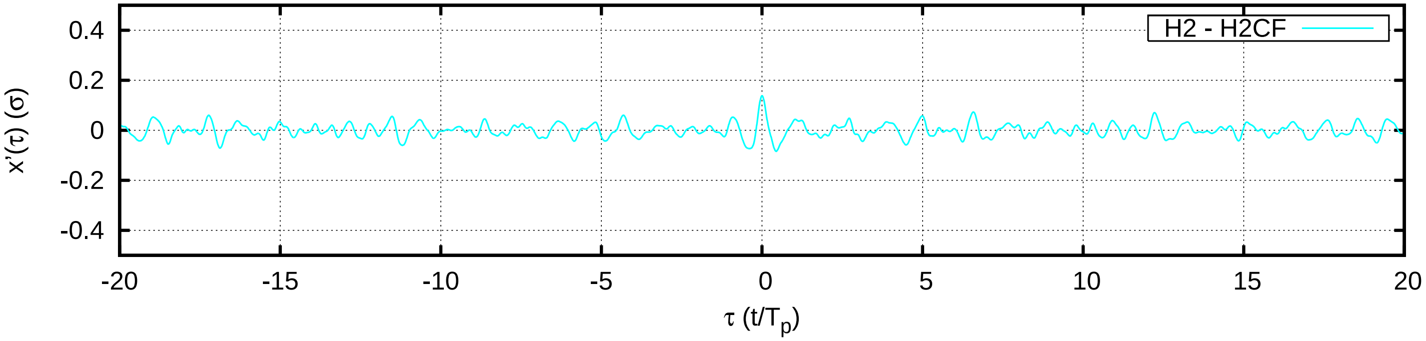

Figure A.71: Comparison of Hypothesis 2 and Hypothesis 2 Curve Fit average time series. The difference between these two average time series is plotted. ITTC Sea State 9: $h_{peak} = 14.0$ m, $T_{peak} = 20.0$ s, $N = 101$, $m = 740$ (a 3.0σ event).

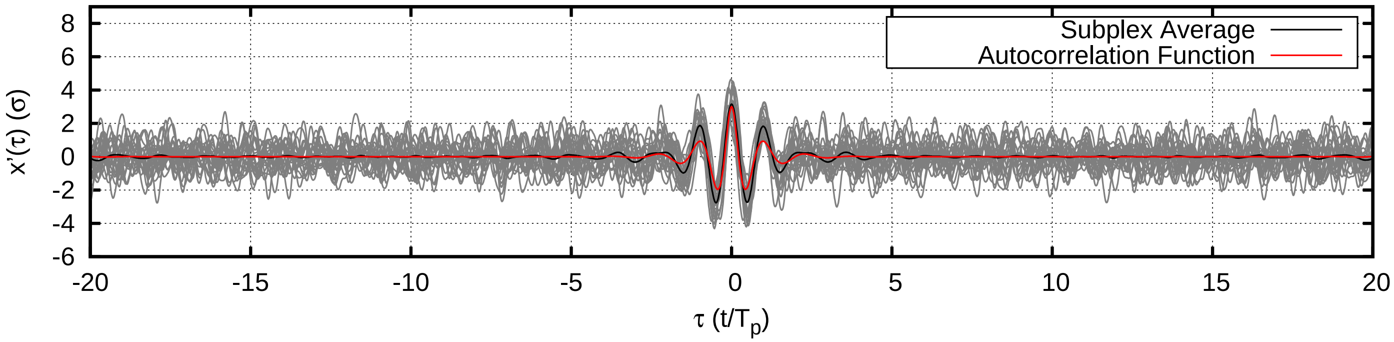

Figure A.72: Sample time series generated by Subplex optimization phases. ITTC Sea State 9: $h_{peak} = 14.0$ m, $T_{peak} = 20.0$ s, $N = 101$, $m = 740$ (a 3.0σ event). Average time series generated from 2000 sample time series; 20 sample time series are plotted.

A.7 Case 7

Case	**7**	
H_{sig}	0.88	m
T_{peak}	7.50	sec
N	101	
ω_{min}	0.451	rad/s
ω_{max}	4.005	rad/s
$\sigma_{spectrum}$	0.220	m
$\sigma_{simulation}$	0.220E+00	MKS units
$\sigma_{simulation}/\sigma_{spectrum}$	99.98%	
maximum attainable value	9.61	σ_{sim}
TEV	5.00	σ_{sim}
TEV/maximum attainable value	0.52	
m	3488555	
Monte Carlo Simulation	no	
time to run subplex optimization	28157.	sec
Extreme Value PDF Comparison		
μ_{Ochi}	**5.10**	
$\mu_{subplex}$	5.09	
σ_{Ochi}	**0.24**	
$\sigma_{subplex}$	0.74	
Subplex: $D_{KL}(f_{x_m}(x)\|f_{x_1}(x))$	0.49	

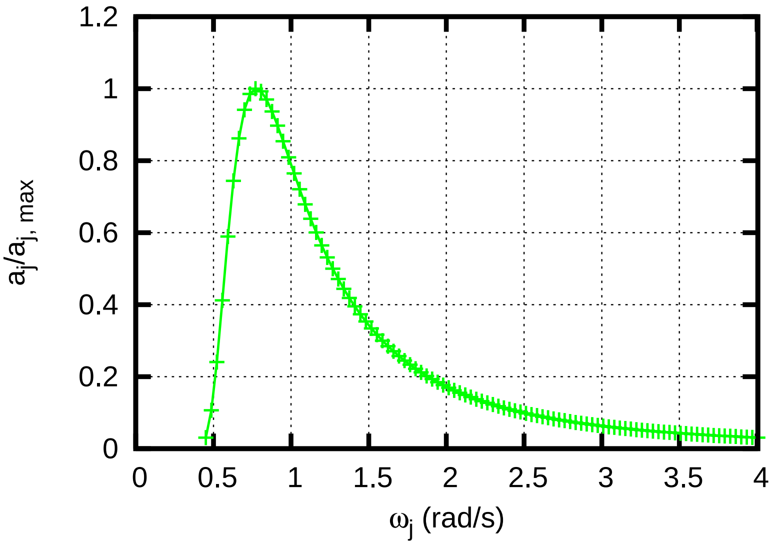

Figure A.73: Amplitudes corresponding to ITTC Sea State 3: $h_{peak} = 0.88$ m, $T_{peak} = 7.5$ s, $N = 101$.

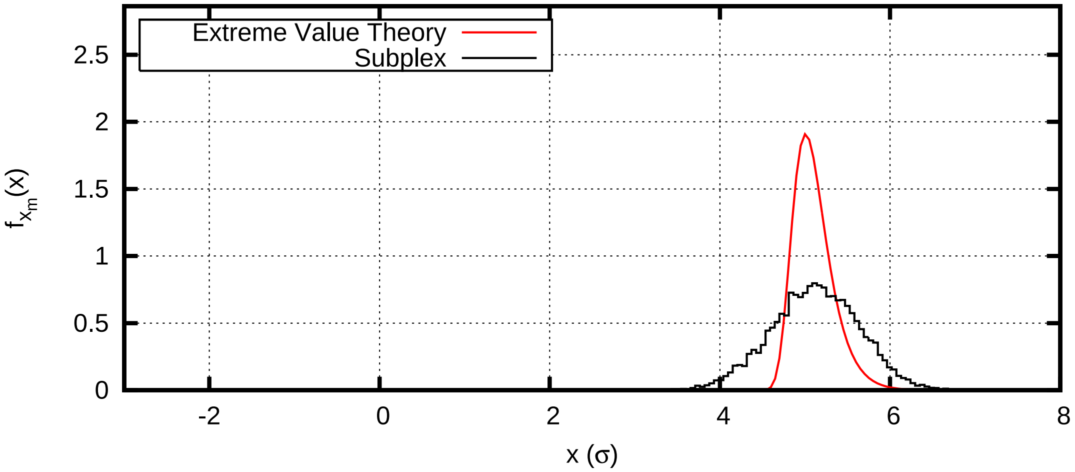

Figure A.74: Comparison of $f_{x_m}(x)$, denoted "Extreme Value Theory", and $f_{x_1}(x)$ as calculated by Hypotheses 1 and 2, Hypothesis 2 Curve Fit, and Subplex optimization. ITTC Sea State 3: $h_{peak} = 0.88$ m, $T_{peak} = 7.5$ s, $N = 101$, $m = 3,488,555$ (a 5.0σ event).

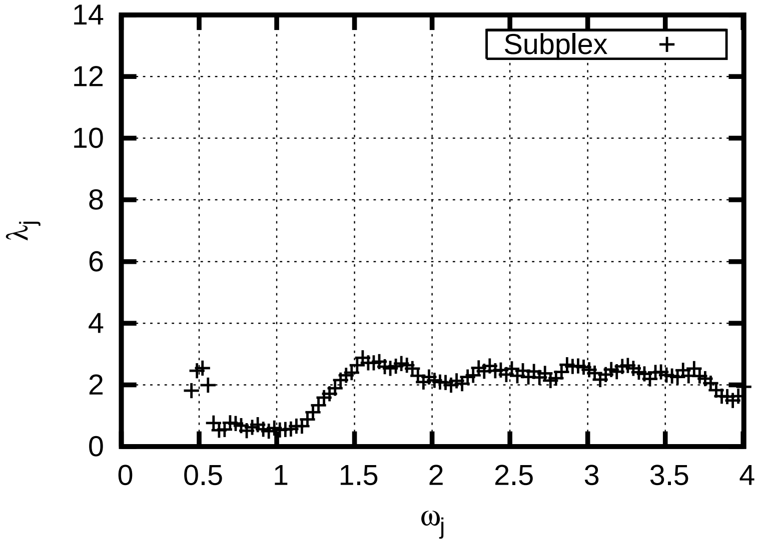

Figure A.75: λ_j as determined by Subplex optimization. λ_j is practically capped at 10, as $\lambda_j \geq 10$ results in a uniform phase distribution. ITTC Sea State 3: $h_{peak} = 0.88$ m, $T_{peak} = 7.5$ s, $N = 101$, $m = 3,488,555$ (a 5.0σ event).

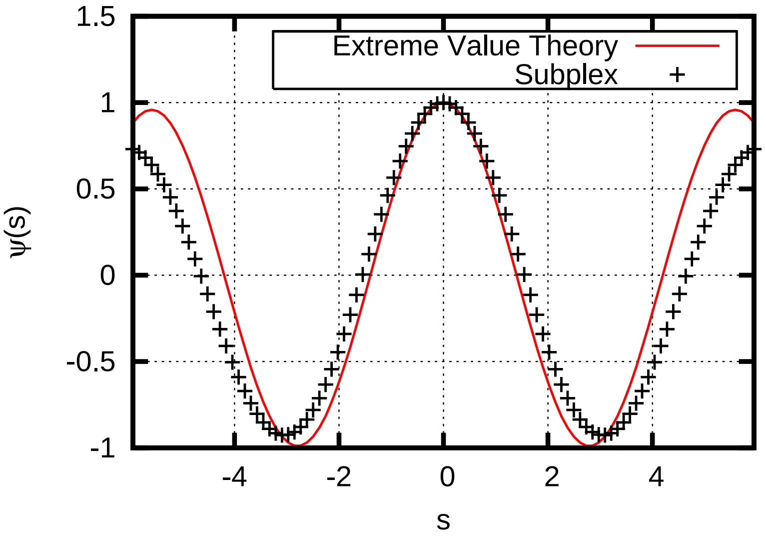

Figure A.76: Comparison of characteristic functions $\psi_{x_m}(x)$, denoted "Extreme Value Theory", and $\psi_{x_1}(s)$ as calculated by Subplex optimization. ITTC Sea State 3: $h_{peak} = 0.88$ m, $T_{peak} = 7.5$ s, $N = 101$, $m = 3,488,555$ (a 5.0σ event).

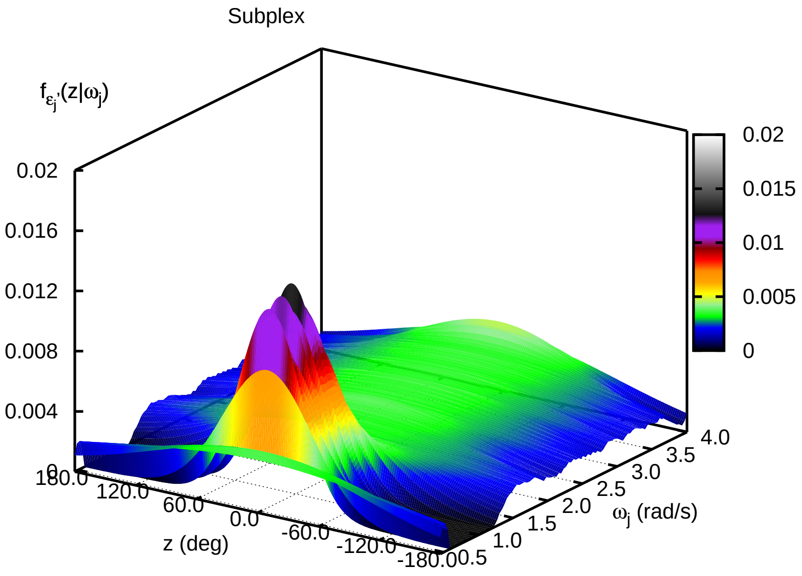

Figure A.77: Phase PDF from Subplex optimization of λ_j. ITTC Sea State 3: $h_{peak} = 0.88$ m, $T_{peak} = 7.5$ s, $N = 101$, $m = 3,488,555$ (a 5.0σ event).

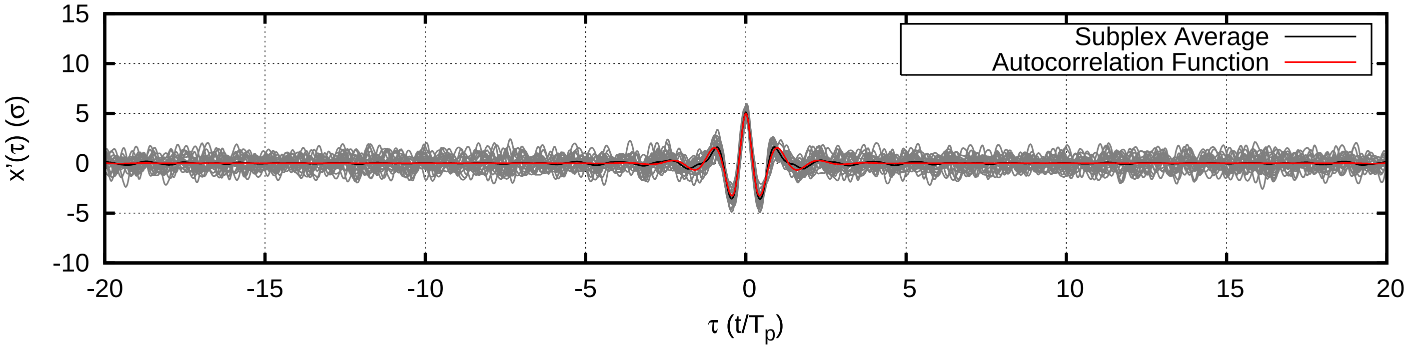

Figure A.78: Sample time series generated by Subplex optimization phases. ITTC Sea State 3: $h_{peak} = 0.88$ m, $T_{peak} = 7.5$ s, $N = 101$, $m = 3,488,555$ (a 5.0σ event). Average time series generated from 2000 sample time series; 20 sample time series are plotted.

A.8 Case 8

Case	**8**	
H_{sig}	14.00	m
T_{peak}	20.00	sec
N	101	
ω_{min}	0.169	rad/s
ω_{max}	1.502	rad/s
$\sigma_{spectrum}$	3.500	m
$\sigma_{simulation}$	0.350E+01	MKS units
$\sigma_{simulation}/\sigma_{spectrum}$	99.98%	
maximum attainable value	9.61	σ_{sim}
TEV	5.00	σ_{sim}
TEV/maximum attainable value	0.52	
m	3488555	
Monte Carlo Simulation	no	
time to run subplex optimization	75098.	sec
Extreme Value PDF Comparison		
μ_{Ochi}	**5.10**	
$\mu_{subplex}$	5.08	
σ_{Ochi}	**0.24**	
$\sigma_{subplex}$	0.71	
Subplex: $D_{KL}(f_{x_m}(x) \| f_{x_1}(x))$	0.41	

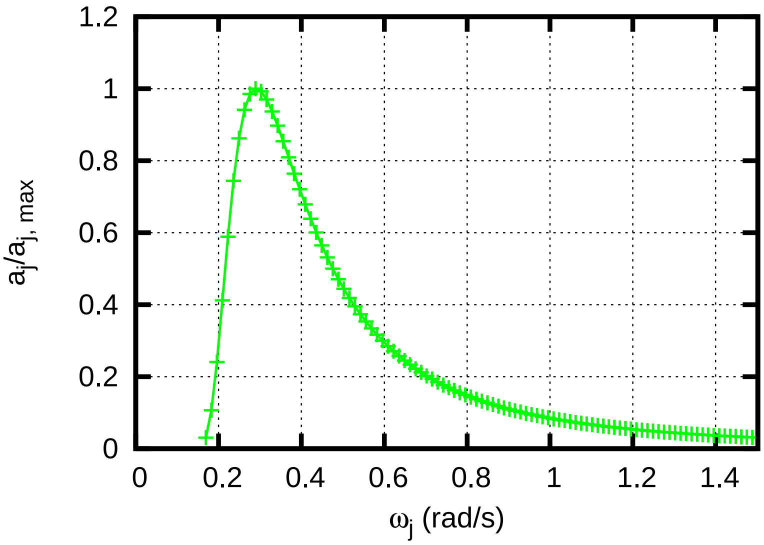

Figure A.79: Amplitudes corresponding to ITTC Sea State 9: $h_{peak} = 14.0$ m, $T_{peak} = 20.0$ s, $N = 101$.

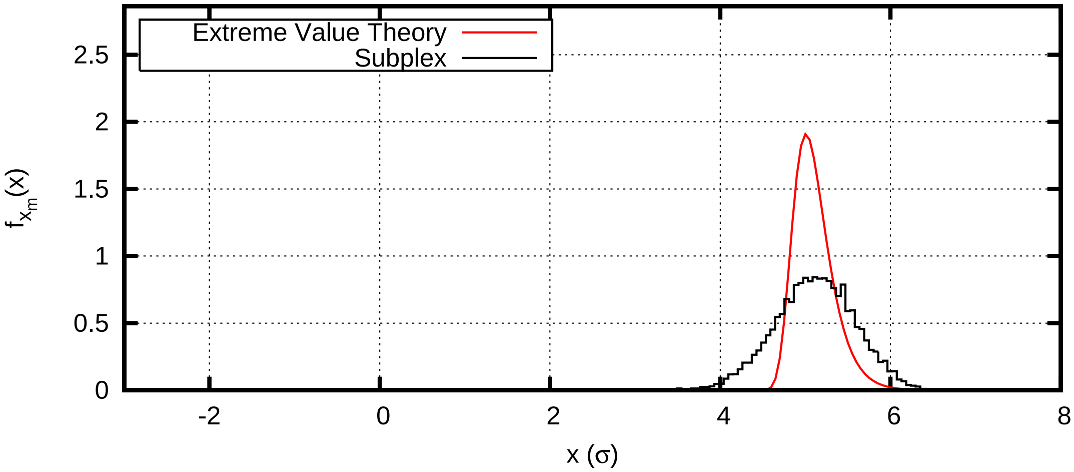

Figure A.80: Comparison of $f_{x_m}(x)$, denoted "Extreme Value Theory", and $f_{x_1}(x)$ as calculated by Hypotheses 1 and 2, Hypothesis 2 Curve Fit, and Subplex optimization. ITTC Sea State 9: $h_{peak} = 14.0$ m, $T_{peak} = 20.0$ s, $N = 101$, $m = 3,488,555$ (a 5.0σ event).

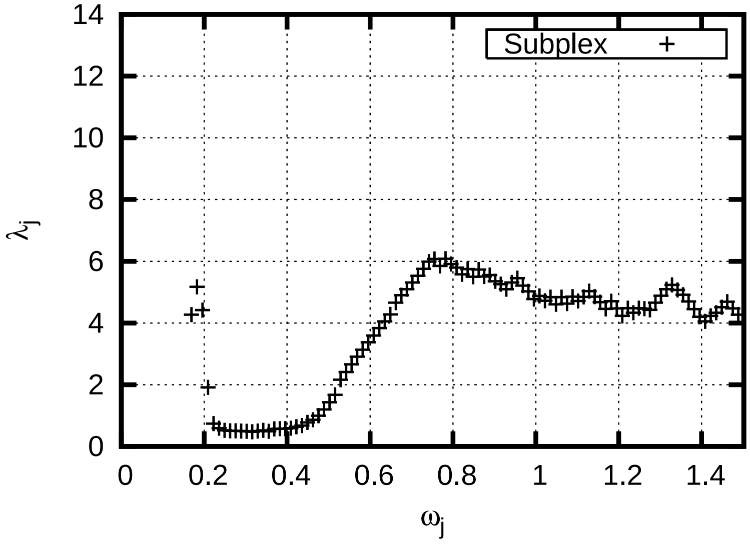

Figure A.81: λ_j as determined by Subplex optimization. λ_j is practically capped at 10, as $\lambda_j \geq 10$ results in a uniform phase distribution. ITTC Sea State 9: $h_{peak} = 14.0$ m, $T_{peak} = 20.0$ s, $N = 101$, $m = 3,488,555$ (a 5.0σ event).

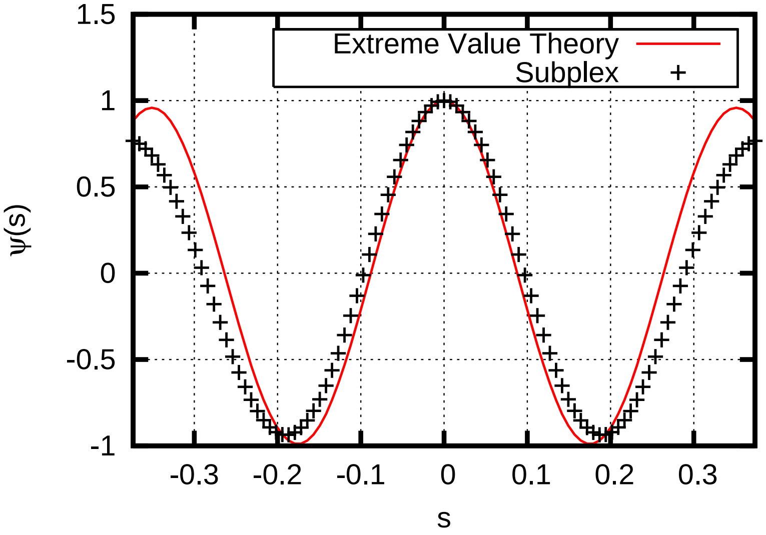

Figure A.82: Comparison of characteristic functions $\psi_{x_m}(x)$, denoted "Extreme Value Theory", and $\psi_{x_1}(s)$ as calculated by Subplex optimization. ITTC Sea State 9: $h_{peak} = 14.0$ m, $T_{peak} = 20.0$ s, $N = 101$, $m = 3,488,555$ (a 5.0σ event).

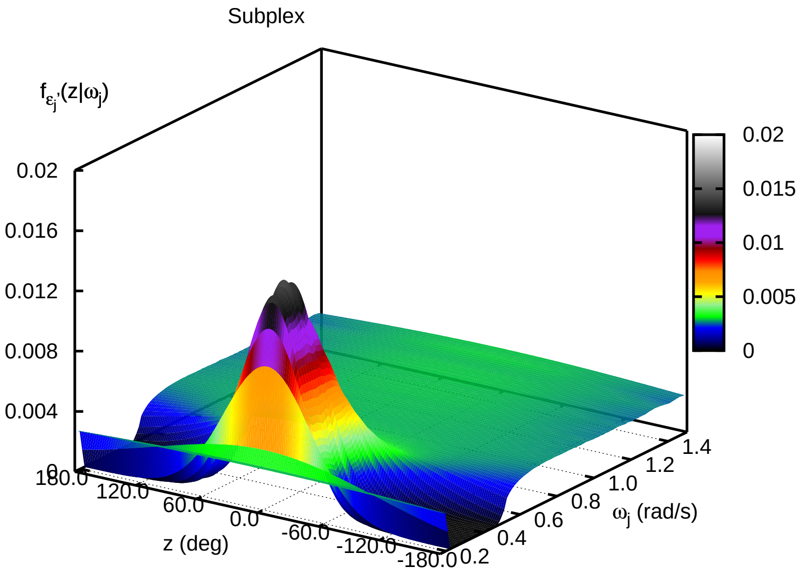

Figure A.83: Phase PDF from Subplex optimization of λ_j. ITTC Sea State 9: $h_{peak} = 14.0$ m, $T_{peak} = 20.0$ s, $N = 101$, $m = 3,488,555$ (a 5.0σ event).

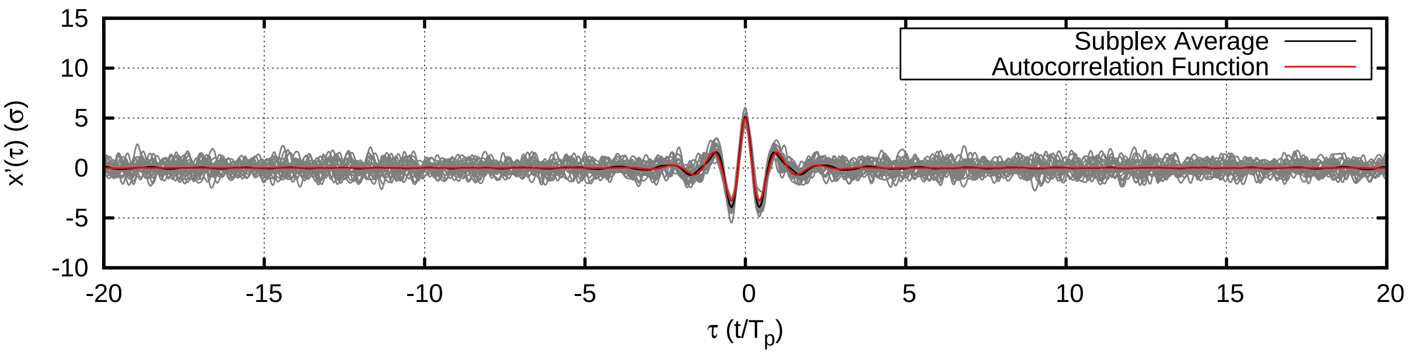

Figure A.84: Sample time series generated by Subplex optimization phases. ITTC Sea State 9: $h_{peak} = 14.0$ m, $T_{peak} = 20.0$ s, $N = 101$, $m = 3,488,555$ (a 5.0σ event). Average time series generated from 2000 sample time series; 20 sample time series are plotted.

A.9 Case 9

Case	**9**	
Heading Angle	180.00	deg
Forward Speed	6.43	m/s
H_{sig}	5.58	m
T_{peak}	8.80	sec
N	101	
ω_{min}	0.350	rad/s
ω_{max}	2.500	rad/s
σ_{wave}	1.395	m
$\sigma_{response}$	0.240E+09	MKS units
maximum attainable value	8.27	σ_{sim}
TEV	3.00	σ_{sim}
TEV/maximum attainable value	0.36	
m	740	
Monte Carlo Simulation	yes	
time to run subplex optimization	38298.	sec

Case	**9**
Extreme Value PDF Comparison	
μ_{Ochi}	**3.15**
μ_{MC}	3.02
μ_{H1}	1.10
μ_{H2}	3.02
μ_{H2CF}	2.93
$\mu_{subplex}$	3.11
σ_{Ochi}	**0.36**
σ_{MC}	0.30
σ_{H1}	1.01
σ_{H2}	0.72
σ_{H2CF}	0.70
$\sigma_{subplex}$	0.68
MC: $D_{KL}(f_{x_m}(x) \| f_{x_1}(x))$	0.08
H1: $D_{KL}(f_{x_m}(x) \| f_{x_1}(x))$	2.27
H2: $D_{KL}(f_{x_m}(x) \| f_{x_1}(x))$	0.30
H2CF: $D_{KL}(f_{x_m}(x) \| f_{x_1}(x))$	0.30
Subplex: $D_{KL}(f_{x_m}(x) \| f_{x_1}(x))$	0.15

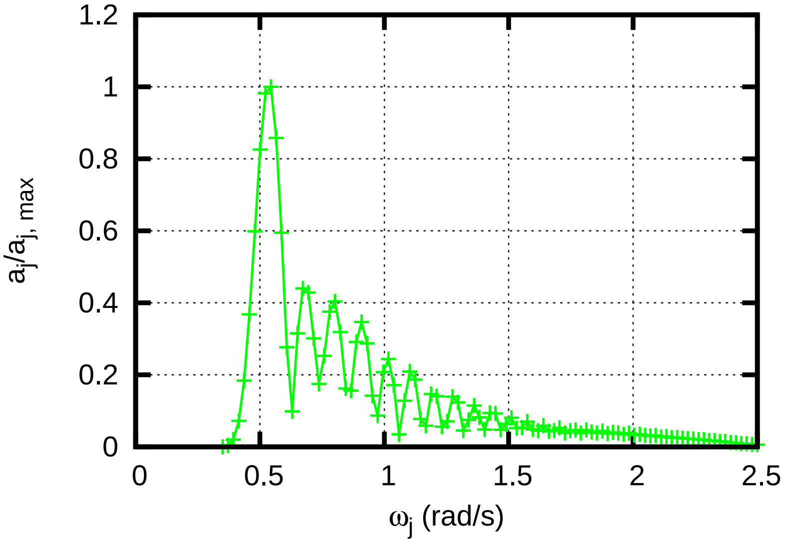

Figure A.85: Rigid body analysis: *Stewart J. Cort*. Amplitudes for midship bending moment. $N = 101$, heading angle $= 180°$, forward speed $= 12.5$ knots.

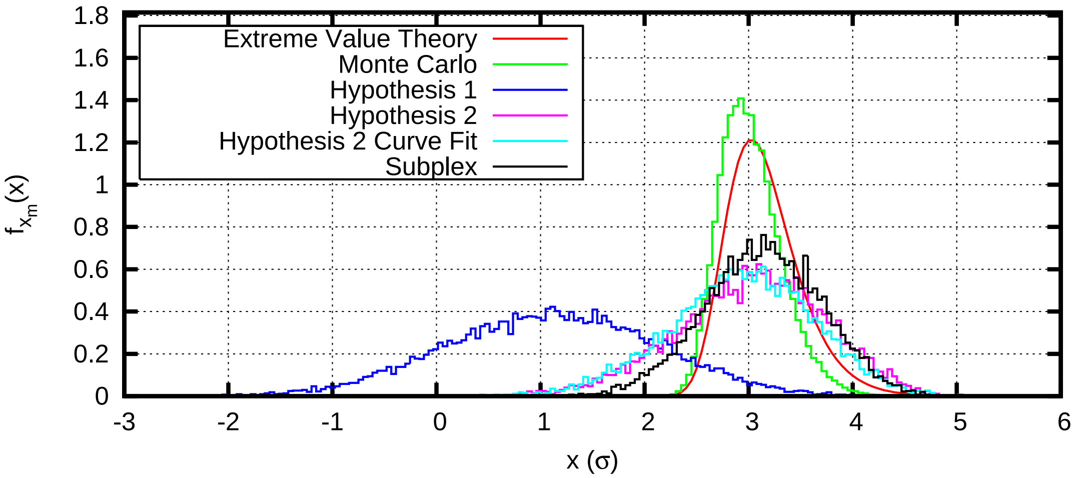

Figure A.86: Rigid body analysis: *Stewart J. Cort*. Extreme value PDFs for midship bending moment. TEV $= 3.0\sigma_{BM}$, $N =$ 101, heading angle $= 180°$, forward speed $= 12.5$ knots.

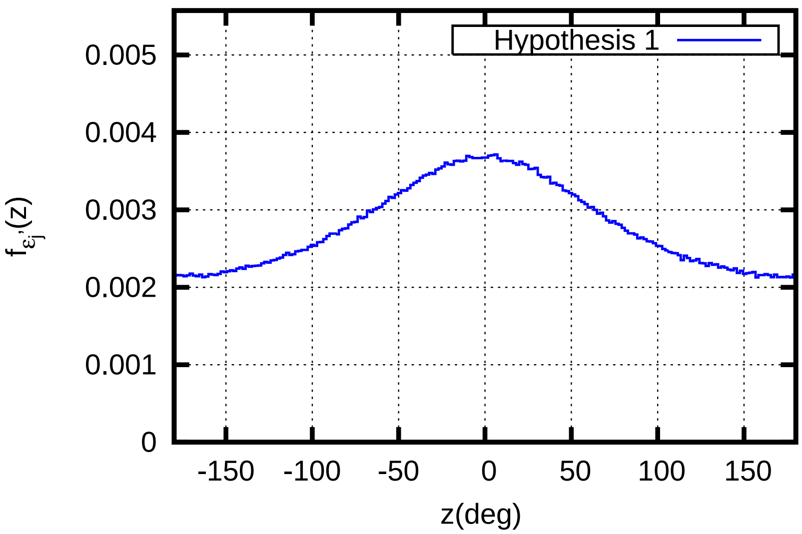

Figure A.87: Rigid body analysis: *Stewart J. Cort.* Phase histogram for Hypothesis 1, midship bending moment. TEV $= 3.0\sigma_{BM}$, $N = 101$, heading angle = 180°, forward speed = 12.5 knots.

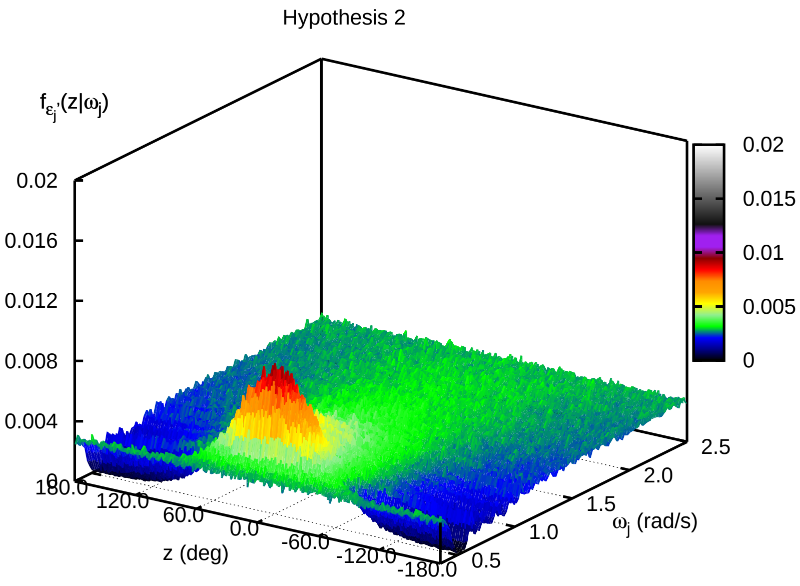

Figure A.88: Rigid body analysis: *Stewart J. Cort.* Phase histogram for Hypothesis 2, midship bending moment. TEV $= 3.0\sigma_{BM}$, $N = 101$, heading angle = 180°, forward speed = 12.5 knots.

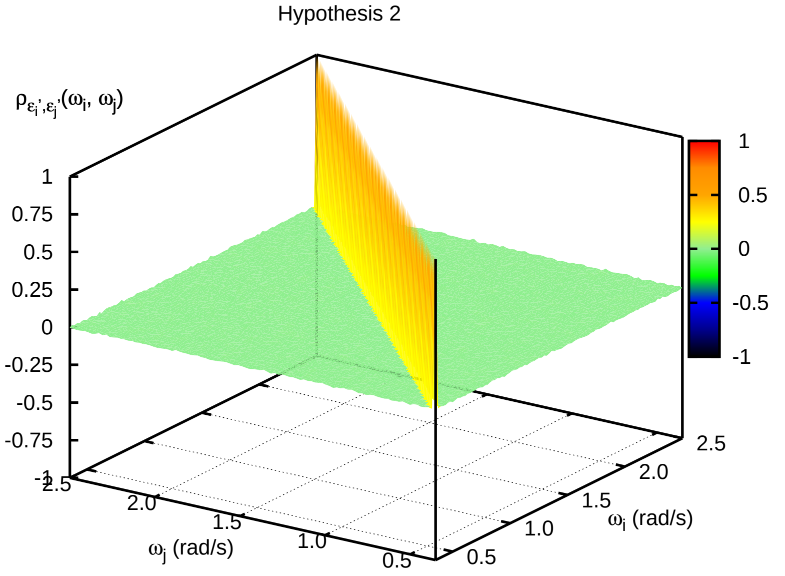

Figure A.89: Rigid body analysis: *Stewart J. Cort.* Correlation of phase pairs $(\epsilon_i', \epsilon_j')$ for Hypothesis 2. TEV $= 3.0\sigma_{BM}$, $N = 101$, heading angle = 180°, forward speed = 12.5 knots.

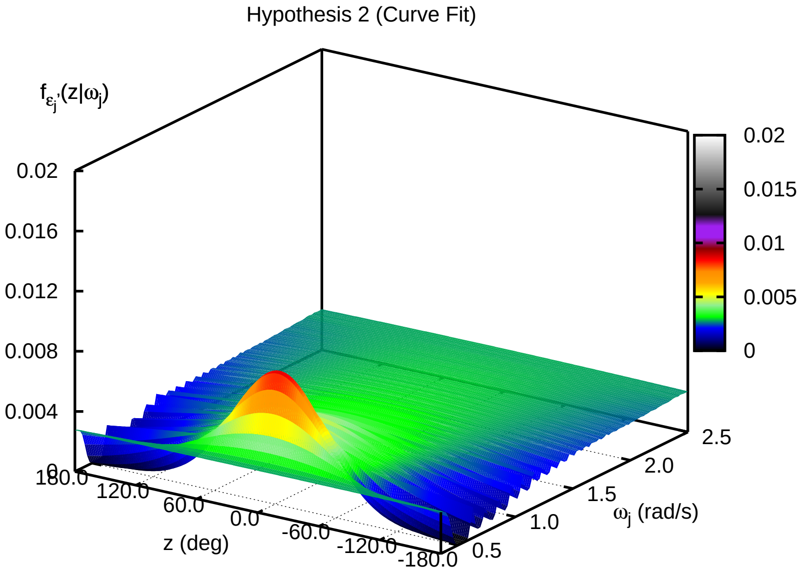

Figure A.90: Rigid body analysis: *Stewart J. Cort.* Phase PDF for Hypothesis 2 Curve Fit, midship bending moment. TEV $= 3.0\sigma_{BM}$, $N = 101$, heading angle = 180°, forward speed = 12.5 knots.

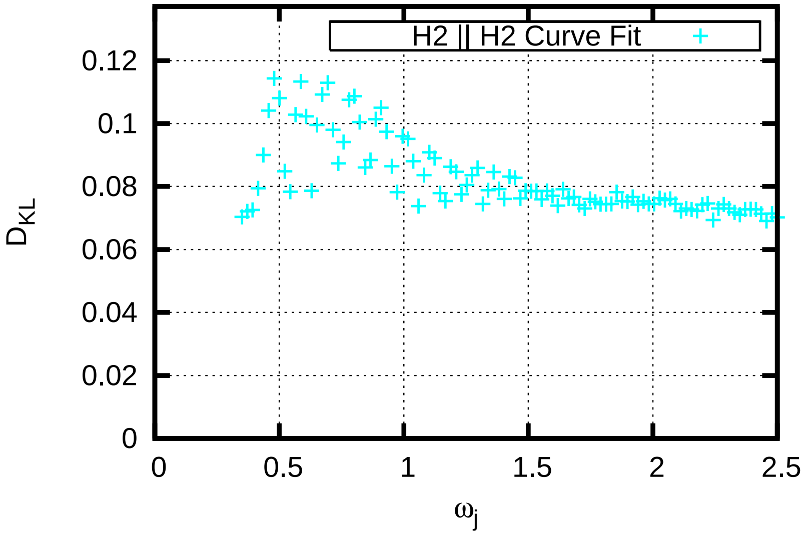

Figure A.91: Rigid body analysis: *Stewart J. Cort.* Comparison of Hypothesis 2 and Hypothesis 2 Curve Fit phase PDFs using the Kullback-Leibler divergence, $D_{KL}(f_{\epsilon'_j,MC}(z) \| f_{\epsilon'_j,MG}(z))$. TEV $= 3.0\sigma_{BM}$, $N = 101$, heading angle = 180°, forward speed = 12.5 knots.

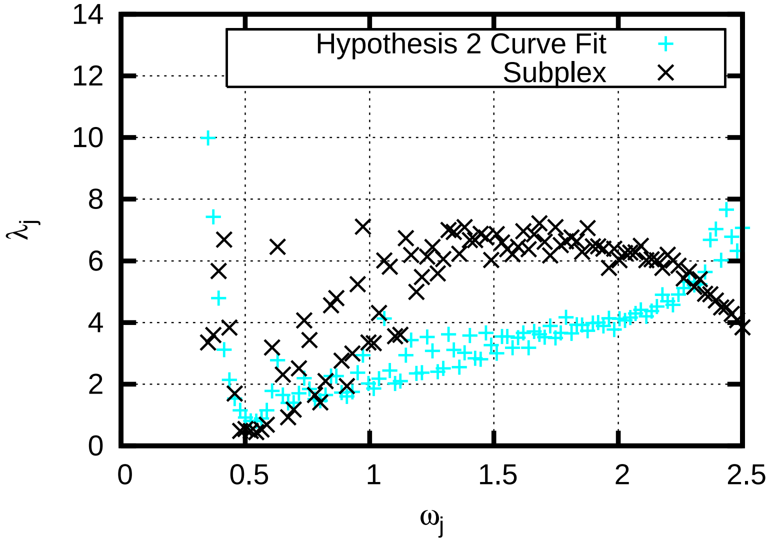

Figure A.92: Rigid body analysis: *Stewart J. Cort.* λ_j for midship bending moment. TEV $= 3.0\sigma_{BM}$, $N = 101$, heading angle = 180°, forward speed = 12.5 knots.

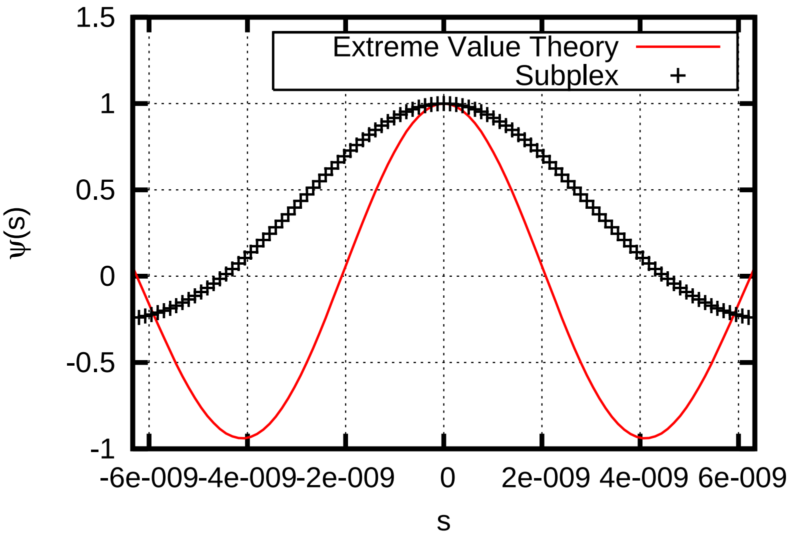

Figure A.93: Rigid body analysis: *Stewart J. Cort*. Characteristic functions for midship bending moment. TEV = $3.0\sigma_{BM}$, $N = 101$, heading angle = 180°, forward speed = 12.5 knots.

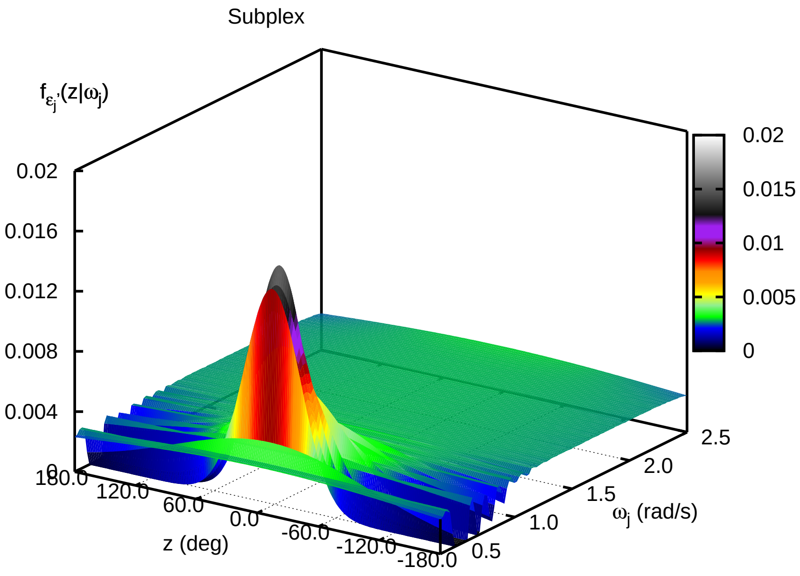

Figure A.94: Rigid body analysis: *Stewart J. Cort*. Phase PDF for Subplex optimization, midship bending moment. TEV = $3.0\sigma_{BM}$, $N = 101$, heading angle = 180°, forward speed = 12.5 knots.

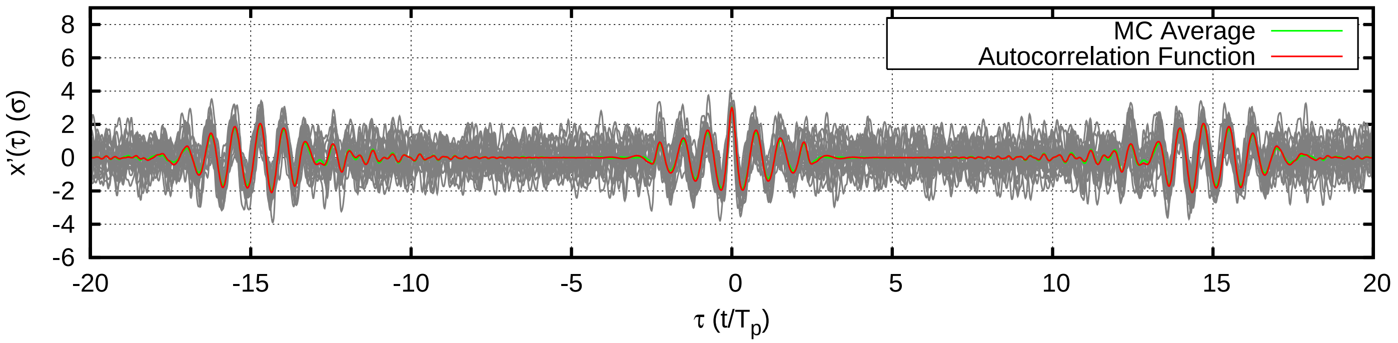

Figure A.95: Rigid body analysis: *Stewart J. Cort*. Sample bending moment time series at midship: Monte Carlo Simulation for midship bending moment. TEV = $3.0\sigma_{BM}$, $N = 101$, heading angle = 180°, forward speed = 12.5 knots. Average time series generated from 2000 sample time series; 20 sample time series are plotted.

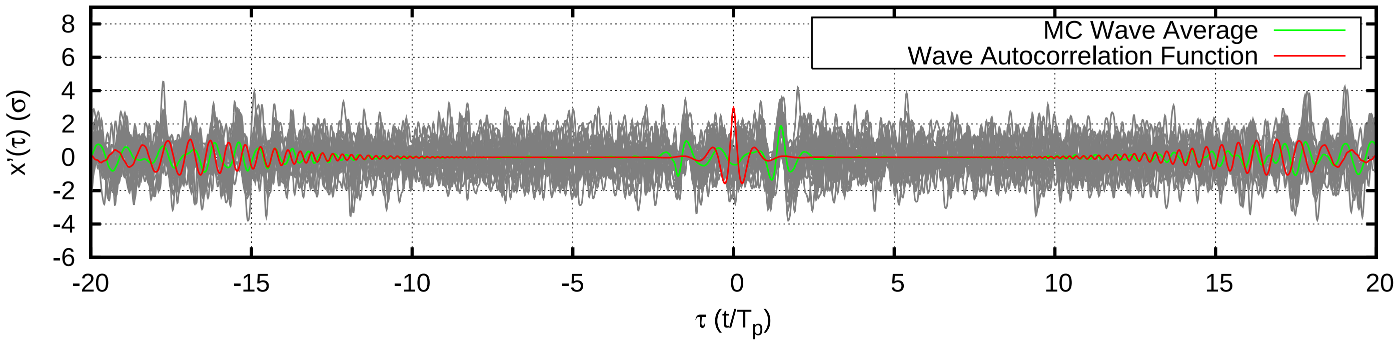

Figure A.96: Rigid body analysis: *Stewart J. Cort*. Sample wave time series at midship: Monte Carlo Simulation for midship bending moment. TEV = $3.0\sigma_{BM}$, $N = 101$, heading angle = 180°, forward speed = 12.5 knots. Average time series generated from 2000 sample time series; 20 sample time series are plotted.

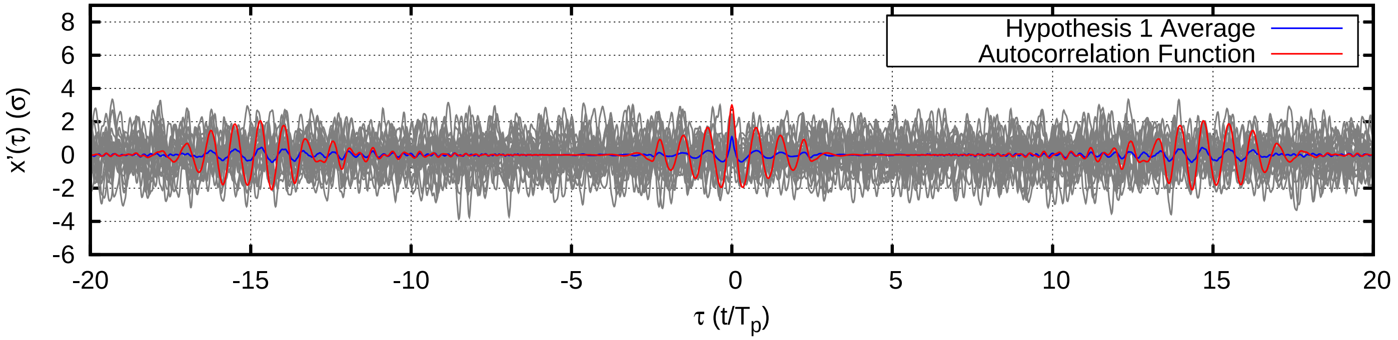

Figure A.97: Rigid body analysis: *Stewart J. Cort*. Sample bending moment time series at midship: Hypothesis 1 for midship bending moment. TEV = $3.0\sigma_{BM}$, N = 101, heading angle = 180°, forward speed = 12.5 knots. Average time series generated from 2000 sample time series; 20 sample time series are plotted.

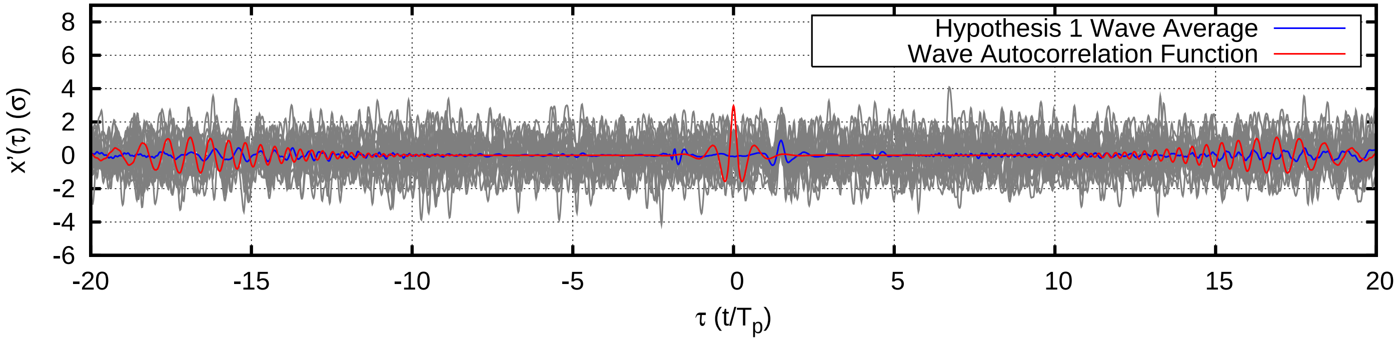

Figure A.98: Rigid body analysis: *Stewart J. Cort*. Sample wave time series at midship: Hypothesis 1 for midship bending moment. TEV = $3.0\sigma_{BM}$, N = 101, heading angle = 180°, forward speed = 12.5 knots. Average time series generated from 2000 sample time series; 20 sample time series are plotted.

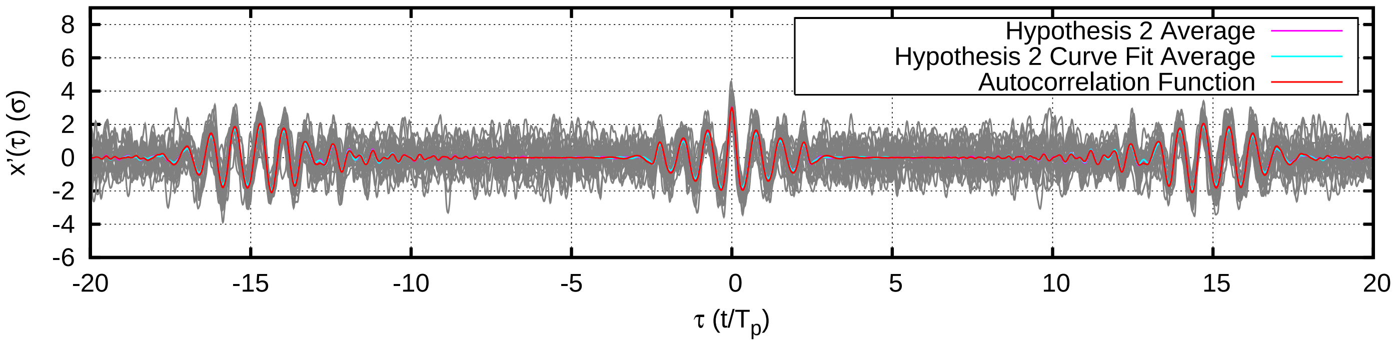

Figure A.99: Rigid body analysis: *Stewart J. Cort*. Sample bending moment time series at midship: Hypothesis 2 and Hypothesis 2 Curve Fit for midship bending moment. TEV = $3.0\sigma_{BM}$, $N = 101$, heading angle = 180°, forward speed = 12.5 knots. Average time series generated from 2000 sample time series; 20 sample time series are plotted.

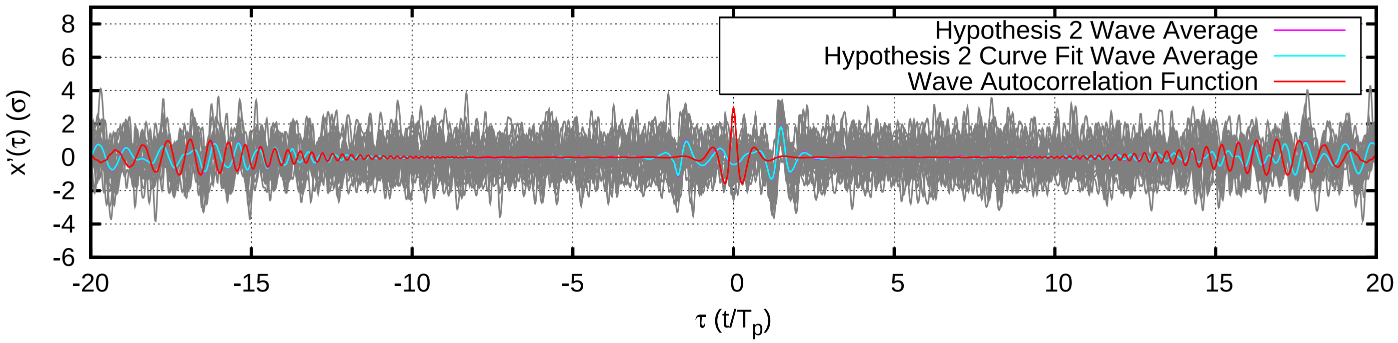

Figure A.100: Rigid body analysis: *Stewart J. Cort*. Sample wave time series at midship: Hypothesis 2 and Hypothesis 2 Curve Fit for midship bending moment. TEV = $3.0\sigma_{BM}$, $N = 101$, heading angle = 180°, forward speed = 12.5 knots. Average time series generated from 2000 sample time series; 20 sample time series are plotted.

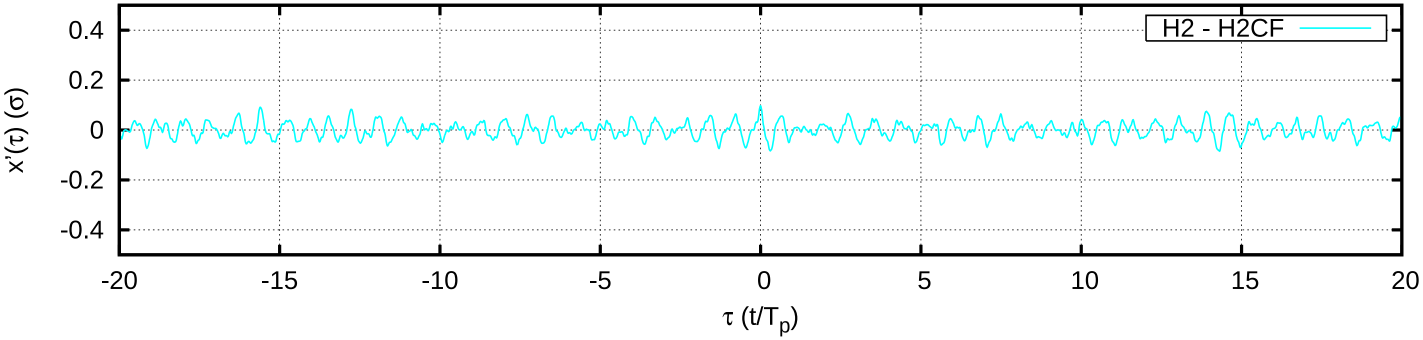

Figure A.101: Rigid body analysis: *Stewart J. Cort*. Comparison of Hypothesis 2 and Hypothesis 2 Curve Fit average time series. The difference between these two average time series is plotted. TEV $= 3.0\sigma_{BM}$, $N = 101$, heading angle = 180°, forward speed = 12.5 knots.

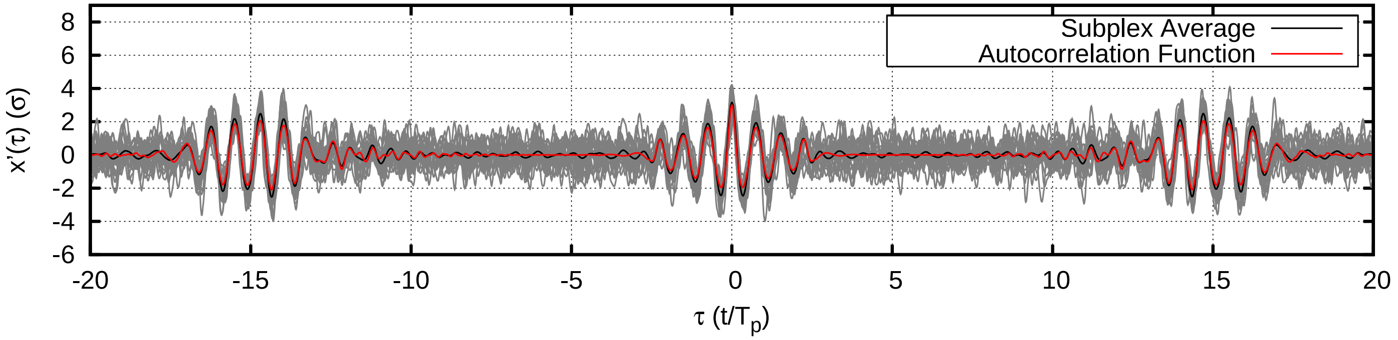

Figure A.102: Rigid body analysis: *Stewart J. Cort*. Sample bending moment time series at midship: Subplex for midship bending moment. TEV = $3.0\sigma_{BM}$, N = 101, heading angle = 180°, forward speed = 12.5 knots. Average time series generated from 2000 sample time series; 20 sample time series are plotted.

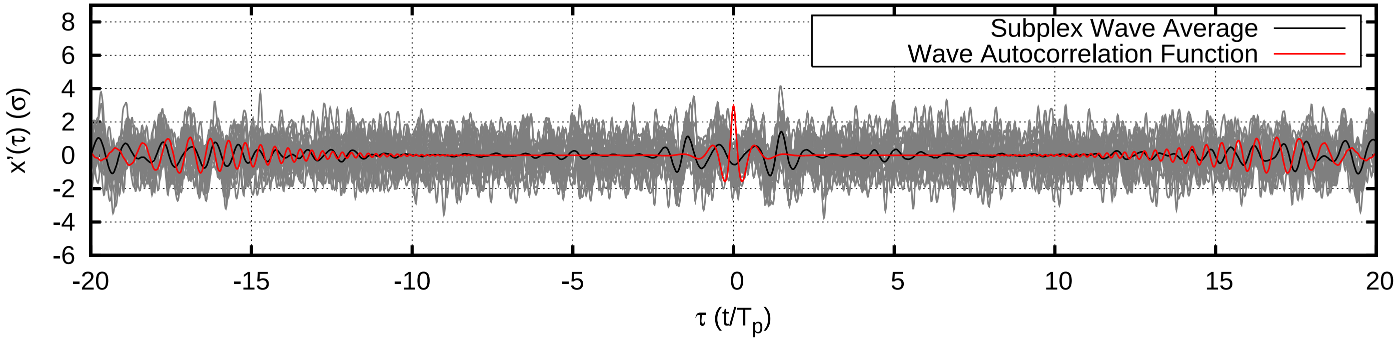

Figure A.103: Rigid body analysis: *Stewart J. Cort*. Sample wave time series at midship: Subplex for midship bending moment. TEV = $3.0\sigma_{BM}$, N = 101, heading angle = 180°, forward speed = 12.5 knots. Average time series generated from 2000 sample time series; 20 sample time series are plotted.

A.10 Case 10

Case	**10**	
Heading Angle	180.00	deg
Forward Speed	6.43	m/s
H_{sig}	5.58	m
T_{peak}	8.80	sec
N	101	
ω_{min}	0.350	rad/s
ω_{max}	2.500	rad/s
σ_{wave}	1.395	m
$\sigma_{response}$	0.240E+09	MKS units
maximum attainable value	8.27	σ_{sim}
TEV	5.00	σ_{sim}
TEV/maximum attainable value	0.60	
m	3488555	
Monte Carlo Simulation	no	
time to run subplex optimization	29089.	sec
Extreme Value PDF Comparison		
μ_{Ochi}	**5.10**	
$\mu_{subplex}$	5.07	
σ_{Ochi}	**0.24**	
$\sigma_{subplex}$	0.64	
Subplex: $D_{KL}(f_{x_m}(x) \| f_{x_1}(x))$	0.20	

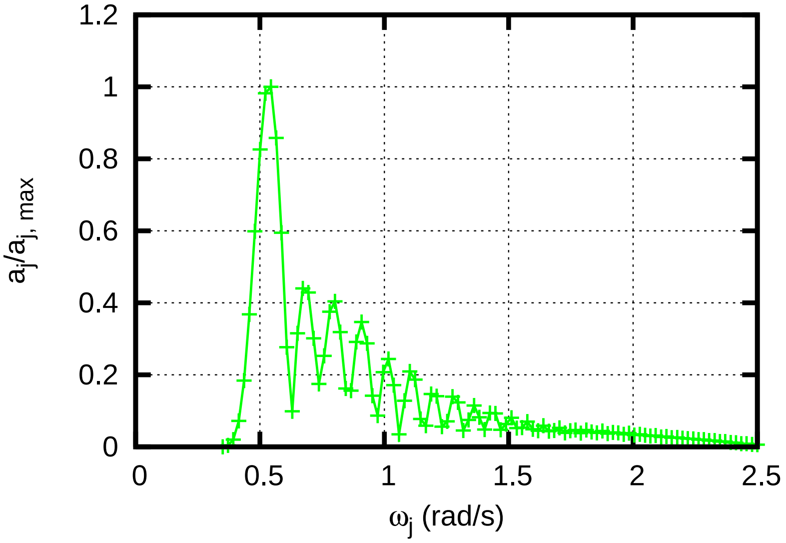

Figure A.104: Rigid body analysis: *Stewart J. Cort*. Amplitudes for midship bending moment. $N = 101$, heading angle = 180°, forward speed = 12.5 knots.

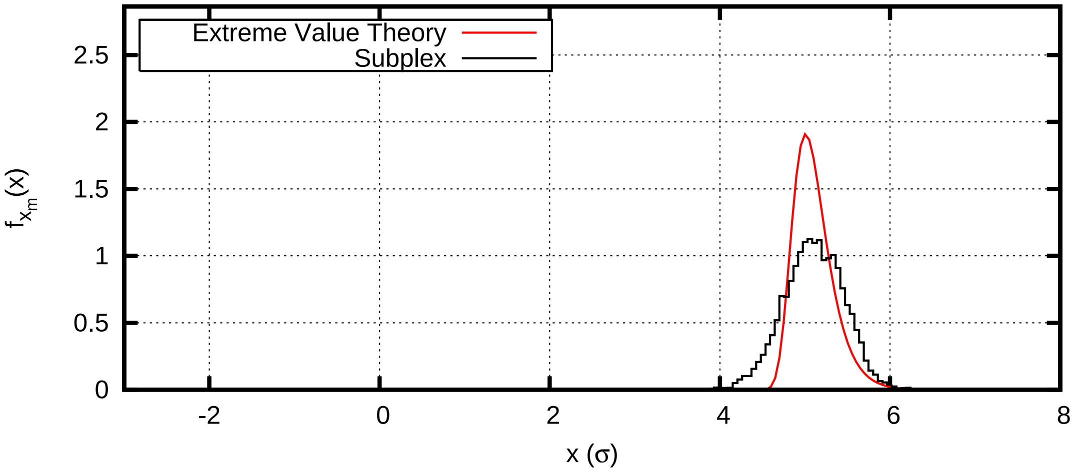

Figure A.105: Rigid body analysis: *Stewart J. Cort*. Extreme value PDFs for midship bending moment. TEV $= 5.0\sigma_{BM}$, $N =$ 101, heading angle = 180°, forward speed = 12.5 knots.

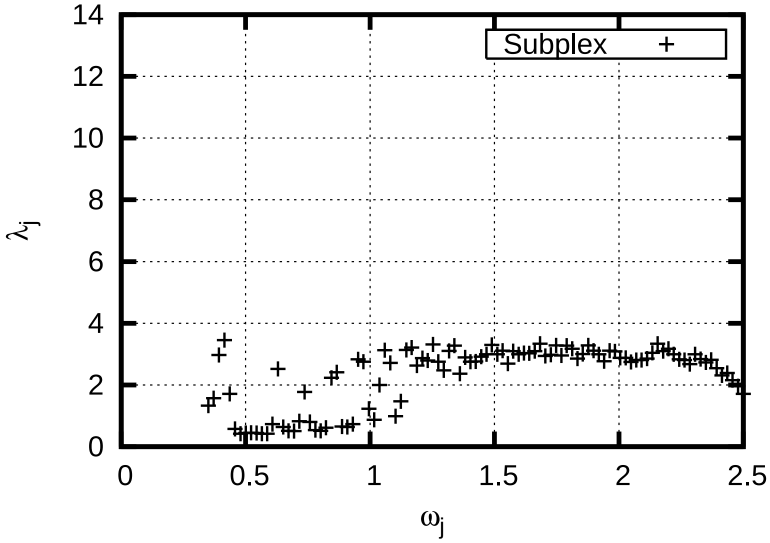

Figure A.106: Rigid body analysis: *Stewart J. Cort.* λ_j for midship bending moment. TEV = $5.0\sigma_{BM}$, $N = 101$, heading angle = 180°, forward speed = 12.5 knots.

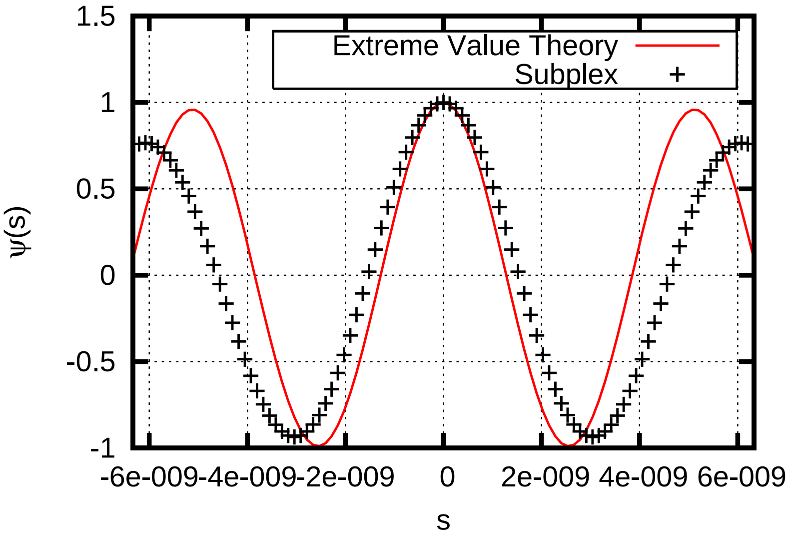

Figure A.107: Rigid body analysis: *Stewart J. Cort.* Characteristic functions for midship bending moment. TEV = $5.0\sigma_{BM}$, $N = 101$, heading angle = 180°, forward speed = 12.5 knots.

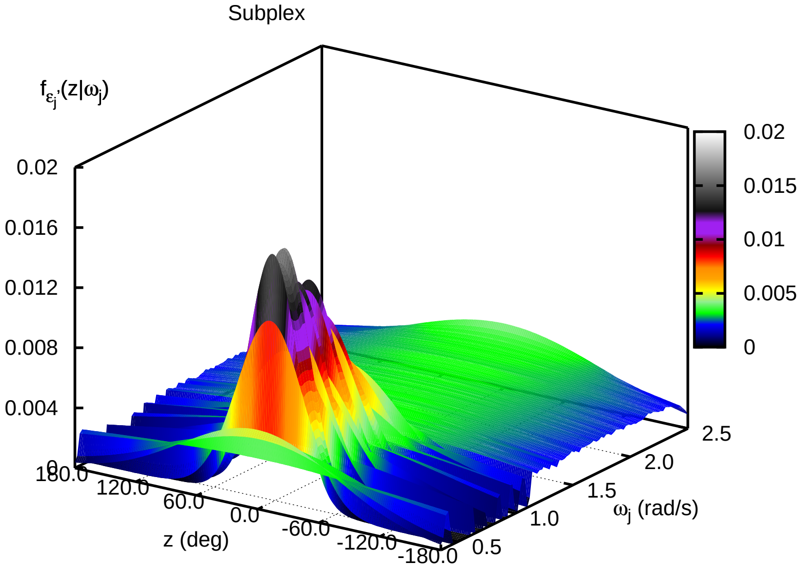

Figure A.108: Rigid body analysis: *Stewart J. Cort*. Phase PDF for Subplex optimization, midship bending moment. TEV $= 5.0\sigma_{BM}$, $N = 101$, heading angle = 180°, forward speed = 12.5 knots.

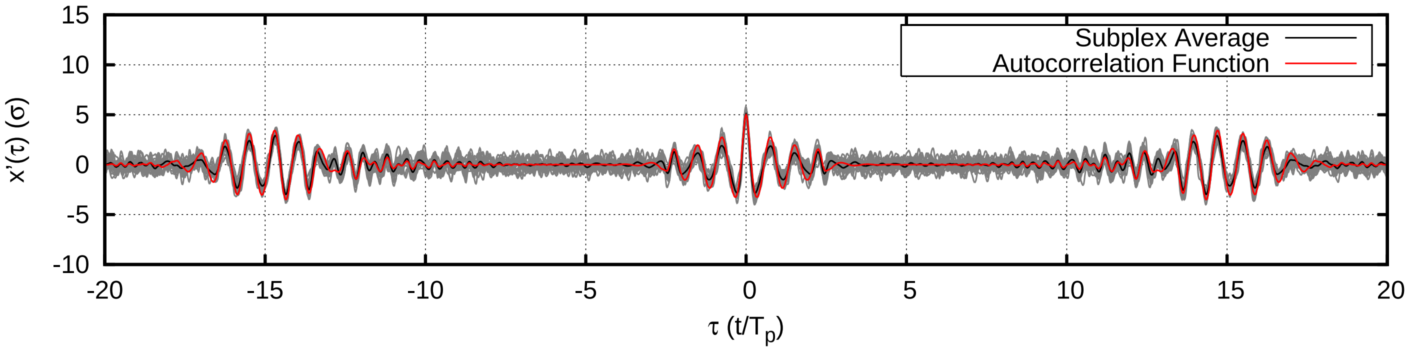

Figure A.109: Rigid body analysis: *Stewart J. Cort.* Sample bending moment time series at midship: Subplex for midship bending moment. TEV = $5.0\sigma_{BM}$, $N = 101$, heading angle = 180°, forward speed = 12.5 knots. Average time series generated from 2000 sample time series; 20 sample time series are plotted.

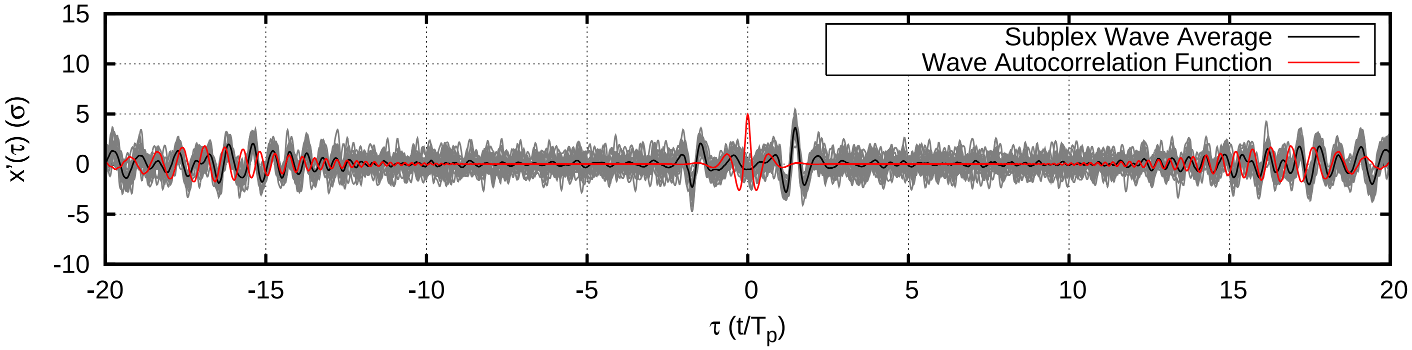

Figure A.110: Rigid body analysis: *Stewart J. Cort.* Sample wave time series at midship: Subplex for midship bending moment. TEV = $5.0\sigma_{BM}$, $N = 101$, heading angle = 180°, forward speed = 12.5 knots. Average time series generated from 2000 sample time series; 20 sample time series are plotted.

A.11 Case 11

Case	**11**	
Heading Angle	180.00	deg
Forward Speed	6.43	m/s
H_{sig}	5.58	m
T_{peak}	8.80	sec
N	101	
ω_{min}	0.350	rad/s
ω_{max}	1.250	rad/s
σ_{wave}	1.395	m
$\sigma_{response}$	0.671E+09	MKS units
maximum attainable value	8.50	σ_{sim}
TEV	3.00	σ_{sim}
TEV/maximum attainable value	0.35	
m	740	
Monte Carlo Simulation	yes	
time to run subplex optimization	62719.	sec

Case	**11**
Extreme Value PDF Comparison	
μ_{Ochi}	**3.15**
μ_{MC}	2.94
μ_{H1}	1.26
μ_{H2}	2.94
μ_{H2CF}	2.87
$\mu_{subplex}$	3.12
σ_{Ochi}	**0.36**
σ_{MC}	0.27
σ_{H1}	1.00
σ_{H2}	0.63
σ_{H2CF}	0.61
$\sigma_{subplex}$	0.61
MC: $D_{KL}(f_{x_m}(x)\|f_{x_1}(x))$	0.22
H1: $D_{KL}(f_{x_m}(x)\|f_{x_1}(x))$	2.05
H2: $D_{KL}(f_{x_m}(x)\|f_{x_1}(x))$	0.25
H2CF: $D_{KL}(f_{x_m}(x)\|f_{x_1}(x))$	0.28
Subplex: $D_{KL}(f_{x_m}(x)\|f_{x_1}(x))$	0.09

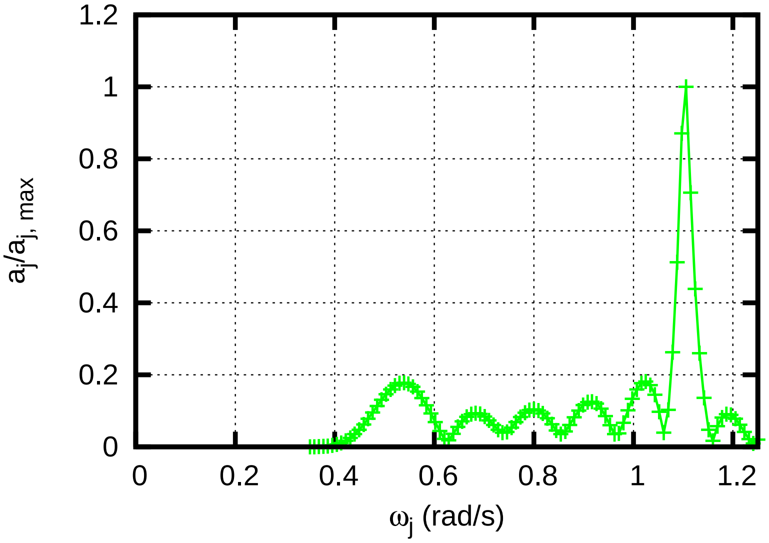

Figure A.111: Elastic body analysis: *Stewart J. Cort.* Amplitudes for midship bending moment. $N = 101$, heading angle = 180°, forward speed = 12.5 knots.

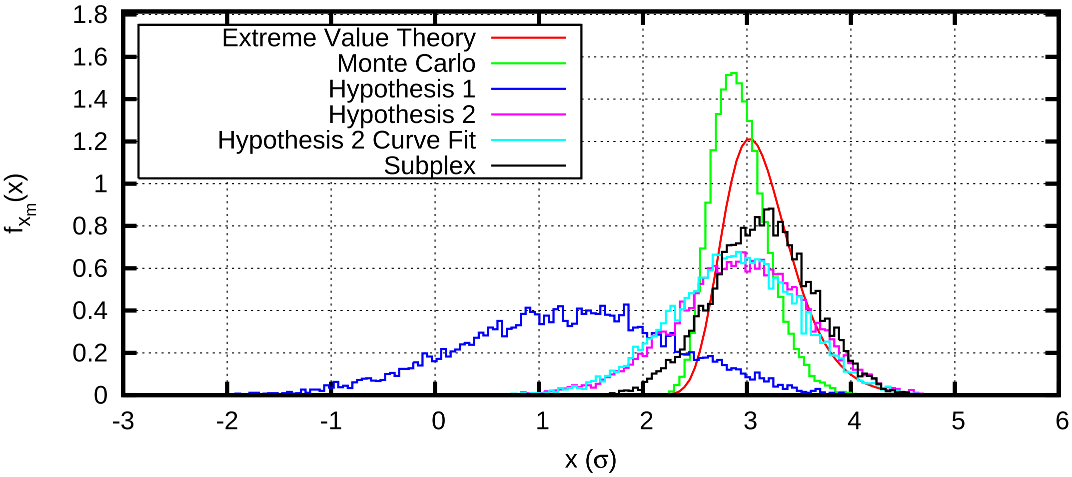

Figure A.112: Elastic body analysis: *Stewart J. Cort.* Extreme value PDFs for midship bending moment. TEV $= 3.0\sigma_{BM}$, $N =$ 101, heading angle = 180°, forward speed = 12.5 knots.

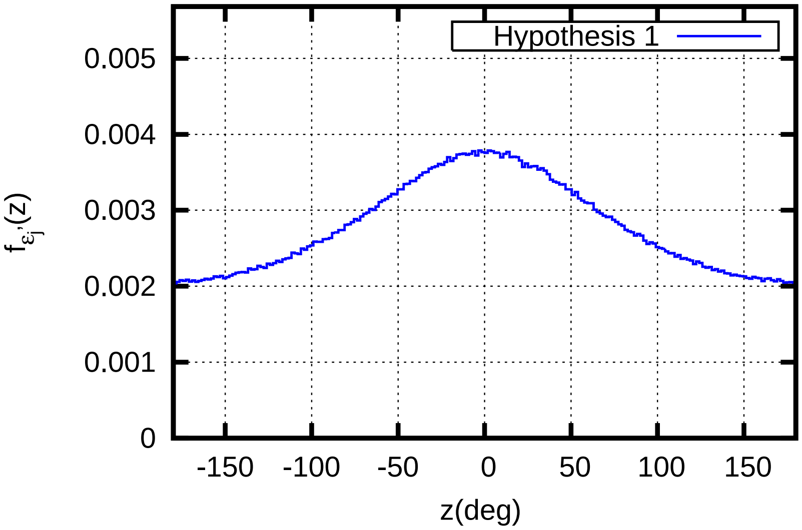

Figure A.113: Elastic body analysis: *Stewart J. Cort.* Phase histogram for Hypothesis 1, midship bending moment. TEV = $3.0\sigma_{BM}$, $N = 101$, heading angle = 180°, forward speed = 12.5 knots.

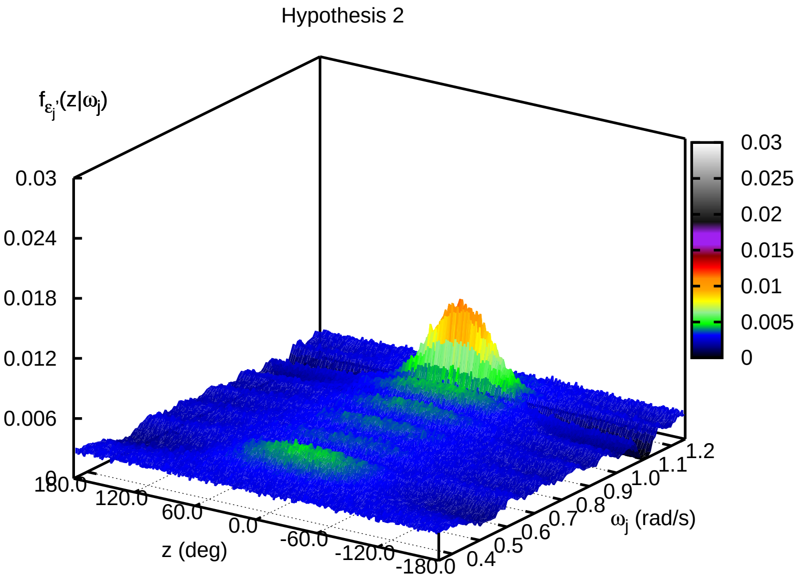

Figure A.114: Elastic body analysis: *Stewart J. Cort.* Phase histogram for Hypothesis 2, midship bending moment. TEV = $3.0\sigma_{BM}$, $N = 101$, heading angle = 180°, forward speed = 12.5 knots.

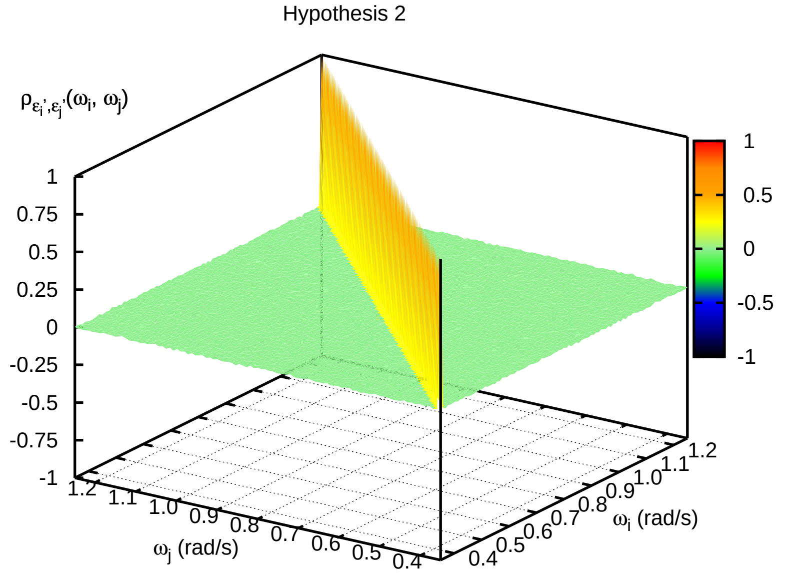

Figure A.115: Elastic body analysis: *Stewart J. Cort.* Correlation of phase pairs $(\epsilon_i', \epsilon_j')$ for Hypothesis 2. TEV = $3.0\sigma_{BM}$, $N = 101$, heading angle = 180°, forward speed = 12.5 knots.

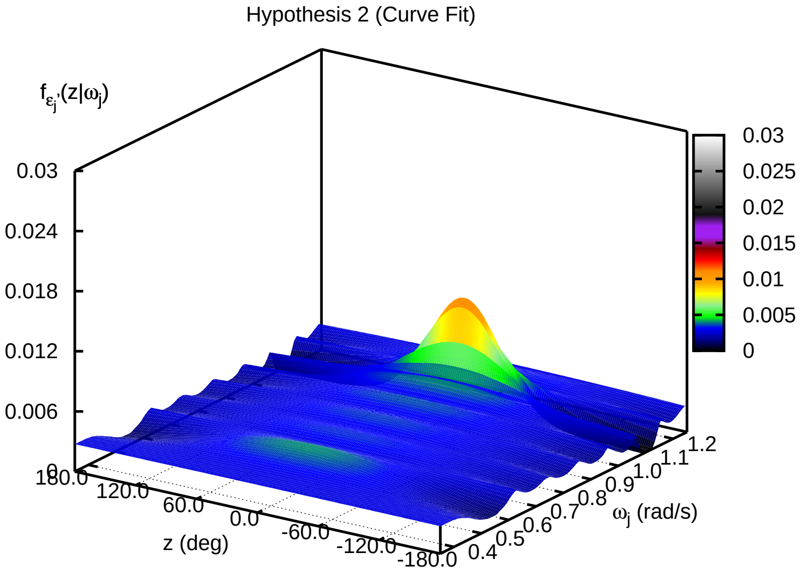

Figure A.116: Elastic body analysis: *Stewart J. Cort.* Phase PDF for Hypothesis 2 Curve Fit, midship bending moment. TEV = $3.0\sigma_{BM}$, $N = 101$, heading angle = 180°, forward speed = 12.5 knots.

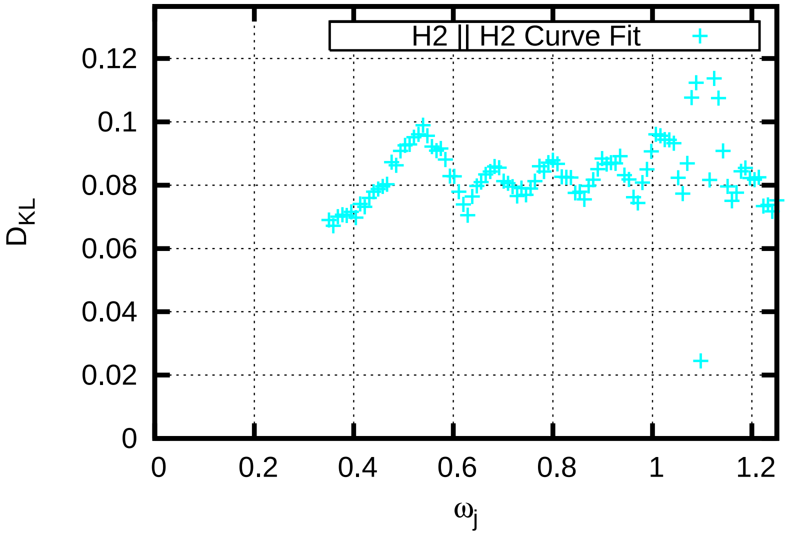

Figure A.117: Elastic body analysis: *Stewart J. Cort*. Comparison of Hypothesis 2 and Hypothesis 2 Curve Fit phase PDFs using the Kullback-Leibler divergence, $D_{KL}(f_{\epsilon'_j,MC}(z)\|f_{\epsilon'_j,MG}(z))$. TEV $= 3.0\sigma_{BM}$, $N = 101$, heading angle = 180°, forward speed = 12.5 knots.

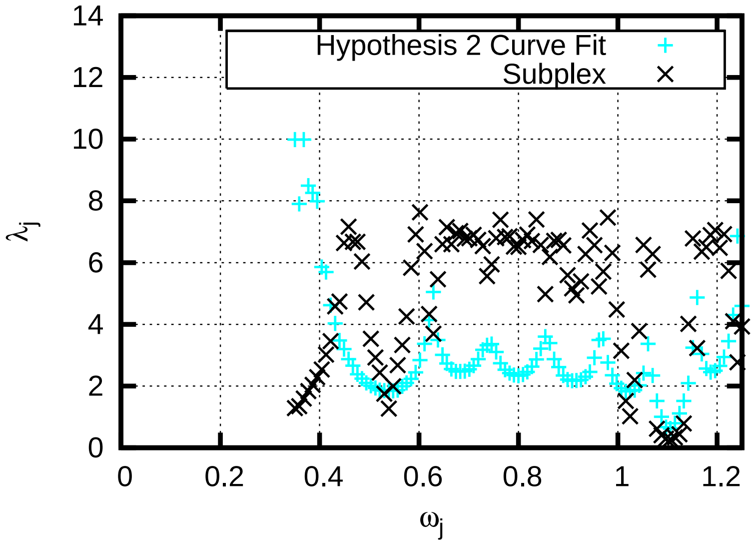

Figure A.118: Elastic body analysis: *Stewart J. Cort*. λ_j for midship bending moment. TEV $= 3.0\sigma_{BM}$, $N = 101$, heading angle = 180°, forward speed = 12.5 knots.

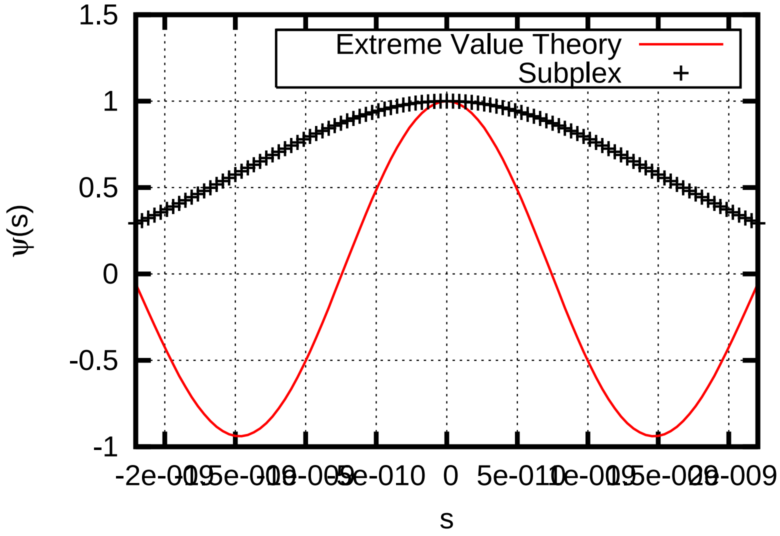

Figure A.119: Elastic body analysis: *Stewart J. Cort*. Characteristic Functions for midship bending moment. TEV $= 3.0\sigma_{BM}$, $N = 101$, heading angle = 180°, forward speed = 12.5 knots.

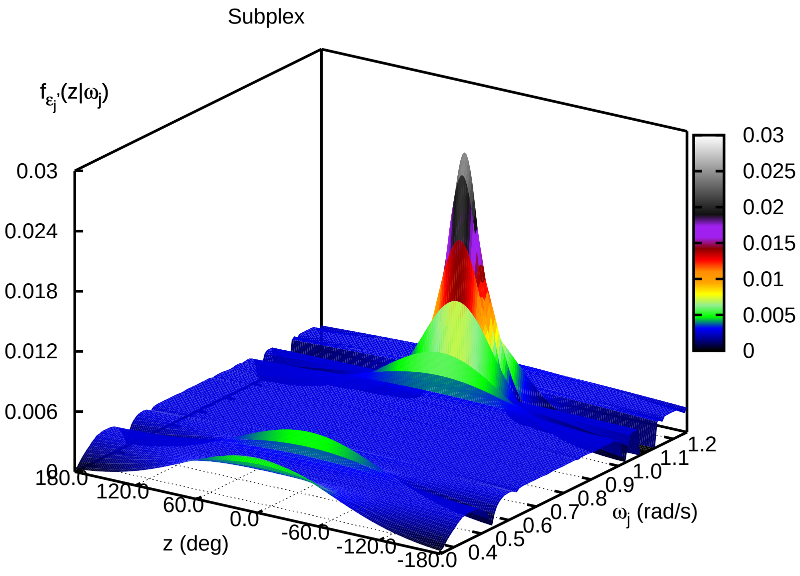

Figure A.120: Elastic body analysis: *Stewart J. Cort*. Phase PDF for Subplex optimization, midship bending moment. TEV $= 3.0\sigma_{BM}$, $N = 101$, heading angle = 180°, forward speed = 12.5 knots.

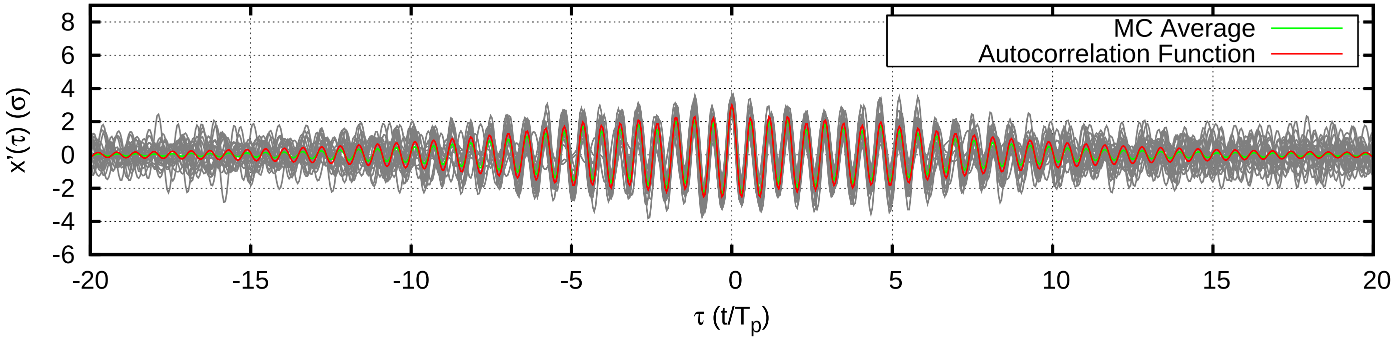

Figure A.121: Elastic body analysis: *Stewart J. Cort*. Sample bending moment time series at midship: Monte Carlo Simulation for midship bending moment. TEV = $3.0\sigma_{BM}$, $N = 101$, heading angle = 180°, forward speed = 12.5 knots. Average time series generated from 2000 sample time series; 20 sample time series are plotted.

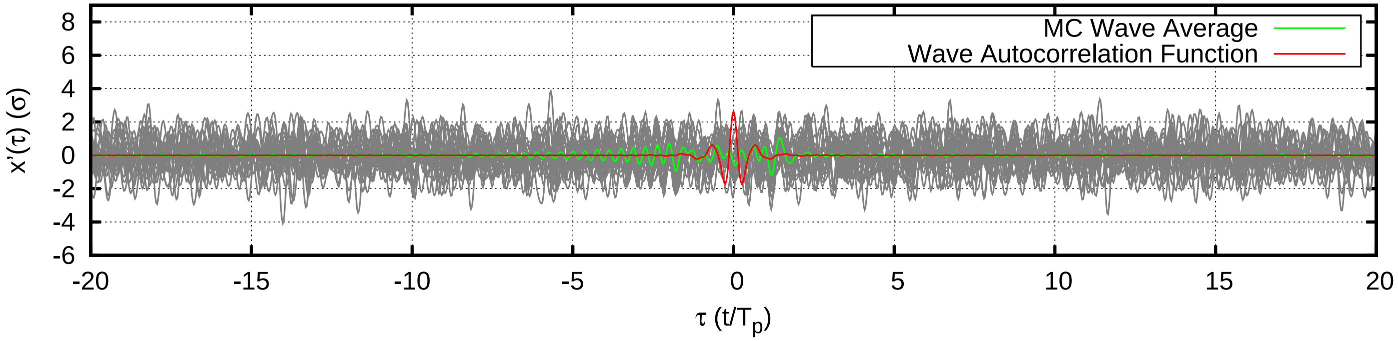

Figure A.122: Elastic body analysis: *Stewart J. Cort*. Sample wave time series at midship: Monte Carlo Simulation for midship bending moment. TEV = $3.0\sigma_{BM}$, $N = 101$, heading angle = 180°, forward speed = 12.5 knots. Average time series generated from 2000 sample time series; 20 sample time series are plotted.

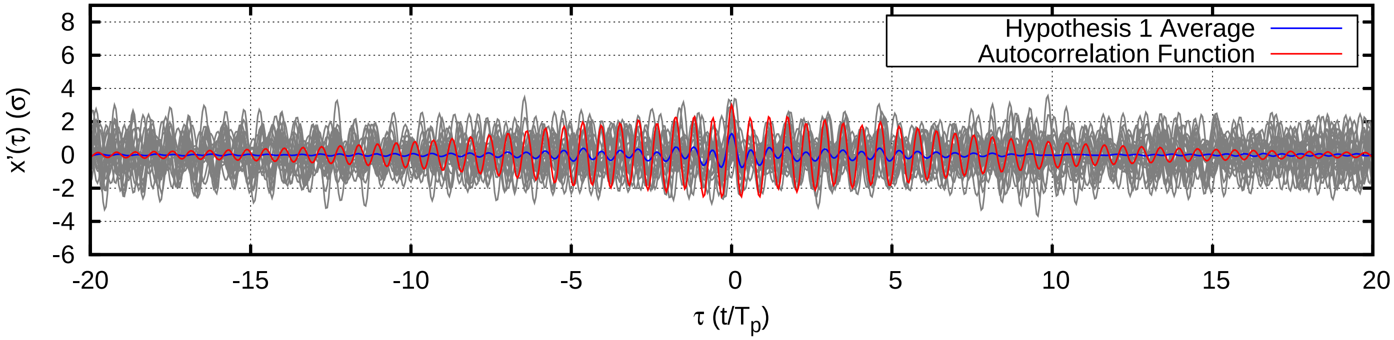

Figure A.123: Elastic body analysis: *Stewart J. Cort*. Sample bending moment time series at midship: Hypothesis 1 for midship bending moment. TEV $= 3.0\sigma_{BM}$, $N = 101$, heading angle = 180°, forward speed = 12.5 knots. Average time series generated from 2000 sample time series; 20 sample time series are plotted.

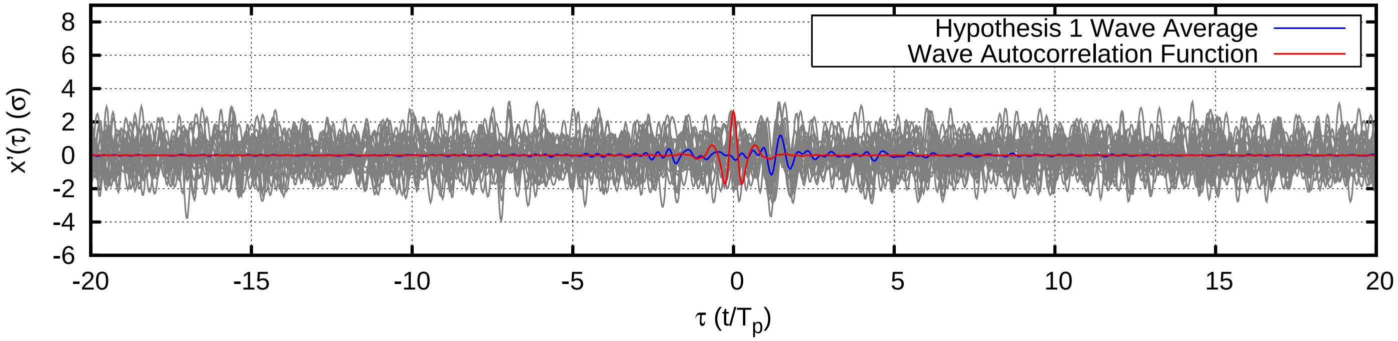

Figure A.124: Elastic body analysis: *Stewart J. Cort*. Sample wave time series at midship: Hypothesis 1 for midship bending moment. TEV $= 3.0\sigma_{BM}$, $N = 101$, heading angle = 180°, forward speed = 12.5 knots. Average time series generated from 2000 sample time series; 20 sample time series are plotted.

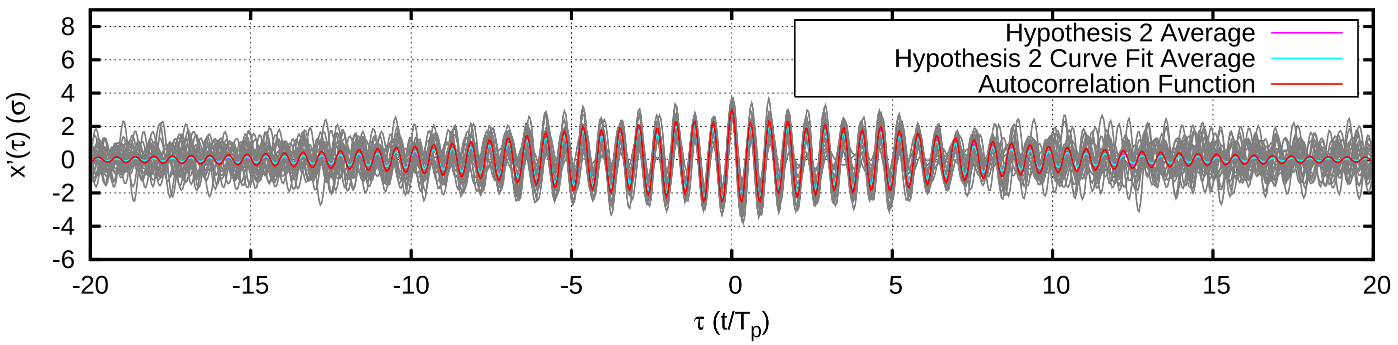

Figure A.125: Elastic body analysis: *Stewart J. Cort*. Sample bending moment time series at midship: Hypothesis 2 and Hypothesis 2 Curve Fit for midship bending moment. TEV = $3.0\sigma_{BM}$, $N = 101$, heading angle = 180°, forward speed = 12.5 knots. Average time series generated from 2000 sample time series; 20 sample time series are plotted.

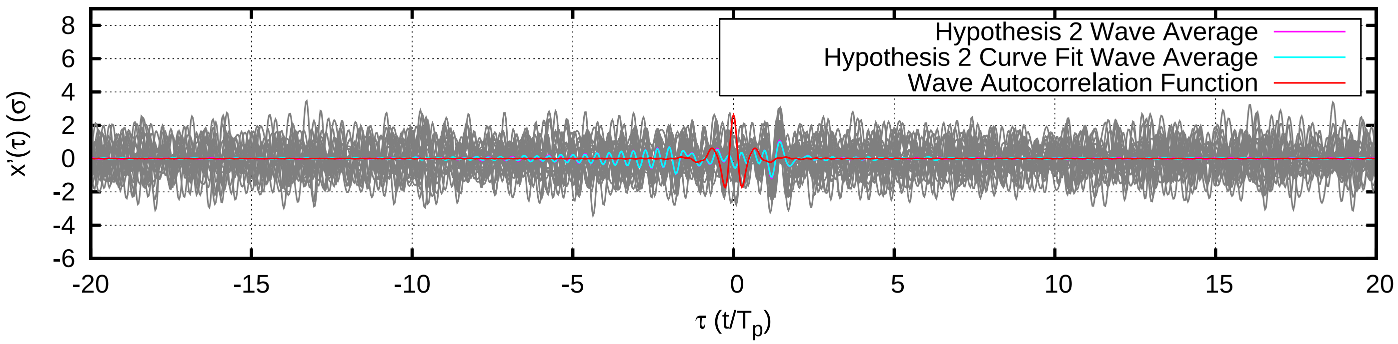

Figure A.126: Elastic body analysis: *Stewart J. Cort*. Sample wave time series at midship: Hypothesis 2 and Hypothesis 2 Curve Fit for midship bending moment. TEV = $3.0\sigma_{BM}$, $N = 101$, heading angle = 180°, forward speed = 12.5 knots. Average time series generated from 2000 sample time series; 20 sample time series are plotted.

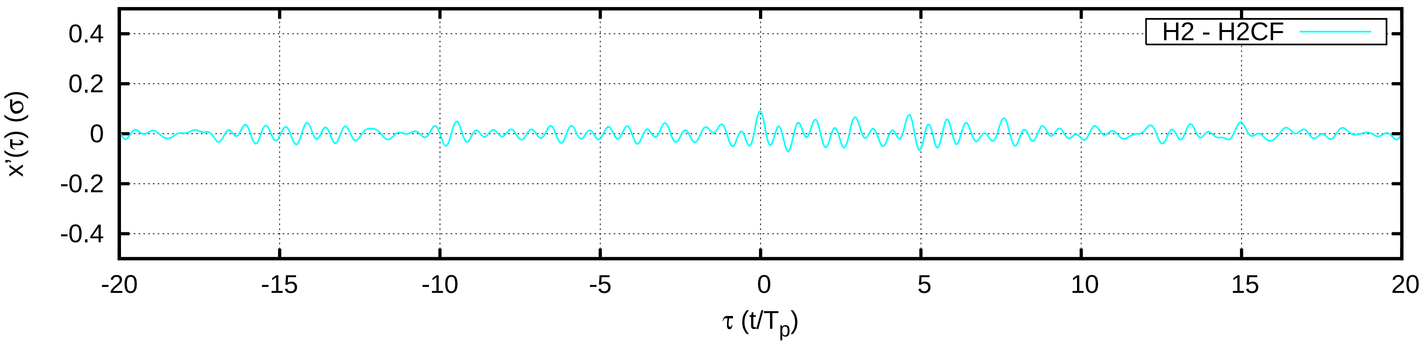

Figure A.127: Elastic body analysis: *Stewart J. Cort.* Comparison of Hypothesis 2 and Hypothesis 2 Curve Fit average time series. The difference between these two average time series is plotted. TEV = $3.0\sigma_{BM}$, $N = 101$, heading angle = 180°, forward speed = 12.5 knots.

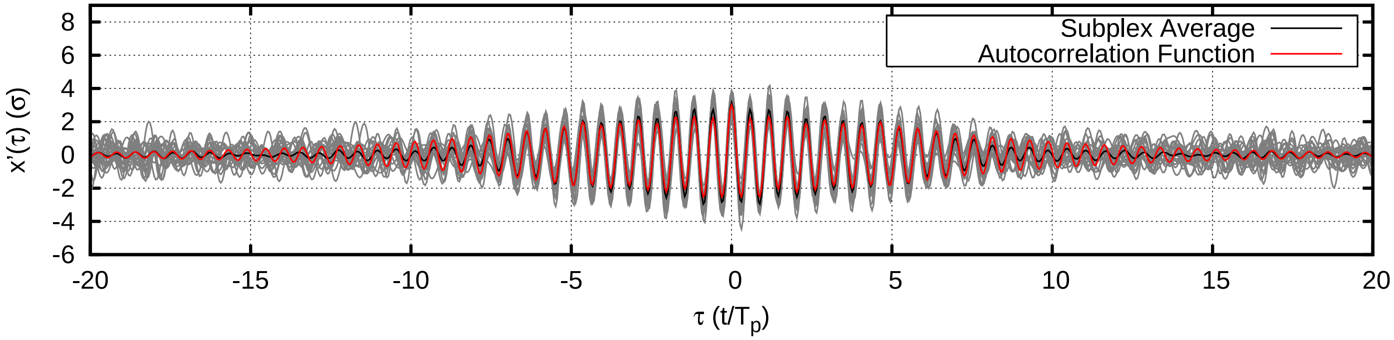

Figure A.128: Elastic body analysis: *Stewart J. Cort*. Sample bending moment time series at midship: Subplex for midship bending moment. TEV = $3.0\sigma_{BM}$, N = 101, heading angle = 180°, forward speed = 12.5 knots. Average time series generated from 2000 sample time series; 20 sample time series are plotted.

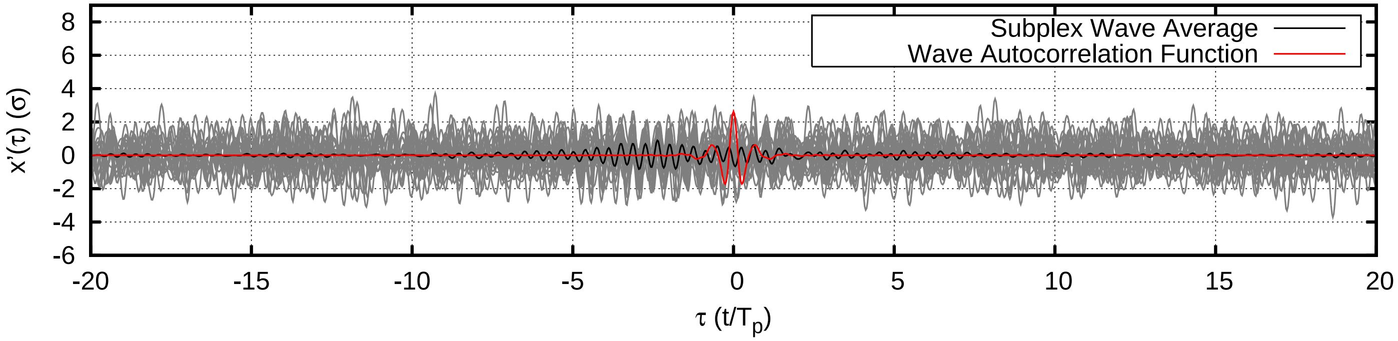

Figure A.129: Elastic body analysis: *Stewart J. Cort*. Sample wave time series at midship: Subplex for midship bending moment. TEV = $3.0\sigma_{BM}$, N = 101, heading angle = 180°, forward speed = 12.5 knots. Average time series generated from 2000 sample time series; 20 sample time series are plotted.

A.12 Case 12

Case	**12**	
Heading Angle	180.00	deg
Forward Speed	6.43	m/s
H_{sig}	5.58	m
T_{peak}	8.80	sec
N	101	
ω_{min}	0.350	rad/s
ω_{max}	1.250	rad/s
σ_{wave}	1.395	m
$\sigma_{response}$	0.671E+09	MKS units
maximum attainable value	8.50	σ_{sim}
TEV	5.00	σ_{sim}
TEV/maximum attainable value	0.59	
m	3488555	
Monte Carlo Simulation	no	
time to run subplex optimization	21651.	sec
Extreme Value PDF Comparison		
μ_{Ochi}	**5.10**	
$\mu_{subplex}$	5.06	
σ_{Ochi}	**0.24**	
$\sigma_{subplex}$	0.72	
Subplex: $D_{KL}(f_{x_m}(x) \| f_{x_1}(x))$	0.42	

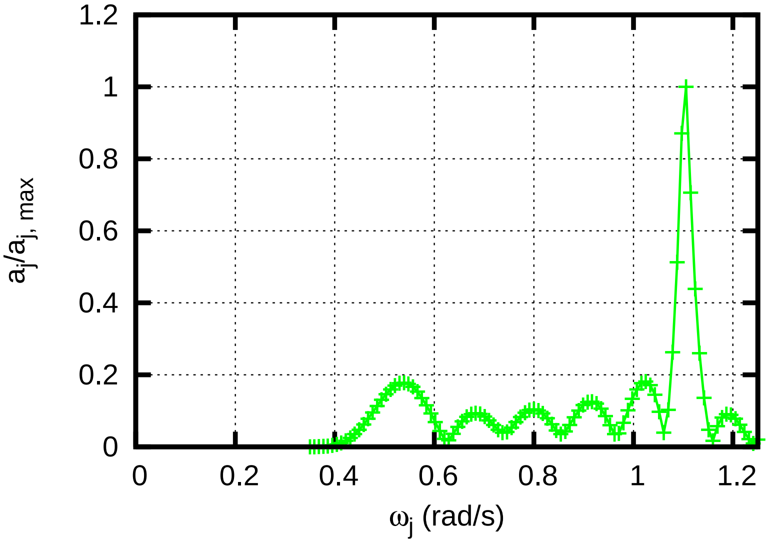

Figure A.130: Elastic body analysis: *Stewart J. Cort*. Amplitudes for midship bending moment. $N = 101$, heading angle = 180°, forward speed = 12.5 knots.

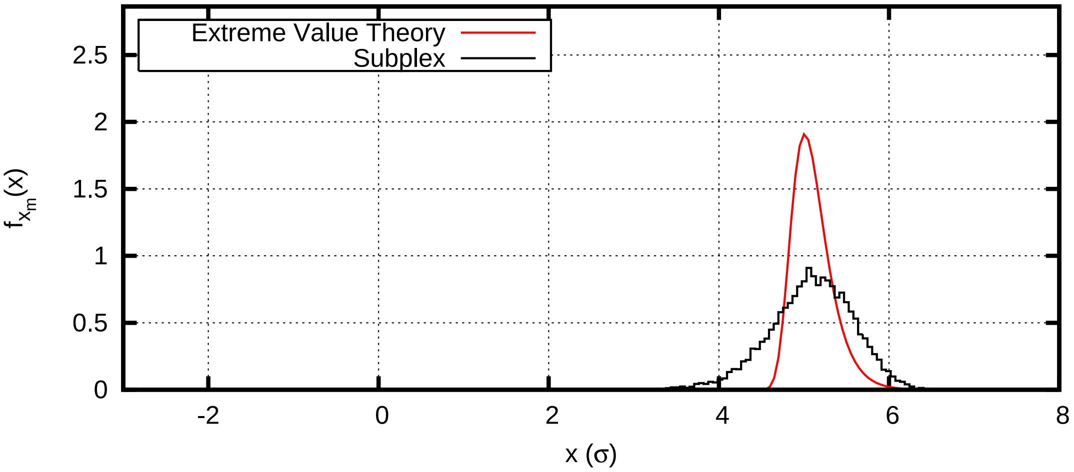

Figure A.131: Elastic body analysis: *Stewart J. Cort*. Extreme value PDFs for midship bending moment. TEV $= 5.0\sigma_{BM}$, $N =$ 101, heading angle = 180°, forward speed = 12.5 knots.

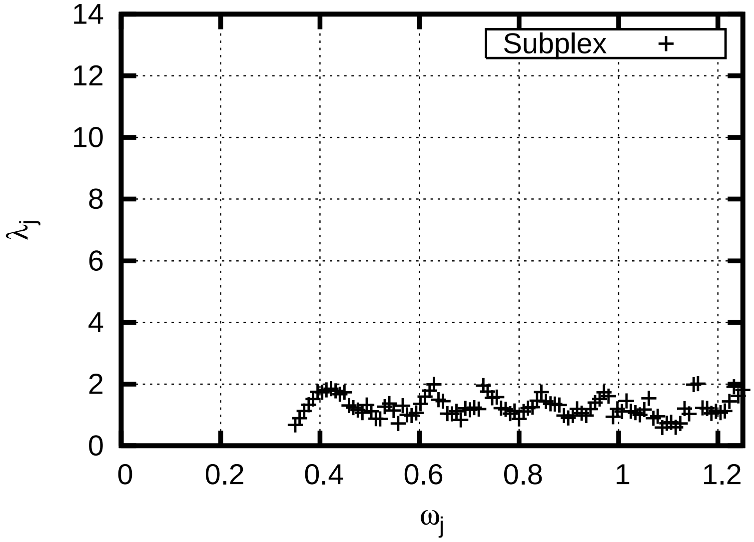

Figure A.132: Elastic body analysis: *Stewart J. Cort.* λ_j for midship bending moment. TEV $= 5.0\sigma_{BM}$, $N = 101$, heading angle $= 180°$, forward speed $= 12.5$ knots.

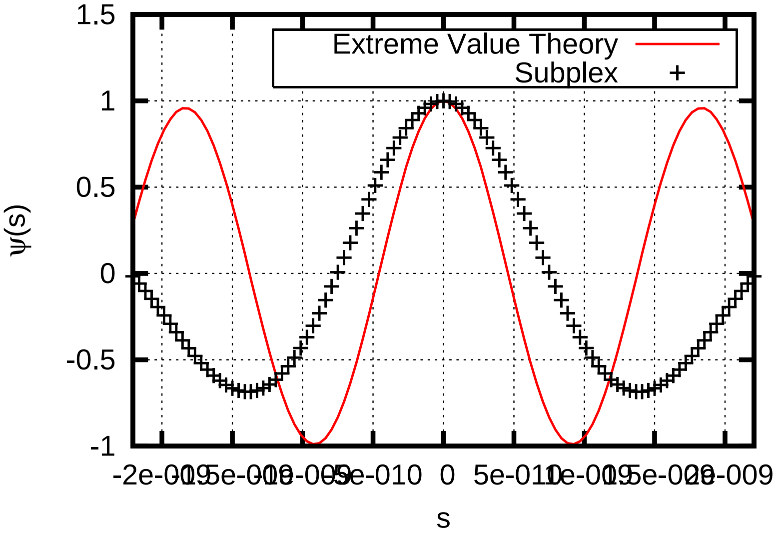

Figure A.133: Elastic body analysis: *Stewart J. Cort.* Characteristic Functions for midship bending moment. TEV $= 5.0\sigma_{BM}$, $N = 101$, heading angle $= 180°$, forward speed $= 12.5$ knots.

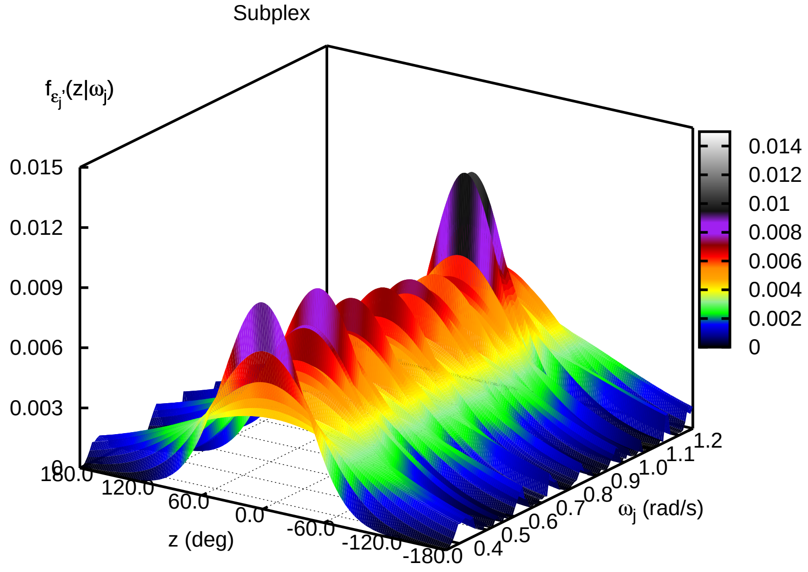

Figure A.134: Elastic body analysis: *Stewart J. Cort*. Phase PDF for Subplex optimization, midship bending moment. TEV $= 5.0\sigma_{BM}$, N = 101, heading angle = 180°, forward speed = 12.5 knots.

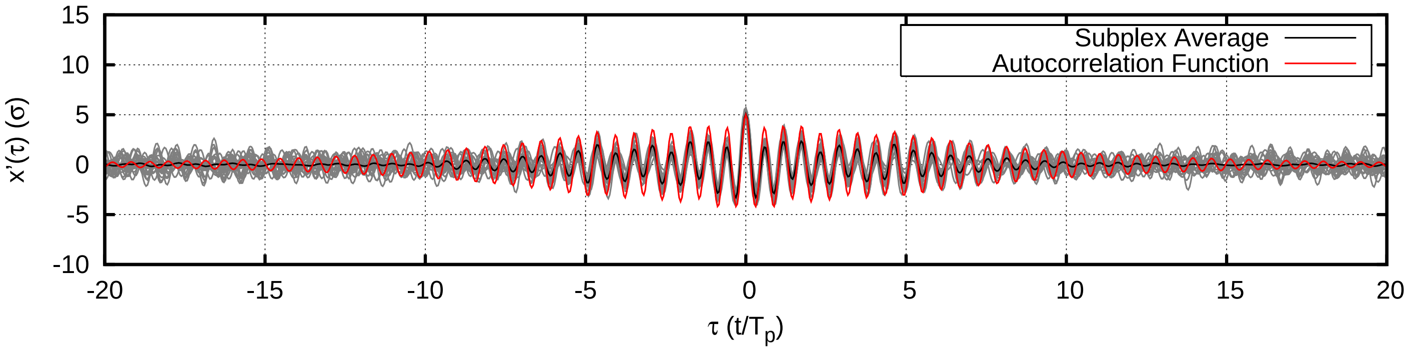

Figure A.135: Elastic body analysis: *Stewart J. Cort*. Sample bending moment time series at midship: Subplex for midship bending moment. TEV = $5.0\sigma_{BM}$, N = 101, heading angle = 180°, forward speed = 12.5 knots. Average time series generated from 2000 sample time series; 20 sample time series are plotted.

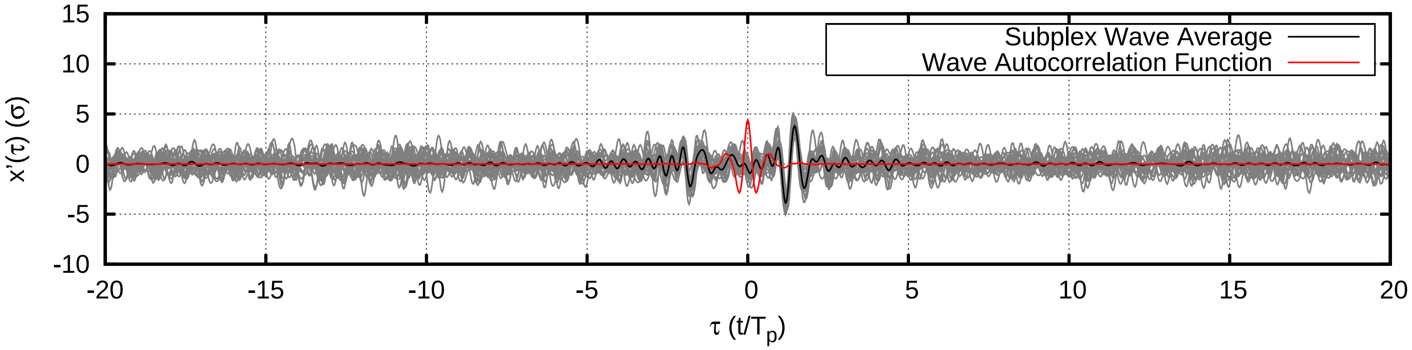

Figure A.136: Elastic body analysis: *Stewart J. Cort*. Sample wave time series at midship: Subplex for midship bending moment. TEV = $5.0\sigma_{BM}$, N = 101, heading angle = 180°, forward speed = 12.5 knots. Average time series generated from 2000 sample time series; 20 sample time series are plotted.

APPENDIX B

Computer Program OPTLAMBDA

B.1 Input and Output Files

Table B.1: Input files for the OPTLAMBDA program (see Table 4.1 for variable assignments)

Input File	**Columns**	**Description**
`InputSpectrum.dat`	ω_j, x_j	the spectrum that describes the operating sea state; depends on incident wave spectrum
`SubplexParam.dat`		parameters for the subplex optimization routine
`TransferFunction.dat`	$\lvert H(\omega_j)\rvert$, γ_j	transfer function of the response in question; depends on speed, heading angle, response, etc.

Table B.2: Output files for the OPTLAMBDA program (see Table 4.1 for variable assignments)

Output File	**Columns**	**Description**
`a.dat`	y_j	the discrete amplitudes of the response (MKS units)
`a_excitation.dat`	x_j	the discrete amplitudes of the incident wave (meters)
`CharFuncs_subplex.dat`	s_k, $\psi_{x_m}(s_k)$, $\psi_{x'}(s_k)$	discretized characteristic functions of $f_{x_m}(x)$ and $f_{x'}(x)$
`lambda_subplex.dat`	λ_j	the set of λ_j as determined by the optimization routine
`OchiEVPDF.dat`	x/σ, $f_{x_m}(x)$	PDF of the extreme value in m samples, as calculated according to Eq. 2.25 (based on MKS units)
`omega.dat`	ω_j	discrete frequencies (rad/sec)
`SubplexOut.dat`		record of the optimaztion results
`TransferPhase.dat`	γ_j	discrete phases of the transfer function (rad)

B.2 Modules, Subroutines, and Functions

Table B.3: Modules used in the OPTLAMBDA program.

Module	**Description**
`nr`	from *NUMERICAL RECIPES in Fortran 90*; defines interfaces for all *NR* routines except those in `nrutil`
`nrtype`	from *NUMERICAL RECIPES in Fortran 90*; defines `KIND` types and frequently used variables
`nrutil`	from *NUMERICAL RECIPES in Fortran 90*; defines implementations of *NR* utility functions; mostly used for error calls
`SharedData`	declares of most of the variables used in OPTLAMBDA; allows for access of parameters and data by various subroutines and functions
`SpecialFunctions`	defines several frequently used special functions, such as the error function, `erf_d`

Table B.4: Subroutines used in the OPTLAMBDA program.

Subroutine	**Location**	**Description**
`runsubplex`	`OptLambda.f90`	initializes variables on first call and runs first pass through `subplx`; thereafter controls subsequent calls to `subplx`
`plotfun`	`OptLambda.f90`	calculates the final error between characteristic functions and writes the `CharFunc_subplex.dat` file
`indexx_dp`	`OptLambda.f90`	reads in an array and creates an index array such that `array(IndexArray(j))` is in increasing order; used to put `a` in decreasing order, expediting the optimization process
`subplx`	`subplx.f`	controls the subplex optimization process; written by Tom Rowan and used “as-is”; see Table B.5 for dependencies

Table B.5: List of dependent files for the `subplx` subroutine; these files were written by Tom Rowan and used "as-is"

`calcc.f`
`dasum.f`
`daxpy.f`
`dcopy.f`
`dist.f`
`dscal.f`
`evalf.f`
`fstats.f`
`newpt.f`
`order.f`
`partx.f`
`setstp.f`
`simplx.f`
`sortd.f`
`start.f`
`subopt.f`

Table B.6: Functions used in the OPTLAMBDA program.

Function	**Location**	**Description**
`fun`	`OptLambda.f90`	evaluates $\psi_{x'}(s_k)$ based on the current set of λ_j then computes cost function f as defined in Eq. 3.21; **boundaries:** if any $\lambda_j > 10$ or < 0.001, returns $f = 9.99$`e`20
`erf_d`	`SpecialFunctions.f90`	from *NUMERICAL RECIPES in Fortran 90*; computes the value of the Error Function at a given value
`gammp_d`	`SpecialFunctions.f90`	from *NUMERICAL RECIPES in Fortran 90*; used by `erf_d`
`gser_d`	`SpecialFunctions.f90`	from *NUMERICAL RECIPES in Fortran 90*; used by `erf_d`
`gammln_d`	`SpecialFunctions.f90`	from *NUMERICAL RECIPES in Fortran 90*; used by `erf_d`

BIBLIOGRAPHY

BIBLIOGRAPHY

Adegeest, L., Braathen, A., & Løseth, R. M. 1998. Use of non-linear sea-loads simulations in design of ships. *Proc. Practical Design of Ships and Mobile Units (PRADS)*, 53–58.

Adegeest, L., Braathen, A., & Vada, T. 1999. Evaluation of Methods for Estimation of Extreme Nonlinear Ship Responses Based on Numerical Simulations and Model Tests. *Proc. Twenty-Second Symposium on Naval Hydrodynamics*, 84–99.

Alford, L. K., & Troesch, A. W. 2007. Maximums of Random Processes and Non-Uniform Phase Distributions. *2007 SIAM Conference on Applications of Dynamical Systems.*

Alford, L. K., Troesch, A. W., & McCue, L. S. 2005. Design Wave Elevations Leading to Extreme Roll Motion. *Proc. 8th International Ship Stability Workshop.*

Alford, L. K., Troesch, A. W., & Khalid, M. S. 2006. Results using response-tailored design waves in simulations of extreme roll of multi-hull ships. *Proc. 9th International Ship Stability Workshop.*

Alford, L. K., Wozniak, C., & Troesch, A. W. 2007. Extreme Responses of Bilinear Stiff Systems. *Proc. of OMAE2007, 26th International Conference on Offshore Mechanics and Arctic Engineering.*

Beck, R. F., & Troesch, A. W. 1990. *Students documentation and users manual for the computer program SHIPMO.BM.* Department of Naval Architecture and Marine Engineering, University of Michigan, Ann Arbor.

Boccotti, P. 1983. Some new results on statistical properties of wind waves. *Applied Ocean Research*, **5**(3), 134–140.

Chakrabarti, S., & Libby, A. 1988. Further verification of gaussian wave packets. *Applied Ocean Research*, **10(2)**, 106–108.

Clauss, G. F. 2002. Task-related rogue waves embedded in extreme seas. *Proc. Twenty-First International Conference on Offshore Mechanics and Arctic Engineering.*

Clauss, G. F., & Bergmann, J. 1986. Gaussian wave packets - A new approach to seakeeping tests of ocean structures. *Applied Ocean Research*, **10(2)**, 190–206.

Clauss, G. F., & Hennig, J. 2003. Deterministic analysis of extreme roll motions using tailored wave sequences. *Proc. Eighth International Conference on the Stability of Ships and Ocean Vehicles*, 441–455.

Clauss, G. F., & Kühnlein, W. L. 1997. Simulation of design storm wave conditions with tailored wave groups. *Proc. First International Offshore and Polar Engineering Conference*, 228–237.

Clauss, G. F., & Steinhagen, U. 1999. Numerical Simulation of nonlinear transient waves and its validation by laboratory data. *Proc. First International Offshore and Polar Engineering Conference*, 368–375.

Clauss, G. F., Hennig, J., Schmittner, C. E., & Kühnlein, W. L. 2004. Nonlinear calculation of tailored wave trains for experimental investigations of extreme structure behaviour. *Proc. Twenty-Third International Conference on Offshore Mechanics and Arctic Engineering.*

Clauss, G. F., Hennig, J., & Schmittner, C. E. 2005. Modelling Extreme Wave Sequences for the Hydrodynamic Analysis of Ships and offshore structures. *Proc. Practical Design of Ships and Mobile Units (PRADS).*

Jensen, J. J., & Pedersen, P. T. 2006. Critical Wave Episodes for Assessment of Parametric Roll. *Proc. 9th International Marine Design Conference*, 399–411.

Kullback, S., & Leibler, R. A. 1951. On information and sufficiency. *The Annals of Mathematical Statistics*, **22**, 79–86.

Lindgren, G. 1970. Some properties of a normal process near a local maximum. *The Annals of Mathematical Statistics*, **41**(6), 1870–1883.

Nelder, J., & Mead, R. 1965. A simplex method for function minimization. *Computer Journal*, **7**, 308–313.

Ochi, M. K. 1990. *Applied Probability and Stochastic Processes.* John Wiley & Sons.

Pastoor, L. W. 2002. *On the Assessment of Nonlinear ship motions and loads.* Ph.D. thesis, Technische Universiteit Delft.

Rowan, T. H. 1990. *Functional Stability Analysis of Numerical Algorithms.* Ph.D. thesis, The University of Texas at Austin.

Rozanov, Y. A. 1969. *Probability Theory: A Concise Course.* Dover Publications, Inc., New York.

Steinhagen, U. 2002. *Synthesizing Nonlinear Transient Gravity Waves in Random Seas.* Ph.D. thesis, Technische Universität Berlin.

Taylor, P. H., Jonathan, P., & Harland, L. A. 1995. Time domain simulation of jack-up Dynamics with the Extremes of a gaussian process. *Offshore Technology*, **1-A**, 53–58.

Torhaug, R., Winterstein, S. R., & Braathen, A. 1998. Nonlinear Ship Loads: Stochastic Models for Extreme Response. *Journal of Ship Research*, **42**(1), 46–55.

Troesch, A. W. 1984. Effects of nonlinearities on hull springing. *Marine Technology*, **21**(4), 356–363.

Troesch, A. W. 1997. Study of the Use of Nonlinear Time Domain Simulation in a Design Loads Generator (DLG). *Final Report to the American Bureau of Shipping.*

Tromans, P. S., Anaturk, A. R., & Hagemeijer, P. 1991. A new model for the kinematics of large ocean waves - application as a design wave. *Proc. First International Offshore and Polar Engineering Conference*, 64–71.

Various. 1979 (January). *Great Lakes Carriers hull stress monitoring system.* Tech. rept. U.S. Department of Commerce, Maritime Administration.

Various. 2007 (March). *Gnuplot.* http://www.gnuplot.info.